UNIVERSITA' DEGLI STUDI DI PADOVA

DIPARTIMENTO DI FACOLTA' DI SCIENZE MATEMATICHE, FISICHE E NATURALI

DOTTORATO DI RICERCA IN FISICA

CICLO XVIII

Light Charged Particles emission and high energy γ-rays from Giant Dipole Resonance in hot nuclei

Coordinatore : Ch.mo Prof. Attilio Stella

Supervisore : Ch.mo Prof. Paolo Mazzoldi **Co-Supervisore** : Dott. Fabiana Gramegna

Dottorando :Sandro Barlini

DATA CONSEGNA TESI
31 dicembre 2005

INDEX

INTRODUCTION

In the last twenty years, the knowledge of nuclear physics has been improved. The performances of new accelerators and the development of new experimental apparatuses, with better time, angular and energy resolution and a greater angular coverage to get an almost complete reconstruction of the events, have been quite important steps. They were necessary to better understand the complex mechanisms acting in nuclear reactions, and the underlying structure properties. Nevertheless, a lot of work is still needed, both from the theoretical and the experimental points of view, before to reach a complete understanding of nuclear reaction mechanisms and of the properties of the nuclei under extreme conditions.

An almost complete reconstruction of the events is needed even in those phenomena which have been extensivly studied, like, for example, the Giant Dipole Resonance (GDR) collective modes. In fact, the GDR is one of the most well known and studied collective modes and it can be built either on the ground state or on different excited states formed through heavy ion collisions. Accelerating a projectile against a target with enough energy, a new thermalized system, the Compound Nucleus (CN), can be formed. The CN-reaction conserves spin, angular momentum and isospin and the mass and at low energy (typically < 10 *MeV/A*) the charge of the new thermalized system will be equal to the sum of the two participants (complete fusion). The excited CN will then decade emitting particles and γ-rays. It can also start vibrating in such a way to create a Giant Dipole Resonance with the subsequent emission of high energy γ-rays. It is really very interesting to investigate this type of GDR built on exited states for its important relation with the structure of the excited nuclei, its connection with the nuclear shape deformation of hot rotating nuclear systems and for the study of the damping mechanism of the GDR themselves.

The complexity of this kind of studies is due to the fact that first of all one should define, as precise as possible, the Compound Nucleus and its configuration of states on which the resonance is built, giving the correct number of mass (A), charge (Z), excitation energy (E*) and temperature (T) of the source. This will permit then to determine the main characteristics of the GDR, its centroid and width. Increasing the beam energy, the growing up of temperature and angular momentum of the system, together with the shortening of particle emission times, make this analysis more difficult in the determination of the properties of the source of the emitting dipole. In fact, other competitive reaction mechanisms which can arise making less probable the formation of a fully thermalized

Compound Nucleus, so that the characterization of the decaying system, as far as A, Z, E* and T, becomes more ambiguous.

This means that, to keep under control the results of the experiment, one needs exclusive measurements. In the experiment, it can be important, for example, to detect at the same time the Evaporation Residue (ER) as hint of the formation of the Compound Nucleus, the Light Charged Particles (LCP), which are important in the estimation of the temperature of the source and to give information on possible pre-equilibrium emission and, obviously, the γ-rays emission. To combine all this information using a unique experimental apparatus is not a simple task.

This work of thesis is based on a campaign of measurements that has been performed within the GARFIELD and HECTOR collaborations. Its purposes are principally two:

- to perform an experiment on which, combining all the information from the detectors, it will be possible to have a good characterization of the emitting source needed for the analysis of the Giant Dipole Resonance;
- to compare the behavior of the same composite system produced using two different reactions, one with a symmetrical mass entrance channel and the other one asymmetrical, in order to underline all possible difference and information on the formation and characterization of a thermalized source.

The complexity and the completeness of the experimental apparatus gave us the possibility of combining directly the information derived from the analysis of the Light Charged Particles emitted in coincidence with the Evaporation Residues, with that one coming from the analysis of the γ-rays spectra measured in the same time and gated through the same ER trigger. Moreover, the use of the same apparatus for the symmetric and asymmetric reaction, has permitted a direct comparison of the two experiments.

In this thesis, we will present the results on the Light Charged Particles and γ-rays measured in the reactions $^{64}Ni + ^{68}Zn$ at 500 e 400 MeV and $^{16}O + ^{116}Sn$ at 250 MeV. A further and interesting information might come from Intermediate Mass Fragment (IMF) emission which starts to be present at these energies. The IMFs have been detected in this campaign of measurements, but their properties have been not yet completely analysed. Up to now, the characteristics of our apparatus do not permit the detection of neutrons, but this is a hope for the future, maybe with the use of some new scintillator detectors based on materials sensitive to the neutrons which are cheep and easily machinable, in a way similar to the inorganic crystals.

In the first chapter of this thesis, we will discuss the characteristics of the GDR built both on the ground state and, especially, on excited states. Moreover, we will spend some time to define the

Compound Nucleus and the nuclear temperature, concepts of particular importance for our analysis. In the second chapter, one will find a complete description of the experimental apparatus used for the measurements, while in the third one some characteristics of the scintillating materials used in the experiment will be studied and discussed. We will present some tests on the energy resolution and on the light output emission of the CsI(Tl) of Garfield and from a BaF_2 crystal, much smaller than the Hector scintillators. As a possible improvement for the experimental apparatus, some results describing new scintillating materials with good characteristics in neutron detection will be shown. In a future experiment, detectors of this kind could be used to complete the experimental apparatus, helping in reconstructing part of the missing information about the neutron emission.
In the fourth chapter, the complete campaign of measurements will be presented with particular attention to the trigger and electronic set up, while in the fifth chapter the analysis is needed to extract the interesting results from the measured data will be described together with information regarding the Light Charged Particle emission and the high energy γ-rays characteristics. The last chapter is devoted to the conclusion and outlook.

Chapter 1

THE PHYSICS CASE

1.1 The Giant Dipole Resonance

1.1.1. General characteristic

The first experimental evidence for the excitation of a vibratory motion in nuclei was obtained in 1937 in measurement of the radioactivity produced in a variety of targets by a source of 14 *MeV* photons. In some of the targets used, it was found that the photo-absorption cross section was displaying a resonance behavior. An other important confirmation of these first results was given by Berman and Fultz in 1975 [Ber75]. They provided information concerning the parameters of the associated reaction cross section. Because the resonance energy ($\hbar\omega_D \approx 15$ *MeV*) corresponds to a wavelength of the incident photon ($\lambda \approx 100$ *fm*) which is much larger than the nuclear radius (R= 5-10 *fm*), the nucleus is exposed to a uniform time-dependent electric field, which causes all protons to move in the same direction. Since in the photo-absorption process, the center of mass of the nucleus is at rest or in uniform motion, the neutrons have to move in opposite direction with respect to that in which the protons move. The strong force acting among nucleons provides the restoring force of this vibrational mode. This type of resonance state was called Giant because all the nucleons are practically involved and it is very large, 4-8 *MeV*.

The Giant Resonances have been extensively studied during the last decades. These modes can be classified making use of the multipolarity L, spin S and isospin T quantum number according to (Fig 1.1) [BBB98]:

- Electric ($\Delta S = 0$) isoscalar ($\Delta T = 0$) vibrations where protons and neutrons oscillate on phase according to a multipole pattern, for example quadrupole;

- Electric isovector ($\Delta T = 1$) vibrations where protons oscillate against neutrons. For the same multipolarity L, the isovector modes lay at higher excitation energy than isoscalar vibrations, due to the extra energy required to separate neutrons from protons.
- Magnetic or spin-flip ($\Delta S = 1$) isoscalar ($\Delta T = 0$) modes associated with the motion of nucleons with spin up which oscillate against nucleons with spin down.
- Magnetic or spin-up isovector ($\Delta T = 1$) modes where protons with spin-up oscillate against neutrons with spin down and viceversa.

COLLECTIVE MODES

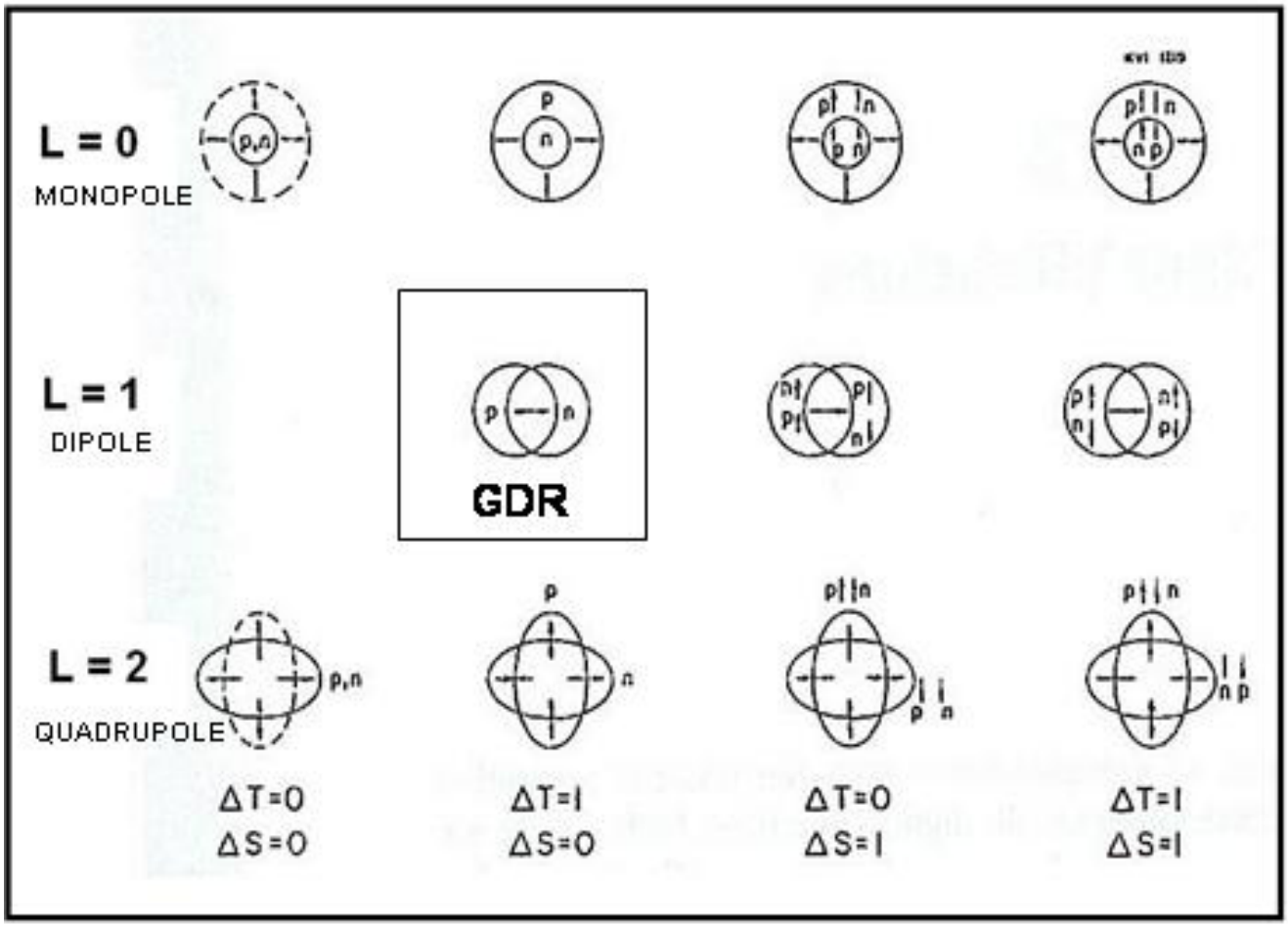

Fig 1.1 : Schematic representation of the nuclear collective modes with multipolarity L = 0 (monopole), L = 1 (dipole) e L = 2 (quadrupole) associated with vibration of all nucleons in phase ($\Delta T = 0$, isoscalar modes) and of protons in the opposite phase with neutrons ($\Delta T = 1$, isovector modes).

1.1.2. GDR at zero temperature

The Giant Dipole Resonance is a collective mode of nucleus in which the protons oscillate against the neutrons. This mode can be built on ground state nuclei or on excited nuclei. In the first case, considering a general reaction of photo-absorption, we can reproduce the cross section with the formula

$$\sigma_{abs}\left(E_\gamma\right) = \sigma_o \sum_{K=1}^{3} \frac{E_\gamma^2 \Gamma_k^2}{\left(E_\gamma^2 - E_{GDR(k)}^2\right)^2 + E_\gamma^2 \Gamma_k^2} \qquad \textbf{(1.1)}$$

where $E_{GDR(k)}$ is the energy of the resonance centroid along the k-axis and it is connected to the vibration frequency of the protons and neutrons along the same axis. If the nucleus is spherical, the frequency is the same along the 3 axis and so also the $E_{GDR(k)}$ becomes the same and the cross section is similar to the one of Fig. 1.2a [Cam92].

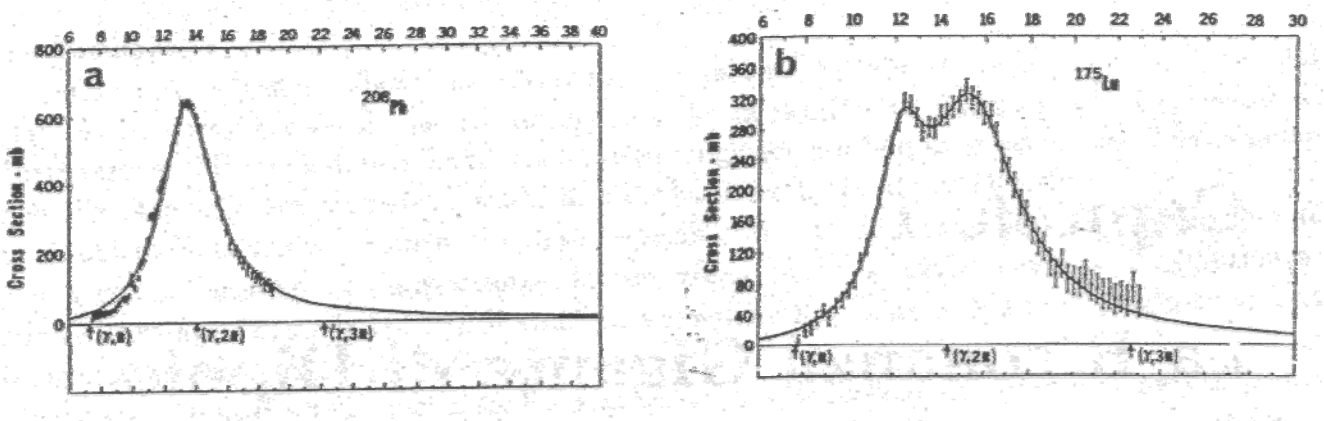

Fig 1.2 :Total cross section for reaction of photoabsorption as a function of the energy Eγ for the spherical nucleus ^{208} Pb (a) and for the deformed nucleus ^{175} Lu (b)

Measuring the resonance width, we can deduce the lifetime in the order of 10^{-22} s. Considering a period of oscillation T ≈ 3-4 10^{-23}, the protons and neutrons involved in the vibrations can do only 3 or 4 oscillations before distributing their energy among all the other degrees of freedom loosing the characteristic of collective mode.

From the systematic studies performed by J.J. Gaardhøje [Gaa92], it's possible to give some empirical formula to describe the behavior of the resonance centroid as a function of the mass of the nuclear system. In fact, in case of spherical nucleus at T = 0, it follows the trend

$$E_{GDR}\left(MeV\right) = 31.2A^{-1/3} + 20.6A^{-1/6} \qquad \textbf{(1.2)} \qquad \textbf{T = 0}$$

where the first part is called “Volumetric” and the second “Surface” term. For nuclei with A > 100, the surface contribution becomes negligible and so the centroid energy can be approximated by

(1.3) $$E_{GDR}(MeV) = 79A^{-1/3}$$ **T = 0**

In case of deformed nuclei, the oscillation frequencies along the 3 axis are different and the cross section σ_{abs} becomes the sum of different Lorentzian distributions, as one can see in fig 1.2b [Cam92]. In this case also the parameterization of E_{GDR} as a function of the nuclear mass changes and it can be expressed considering the type and the width of the deformation using the Hill-Weeler parameter *(β, γ)* [Boh75] [Gaa85] as

(1.4) $$E_{GDR(k)} = E_0 e^{\left[\sqrt{\frac{5}{4\pi}}\beta\cos\left(\gamma+\frac{2\pi k}{3}\right)\right]} \qquad (k = 1,3)$$

(1.5) $$\Gamma_{GDR(k)} = \Gamma_0\left(\frac{E_{GDR(k)}}{E_0}\right)^{\delta} \qquad (k = 1,3)$$

where *Eo* comes from the formula (1.2), the parameter β is connected to the measurement of the deformation, the parameter γ is linked to the type of deformation (three-axial, oblate or prolate), while δ is the ratio between the greatest and lowest energy centroids.

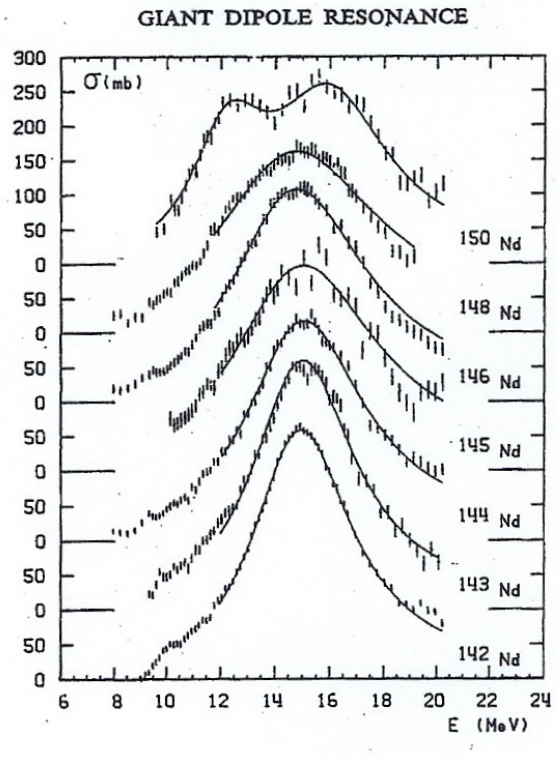

Fig 1.3 : Resonance spectra for various isotopes of Nd measured in photoabsorption reaction.

Taking into account these formulas, a direct measurement of the GDR cross section permits to estimate the size and the type of the deformation. In fact, knowing the centroid and the strength of the different Lorentzian distributions, it is possible to obtain the parameters β and γ. For example, in the case of a prolate nucleus with axial symmetry, the β parameter is given by the relation of Danos [Dan58]

(1.6) $$\beta = \sqrt{\frac{4\pi}{5}} \frac{\delta - 1.0}{0.5\delta + 0.87}$$

while the type of deformation can be extracted through the ratio between the areas under the distributions connected, respectively, to the highest and lowest energy components.

In fig. 1.3 [Car71], the variation in the resonance peak is visible for Nd isotopes. Adding neutrons, the initial spherical shape becomes more and more deformed and this is clearly shown by the cross section that at the beginning is described by a single Lorentzian distribution, while after 8 neutrons it is formed by the two different distributions, each of them corresponding to a different vibration frequency.

As in this work the Giant Dipole Resonance is built on an excited state of a Compound Nucleus formed through ion collisions, before describing its characteristics, it is important to shortly remind the concept and the meaning of the CN and its thermalization. The nuclear temperature concept and the experimental technique used to measure it will be also described.

1.1.3. The concept of Compound Nucleus

The study of reaction mechanisms aims to classify collisions according to some global topological features for a better identification and characterization of the source(s) of the detected reaction products. A first important classification in the nuclear reaction is connected to the available energy per nucleon, i.e. the maximum excitation energy which can be brought into the system. According to this, we can distinguish at least three main regions [DST01a]:

- nuclear reactions close to the Coulomb barrier (below 10-15 *MeV/u*)
- nuclear reactions in the Fermi energy region (from 10-15 *Mev/u* up to 200 *MeV/u*)
- nuclear reactions in the relativistic energy range (more then 200 *MeV/u*)

It is clear that these regions are not so clearly separated and the energy ranges suggested are just indicative and can surely overlap.

For our purpose, we will focus on the nuclear reactions with low bombarding energies.

Considering the relative velocity between the colliding nuclei, v_{AA}, one can define the reduced relative wavelength associated with nucleon-nucleon collisions like

$$\text{(1.7)} \qquad \lambda\!\!\!^{-} = \frac{\lambda}{2\pi} = \frac{h}{2\pi m v_{AA}}$$

where m is the nucleon mass.

For example, the following values of reduced relative wavelength 6.5, 2.1, 0.67, 0.24 *fm* are obtained respectively for beam energies of 1, 10, 100 and 1000 *MeV/u* for symmetric systems. These values have to be compared with the mean nucleon-nucleon distance in a nucleus, typically 2 *fm*. If $\lambda/2\pi$ exceeds this distance, a collective behaviour of nucleons during the collision is expected. In other words in the low-energy region (below 10-15 *MeV/u*), the interaction can be schematized using a mean-field theory (called also one-body interaction), while, increasing the energy, the picture changes completely and the nucleon-nucleon collision effects (called two-body interaction) becomes decisive.

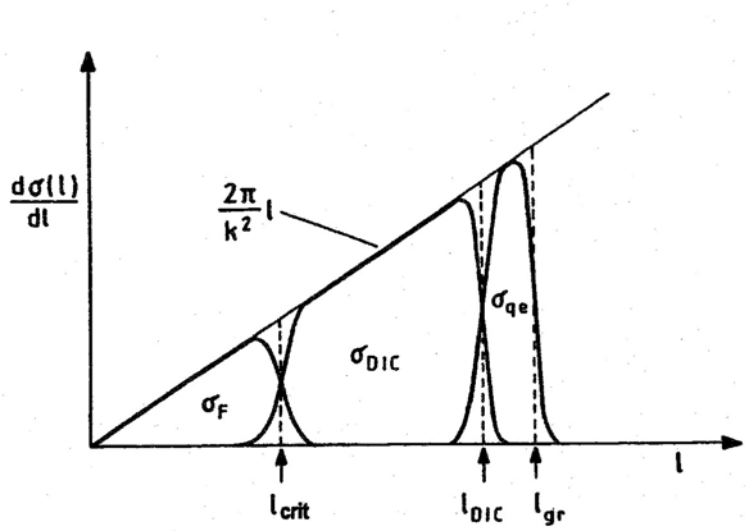

Fig 1.4 : A schematic diagram of the partial wave decomposition of the reaction cross-section in low incident heavy-ion reaction. The abscissa refers to orbital angular momentum or to the impact parameter.

Furthermore, the different reaction mechanisms can be distinguished using the impact parameter b, i.e. the distance between the center of the ideal sphere corresponding to the target and the center of that one connected to the projectile, or the angular momentum l correlated to this one. Referring to Fig. 1.4, one can point these regions at low energy (E < 10 *MeV/u*) connected to different reaction mechanism:

- elastic scattering for $l > l_{gr}$, because the incident particle does not arrive close enough to the target nucleus to interact with the nuclear force and so the interaction is purely coulombian;
- quasi-elastic scattering for $l_{DIC} < l < l_{gr}$ where the kinematics of the two nuclei is just slightly perturbed and only few nucleon transfer can exist;
- deep inelastic scattering (DIC) for $l_{crit} < l < l_{DIC}$, characterized by a strong interaction between the two nuclei with interchanging of nucleons (from few nucleons transfer to highly dissipative processes);
- central collisions for $l < l_{crit}$, where the main process is the complete fusion with the creation of a Compound Nucleus, defined like the complete thermalized sum of the projectile and target nucleons without memory of the entrance reaction channel.

To create a CN a central collision with energy high enough to overcome the Coulomb barrier is needed. In fact, the projectile and target are obviously charged with the same positive charge due to the presence of the protons, but if they arrive close enough, they can enter the range of the attractive nuclear strong force. The process of merging of the single nucleons from the two initial nuclei can be schematized like the mixing of two different gases with different temperatures inside a fixed volume. Through following collisions, the nucleons from the projectile loose some of the energy giving it to the nucleons of the target, initially at zero energy. After the thermalization process which means the equipartition of energy over all the nucleons, there is the creation of a new system, with mass and charge equal to the sum of the two partners, and a total dissipation of the initial available kinetic energy from the projectile into excitation energy, and consequently temperature, for the whole system.

If the thermalization process is complete, we will have a CN without memory of the entrance reaction channel that has been used to create it and the CN will be properly characterized through the definition of few parameters like the number of mass, charge, spin and the excitation energy, expressed as

$$\begin{aligned} A_{CN} &= A_{target} + A_{projectile} \\ Z_{CN} &= Z_{target} + Z_{projectile} \\ E^{*} &= E_{CM} + Q \end{aligned} \qquad \textbf{(1.8)}$$

where E_{CM} is the energy of projectile in the center of mass system and Q is the Q-value of the reaction, respectively, defined as

$$E_{CM} = E_{projectile} \frac{A_{target}}{A_{target} + A_{projectile}}$$
$$Q = c^2 \left(\left(M_{target} + M_{proiectale} \right) - M_{CN} \right) \quad \textbf{(1.9)}$$

These characteristics make the Compound Nucleus a system to be described through the statistical mechanics. Considering the golden rule of Fermi that describes the decaying probability from an initial state *i* to a final state *f* written as [DST01b]

$$\frac{dN_{i \to f}}{dt} \propto \left| M_{i \to f} \right|^2 \rho_f \quad \textbf{(1.10)}$$

where the first part is linked to the matrix that describes the changing of state and the second is the density of state of the final system, in a completely thermalized system, we can consider the matrix element always equal for every possible decay channel.

The decay of a thermalized source in the statistical approach is, in fact, based on the equal probability of all possible final states. The emission probability becomes, therefore, connected to the different variation in density of states between the initial and final state. The angular distributions of the emitted products are essentially isotropic in the centre of mass system and only those particles which carry angular momentum can follow a slightly different angular distribution due to the coupling with the angular momentum of the emitting source. During the decay of the Compound Nucleus, also a collective mode can be excited with the following emission of high energy γ-rays.

The relevant parameter is the timescale which consist of the time needed to form a composite system (~ 10^{-22}), the thermalization process time (~ 10^{-19}) and the particle emission time. When the later becomes shorter than the time needed for the thermalization, the pre-equilibrium emission starts to take place. This can depend both on the bombarding energy and on the size of the composite system. When this process starts to arise, the whole process can not be described anymore only through a statistical approach. On the contrary, dynamical effects start to have strong influence. In fact, in this case a memory of the entrance channel will be maintained, which will be reflected in a fast emission prior then thermal equilibrium is reached, peaked in the forward direction. This process will subtract excitation energy from the final system which has to be formed. In the Fig. 1.5 a schematic picture of the decay process of a compound system is shown.

In the energy range where this time competition starts is, therefore, a challenge to characterize the system, to understand if it can be considered thermally equilibrated, to associate to the starting configuration of the system global variables like A, Z and E*.

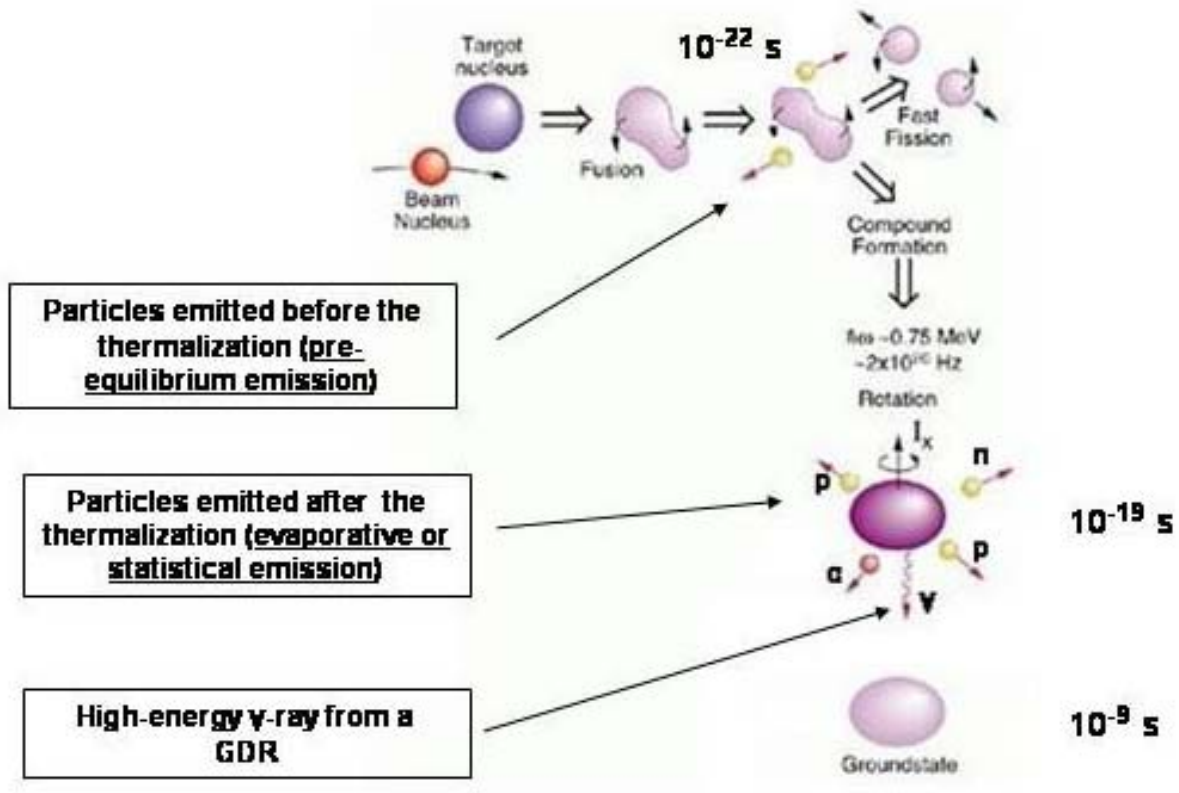

Fig. 1.5 : Schematic picture of the creation and following decay of a Compound

The challenge is also to be able to recognize and quantify the pre-equilibrium emission. This will permit to get information on the mass, charge and energy lost in the first part of the process due to the dynamical effects. We will come back to this question in the Chapter 5 that is dedicated to our analysis. After this short discussion on the concept of CN, we are ready to discuss some general characteristics of the GDR built on excited states at finite temperature.

1.1.4. GDR at finite temperature

The first evidence for the existence of the giant dipole oscillations in excited nuclei was found in the early 1980s in Berkeley measuring the spectra of γ-rays with transition energy between 5 to 25 *MeV* emitted by compound nuclei formed in heavy-ion induced collisions [New81].

The Giant Dipole Resonance was seen as a change in the slope of the γ-ray yield taking place in the range of the resonance energy (Fig 1.6) [Bra89]. In Fig. 1.7 the variety of decays which cools the compound nucleus are shown schematically. Giant-dipole photons indicated by the label (1) in the

figure are emitted in an early stage in competition with neutrons. When the intrinsic energy of the system becomes lower than the neutron separation energy, slower γ-transitions have time to occur, that is, transitions of type (2) in Fig 1.7. Most of the angular momentum is carried off in the final stage of the decay by quadrupole radiation, indicated by (3) in the same figure. The GDR emission is reflected in the changing of the slope of the energetic γ-ray spectra, as shown in Fig.1.6. The emission type "(3)" in this picture is cut because it is dominant for $E_\gamma < 3,4$ *MeV*.

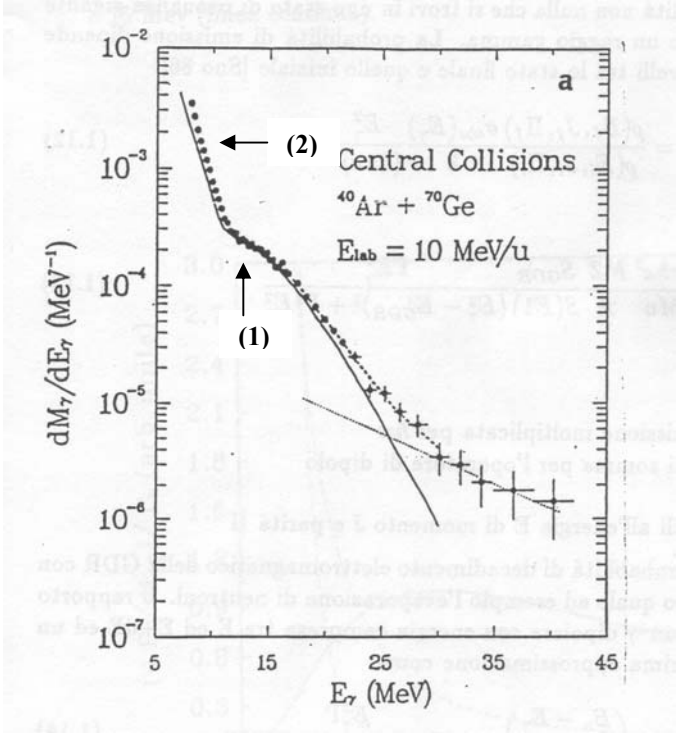

Fig. 1.6 : Measured γ-ray spectrum from the decay of excited ^{110} Sn.

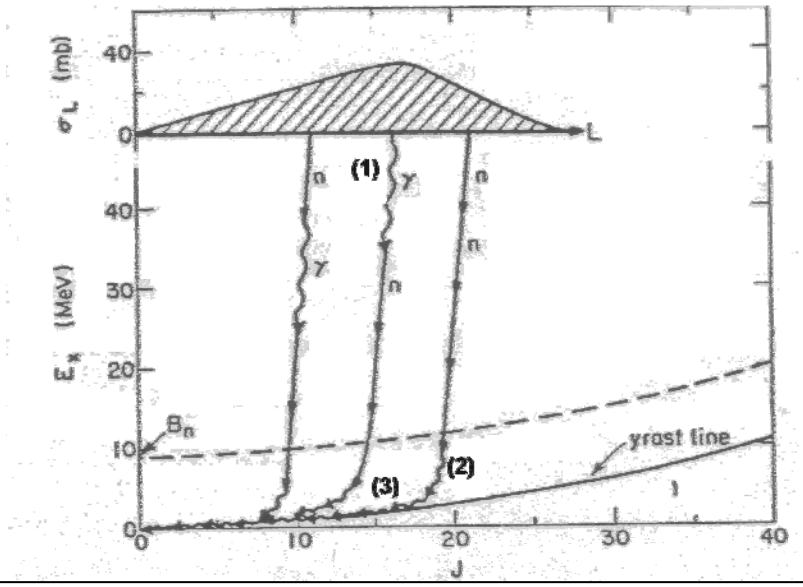

Fig 1.7 : Decaying scheme for a compound nucleus. One can see the different γ-ray emission described in the text.

Only a few years after of the Berkeley experiment, another evidence for the presence of giant dipole vibrations built on excited states was obtained in a measurement of proton capture cross section. Studying reactions of the type *A-1(p,γ)A** as a function of the proton bombarding energy leading to a given final excited state in the residual nucleus A, a resonant behavior was found at excitation energies equal to the sum of the energy of the final state and the energy of the GDR [Sno86].

In fact, the presence of the GDR in hot nuclei can be considered like the addition of a quantum of vibrational excitation to the system, which raises the energy of the state by $\hbar\omega_{dipole}$.

Since the time this process was established, a lot of experimental and theoretical works have been dedicated to this subject. The experimental findings are mainly based on measurement of γ-decay following fusion reactions induced by heavy-ion collisions. From this type of studies the photoemission cross section integrated over the energy (oscillation strength), the centroid energy of the resonance and the resonance width can be derived.

It is interesting to make a comparison between the properties of GDR based on ground and excited states [Gaa92b], [Gaa92c]. A summary of such a comparison, which averages over mass number as well as over excitation energy and rotational frequency, is displayed in fig 1.8 ([BBB98]). The main feature emerging from this comparison is that the energy weighted sum rule (Fig 1.8a), which is a strong signal that GDR is a collective mode, and the energy centroid (Fig 1.8b) essentially do not depend on temperature. Keeping the fact that in most cases the compound nucleus is strongly rotating, these quantities do not seem to depend on angular momentum either. On the other hand, conspicuous differences are observed in the total width of the resonance (Fig. 1.8c), in the dispersion of the mean value of the effective quadrupole deformation parameter (Fig. 1.8d) and in the ratio between the upper and the lower components of the two peak resonances (Fig. 1.8e).

In fact, while the average value of the total width of the GDR based on ground state is ≈ 5.8 *MeV*, that one associated with thermally excited dipole vibrations in hot, rapidly rotating nuclei is ≈ 10 *MeV*. Furthermore, the strong shell structure displayed by the total width of GDR in cold nuclei is absent from the corresponding quantity measured in the γ-decay of compound nuclei. Concerning the dispersion of the mean value of the effective quadrupole deformation parameter, one observes a value of 0.2 in cold nuclei and of 0.36 in compound nuclei. Once again, the strong shell structure displayed by the values associated with cold nuclei is absent from the finite temperature data. From the 28 experimental values of the ratio of strengths associated with the upper and lower Lorentzian components used to fit the giant dipole strength function based on the ground state, only 6 (20%) fall within 20% of the limiting values corresponding to oblate (0.5 ± 0.1) and prolate (2.0 ± 0.4) nuclear shape in the case of cold nuclei. For hot, strongly rotating nuclei out of the 28 cases, 18 (60%) fall within these limiting values (Fig 1.8e).

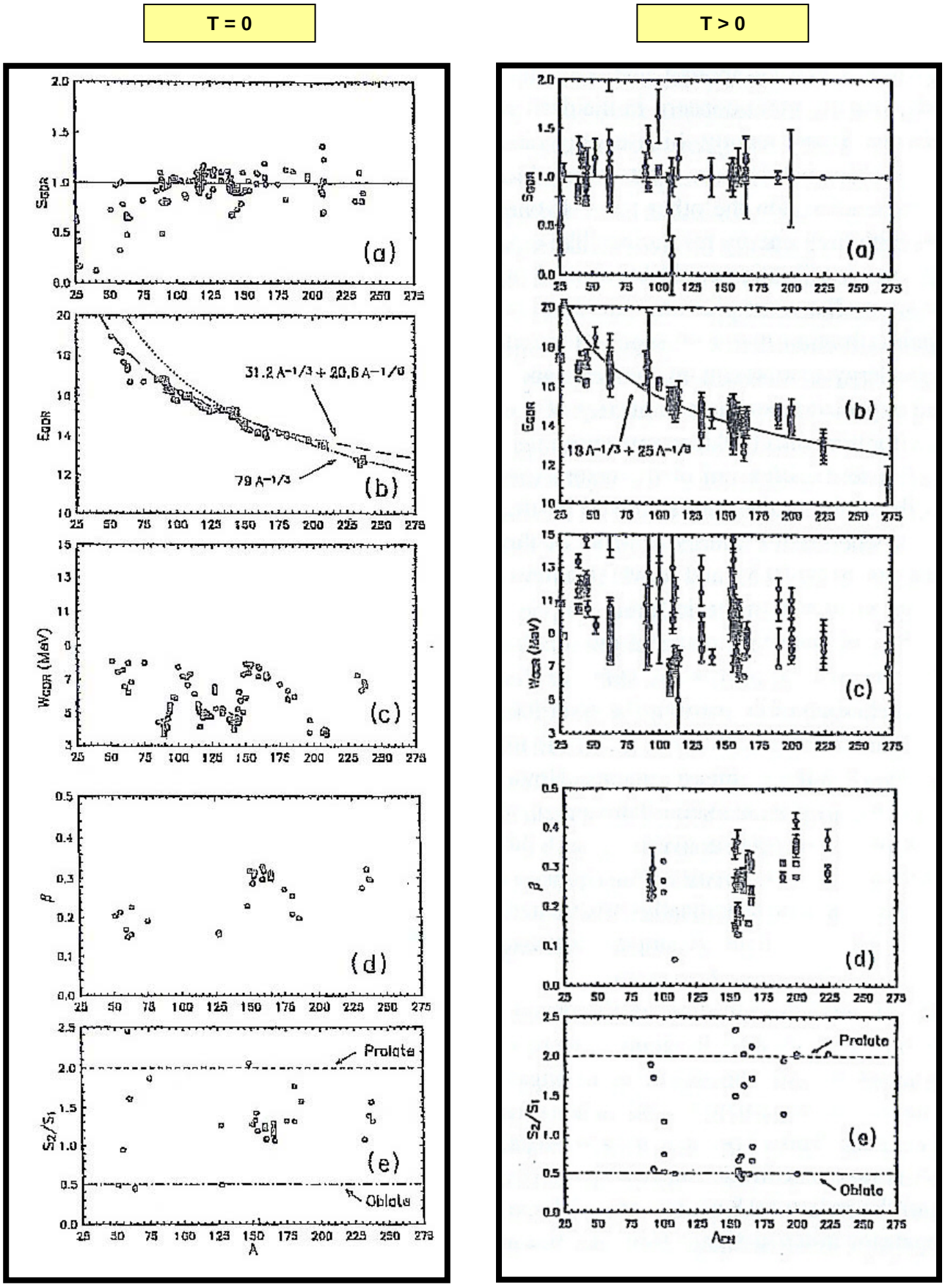

Fig 1.8 : Comparison between the characteristics of the GDR built on ground state and excited state. In the first picture the Strength is plotted, in the second the centroid energy. In the third one there is the total resonance width and after the effective quadrupole deformation parameter β. At the end, the ratio between upper to lower components of the two peak resonances is presented.

Using the theory, it is possible to provide an overall account of the main trends of the experimental findings. The independence of the oscillator strength and of the energy centroid (cf. Figs. 1.8a and 1.8b) with the temperature and angular momentum can be understood in terms of the resilience of the main field, where nucleons move essentially independently from each other, with respect to those quantities. In fact, the parameter which controls the rigidity of the mean field is $\hbar\omega_0$ ($\approx 41\ A^{-1/3}\ MeV$), is the energy difference between major shells. This quantity is 7-9 *MeV* for medium-heavy nuclei ($100 \leq A \leq 200$), an energy which has to be compared with the value of the temperature of 2-3 *MeV* and the rotational frequency $\hbar\omega_{rot} \approx 1\ MeV$.

The behavior of *FWHM* is controlled by the coupling of the resonance to the nuclear surface and reflects both the static (inhomogeneous damping) and dynamical (collisional damping) deformation of the nuclear shape. The typical shell structure that one can see in the distribution of *FWHM* as a function of the mass number for cold nuclei is due to the fact that the closed shell nuclei are spherical in average and less plastic than the open shell nuclei. Heating up the system, it displays a large amplitude shape fluctuations which are thermally activated. Furthermore, the rapid rotation to which the compound nucleus is subject can induce conspicuous deformation in the system.

This can explain the different behavior between cold and hot nuclei in the distribution of *FWHM* (cf. Fig 1.8c) and in the parameters β and S_1/S_2 that are connected to the deformation of the nucleus (cf. Fig 1.8d, Fig1.8e).

A particular aspect important to investigate is the damping mechanism of the GDR in the region of high excitation energy. From the theoretical assumptions, we can consider two different damping mechanisms:

- collisional damping, associated to the coupling of the giant vibrational mode with the quantum fluctuation of the nuclear surface
- thermal damping, associated to the coupling of the giant vibrational mode with the large fluctuation in the nuclear shape due to the increasing temperature.

The damping mechanism has been observed in several experiments where quite large excitation energies have been reached in the decaying system. Evidences have been found for a small increasing of the number of the high energy γ-rays, with respect to that expected if considering the increased available energy for a prompt dipole γ-ray emission before the thermalization process ([Bru04]). Besides that, a saturation in the resonance width was also underlined ([Gaa92]).

The interpretation of this phenomenon is, nevertheless, quite difficult and the comparison between existing experimental data are often limited by the different choice in the theoretical model used to analyze and interpret the experimental results. Trying to get information from the large amount of

experimental data existing on the subject, some work has been done from the group of J. Kasagy et al., who tried to propose a quite simple empirical law to describe the expression for a limiting temperature after which no collective giant mode is supposed to be possible [Yos90].

The following expressions were proposed

$$T_{\lim} \approx 17 A^{-1/3} \qquad \textbf{(1.11)}$$

$$\Gamma_{GDR}\left(E^*\right) = \Gamma_0 + c_1 E^* + c_2 \left(E^*\right)^4$$

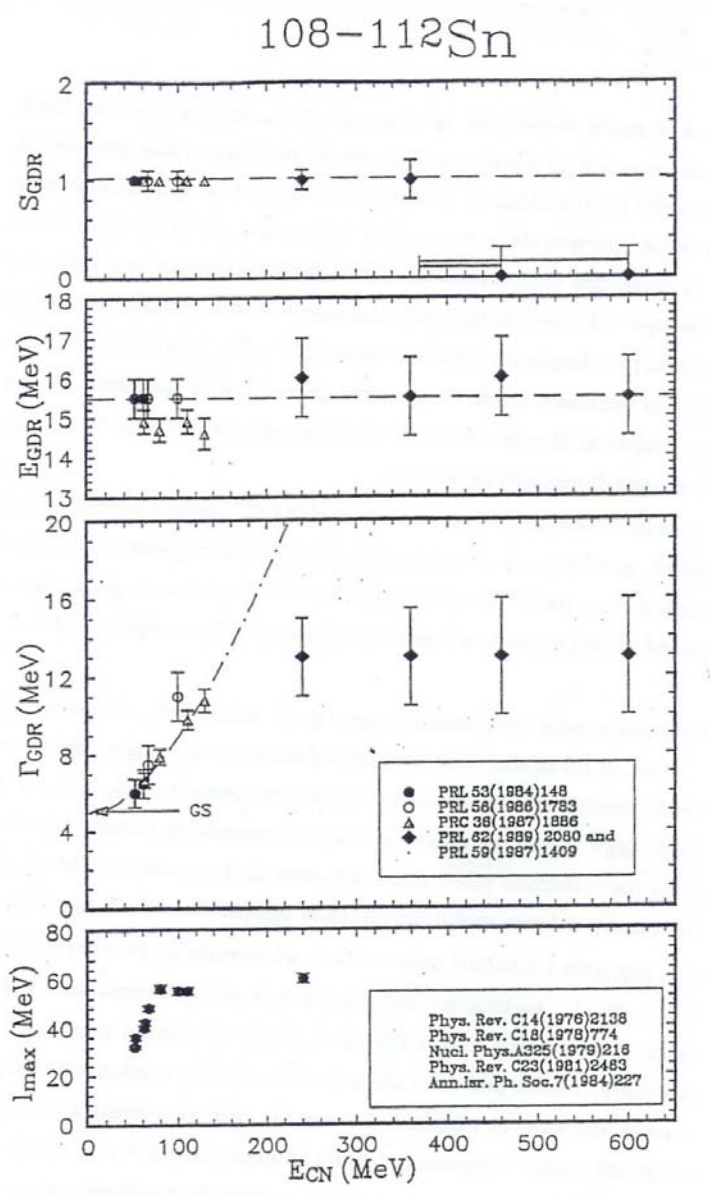

Fig 1.9 : Systematics of the GDR parameters (strength, centroid, width) as a function of the excitation energy for the $^{108\text{-}122}$Sn isotopes. In the last part of the figure, the maximum angular momentum that can be transferred in the CN is shown ([Gaa92]).

A strong dependence of the resonance width as a function of the temperature is obtained using this expression. This is attributed to the opening of new decay channels for the nucleons-nucleons

collision when the excitation energy is high enough to overcome some of the limits put by the Pauli principle. In fact, an increasing of the incident energy induces an opening of the available phase space for outgoing nucleons, which leads to some decreasing in the Pauli blocking effects.

According to the Kasagy group, these formulas work properly on the Sn isotopes, as one can see in the general systematics of the GDR characteristics shown in Fig. 1.9. In this formulation, when the excitation energy is around 130 *MeV*, the GDR emission is predicted to become so large ($\Gamma_{GDR} \approx 50$ *MeV* for E* < 200 *MeV*) that no more peak will be present in the γ-spectra. They also affirm that for energy greater than 130 *MeV*, the effective emission which can be seen in the experimental data is only produced by some of the "daughter" nuclei created in the decaying chain.

But this is not the unique possible interpretation of the data. In literature, there are a lot of other models that tries to explain this question and in particular we will discuss the interpretation proposed by the A. Bracco group ([Bra89]). With respect to the J.Kasagy's idea, a statistical approach has been used that predicts a slower dependence of the resonance width on the temperature, together with a prediction which links the observed increasing of the GDR resonance width at low-middle excitation energy to the increasing shape deformations of the nucleus. In fact, pumping energy in the system, high values of angular momentum can also be transferred to the system, increasing the thermal fluctuation induced in the shape of the nucleus. As already underlined, the resonance frequency of the GDR emission is very sensitive to the shape of the nucleus. A variation in the shape will be then reflected in a change of the emitted resonance frequency. Consequently, there will be a spreading of the Lorentzian function which describes this emission.

This new interpretation of the resonance width is supported by the fact that in the nuclear reaction used to create the Sn compound system, the transferred angular momentum increases with the bombarding energy until it arrives to a saturation value, that is the value after which the fission barrier vanishes. This corresponds to a transition in the behavior of the GDR width, as shown in Fig. 1.8. In fact, we pass from a region where a strong increasing of the GDR width as a function of the temperature is present, to another one where this behavior is less strong due to the fact that the contribution to the width given by the angular momentum is saturated, while a second contribution due to the thermal fluctuation still remains.

In this statistical approach, the key point necessary to understand the existence of a critical temperature for the γ-emission from GDR is the timescale of the different decaying processes. We should imagine the GDR state like an energetic state built on ordinary excited states to which the average energy of the resonance is summed (Fig. 1.10) [Gel93]. To produce the GDR state an equilibration time is needed, which is connected to the resonance width. The limiting temperature is

then reached when the emission time of the particles or fragments from the compound nucleus become comparable to this time needed to create the GDR collective state. In fact, at that point, the probability of having a GDR state is dramatically suppressed and the de-excitement of the nucleus goes completely through the emission of particles or fragments.

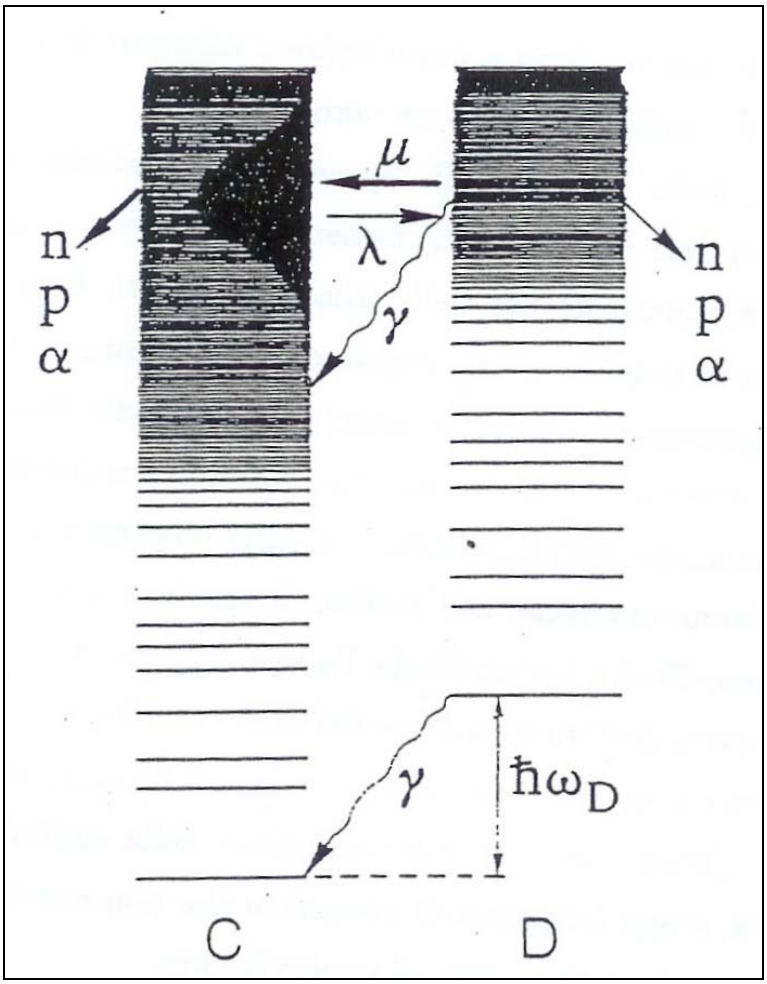

Fig 1.10 : Representation of the nuclear energetic state. Those one labeled with C are the ordinary ones, the other labeled with D are the GDR states built on the other increasing the energy for the value of the energy centroid of the resonance.

To describe this situation, we should consider two classes of states, one for non-collective compound nucleus states (indicated with C in Fig 1.10) and one for GDR states built on the other (states D in Fig. 1.9). The transition frequency to pass from one to the other are indicated with λ and μ. Both of these states can decay emitting p, α and n but only the D states can use the high energy γ-ray channel. The probability to be in one of these states is defined by

$$\frac{dP_D}{dt} = -\left(\mu + \gamma_\gamma + \gamma_{ev}\right)P_D + \lambda P_C$$

(1.12)

$$\frac{dP_C}{dt} = -\left(\lambda + \lambda_{ev}\right)P_C + \mu P_D$$

where γ_γ and γ_{ev} are the decay frequency through γ and particles emission, respectively.

Considering that

$$\frac{\lambda}{\mu} = \frac{\rho_D}{\rho_C} = \frac{\rho_C(E - E_{GDR})}{\rho_C} << 1 \qquad \textbf{(1.12)}$$

on which ρ_D and ρ_C are density states of the two C and D types, one can deduce the electromagnetic decay probability P_γ for a system that starts from a C type state using

$$P_\gamma = \frac{\gamma_\gamma}{\gamma_{ev}}\left(\frac{\lambda}{\gamma_{ev} + \lambda + \mu}\right) \approx \frac{\gamma_\gamma}{\gamma_{ev}}\left(\frac{\lambda}{\gamma_{ev} + \mu}\right) \qquad \textbf{(1.13)}$$

Behind a critical temperature T_c, one assumes $\gamma_{ev} >> \mu$ for the increasing temperature that should be dissipated. The Eq. 1.13 for $T > T_c$, can be simplified with

$$P_\gamma \cong \frac{\gamma_\gamma \lambda}{\gamma_{ev}^2} \qquad T > T_C \qquad \textbf{(1.14)}$$

that shows in a clear way how from the increasing probability to emit a particle following a rapid decreasing of the production of high energy γ. The critical temperature suggested by P.F Bortignon is $T_c \approx 5\ MeV$ [Bor91], corresponding to an excitation energy of $E^* \approx 250\ MeV$ for nuclei with $A = 110$. For the temperature larger then the critical, the particle time emission becomes shorter than that one needed to produce a GDR state and, therefore, the decay of the Compound Nucleus in the first part is strongly dominated by the particle emission without emission of high energy γ-rays.

Up to now, it is quite hard to discriminate between these two completely different theoretical approaches using the existing experimental data, because the interpretation is not so clear. For this reason, new and more complete measurements are needed, using new apparatus able to study in detail the γ-emission and also the Light Particles and fragment emission to determine well the characteristics of the emitting source, together with a possible further selection of the kind of event.

At this point, to describe the problems linked to the behavior of the width of the GDR built on exited states, the concept of nuclear temperature has to be described.

1.2 The concept of nuclear temperature in thermalized system

The nuclear temperature in nuclei is a quite hard and complex concept, due to the fact that we are dealing with finite size system made by few nucleons. Anyway, using all possible connections with the general thermodynamical concepts, the important considerations can be made. In fact, bridges between different fields of physics have always provided important information into the exploration of new phenomena. One example of this process can be the link between the microscopic atomic nuclear systems and the complex macroscopic systems. For the latter, thermodynamics and statistical mechanics have been effective tools and it was reasonable to develop the thermodynamical concepts, such as temperature and entropy, also for nuclear systems. This development permits a discussion of new nuclear phenomena in a way which was more often used for macroscopic systems.

The concept of a nuclear temperature was introduced in the pioneering works of Bethe [Bet37] and Weisskopf [Wei37]. That works were intimately connected with the exploration of the CN created with the bombardment of nuclear targets by the light projectiles. The early works demonstrated the usefulness of the concept of temperature in a nuclear context. The subject of temperature has been reexamined in the context of reaction at higher energies ([Sur89] and [Tam91]) and some questions about its validity have been raised together with new methods for its measurement. In this paragraph, we will examine some of these questions and problems, and discuss some methods that one can apply to the measurement of temperature without the idea to be completely exhaustive for the extreme complexity of the argument.

1.2.1. Basic definition of temperature and its application.

In collisions between large nuclear systems, the collective kinetic energy of the projectile can be deposited into other modes, mostly in the microscopic degrees of freedom of the total system. One area of nuclear research tries to explore this process and the subsequent role that the energy deposition plays in determining the type and behavior of the final-state particles produced in the collision. Full damping, with the attainment of equilibration, represents a limit to this process, and

nuclear temperature is one of the natural variables used to characterize systems that have reached this limit.

Using the classical statistical mechanics, we can define with great precision the concept of temperature for isolated systems. Considering $\Gamma(E, N)$ like the number of state for a given system, with fixed volume and particle number N, which lie in the vicinity (ΔE) of energy E, we can write [Mor94]

$$\Gamma(E,N) = \rho(E,N)\Delta E \tag{1.15}$$

where $\rho(E, N)$ is the density of states at energy E. It is also convenient to introduce the entropy of the system by

$$S(E,N) = \ln \rho(E,N) + \ln \Delta E \tag{1.16}$$

With these quantities, the definition of temperature provided by statistical mechanics is

$$\frac{1}{T} = \frac{\partial S(E,N)}{\partial E} = \frac{\partial \ln \rho(E,N)}{\partial E} \tag{1.17}$$

where we have taken ΔE to be independent of E. This definition is applicable to a nuclear system and as well to any other isolated system. The only difference is that the appropriate density of state $\rho(E,N)$ must be used. This definition of temperature is quite simple, but the applicability to our case is not so trivial. In fact, it works only if the density of state is well known and if the system is in full statistical equilibrium. In particular, this request means that each of the state included in $\rho(E, N)$ is populated with equal probability. As the excitation energy increases, the lifetime for highly excited nuclear system becomes shorter, reducing the possibility that all the states are populated with equal probability. It is difficult to know, a priori, the degree to which equilibrium is achieved because the dynamics governing the evolution of the nuclear system can not be perfectly known.

Nonetheless, in order to explore the question of equilibrium, it is instructive to assume that the population of states is sufficiently complete to permit the use of the concept of temperature. Practically, the predictions of statistical equilibrium for specific nuclear system are often compared to experimentally observed distributions as a test for thermal equilibrium. In fact, if the system is truly in equilibrium, a variety of consequences follows like, for example, the isotropy of the emission in the centre of mass reference frame and the fact that the different methods for measuring the temperature should all provide the same result. Differences in experimental results can be found since the measurements can be influenced by aspects other than equilibrium.

Just as a determination of temperature requires an assumption about the degree of equilibrium, it also requires additional assumptions about the density of states. This aspect of nuclear systems can not be precisely determined from first principles.

Up to now we have not distinguished nuclear system and macroscopic systems on the basis of their size, but there is, at least, one important difference between the two: the way in which the entropy *S(E)* is commonly evaluated. In statistical mechanics one considers different physical situations (ensembles) for evaluating thermodynamic quantities: fixed energy and particle number (microcanonical ensemble), fixed temperature and particle number (canonical ensemble), and fixed temperature and chemical potential (grand canonical ensemble).

In the evaluation of thermodynamical quantities for macroscopic system each of these approaches provides essentially the same result. Thus, the entropy may be evaluated by obtaining any of the following: $S_{microcanonical}$, $S_{canonical}$, $S_{grandcanonical}$. This is not the case for the smaller nuclear system because the only appropriate ensemble is the microcanonical ensemble used for isolated system. The fundamental definition of nuclear temperature is, thus,

(1.18) $$\frac{1}{T} = \frac{\partial S_{microcanical}(E,N)}{\partial E}$$

and it is not correct to substitute an entropy obtained with a different ensemble in this expression.

A lot of studies have shown that the level densities of nuclei at low excitation energies have an energy dependence similar in form to that of a Fermi gas. Standard procedures permit the evaluation of the entropy of a Fermi gas under the conditions of a grand canonical ensemble. For low excitation energies E^*, the entropy is

(1.19) $$S_{grandcanonical}(E^*,N) = 2(aE^*)^{\frac{1}{2}}$$

where a is a constant proportional both to the number of particles and to the density of a single-particle levels of the Fermi gas at the Fermi energy ε_f. If $S_{grandcanonical}$ is used to replace $S_{microcanonical}$ in Eq.1.18, one obtains

(1.20) $$T = \left(E/a\right)^{1/2}$$

as the normally used link between temperature and excitation energy. This result would be appropriate for macroscopic system, but it must be modified for isolated nuclear system. In fact, for the small system the correct expression should be

(1.21) $$S_{microcanonical} = S_{grandcanonical} + \Delta S$$

where ΔS becomes vanishingly small compared to $S_{grandcanonical}$ as the number of particles or the excitation energy becomes large. An approximate expression for ΔS is available for a Fermi gas, where, at relatively low energy, one finds

(1.22) $$\Delta S \approx -\gamma \ln\left(E^*\right)$$

with γ being a number of the order of unity, ranging from 1 to 2 depending on whether isospin and angular momentum are explicitly considered in the labeling of the states. When the appropriate $S_{microcanonical}$ is used to evaluate the nuclear temperature one has

(1.23) $$\frac{1}{T} = \frac{\partial S_{grandcanonical}}{\partial E} + \frac{\partial \Delta S}{\partial E}$$

For the moderately low energies this provides

(1.24) $$\frac{1}{T} \approx \left(\frac{a}{E^*}\right)^{1/2} - \left(\frac{\gamma}{E^*}\right)$$

as the real link between excitation energy and nuclear temperature. For large excitation energies E* and large particle number, the correction term proportional to γ vanishes.

Following the development of Fermi gases, one can take the density of nuclear states as

(1.25) $$\rho\left(E^*\right) \propto \frac{a}{\left(aE^*\right)^{\gamma}} e^{\left(2\left(aE^*\right)^{1/2}\right)}$$

The factor *a* is called the level density parameter and is adjusted to correspond to the level density measured at low excitation energy ([Gil65], [Hui72]). These fits suggest that *a* is proportional to the mass of the nuclear system *A*, and it is further found that $a \approx A/8\ MeV^{-1}$.

At the higher excitation energy produced in collisions between massive nuclei with large relative energies, the level density of the many-body system is less known, and dynamics are important. In this regime there are some considerations to do. First of all, one should extend the relation of Eq. 1.23 from the Fermi energy to a higher range, secondly, the level density for highly excited nuclear system is based on a more complete treatment of the quantum mechanism of the many-body system. In particular, one might expect energy and momentum dependencies in the mean-field which binds the particles. This effect can be treated by introducing an effective mass for nucleons ([Lej86]). An other aspect to take into account is associated with the short-lived nature of the excited single-particle states which are occupied by the nucleons.

With some complicated approaches it is possible to overcome this problem, but while there have been a lot of theoretical efforts in this interesting area, it is difficult at this time to find specific experimental evidence to suggest the greater validity of any one of these approaches. This is probably due to the fact that at high energies the influence of the level density is diluted by a wide range of other phenomena which contribute to the experimental spectra.

After this theoretical discussion, we will try to describe some experimental procedures for temperature determination. All of them involve the examination of three aspects of the emitted particles: their kinetic energy spectra, their relative number, and their excited state populations. We will show that, in an ideal situation, each of these aspects can provide measurements of the same quantity. Under realistic situations, however, each may be influenced in different ways by the prevailing nuclear conditions. For this reason it is important to apply as many different techniques and variations as possible to determine a nuclear temperature.

1.2.2. Temperature from the particles spectra

Let us consider the fundamental features of the distributions of emitted particles that permit the determinations of the temperature for the ideal case. We consider the case in which a portion of the system is emitted and leaves behind a residue which we call the "daughter". If equilibrium has been achieved prior to emission, then the energy will be shared between the emitted portion and the daughter. If the energy and the number of particles in the primary system are large enough, and the emitted energy and emitted portion are small enough, then the daughter can serve the role of a heat bath in classical thermodynamics. Following the procedures of standard statistical mechanics, the relative weight for each final state of the emitted system is given by the number of states available to the daughter.

It follows from counting states that the general expression for the relative probability, $P(\varepsilon, n)$, for obtaining an emitted portion with mass number n and energy ε is given by

$$P(\varepsilon, n) \propto \Gamma(\varepsilon, n) x \Gamma(E - \varepsilon, N - n) \tag{1.26}$$

where $\Gamma(E, N)$ is the number of states in the vicinity of energy E for a system of mass number N. In Eq. 1.26, the first factor is the contribute from the emitted system, while the second is from the daughter. Various models have been proposed to relate the rate of emission to $P(\varepsilon, n)$. One of the best known models for the emission rate, used for the sequential emission of nuclear fragments, is based on detailed-balance and was first proposed by Weisskopf [Wei37]. This model provides that

$$\frac{d^2 N}{dt d\varepsilon_k} \propto \frac{(\varepsilon_k)^{\frac{1}{2}} \sigma}{\Gamma(E, A)} x P(\varepsilon, n) \tag{1.27}$$

where $d^2N/dtd\varepsilon_k$ is the rate for emission of a specific portion of size n and translational kinetic energy near ε_k from an original system of size A and energy E. The factor σ provides the cross

section for the inverse reaction, i.e. the absorption of the emitted portion by the daughter. Substituting the probability given in Eq. 1.26 for that in the rate of emission Eq. 1.27, one finds the ratio

$$\frac{\Gamma(E-\varepsilon, A-n)}{\Gamma(E, A)} = e^{-(S(E,A)-S(E-\varepsilon,A-n))} \quad \textbf{(1.28)}$$

where the exponential of the entropies, defined in Eq. 1.16, has been inserted for the level density. For small values of ε/E and n/A this ratio can be approximated by a Taylor series expansion. If we consider the emission of charged particles, we should also consider the Coulomb potential Vc and the resulting expression for the emission rate has the form

$$\frac{d^2N}{dtd\varepsilon_k} \propto (\varepsilon_k - V_c) e^{\left(-\frac{\varepsilon_k}{T}\right)} \quad \textbf{(1.29)}$$

Starting from this, one might expect that the observed spectra could be compared with the emission rate (Eq. 1.28) to give the temperature, but there are some questions to discuss. The equation Eq. 1.29 must be integrated in time to obtain the measured spectra $dN/d\varepsilon_k$ and the temperature during the process change, starting from a higher value which will decrease during the particle emission. Thus, the real experimental spectra are a convolution over these temperatures. The situation is further complicated by the fact that also V_c is temperature-dependent.

Another important effect is the possible contamination of the measured spectra from a pre-equilibrium emission or from a binary decay of some of the emitted particles. Only a sudden disintegration of the source into the observed fragments can be invoked to justify using the simple expression above, and the real hard task in heavy ion reaction is to understand when it is possible to have this condition. Another big problem is also the fact that in any case one should also take into account the correction to the spectra needed for the influence of collective dynamical effects, like collective rotation, translational motion and collective expansion of the source.

If one selects the best condition using a light projectile to minimize the importance of angular momentum and at low energies where the fusion is complete, the expansion of the source negligible and the pre-equilibrium emission not important, the spectra can provide a good measure of the temperature. This temperature is usually called *"kinetic temperature"*.

This was the temperature used in our analysis, as one can see in Chapter 5, which would give an indication of the condition of the emitting CN.

1.2.3 Temperature from double ratio of isotopic yields.

This method can be used at higher energies when the intermediate mass fragments emission is allowed. In the framework of the statistical approach, the probability of fragment or particle emission is mainly governed by phase space constraints, in particular, by the separation energy ε associated with the emission process. This separation energy is nothing but the opposite of the chemical potential. The probabilities of formation of a given cluster depend therefore on the chemical potential, but this quantity is not easily accessible experimentally, especially if the matter involved is at low density. Albergo et al. [Alb85] have, thus, proposed a method to measure the temperature in which the chemical potentials are not needed. The idea is to study ratios of populations of clusters differing either by a single neutron or by a single proton so that the chemical potentials will be canceled in the final expression. We can define R as the following double ratio of particle yields

$$\mathbf{(1.29)} \qquad R = \frac{Y(A_i, Z_i)}{Y(A_{i+1}, Z_i)} x \frac{Y(A_{j+1}, Z_j)}{Y(A_j, Z_j)} = R_1 R_2$$

where $Y(A_i,Z_i)$ is the yield of a generic particle with mass A_i and charge Z_i and $Y(A_{i+1},Z_i)$ is the yield of a particle with number of mass greater of only one units. A similar definition can be used if we would use the changing of the charge of the different particles of one unit.

In the Quantum Statistical Model (QSD) proposed in [Hah88], the population of each species i is expressed like the integration of the density of states in the phase space, multiplied by the volume and taking into account the degeneracy factor of each species. In particular, we can write

$$\mathbf{(1.30)} \qquad Y_i = \frac{V_{fo} g_i}{h^3} \int_0^\infty n_i(p) d^3 p$$

where V_{fo} is a fixed volume, g_i is the degeneracy factor and n_i the occupation factor of each species i in momentum space. Developing the formula, one can obtain

$$\mathbf{(1.31)} \qquad Y_i = \frac{8\pi V_{fo} g_i (m_i T)^{\frac{3}{2}}}{\sqrt{2} h^3} \int_o^\infty \sqrt{z} e^{(-z + \frac{\mu_i}{T} - \frac{E_i}{T})} dz$$

where $z = \varepsilon/T$ is the integration variable and E_i and μ_i are respectively the mass energy (taking into account a possible internal excitation energy) and the chemical potential of species i. The chemical

potential can be expressed separating the contribution of the number of neutrons N_i and protons Z_i of every species *i* as

$$\mu_i = \mu_Z Z_i + \mu_N N_i \qquad \textbf{(1.32)}$$

where μ_Z and μ_N are proton and neutron chemical potentials.

Coming back to the formula 1.29, including the expression 1.31, we can express the first ratio R_1 (R_2 is obtained in similar way) as

$$R_1 \approx \frac{(2s_{i,i}+1)e^{(\frac{\mu_{i,i}}{T})}e^{(\frac{B_{i,i}}{T})}}{(2s_{i+1,i}+1)e^{(\frac{\mu_{i+1,i}}{T})}e^{\frac{(B_{i+1,i})}{T}}} \qquad \textbf{(1.33)}$$

in which *B* is the binding energy of each considered cluster *(i, j)* with mass number A_i and charge Z_i and spin $s_{i,j}$. Using this formula, one can obtain a simple expression for R. In fact, according to equation 1.32, the exponential terms containing the chemical potential will give altogether a factor 1. So, combining the spin factor into a single variable α_s and expressing the binding energy according to

$$\Delta B = B(A_i, Z_i) - B(A_{i+1}, Z_i) - B(A_j, Z_j) + B(A_{J+1}, Z_j) \qquad \textbf{(1.34)}$$

one can finally obtain this simple formula

$$R = \alpha_S e^{(\frac{\Delta B}{T})} \qquad \textbf{(1.35)}$$

By measuring R experimentally, the temperature is readily obtained as

$$T = \frac{\Delta B}{\ln(\frac{R}{\alpha_S})} \qquad \textbf{(1.36)}$$

This method has been applied first to ^{3}He, ^{4}He, ^{6}Li and ^{7}Li species by the ALADIN group [Poc95], but other isotopes have been used by the INDRA [Ma97] and MSU [Tsa96] collaborations. The main drawback of this method certainly lies in "side-feeding" effects. This effect follows from the fact that some of the observed particle can be emitted as result of a secondary decay process from more massive cluster and not from the primary process of decay of the studied emitting source. There is also another limitation in this method connected to the sensitivity of the procedure for temperature exceeding 5 *MeV*, but this aspect is not clear and the results are contradictory (see for example [Majk96], [Ma97], [Tsa96]) .

1.2.4 Temperature from yields of states of the same emitted particle.

A great part of the difficulties in determining the mass and isospin dependence of the separation energy ε_s, can be removed by considering the thermal population of states within a given product that is emitted from the system. In other word, fixing the product emitted by the source we can study the different population of excited states of this one. In this restricted case, we can safely assume that spin, isospin and dynamical aspects involved in the emission of each of the state are the same. The main difference still remain the separation energy ε_s, and the relative emission rate will be proportional to $e^{(-\Delta\varepsilon_s/T)}$, where $\Delta\varepsilon_s$ is the difference in energy between the states.

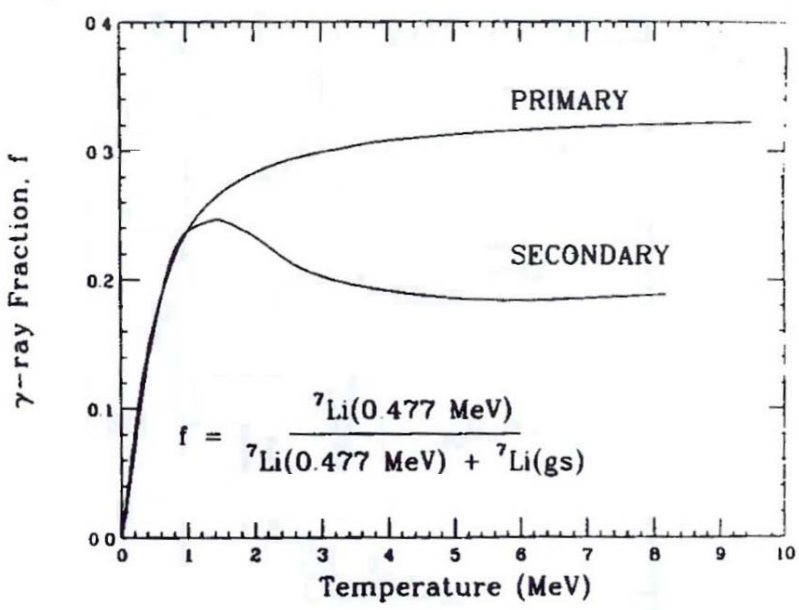

Fig. 1.13 : The variation of the fraction of 7Li in the excited state as a function of the temperature . The predicted effect of a sequential decay on the population ratio is shown by the curve labeled "SECONDARY" [Hah87].

Particularly in light nuclei, we should add some consideration relative to a factor for the ratio of the spin degeneracies because pairs of levels usually do not have the same spin. Thus, the ratio R of two levels in a single nucleus should be given by

$$R = \frac{2J_u + 1}{2J_l + 1} e^{\left(\frac{-\Delta E}{T}\right)} \qquad \textbf{(1.37)}$$

where J_u and J_l are, respectively, the spins of the upper and lower state, and $\Delta E = E_u - E_l$ is their energy separation. In Fig. 1.13 [Mor85], the variation of this ratio for two bound state of ^{7}Li as a function of the temperature is shown.

The primary difficulty with this type of measurement comes from the subsequent redistribution of the population after the emission of one fragment [Boa84] [Hah88]. In fact, in our discussion we consider always the emission from the primary source but in the experimental spectra there is a contamination from the secondary emission. To extrapolate from the experimental data the real primary emission is needed a model of the emission process and detailed knowledge of the nuclear isotopes which take part. One should also remember that even in the ideal case in which everything is under control, the sensitivity of this method is limited to temperature values which are of the magnitude of the separation energy of the species that are measured. If we exceed this temperature, the exponential part of the Eq. 1.37 will disappear and the relative yield becomes saturated, a phenomena that is well known in classical system.

Chapter 2

THE EXPERIMENTAL APPARATUS

Introduction

The GDR experiment analyzed in this thesis was performed in the framework of a collaboration between the STREGA group (Laboratori Nazionali di Legnaro and I.N.F.N. section of Bologna, Firenze, Trieste, Milano and Napoli) and the HECTOR group from Milan and Krakow, with the main goal to characterize the Giant Dipole Resonance emission through the simultaneous detection of high energy γ-rays and charged particles emitted from a Compound Nucleus formed at high excitation energy. Analysing the light charged particles emitted in the process, it is possible to obtain information on the characteristics of the emitting source and in particular to disentangle those particles emitted in the early stages of the reaction, if present. It is therefore possible to determine, at least as a lower limit, the amount of energy taken away from the Compound Nucleus due to the pre-equilibrium process. A much proper description of the remaining CN is then available and this is important for a correct analysis of the GDR emission.

A quite complex apparatus has to be used in order to measure in the same experiment the signals from charged particles, in the range from protons and α-particles up to Carbon and more, and the γ-rays together with the heavy residues which remain after the evaporation process. In this way, one can perform an exclusive measurement and select the events of interest in a proper way.

Using a large scattering chamber installed in the III experimental hall of LNL (a cylinder of $\approx$ 3 m of diameter and 5 m of length), the apparatus was setup coupling a drift chamber of the GARFIELD apparatus (General ARray for Fragment Identification and for Emitted Light particles in Dissipative collision) to 8 big BaF_2 crystals from the HECTOR apparatus. The Evaporation Residue have been detected through a system of Position Sensitive Parallel Plate Avalanche Counters (PSPPACs)

filled with the heptane gas (C_7H_{16}) with the dimension of 20x20 cm^2. They were positioned at forward angles ($4° < \theta < 12°$), two for each side of the beam, one placed in front of the other at a distance of 150 *cm* from the target. In this way, each couple subtended an angular range of 8°. A 25 *mm* Upilex absorber was mounted in between each PSPPAC couple in order to be sure that all the Evaporation Residues would be detected only in the forward PSPPAC, while elastic scattered beam and fast projectile-like fragments would have joined also the second detector.

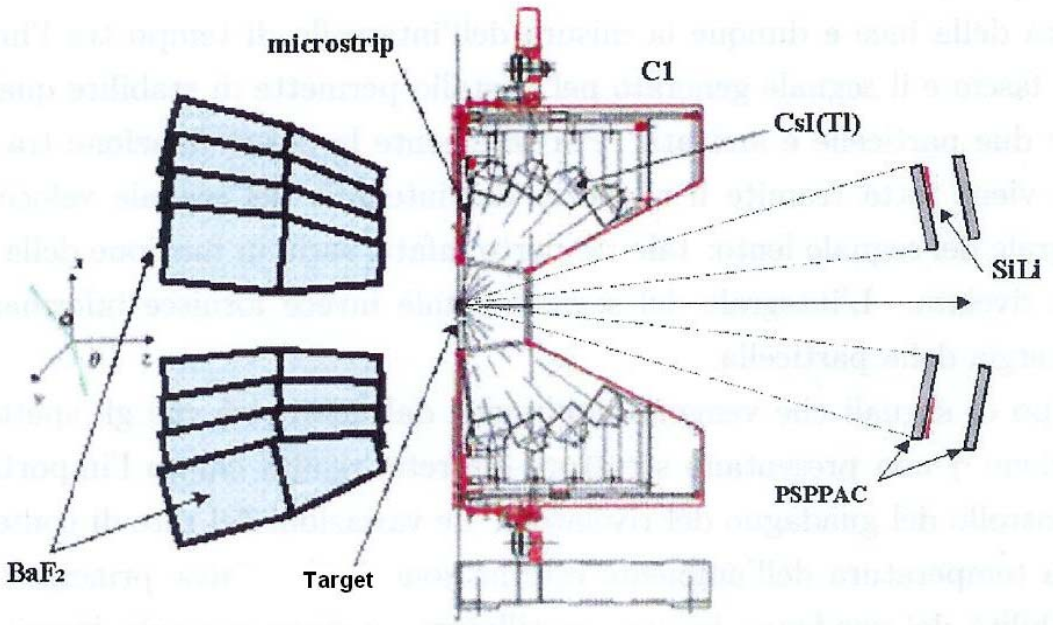

Fig. 2.1 : Picture of the set-up for the GDR experiment done at L.N.L. One can see the Garfield apparatus to reveal charged particles, the BaF for γ-rays and the PSPPAC for the ER.

Behind the first PSPPAC, some Silicon-Lithium drift detectors were placed at large angles, where lower radiation damage could be expected. The Silicon detectors (5 *cm* X 5 *cm* each) were covering from 8° to 12° and from 10° to 12° respectively on the right and on the left part of the beam, and permit the estimation of the residual energy of the fragments.

From the Time of Flight (ToF) measurement and the position reconstruction the velocity plot of the fragments can be reconstructed. Adding the measurement of the residual energy, a further information on the mass can be obtained, even though with a limited resolution ($\Delta A/A \sim 2 \div 4\%$ for $v_{cm} = 0.66$ *cm/ns* and $v_{cm} = 1.89$ *cm/ns*).

In fig 2.1 one can see a complete scheme of the experimental apparatus used for the GDR experiment, with the different detectors: the drift chamber of Garfield, the BaF_2 from the Hector apparatus and the two couples of PSPPAC completed with the SiLi detectors. In the following

chapter, we will describe the single parts of the set-up used in this experiment, describing the working parameters and the characteristics of the different detectors.

2.1 The G.AR.F.I.E.L.D. apparatus

In heavy ion reaction one has to deal with a very large range of energies and products. Often, going from the typical processes at low energy up to the most complex and dissipative phenomena at the higher energies, one can obtain the major information on a process, when dealing with the transition regions from a regime to another one.

This is the case passing from the Compound Nucleus evaporation or Intermediate Mass Fragment sequential emission to the multi-fragmentation regime, and, again, going from the multi-fragmentation towards the vaporization regime etc. The opportunity of studying the behaviour of the nuclear system which develops from one stage to another is very important: any modification in the nuclear matter characteristics (pressure, density, isospin etc…), in fact, can be reflected in a variation of the experimental signatures, which carry important information.

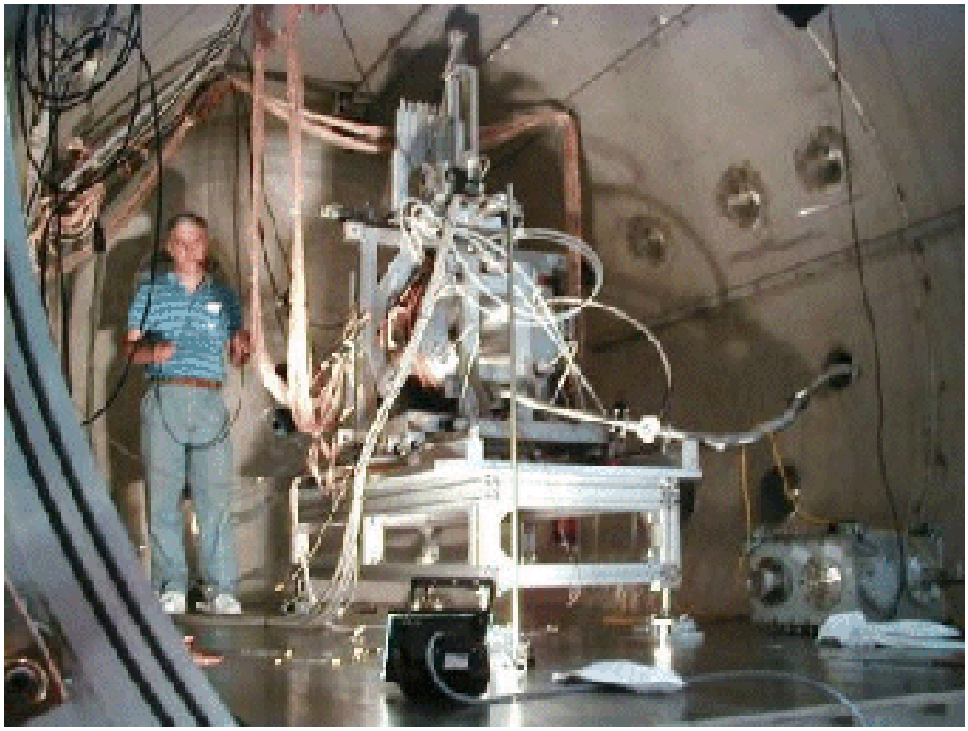

Fig. 2.2 : ***The Garfield apparatus inside the Huygens-Watt vacuum chamber.***

For this reason the GARFIELD apparatus ([Gra], [Gra97]) is particularly important: it represents, in fact, a powerful tool that can be used to study the evolution of the nuclear system from the low

energy regime where mean field proprieties are predominant to the intermediate energy regime where new open channels start to be present, due to the contribution of the nucleon-nucleon forces ([Gra03a], [Gra04a]). In Fig. 2.2, one can see a picture of the GARFIELD apparatus inside the large scattering chamber.

We have to deal with reaction products the mass and energy of which can vary a lot: they go, in fact, from Light Charged Particles up to heavy fragments and from few *KeV* up to hundreds of *MeV*. The situation is, therefore, complex and it is very important to develop a detection system capable of detecting and identifying such a variety of reaction products [Gra03b].

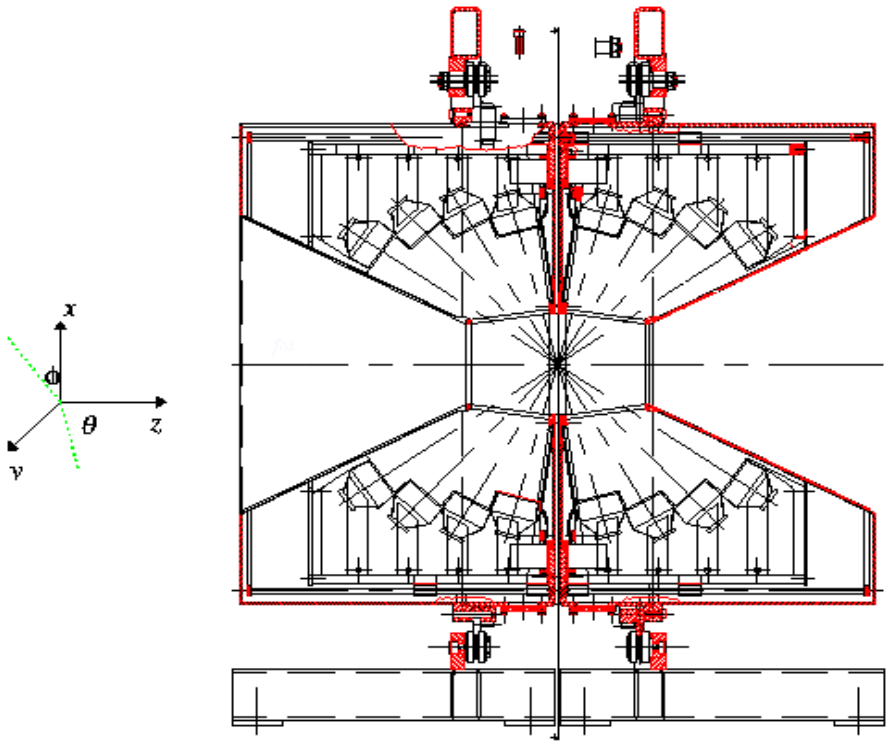

Fig. 2.3 : Trasversal section of the two chambers of Garfield

The GARFIELD apparatus is based mainly on the ΔE-E technique, where the ΔE signal is given by the drift chamber where several microstrip detectors collect and amplify the primary electrons which were produced along the ionization track of the detected particle. Some CsI crystals, Thallium doped, are then used as stop detectors to get information on the residual energy E_r. Fig. 2.3 shows a transversal section of the two drift chambers.

GARFIELD is made by two independent chambers, one for the forward angles and the other for the backward angles. In particular, with respect to the beam direction, they cover the range from $30° < \theta < 85°$ and from $95° < \theta < 150°$. For the azimutal angle φ, the backward camera covers $0° < \varphi < 360°$ and the forward chamber the part $0° < \varphi < 70°$ and $110° < \varphi < 360°$. The side opening in this chamber was designed to permit the positioning of possible ancillary detectors in this region. In

particular, it is planned to use in this position the Side Isotope Array, i.e. a system of 15 three stages telescopes (ionization chamber, 200 μm strip silicon detectors and CsI(Tl)).

One important parameter to be considered when designing a 4π apparatus is the possibility that 2 particles hit at the same time the same detector (double hit). To avoid this problem, it is important to have a high granularity. Normally a desired number of detectors is at least 10 times more than the maximum multiplicity expected for the product of interest. At relatively low energy, which is the range of interest for the physics to be studied with GARFIELD, maximum multiplicities around 15 for light particles plus 4-5 for heavy fragments (A > 4) are expected. We need, therefore, around 200 indipendent telescopes to perform a reasonable reconstruction of our events.

This granularity is obtained in the GARFIELD drift chambers dividing each of them in sectors of $\Delta\varphi = 15°$. This means that the forward chamber is divided into 21 sectors, while the backward chamber into 24. Each sector contains 4 CsI(Tl) crystals positioned at different θ angles plus a microstrip pad (metallic strip photolithography on glass). The microstrip pad is divided in the 4 collection regions up-right, up-left, down-right and down-left (see the following paragraph 2.1.2 for details). In figure 2.4, one can see the scheme of a drift sector.

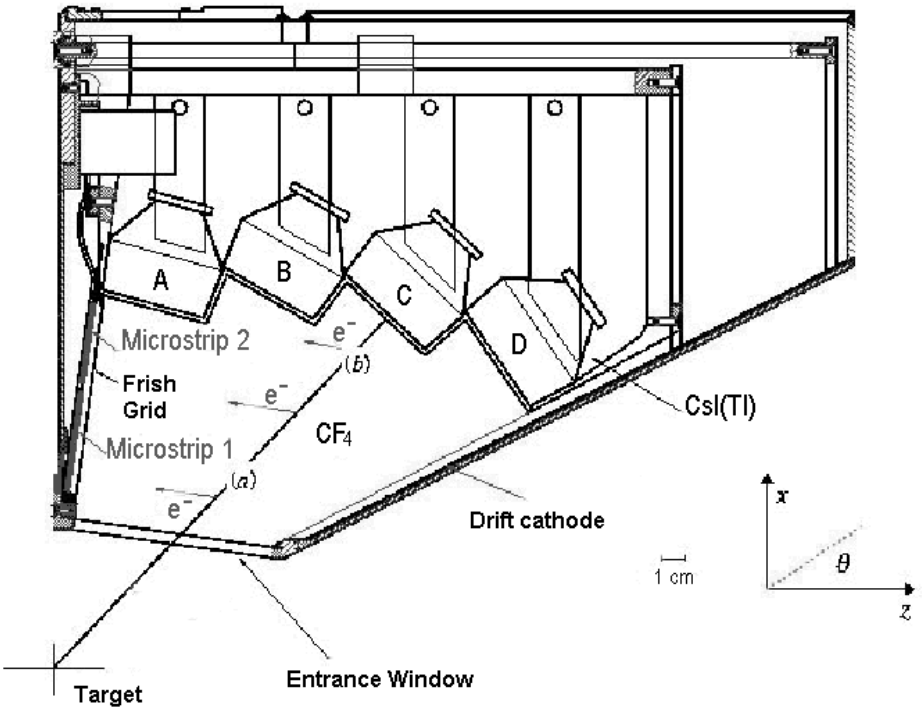

Fig. 2.4 :Scheme of a drift sector of GARFIELD.

One telescope in GARFIELD consists, therefore, of the combination of μstrip down left (or right), μstrip up left (or right) and one cesium: we arrive in this way to have at least 8 telescopes per sector, which means in total 192 for the backward chamber and 168 for the forward chamber.

2.1.1 The CsI(Tl) crystals.

CsI(Tl) crystals have been chosen due to their excellent characteristics, like the high stopping power, the good energy resolution (close to 3-4 % with 5.5 *MeV* α particles from ^{241}Am source), the small sensitivity to the radiation damage, the relative small hygroscopy and the fact that they are quite easy to cut and machine so to obtain easily the shape needed for the experiment. Moreover, the CsI(Tl) crystals are relativity cheep.

In the GARFIELD apparatus there are 4 CsI(Tl) per sector, with a total number of 96 in the backward chamber and 84 in the forward chamber. The shapes are different as a function of the different θ angles where they are positioned. In fig. 2.5, one can see a drawing of the different dimensions of the crystals. Their shapes are designed so that the front face is always perpendicular to the radial trajectory of the particle emitted from the target.

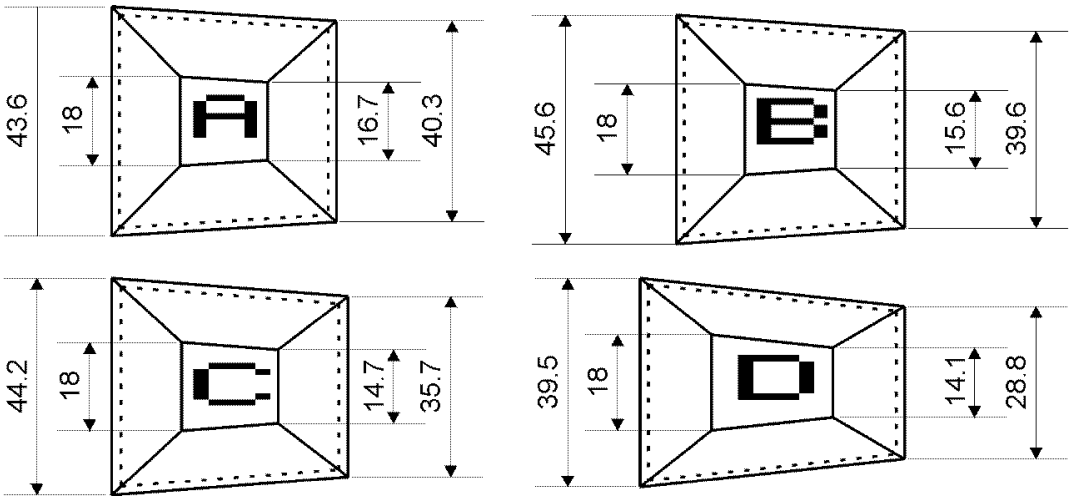

Fig. 2.5 : A drawing of the different shape of Garfield CsI(Tl) crystals. The A shape corresponds to the most near to the plane of micro (θ more big respect with to a beam line)

A particular procedure to wrap the crystal in order to maximize the light collection has been studied ([Lan01], [Ton99]). Moreover the shape of the backward part of the crystal is like a light guide to optimize the coupling with the photodiode S3204-05 produced by Hamamatsu (18 *mm* X 18 *mm* of dimension and 500 *μm* as depth). The use of photodiode instead of photomultiplier tubes is due to the good stability of the first, its smaller dimension which makes its mounting inside the gas volume much more feasible.

Before being mounted inside the apparatus, every crystal is tested using radioactive sources like the three peaks mixed α-source (^{241}Am (E=5.484 *MeV*), ^{239}Pu (E=5.155 *MeV*), ^{244}Cm (E=5.806 *MeV*)) and a γ source (like ^{60}Co which produces two lines at E_γ = 1.17 *MeV* and E_γ = 1.33 *MeV*) for

investigation of the bulk. We calculated the resolution with the α-source using the average value of the FWHM (Full Width Half Maximum) of the 3 peaks. The results obtained as resolution and light output from the α-source and from the γ-source are an indication on the crystal properties and on the gluing to the photodiode. If the result is not satisfactory, i.e. larger than 4.5% for α-particles, we repeat at least one more time the procedure of preparation of the CsI crystal (cleaning with powder of diamond, gluing the photodiode, wrapping procedure).
Further aspects connected with the intrinsic characteristics of this type of scintillator will be discussed later in a following chapter, together with other scintillators.

2.1.2 The drift chamber

One of the most important requirements that a complete apparatus should fulfil, when used for studies of nuclear reaction mechanism with heavy ions, is the capability of identifying the reaction products with a low energy threshold, which permit to reconstruct the events where slow products are emitted.

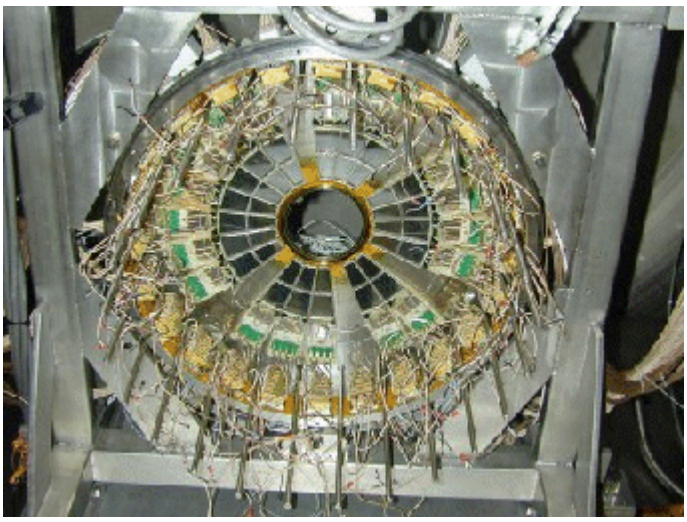

Fig. 2.6 : Ground of the cylinder of the Backward Camera. The microstrip plane can be seen

The use of a gas detector is of great importance to fulfil these requirements, allowing an easy selection of the effective ΔE thickness, which is a compromise between a very low identification threshold and the necessity to handle large dynamical ranges of detected products. New possibilities for the gas ΔE section arose a few years ago with the development of micro-strip gas chambers

(MSGC), initially designed to meet the severe needs of counting rate, high gain and position resolution of high energy physics. The originality of Garfield is in the use of this type of detector also in low energy physics ([Gra94], [Chi02]).

The advantages of using MSGS's are mainly due to the large dynamical range and to the signal-to noise ratio for the low ionizing ions, which is much higher as compared to ionization chambers. These two characteristics allow the simultaneous identification, with low energy threshold, of both light charged particles and heavy ions with an only two-stage telescope. In fact, the detector is characterized by a wide acceptance in Z, from 1 up to at least 28, with an identification threshold of about 0.8 *MeV/A* and a detection threshold much lower (in the order of 10-20 *KeV/A*).

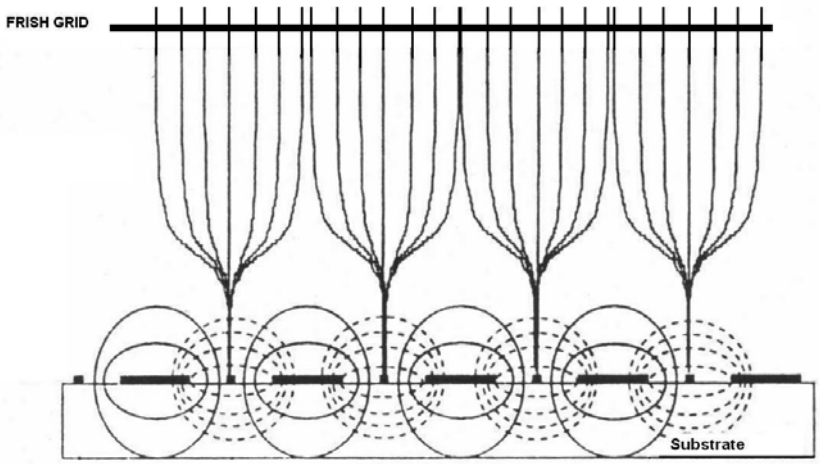

Fig 2.7 : Drift line of the electric field inside a gas drift chamber with microstrip as collecting electrodes.

In fig. 2.7, one can see the drawing of the electric field inside a gas drift chamber of this kind. The drift lines are perpendicular to the microstrips plane and the intensity of the field is constant. After the Frish grid close to the microstrip plane, the field starts to have the dependence of *1/r*, where *r* is the distance from the anodes, and the field intensity increases allowing an avalanche phenomena of multiplication of the primary electrons. In this way, we obtain a good electric signal which is still proportional to the initial ionization produced by the particle in the gas.

Each microstrip (fig. 2.8), as just told, is divided in 4 parts and it is made by hundreds of very small alternated metallic electrodes which are prepared through photolithography on glass. A very small distance (50 μm) between the single cathode and anode permits a fast collection of electrons and positive ions formed close to the microstrips plane, which results in a faster signal and a better reliability due to the fact that the electric field near the microstrip remains almost the same in time.

The anode strips, which are 10 μm large, are biased at $\approx 400\ V$ and connected in 4 groups, while the cathode strips are connected all together and grounded. In this way we have only 4 signals from

every microstrip. In fact, for our purposes, it is not needed to read the single anode. The angular resolution along the θ angle is given by the correlation with the different CsI(Tl) crystals, with a resolution of ± 7.5°. This resolution can be improved down to 1° when the drift time information given from the microstrip electrons is used. The φ resolution is fixed by the fact that a single microstrip is 15° and is divided longitudinally into two parts, so it can arrive down to 7.5°.

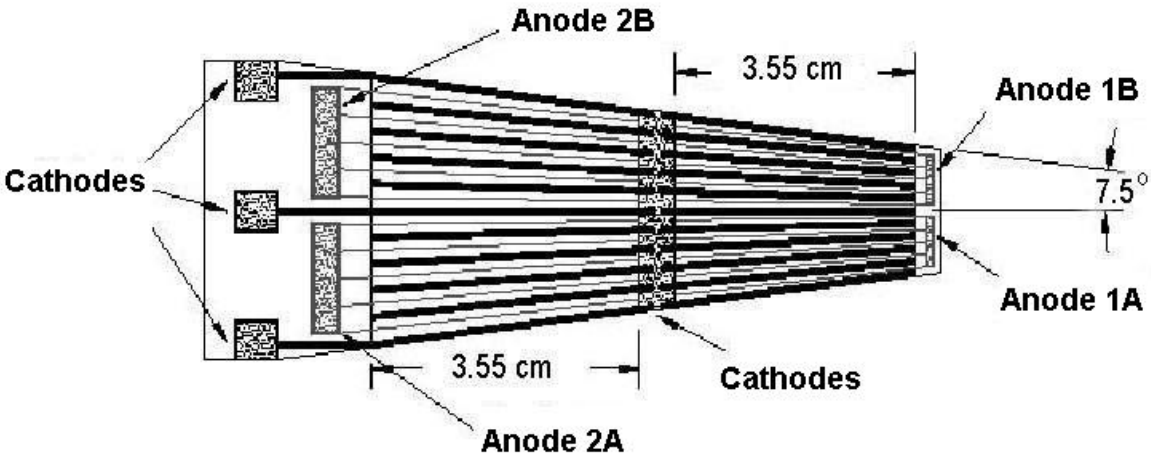

Fig 2.8 : Scheme of a microstrip of Garfield.

The gas inside the chamber is CF_4, a gas characterized by a high stopping power and a high drift velocity (10 *cm/μs* at 1 *V/cm·Torr*) of the electrons produced in the ionization process. Due to this characteristic of the gas, the working pressure can be relativity low (50 ÷ 200 mbar), with a great advantage for the safety of the entrance windows of the detector that can be thinner and for the field cage that can be maintained at lower voltage and have, therefore, less damage due to possible discharges.

In the GARFIELD apparatus, there is also a semi-automatic recycling gas system to circulate the CF_4 inside the drift chamber. In this way we do not have problems connected to possible decrease of the gas quality.

2.2 The HECTOR apparatus

The HECTOR apparatus (Fig.2.9) is formed by 8 big crystals of BaF_2 and a multiplicity filter (HELENA) composed by 38 smaller crystals also of BaF_2 [Maj94].

In this experiment only the main part of HECTOR, i.e. the 8 big scintillators, have been used. The BaF_2 are inorganic crystals and due to the large dimension which they can reach, they are

particularly suited to study high energy γ-rays ($5 < E\gamma < 30$ *MeV*), exactly in the range important for the Giant Dipole Resonance emission.

Fig 2.9 : Picture of the complete Hector apparatus.

Every BaF_2 is shaped like a cylinder with 14.6 *cm* of diameter and 17.5 *cm* of height. The last piece of 5 *cm* is shaped like an ended pyramid with hexagonal base to be better coupled with the phototube that converts the photons produced inside the crystal into an electric signal processed by the electronics [Boi]. In particular, they are coupled to the phototube model 9823QA produced by EMI through a window made by quartz. Obviously, all the surfaces of the scintillators are prepared in the proper way and covered by Teflon and aluminium to reflect all the light inside the material and to minimize the signal loss. In addition to this, every crystal is screened with 3 *mm* of lead to suppress the low energy γ-rays ($E\gamma < 500$ *KeV*), in order to decrease the total counting rate and the noise. An external capsule is provided to isolate and screen them from the outside light.

Another aspect, particularly important in the use of this detector, is the possibility of a fluctuation of gain during the experiment with the consequent hard problem in the calibration. In particular, this is due to the problems of the phototube, like the decrease of the electric field in the last dynode for the creation of plasma and the instability of the differential potentials between the different levels of amplification chain, and to an intrinsic variation of chemical-physical characteristics of BaF_2. In fact, the change of transparency and of the properties of scintillation of these materials as a function

of the temperature are well known. Also the phototube, like every electronic device, is strongly sensitive to fluctuation of the external temperature.

To minimize the problem on the phototube, a particular scheme in the voltage divider is used applying a bias to the dynode. In particular, with respect to the standard base produced by the EMI, we do not use all the 14 dynodes available and a smaller voltage is applied. In this way, the energy resolution becomes slightly worse, but not in a sensible way for the GDR measurement, while we have an improvement in the stability of the gain.

To take under control the fluctuation on the gain of the HECTOR detector it has been decided to put an artificial point of reference in the energy spectra using the light from a LED mounted on the lateral side of the crystal. One can change from outside the frequency in a range from 1 *Hz* to 10 *kHz*, and also the intensity of the single pulse. The light emission is centred around 568 *nm*, that means a Gaussian peak at equivalent energy of 25-30 *MeV*. To have a good peak from the light of the LED around 3000 pulses are needed, which means that one can create it without error for the gain fluctuation connected to the temperature. Therefore, the use of this artificial source gives a quite easy point of reference to keep under control during the experiment the behaviour of the detector with respect to the temperature.

With respect to the normal configuration just described, some changing, especially in the connection with the voltage divider, was done for the fact that in this experiment the BaF_2 detectors were operated inside the vacuum chamber and not on air like usual. In fact, to avoid the problem of heat dissipation inside the resistors which form the voltage divider, this one was placed out of the scattering chamber. The opportune voltage created just after every resistor of the chain was carried to the correct dynode inside the photomultiplier tube with a cable. The LED light was not used in the present experiments. More detailed information on the intrinsic characteristic of the BaF_2 crystal will be given in the Chapter 3 in the more general discussion about the scintillating materials.

2.3 The Position Sensitive Parallel Plate Avalanche Counter (PSPPAC).

The detection system used to detect the Evaporation Residues was made essentially by two couples of PSPPAC. In every couple one PSPPAC was placed after the other with a dead layer (25 μm of

Upilex) in the middle to stop the slow products. In such way it was possible to recognize the ER events through an anti-coincidence between the two coupled PSPPAC. After the first PSPPAC, at larger angles for problem of radiation damage, there were placed Si-Li detectors to determine the residual energy. In fig. 2.10, one can see a picture of a couple of PSPPACs detectors used for the experiment, with the Si-Li visible in the middle.

A single PSPPAC detector works like usual multiwire gas chamber in the proportional range [Cas99]: when the charged particles cross the gas, some electrons are created in the ionization process. These electrons feel the electric field and start to move versus the anodic wires. The electric field becomes very strong in the proximity of the wires so that the process of avalanche multiplication of the electrons starts. The final signal is collected by the wire which is closer to the position of the avalanche and it is proportional to energy lost by the initial particle.

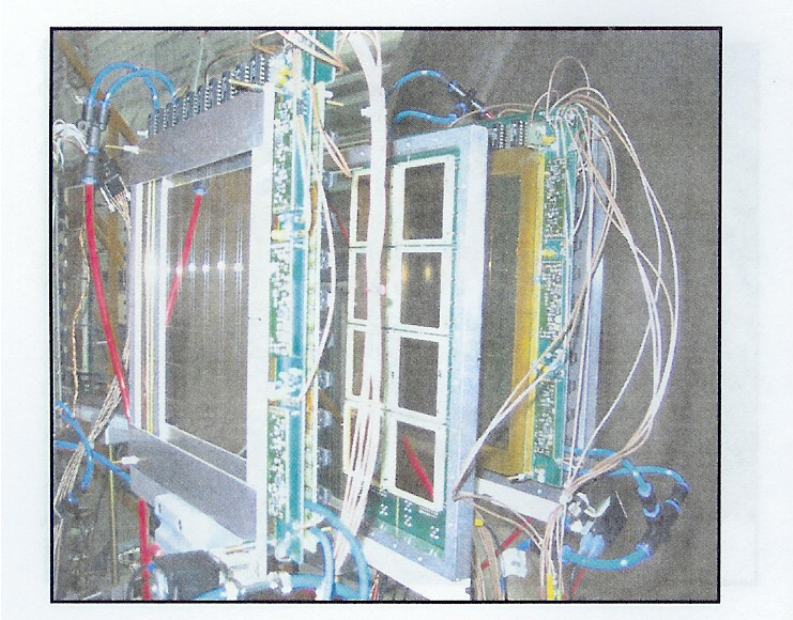

Fig. 2.10: Couple of PSPPAC- SiLi placed in between at large angle. The beam line is from the left to the right.

These particular detectors are assembled in a square shape with 20x20 cm^2 active area. The core of them consists of a central cathode made by a Mylar foil (1.5 μm thick double aluminized) and in two anodic plains, one perpendicular to the other, made by 200 of parallel tungsten wires. The two plains, one for the x coordinate and the other for y coordinate, are placed at 3 *mm* from the central cathode. Every wire of the anodic plane is 20 μm of diameter, and placed at the distance of 1 *mm* from the other. They are connected to the ground through the preamplifier, while the cathode is at negative voltage around 500 *V*. Another foil of Mylar, positioned at 7 *mm* from the cathode, is used to close the internal volume, on which heptane gas (C_7H_{16}) is fluxed at typical pressure of 3.5 *hPa*.

The wires are grouped two by two and every group is connected to the following with a delay line corresponding to t_d of 3.3 *ns*. In this way one has a greater signal collected from every group with

respect to the single wire and the position of the incident particle can be identified with only two preamplifiers, one for each side of the grid. In fact, considering the total delay T_d = 50 x t_d, and calling t_1 the time needed for the signal to arrive from the single wire hit to one preamplifier and t_2 the time needed for the same signal to arrive to the second preamplifier, with t_v we call the time needed to have an avalanche production and with t_0 the delay time produced by the wire, we have that

$$t_1 = T_d - nt_d + t_0 + t_v$$
$$t_2 = nt_d + t_0 + t_v$$

where *n* is the position of the group of wires that produce the signal. Therefore, we can obtain the position by

$$n = \frac{T_d - (t_1 - t_2)}{2T_d}$$

In this way only 5 preamplifiers are needed, 2 for every position and one for the cathode signal, to have the complete readout of the signal from the PSPPAC. To avoid a problem due to the connection cable, these preamplifiers are mounted directly on the detectors. In the normal working condition, these detectors have a time resolution less than 1 *ns*, a detection efficiency around 100% for Z > 10 and a spatial resolution of 2 *mm*.

2.4 The ELECTRONICS.

To describe briefly the electronics of the experiment, we can divide it for the three kinds of detectors, GARFIELD, HECTOR and PSPPAC that are used. Let us start with the description of the more complicated GARFIELD electronics.

2.4.1 The GARFIELD electronics.

The electronic scheme of the Garfield apparatus can be explained referring to the sector modularity (Fig. 2.11). The 8 signals, 4 from the microstrips and 4 from the CsI, are processed by the pre-amplifiers placed inside the gas volume, very close to each detector. The pre-amplifiers work inside the drift chamber and therefore they have been designed to minimize the hot dissipation. A water

cooling system to keep the temperature under control has been provided around the GARFIELD chambers.

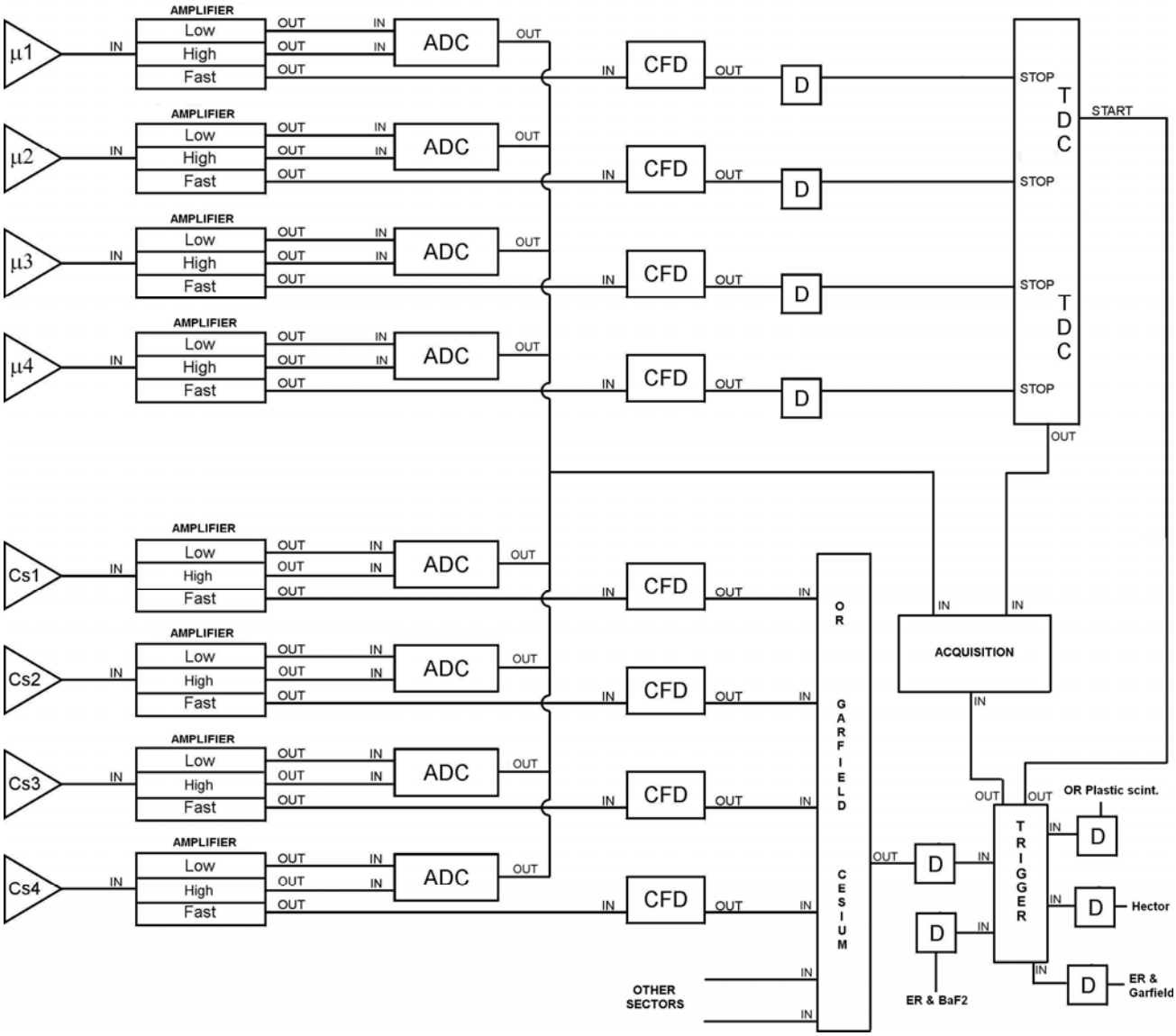

Fig 2.11 : The electronic scheme of one Garfield's sector.

The amplifier modules (CAEN N568B) are placed out of the scattering chamber, connected to the vacuum flange through ~ 6 *m* of coaxial cables. They were opportunely designed for this apparatus. Each module can have 16 channels, so it can analyze the signals coming from 4 sectors of CsI(Tl) crystals or 4 microstrips. The shaping time parameters are set to 3 μs for the two different detectors. Each entrance channel of the module is correlated to 3 output signals: one is fast and negative, the other two are slow and positive and different only for a gain factor. The two positive signals are the linear energy signals and they are fed into an ADC (Analogical-Digital Converter) and registered in

the stored data. The choice to have two different gains is due to the fact that the energetic range of particles detected in GARFIELD is quite large. The High Gain factor in the case of ΔE signal has been selected to better amplify signals of the light particles (Z = 1, 2) that loose a small quantity of energy in the gas. In the case of residual energy the High Gain factor is important for the heavy fragments that arrive to the CsI with a small amount of energy and undergo to a strong quenching of the light output.

The fast and negative signal from the amplifier is fed into a Constant Fraction Discriminator (CAEN C208). The CFD, which has 16 input channels, has got two ECL signals for every input. Besides that, an OR signal per module plus a sum (Σ) signal are present. The Σ signal can be chained in several CFD modules, so to obtain the final multiplicity signal. Different multiplicity trigger signals can be obtained by sending the multiplicity signal ina a discriminator whose threshold can be set opportunely.

The fast signal of a CsI(Tl) crystal after being processed through the CFD is sent to form an OR with all the other CsI(Tl) signals so to have the main trigger of GARFIELD. The fast signal of a microstrip detector is fed into some delay modules and then sent to the TDC to give the STOP signal. This signal is used for drift time measurement purposes. The START of the TDC is given by the main trigger, which is made by the general OR of all the trigger signals present in the experiment. To get the real time of reference, the START signal will be then corrected event by event through the Radiofrequency (RF) pulse, which has been registered event by event.

2.4.2 The HECTOR electronics.

The signal from the last dynode and the last signal from the anode are read out and fed into processing electronics. We have a fast signal sent to CFD which gives both the fast output for Time of Flight purposes which goes into a TDC, and an OR signal which is useful for the final trigger. The second output is sent to a splitter module which gives for every input a fast linear output and a slow linear output.

The fast output is opportunely stretched and both signals are fed into the ADC channels. The time of flight spectrum and the fast versus slow correlations are used for γ-neutrons discrimination. All parameters of the amplifier modules, the CFDs and High Voltage System are controlled through a control system based on LABVIEW ([Gia05a], [Gia05b]) developed on purpose for the GARFIELD electronics.

2.4.3 The PSPPAC electronics.

The pre-amplifiers are 5 per PSPPAC: 4 signals of position (x_i, x_a, y_i and y_a) and 1 signal from the cathode. They are fed into a CFD module with fast delay. The output signals from the 4 cathodes are fed into a short range TDC (800 μs), while the 16 positions are fed into 1200 μs range TDCs.

2.5 The acquisition system.

The GARFIELD apparatus is complex: both the number of parameters that have to be recorded and the acquisition rate (≈ 2 *KHz*) can be large, so the acquisition system has to be really powerful and flexible. The system, based on FAIR front-end (Fast Advanced Interface Read-out) developed by the I.N.F.N. section of Napoli, is an ECL bus dedicated to the fast read-out of electronic acquisitions modules ([Ord95], [Ord98]).
The velocity transmission of data on the bus is 1.25 *Gbits/s* and the architecture of the system is on two levels (Fig. 2.12):

- at low level, the single electronic modules (ADC e TDC) are grouped in segments. Every group is controlled by its own Segment Controller (SEGC). In the present experiment 4 segments have been used.

- at high level , every Segment Controller can communicate with the System Controller.

Due to the performances of the Segment Controller, it is possible to have an event by event identification of the trigger pattern. In fact, the main trigger is composed by an OR logical condition of several trigger signals, like it will be described in the following chapter.
Through the acquisition system it is possible to modify remotely the ADC and TDC set up (thresholds, ranges, etc…). We will explain better all these possibilities in the fourth chapter, where the present experiment will be discussed in detail.
In conclusion, this acquisition system can work up to 10^7 parameters, with 32 bit for each. All the operations needed are done without any software protocol, using an auto-configuration procedure,

which is able to recognize directly the kind of module (ADC, TDC, delay etc.) and assign to each module a virtual station number (VSN) to make it recognizable in the off-line analysis.

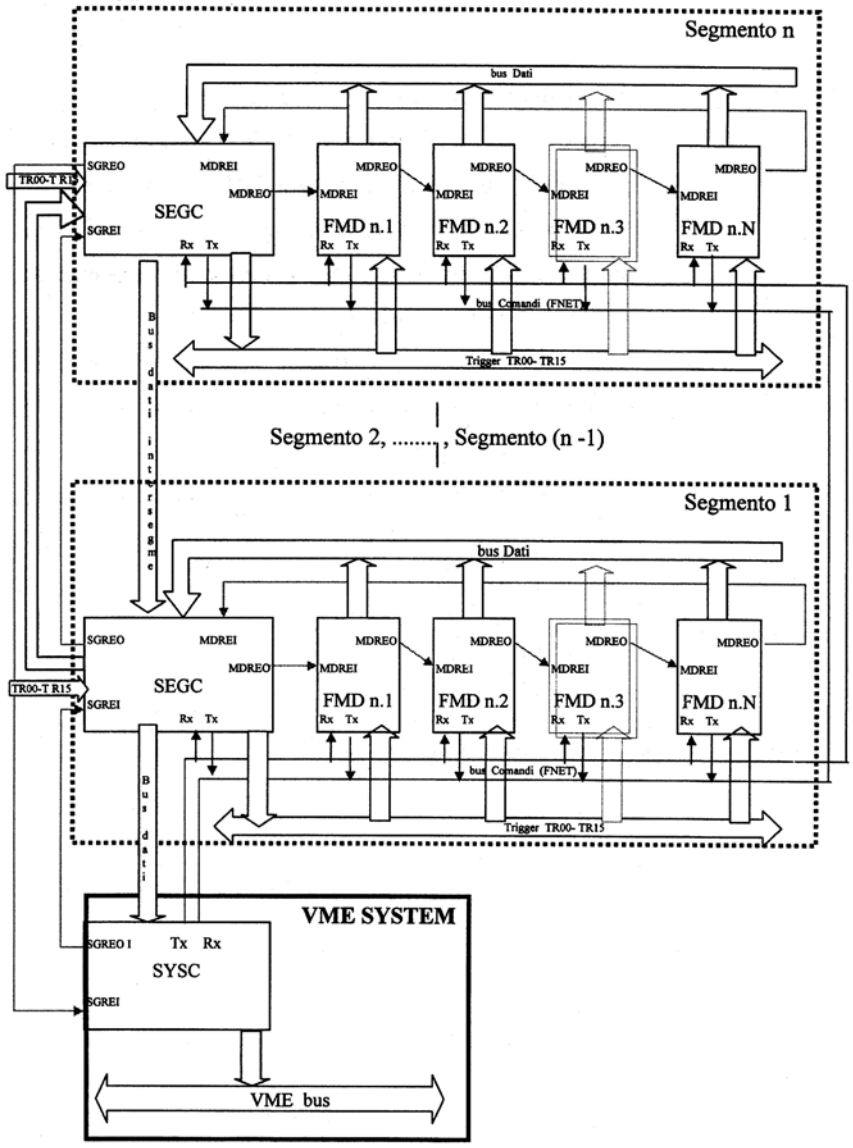

Fig 2.12 : The FAIR acquisition system

The final data are written on the disks of a Personal Computer used like a storage. It is also possible to monitor the experimental spectra with a graphic interface of the acquisition system.

Chapter 3

THE SCINTILLATING MATERIALS

Introduction

The scintillation process is one of the most useful methods available for the detection and spectroscopy of a wide assortment of incident radiations. The available scintillators can be liquid, solid or in form of gas, organic and inorganic, pure or doped, with crystal structure or amorphous. Depending on the type, they can detect charged particles, neutrons or γ-rays with a huge spread of different time reaction, resolution, efficiency and light output spectra. For this reason, it is quite easy that at least one of these materials fits part of the experimental request of an experimental apparatus in nuclear physics.

An ideal scintillation material should satisfy a lot of properties, among which we can underline the high scintillation efficiency, the transparency to the light produced by itself and a short decay time of the induced luminescence in order to generate a fast signal pulse. It is clear that the material should be suitable to be manufactured in dimension which must be large enough to become a detector. Moreover, a linear dependence of the light output from the energy lost by the incident radiation is preferable to simplify the calibration procedure. Obviously no material can simultaneously meet all these criteria, so the choice of a particular scintillator is always a compromise among different factors, strictly connected to the experiment that has to be performed.

The light produced inside the scintillators can be divided in fluorescence, that is the prompt emission of visible radiation from a substance following its excitation, phosphorescence that corresponds to the emission of longer wavelength with respect to fluorescence and with a characteristic emission time that is generally much slower, and finally the delayed fluorescence which shows up the same emission spectrum of the prompt fluorescence but again it is

characterized by a much longer emission time following the excitation. A good scintillator should convert a fraction as large as possible of the incident radiation energy into prompt fluorescence, minimizing the other two contributions which are generally not useful. This light emission is normally collected by a photomultiplier tube or by a photodiode which have the function of converting the photons into electrons. The following electronic signal is then processed by the electronic chain (shapers, amplifiers, Analogical Digital Converter etc…). The internal scintillator mechanism which creates this prompt fluorescence is different depending on whether the material is organic or inorganic. In this chapter, we will discuss separately the two cases and in a second case we will focus the attention on some particular scintillators dedicated to the detection of charged particles (crystal of CsI(Tl)), to the detection of γ-rays (crystal of BaF_2) and finally we will show some preliminary studies performed at the National Laboratory of Legnaro on some new and interesting scintillating glasses made of Lithium and Boron to capture the neutrons and activated with Ce^{3+} or Eu^{3+}. Using these materials, it is not possible to perform neutron spectroscopy measurements because the neutron capture cross section on Li or B is effective only up to ~ 1 *MeV* of energy. The neutrons to be detected have, therefore, to be thermalized before the detection. In this way the energy information is then lost and one can only use them as neutrons counters or multiplicity filters. This could be useful for the apparatus like Garfield, because in any case due to the big amount of materials around, the energy and the direction information of the neutrons would be destroyed by the multiple scattering on them.
A good measurement of the multiplicity of neutron could be in any case a further information to complete the events reconstruction. A preliminary investigation on their properties is, therefore, considered important in our case. To investigate the quality and the characteristics of the different materials, we have performed some tests using α and γ sources. Other technique, like the Ion Beam Induced Luminescence (IBIL) and photoluminescence studies in collaboration with the University of Trento have been also performed.

3.1 The organic scintillators

In case of organic materials, the scintillation process arises from transitions in the energy level structure of a single molecule. For this reason, the light output spectrum produced will be connected to the particular molecular species choosen and not from the physical state, liquid, solid or gas on which the material will be used. Generally, this type of scintillator is based on the transition of the

electron contained inside the π orbital. As one can see in the left part of Fig 3.1, the energy released by the incident radiation can be adsorbed by exciting the electron from the ground configuration S_{00} to one of the available excited states. These excited states are divided into a series of singlet states (spin 0) labeled as S_0, S_1, S_2 etc. and similar set of triplet (spin 1) showed as T_1,T_2,T_3 etc… Each of these electronic configurations is further subdivided into a series of levels with much finer spacing (named S_{00}, S_{01}, S_{O2} etc…) which correspond to various vibrational states of the molecule. In the molecules of interest for organic scintillator, the energy difference between the S_0 state and the S_1 state is around 3 or 4 eV, while the distance between the other states S_1 and S_2 etc.. is generally less. The typical spacing of two following internal vibration energy is around 0.15 eV, much more of the thermal energy 0.025 eV. For this reason nearly all molecules at room temperature are in the S_{00} state.

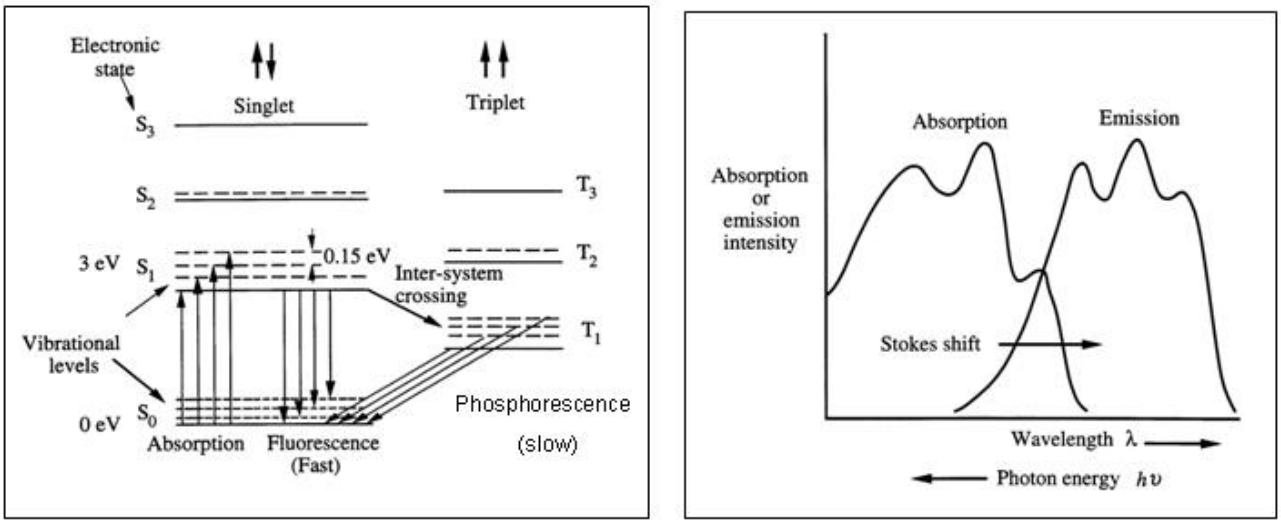

Fig. 3.1 : In the left part, the typical energy levels scheme of an organic molecule is shown. In the right part, it is plotted the emission and the absorption spectra of such type of scintillator materials [Kno79].

When the kinetic energy from the incident radiation is transferred to the electron, this one can jump to the corresponding excited state. The higher singlet electronic states are quickly (on the order of picoseconds) de-excited to the S_1 electron state through radiationless internal conversion. Other fast and relevant transitions occur from the S_{11}, S_{12} etc.. states to the S_{10} state in order to have a perfect thermal equilibrium. Thus, the final effect of the incident radiation in a simple organic scintillator is to produce in a really short time a population of excited molecules in the S_{10} state. The following decay from this state to one of the different states S_{00}, S_{01}, S_{02} etc… available is the responsible of the prompt fluorescence mechanism. On the contrary, the phosphorescence mechanism is due to the decay of the triplet states. In fact, through a transition called “intersystem crossing”, some excited singlet states may be converted into triplet states, which have much longer characteristic lifetime.

Because T_1 lies below S_1, the wavelength of this phosphorescence spectrum will be longer than that for the fluorescence spectrum. If some states are excited back to the S1 state and subsequently decay through the normal channel, we have the so called delay fluorescence.

This emission mechanism can also explain why in the right part of the Fig 3.1 the absorption spectrum is shifted with respect to the emission spectrum. The minimum energy needed to excite the molecule is the distance between the S_{00} states (at room temperature practically all the molecules will be in this state) and the S_{10} state. Considering all the possible transitions from the following decay of the S_{10} state through the fluorescence channel, the great part of them will have a lower energy and consequently only a small part of the emission spectrum and absorption spectrum will be overlapped.

Not all the incident radiation will create the fluorescence emission. In fact, there are other possible mechanisms which are not connected to a light emission through which the incident radiation can loose energy inside the scintillator materials (primarily the lattice vibrations or heat). For this reason, we can define the scintillation efficiency as the fraction of all incident radiation energy which is converted into visible energy. Sometime, the excitation energy can be transferred from molecule to molecule and this mechanism can be used to create a "binary" organic scintillator where a small concentration of an efficient scintillator is added to a bulk solvent. The energy is absorbed primarily by the solvent and after can eventually find its way to one of the efficient scintillator molecules and cause light emission at that point. In some case, another element is added, a so called "waveshifter", in order to absorb the light produced by the primary scintillant and reradiate it at different wavelength. Normally in this way it is possible to have a better coupling with the following photomultiplier tube or to minimize the bulk self-absorption in large liquid or plastic scintillators.

The organic scintillators can be divided in: pure organic crystals (Anthracene and Stilbene are the most well known in this category); liquid organic solutions (as for example NE213); plastic scintillators that can be used as bulk detectors of residual energy but also as thin films (with a thickness as low as 20 $\mu g/cm^2$) to perform a transmission detectors; loaded organic materials, where some high-Z elements are added to a standard organic scintillator to have a more efficient behavior in the detection of γ-rays (for example the addition of lead or tin up to 10% of the weight to a plastic scintillator) or of neutrons. In this second case, the standard method is the addition of gadolinium to increase the neutrons capture cross section in liquid scintillators. It is clear that adding these high-Z elements, one reduces the scintillation efficiency of the material.

Speaking about some general characteristic of organic scintillators, the Anthracene has the best scintillation efficiency, but its time response is much slower then the others (30 *ns* instead of few

ns). The liquid organic solutions are used especially in case of quite large volume detectors because they can be easily placed into a sealed glass or metal containers with the shape and the dimension needed for the experiment with a reasonable cost. Normally one should pay attention to the possible contamination of them because the presence of impurity, like oxygen, will increase the quenching phenomena. There are a lot of different mixtures available, obtained changing the bulk solvent, the efficient scintillation molecules dissolved or the waveshifters, but working with them one should take into account the toxicity of the major part of them. If the solvent used in the mixture can be subsequently polymerized, one can create a solid solution, the so called plastic scintillators.

3.2 The inorganic crystal scintillators

The scintillation mechanism in inorganic materials depends on the energy states of the crystal lattice which results available for the electrons. The usual electronic shell configuration in the case of the inorganic crystal scintillator can be schematized as shown in Fig. 3.2, where a Valence band and a Conduction band are separated by an energy gap. The Valence band represents all the electron states that are essentially bound at lattice sites, whereas the Conduction band is linked to those electrons that have sufficient energy to be free to migrate throughout the crystal. If the crystal is doped with some impurity, other electron states are created in the middle of the energetic gap between these two bands. These impurities, called "activators", are particularly important because they are responsible for the scintillating photon emission.

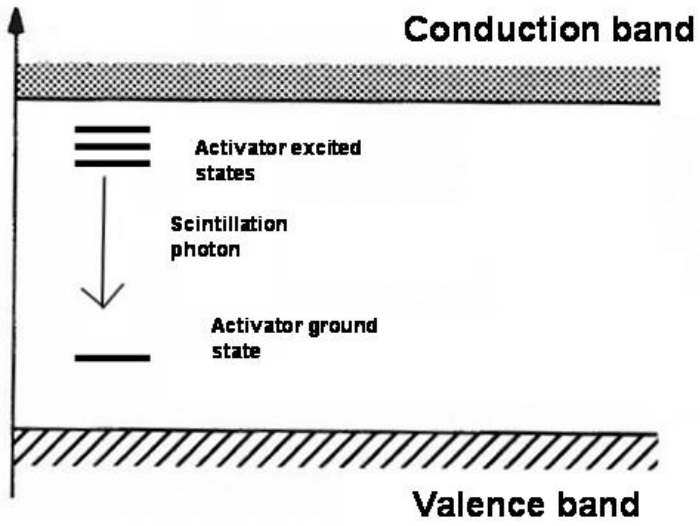

Fig. 3.2 : Energy band structure of an activated crystalline scintillator.

When the incident particle passes through the crystal, an electron can jump from the valence band up to the conduction band, leaving a hole in the normally filled valence band. In the pure crystal, the return of the electron back to the initial position is an inefficient process for the emission of photons because there is a high possibility that the photon is reabsorbed by another electron and normally its wavelength is not in the visible range. So the presence of the activators is necessary.
In fact, the positive hole left in the valence band by the electron can drift inside the band arriving to the location of an activator site. The ionization energy of the impurity will be less than that of a typical lattice site, so the hole will pass to the ground state of the activator. In the meanwhile, also the electron is free to migrate through the crystal until it joins such an ionized activator. In this case, the electron will pass from the conduction band to this ionized activator to create a neutral impurity configuration which can have its own set of excited energy states. As it was told, these energy levels are positioned inside the energy gap between the valence and conduction band of the pure crystal, so the emission coming out from the de-exciting of this states of the activators is free to migrate inside the lattice because it is not enough energetically to create a new couple electron-hole in the crystal. If the activator is properly chosen, these transitions can be in the visible energy range.
The time emission for this type of materials is mainly determined by the typical half-lives of the excited states of the activators (normally on the order of 10^{-7} *s*) because the migration time for the electron is much shorter and it can be considered as negligible. In some cases, more complex time behavior is observed and sometimes the introduction of two different decay times is needed.
To complete our description, other processes should be mentioned. For example, the electron which arrives at the impurity site can create an excited configuration where transition to the ground state is forbidden. This type of states needs an additional increment of energy, which normally comes from the thermal excitation, to arrive to an energy state allowed to decay directly to the ground state. This type of mechanism can create a relevant phosphorescence emission. Another possibility is that the activator energy state is such that it can decay without the emission of a photon. These processes are called “quenching” because they absorb energy without production of visible light. It can also happen that the electron-hole couple created in the crystal remains associated with each other in a configuration called exciton. The exciton is free to move inside the crystal until it reaches the site of an activator atom where the normal process of fluorescence emission can start.
The total efficiency of this inorganic crystal scintillator is normally greater then that one obtained using the organic scintillator. In fact, if we compare the efficiencies for the best organic scintillator Anthracene and for the NaI(Tl) crystal, the resulted value for the latter will be 2.3 time larger.

3.3 The CsI(Tl) crystal

The CsI crystal is one of the mostly used scintillator for the detection of charged particles. It is commercially available with either Thallium or Sodium as the activator materials, with consequent different characteristics as efficiency and emission spectra. In general, this type of crystal has the highest gamma ray absorption coefficient per unit size of any scintillator and it is less brittle than NaI, characteristic which permits to cut this crystal into various shapes without breaking. This material is also less hygroscopic than NaI crystals, but still one should pay attention in the conservation of the detector because a long exposition to high humidity can deteriorate the detectors. In the Tab. 3.1 one should compare some characteristic of the NaI(Tl), CsI(Tl) and CsI(Na) crystals.

Material	**λ_m (nm)**	**Decay constant (μs)**	**Index of Refraction at λ_m**	**Specific Gravity**	**Scintillation efficiency relative to NaI(Tl)**
NaI(Tl)	410	0.23	1.85	3.67	100%
CsI(Na)	420	0.63	1.84	4.51	85%
CsI(Tl)	565	1.0	1.80	4.51	45%

Tab. 3.1 : Some of the main characteristics for the NaI(Tl), CsI(Na) and CsI(Tl) crystals.

Reading the previous table, it is clear that the choice of CsI(Tl) in the GARFIELD apparatus is not connected to a better light efficiency, but to an emission spectrum more suitable for a good coupling to a silicon photodiode. In fact, for geometrical reasons inside the apparatus and dissipation problems, the light output produced by the scintillators will be converted through a compact photodiode. As one can see in Fig. 3.3, the crystal of CsI(Tl) meets in a satisfactory way the absorption spectrum of the series S3204-05 Hamamatsu photodiode, choosen for the GARFIELD apparatus.

It is important to underline that the scintillation efficiency is also connected to the concentration of the doping element used. In fact, one should imagine an increasing of the efficiency with the increasing concentration of doping until it reaches a maximum. After reaching this quantity, the efficiency will remain stable or start to decrease for quenching mechanisms which could arise. The general characteristics reported in the Tab. 3.1 should be considered calculated for an optimized doped crystal. The doping procedure is obviously dependent on the production company.

Comparative tests between the same type of crystals produced by different companies can point out any possible difference in the doping showing, for example, a slightly different emission spectrum or different intrinsic resolution.

We have the possibility to compare the CsI(Tl) crystals produced by the Russian Company ATOM INTECH-Ltd. used for the GARFIELD apparatus (for example the number 407) with the CsI(Tl) crystal produced by the Scionix Company type VLGS TEK 2 serial SSY822 (for example the number S7-2). These last are used for a three stages detector, called Ring Counter detector (RCo), which can complete the GARFIELD apparatus covering the forward angles ([Mor05]). The geometric shapes of these crystals are also different because they have been designed for the different geometries of the detectors.

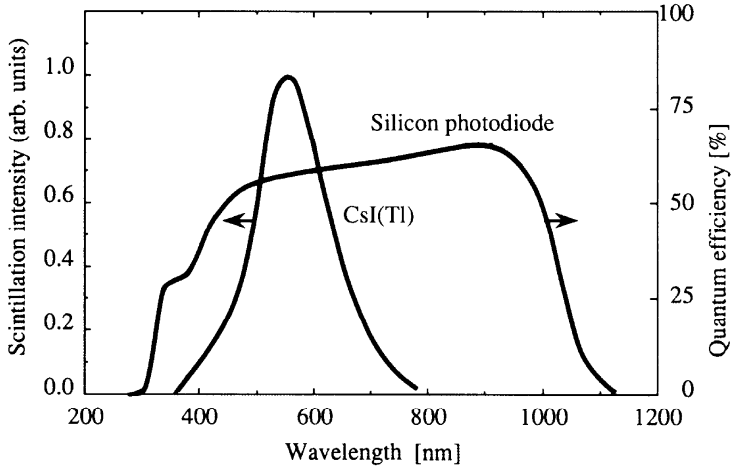

Fig. 3.3 : Matching of the emission spectrum of a CsI(Tl) crystal and the absorption spectrum of the Silicon photodiode used in the Garfield apparatus [Bar02].

Even if the geometrical shape can influence the relative quantity of photons which arrive to the same type of photodiode used to read out the signal, a simple geometric consideration can not modify the intrinsic characteristics of the crystal, as the emission spectrum. The energetic resolution can also be linked to intrinsic proprieties of the crystals, overall inhomogenities during the growing procedure, but it can also be due to the quality and quantity of the doping. Fig. 3.4 shows the results obtained in the laboratory for an equal time and equal amplification measurement with a 3 peaks α-source and a ^{60}Co γ-source for the best crystals of the two species. The α-source is formed by ^{239}Pu, ^{241}Am and ^{244}Cm which emit α-particles of energies 5.15 *MeV*, 5.48 *MeV* and 5.79 *MeV* respectively, while the ^{60}Co source emits two γ-rays with energy of 1.173 and 1.332 *MeV*. To exclude any effects from the different amplifications or from the different scintillation efficiencies, we can estimate the resolution of these crystals through the ratio between the Full Width Half Maximum (FWHM) expressed in *MeV* and the well known centroid for every peak of the two

sources always in *MeV*. In the Tab 3.2 the results of the Gaussian fits for every peak of the sources are shown.

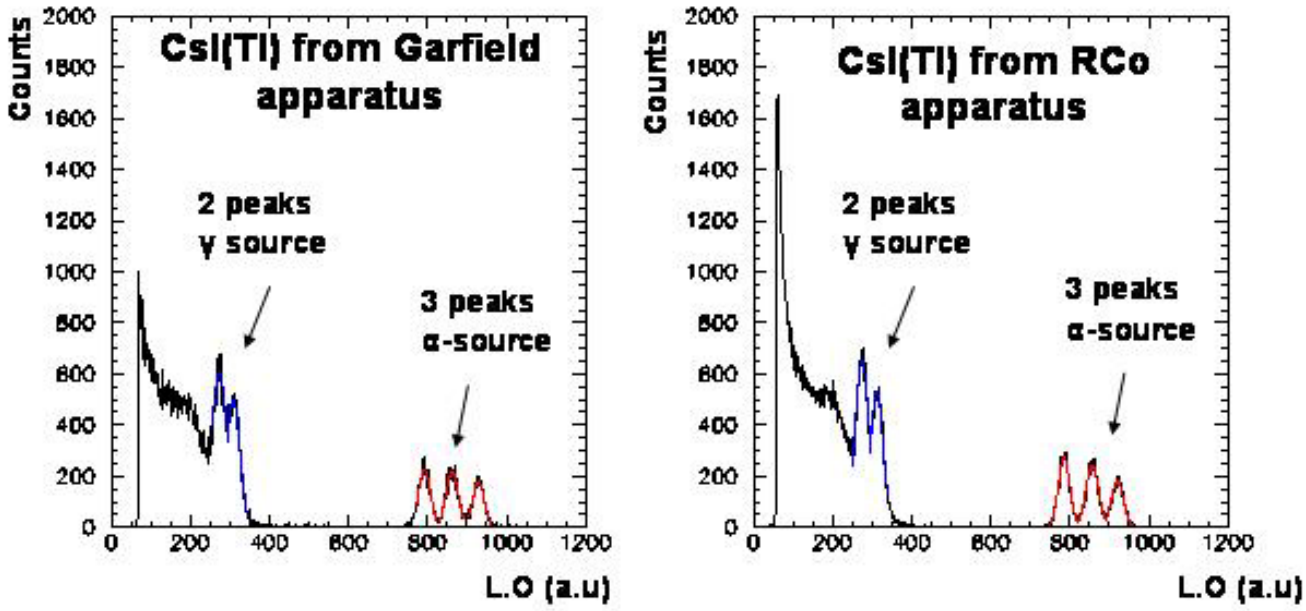

Fig. 3.4 : Measured spectra of the two different CsI(Tl) crystals (number 407 on the left and S2-7 on the right side) using a 3 peaks α-source and the ^{60}Co γ-source

α-source

	I° Peak			II° Peak			III° Peak		
	Centroid	**Sigma**	**Height**	**Centroid**	**Sigma**	**Height**	**Centroid**	**Sigma**	**Height**
Garfield CsI(Tl)	792.08	14.17	233.10	862.15	15.49	217.18	928.63	14.38	177.67
RCo CsI(Tl)	785.77	14.02	277.60	856.77	15.44	249.09	921.29	14.31	187.53

γ-source

	I° Peak			II° Peak		
	Centroid	**Sigma**	**Height**	**Centroid**	**Sigma**	**Height**
Garfield CsI(Tl)	272.63	15.38	619.12	309.00	14.02	504.79
RCo CsI(Tl)	274.93	14.93	679.12	313.24	15.25	532.46

Tab. 3.2 : Results of the Gaussian fits for the three peaks of the α-source and two peaks of the γ-source for the two CsI(Tl) crystals.

Starting from the σ fitted values of every single distribution, one can obtain the FWHM needed to calculate the energy resolution using

$$FWHM = \sigma\sqrt{8\ln(2)} = 2.35\sigma \quad \textbf{(3.1)}$$

The last step before calculating the energy resolution is to convert the FWHM from an arbitrary light output (L.O.) channel into energy. The correlation between the L.O. produced inside the crystal and the energy of the incident particles is a complicated and semi-empirical formula that depends on the charge, mass and energy of the particle ([Cas04], ([Mas03]). For our purpose, a simple linear calibration, performed using the relative distance in channel and in energy between the 3 different peaks, can be a good approximation for an energy calibration in the limited range covered by the α source. In Tab. 3.3, one can read the conversion of the FWHM from L.O. channel to energy using this approximated linear calibration and all the consequent energies resolutions for every peak produced by the α source.

α-source

	I° Peak			II° Peak			III° Peak			
	FWHM (a.u.)	FWHM (MeV)	Energy resolution	FWHM (a.u.)	FWHM (MeV)	Energy resolution	FWHM (a.u.)	FWHM (MeV)	Energy resolution	Averaged value
Garfield CsI(Tl)	33.30	0.16	3.03%	36.41	0.17	3.11%	33.80	0.16	2.74%	**2.96%**
RCo CsI(Tl)	32.95	0.16	3.02%	36.28	0.17	3.13%	33.62	0.16	2.74%	**2.96%**

Tab. 3.3 : Energy resolution for the α-source for the two CsI(Tl) crystals.

In the same way, using a new linear calibration produced with only the relative distance between the two γ-peaks because the energetic range and the incident radiation are completely different from the previous case, one can produce the same results for the ^{60}Co source that are showed in Tab. 3.4.

γ-source

	I° Peak			II° Peak			
	FWHM (a.u.)	FWHM (MeV)	Energy resolution	FWHM (a.u.)	FWHM (MeV)	Energy resolution	Averaged value
Garfield CsI(Tl)	36.14	0.16	13.47%	36.95	0.16	12.01%	**12.74%**
RCo CsI(Tl)	35.09	0.15	12.79%	35.83	0.15	11.26%	**12.03%**

Tab. 3.4 : Results of the energy resolution for the γ-source for the two CsI(Tl) crystals.

The Tab. 3.3 and 3.4 suggest that the two CsI(Tl) crystals are practically equivalent from the point of view of the energy resolution obtained through the α-source, while they are slightly different

from the point of view of the γ-source. The information extracted from the α-source is strictly connected to the surface of the crystal because they will be stopped in the very first layers of the crystal, while the information derived from the γ-source can give us a more complete exploration of the bulk properties of the crystal. From the technical documentation, we know that the doping of the RCo crystal is about 1200 *ppm*, which has to be considered with respect to the range of values (between 200 and 2000 *ppm*) of doped Thallium atoms which can be normally used. No direct information about the concentration of the doping atoms is known for the GARFIELD CsI(Tl) crystal. Another way to test and compare the two crystals is through the Ion Beam Induced Luminescence (IBIL) technique.

The IBIL technique consists on bombarding the sample with a known ion source or beam and to study the emission spectrum characteristic of the crystal. Of course using an ion beam it is also possible to study the emission yield as a function of the incident rate. The IBIL measurement was therefore performed at the AN2000 Van de Graaf accelerator of the National Laboratory of Legnaro, using an α beam of ~ 4 *nA* of current and 2 *MeV* of energy.

The detection system, which is shown in Fig. 3.5, is made by a focalizing system and a fiber bundle which address the light towards a spectrometer which separate through a diffraction grating the different wavelength produced by the sample. A nitrogen cooled Princeton CCD detector, equipped with an array of 1340 x 100 pixels, each of them 20 x 20 μm^2 is used to convert the light. Its signal is sent to a computer for the on-line acquisition and analysis of the emission spectra. Before the measurement, the system must be calibrated using a calibration lamp, which produces some peaks at known and precise energetic values.

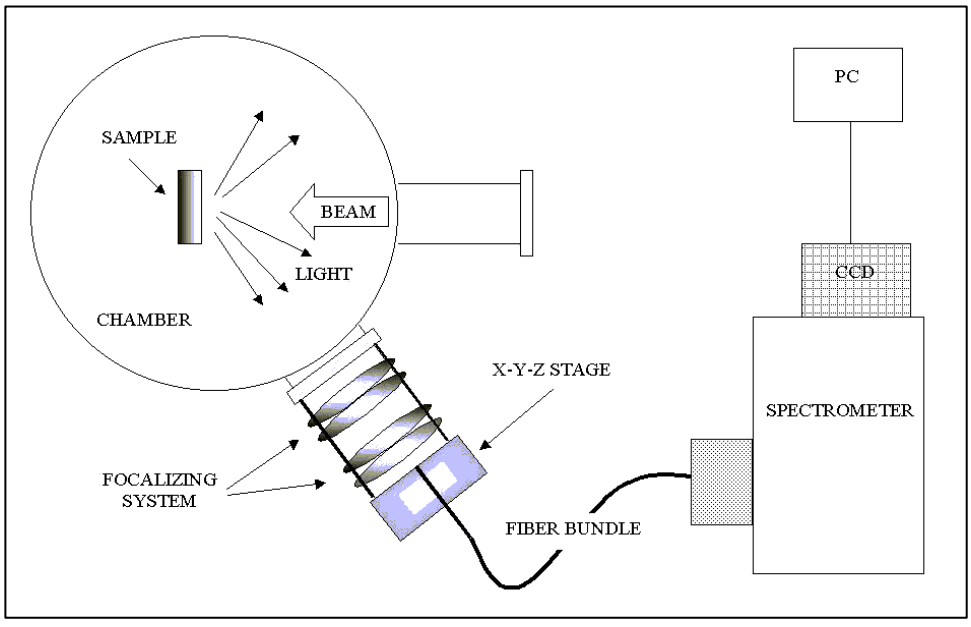

Fig. 3.5 : Picture of the system used to perform all the Ion Beam Induced Luminescence showed in this thesis [Qua05].

As a further measurement, the degradation in the response of the scintillator materials as a function of the beam current has been studied. In fact, the beam is opportunely focused (3 x 3 *mm* is the dimension of the beam) on the sample and it possible to know the integrated charge deposited by the beam because the sample is placed inside a Faraday Cup. Similar test was performed by A. Quaranta et al. on plastic scintillator using the same apparatus (see [Qua05] and [Car05]). Monitoring the scintillation light emitted as a function of an increasing value of the integrated charge absorbed by the material, one can study how it reacts to the radiation damage induced by the beam. This is a quite important parameter in the case of very long time experiments, especially if the substitution of the damaged detectors is impossible (for example experiments performed in the space with artificial satellite). The experimental data obtained from the measurements apparatus have to be corrected with a response function of the apparatus which depends on the detected wavelength. In fact, the detection efficiency of the apparatus is not equal along all the wavelength scale and this results in a distortion of the measured spectra. Through an opportune calibration routine, which can trace back the different response as a function of the different wavelengths, the correct emitted spectrum can be reproduced.

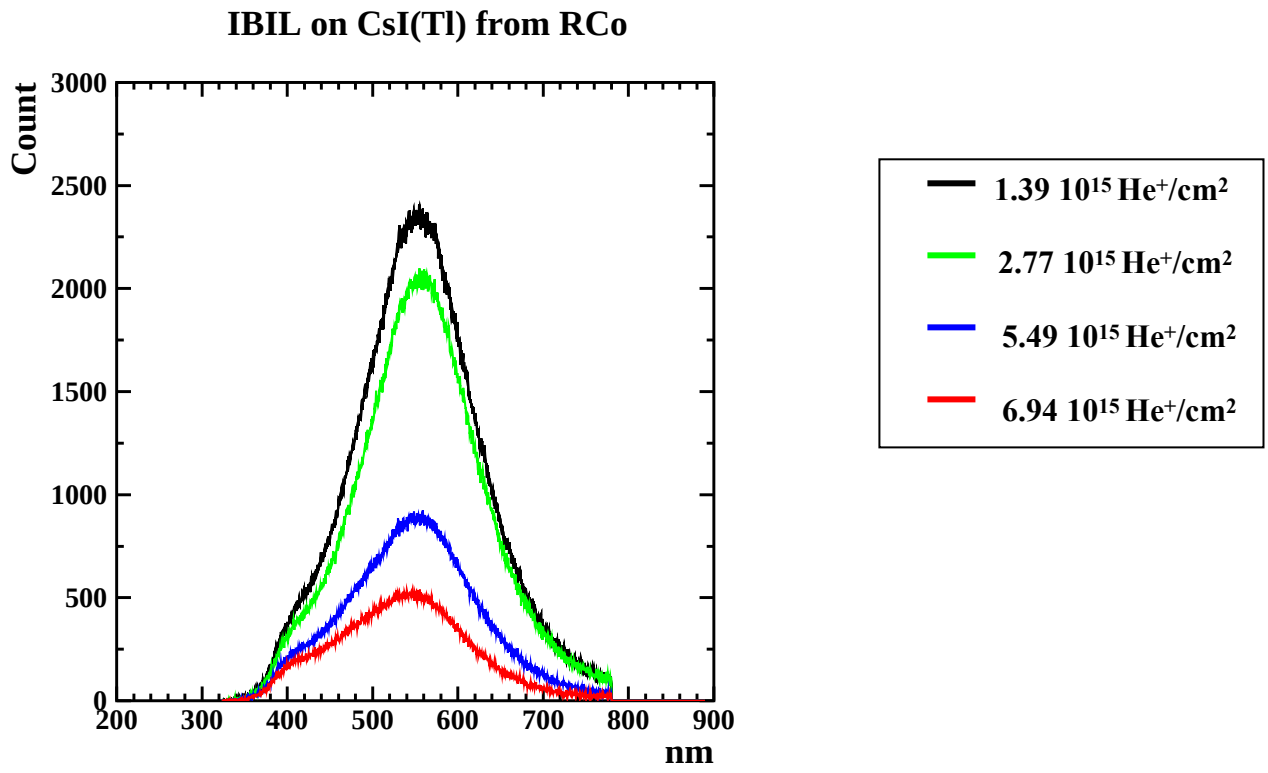

Fig. 3.6 : Emission spectra from the CsI(Tl) crystal S2-7. Different colors mean different total charge absorbed.

Fig. 3.6 and 3.7 represent the emission spectra of the two CsI(Tl) crystals 407 and S2-7, previously described. The emission spectra have been obtained bombarding the crystals with an α-beam of 2

MeV. The spectra shown in the figures have been already corrected through the response function of the IBIL apparatus.

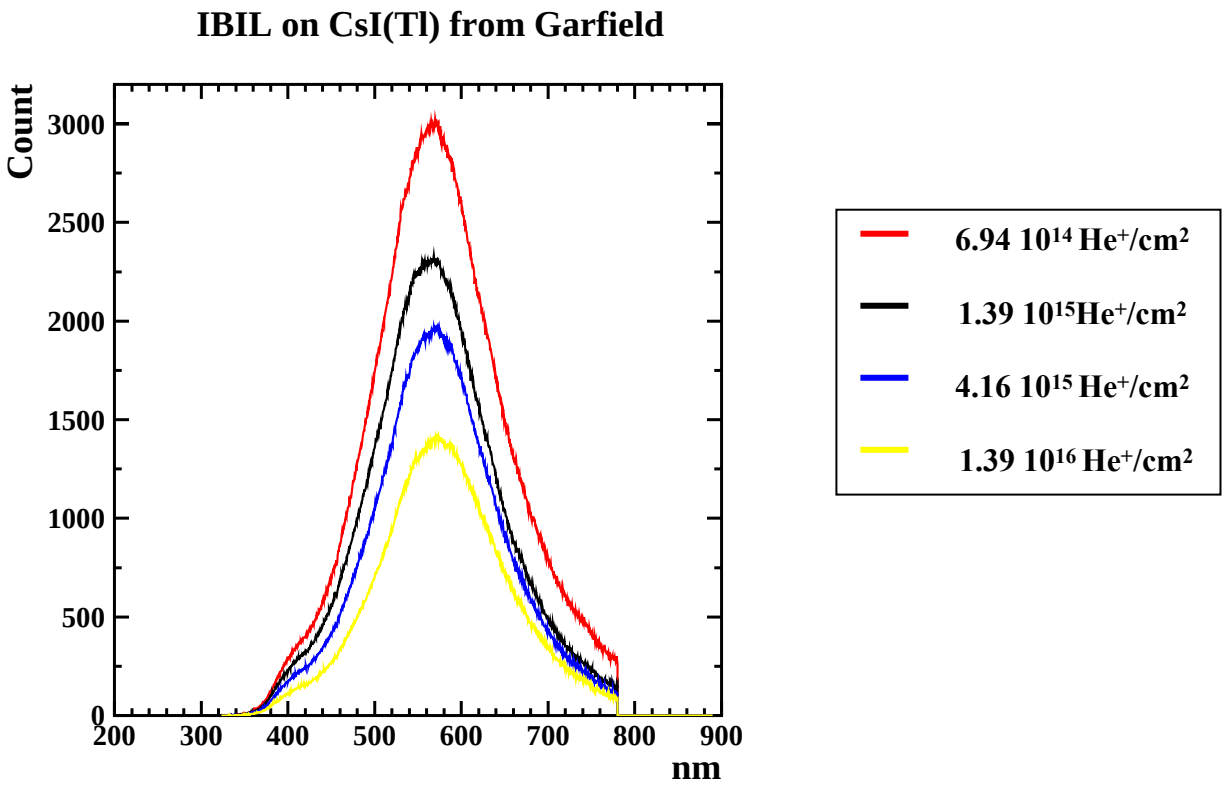

Fig. 3.7 : Emission spectra from the CsI(Tl) 407. Different colors mean different total charge absorbed.

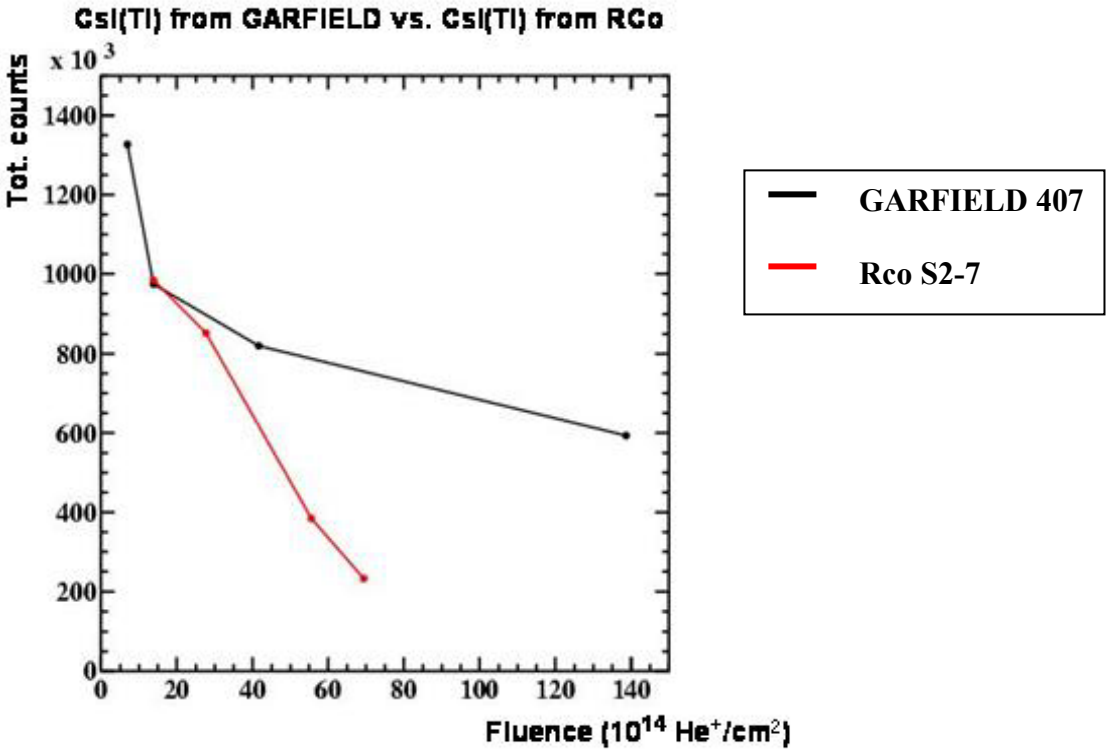

Fig. 3.8 : Integral of the emission spectra as a function of the ion fluence. The lines are used to guide the eye. The black line is CsI(Tl) 407 and red line is CsI(Tl) S2-7.

Comparison of different emission spectra derived after different total charges detected are shown through the different colors. This is an indication of the behavior of the crystals as a function of the radiation damage, as summarized in Fig. 3. 8. This can be a qualitative sign of the different quantity of doping because the decrease of counting for the radiation damage is connected to the probability of an emitted center to be close to a quenching center created by the incident radiation. If the doping concentration is different, also this probability will be different.

Particularly important for our purpose is to compare the emission spectra of the two types of crystals, as showed in Fig. 3.9. In fact, with the normalization on the total counting integral, one can put in evidence small differences in the shapes of the two emission spectra using the same incident particles (α particles of 2 MeV), the same beam current and the same experimental set-up. The shift in the maximum of the wavelength emission is around 20 *nm*, but also the shapes of the two curves are slightly different, underlying a different crystalline structure.

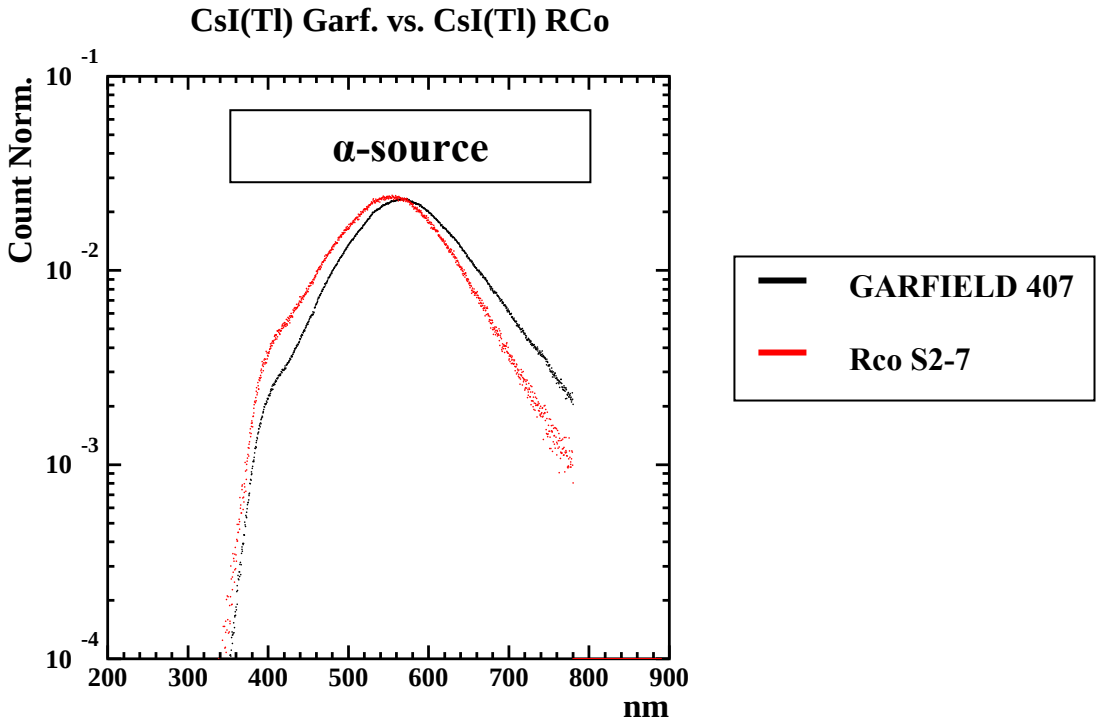

Fig. 3.9 : Comparison of the emission spectra from the two CsI(Tl) crystals from Garfield (black line) and RCo (red line) apparatus. Both of the distributions are normalized to the total integrated number of counts.

In fact, the relative position in the crystal lattice and the type of bonds can change the structure of the level available to the electron and, consequently, the emission spectra after the excitation.

We can continue our scan of the CsI(Tl) characteristics using another technique. It can be interesting to investigate the response of the two crystals using a single excitation wavelenght instead of exciting a whole band through the bombardment with an ion beam source. In fact, varying opportunely the input wavelength from a monochromator, one can study the difference in

the emission spectrum as a function of a known and fixed wavelength. In other words, it will be possible to study the emission from the de-excitation of all the electronic states of the scintillator with energy minor or equal to that one pumped into the materials.

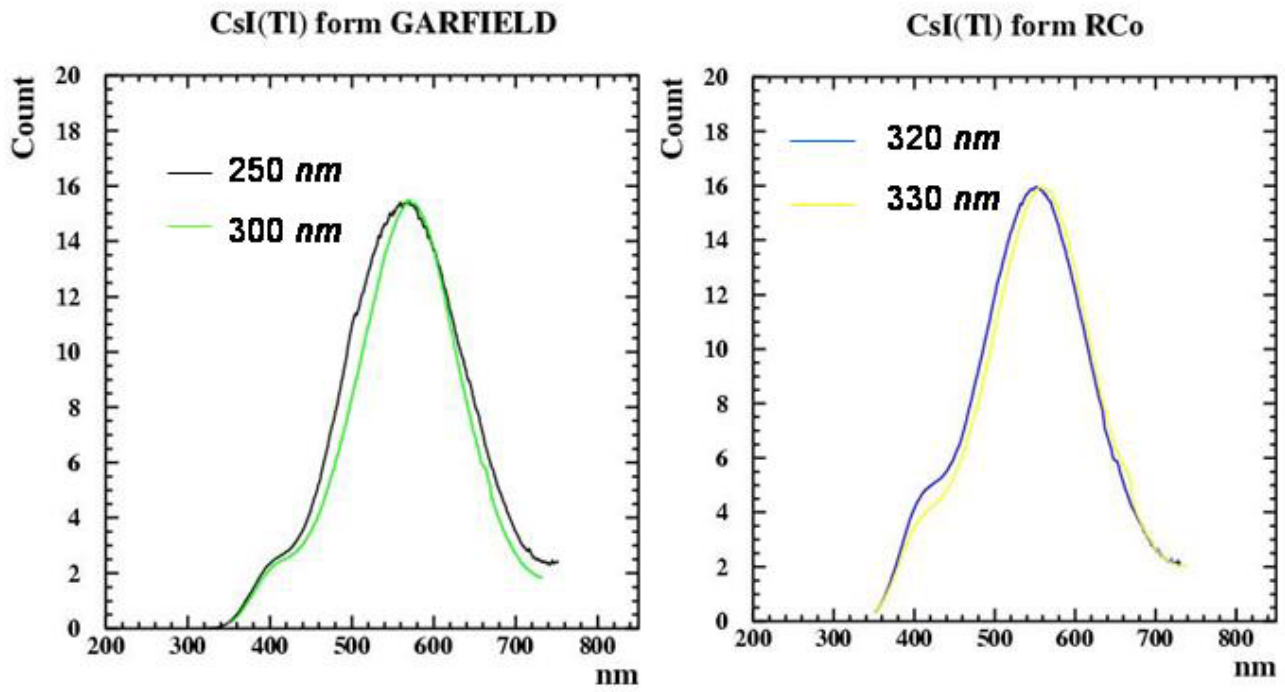

Fig. 3.10 : Emission spectra from the two CsI(Tl) crystals 407 (left plot) and S2-7 (right plot) for different excitation wavelengths.

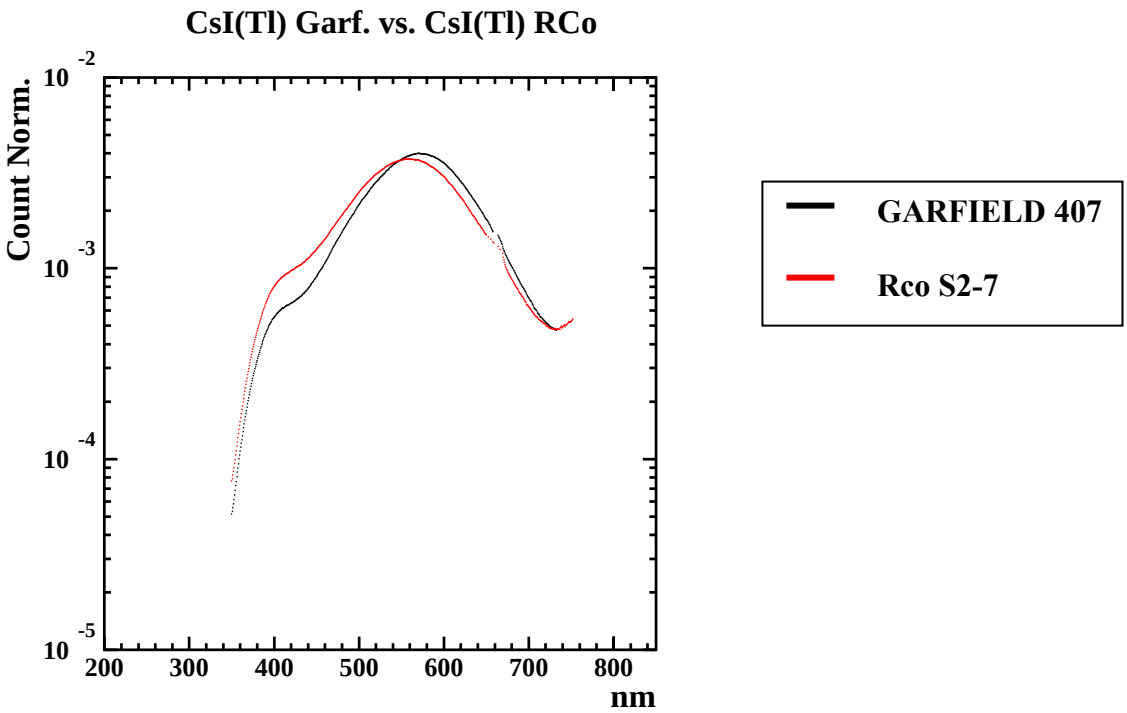

Fig. 3.11 : Comparison of the emission spectra from the two CsI(Tl) measured using an excitation wavelength of 330 *nm*. The counts are normalized to the integral.

In the Fig. 3.10, the emission spectra of the two crystals for two different input wavelengths are shown. The excitation spectra produced by the same crystal changing the wavelength of the incident photon is slightly different, in the shape but also in the position of the peak corresponding to the maximum emission (shift around 10 *nm*). So we are exciting a different distribution of electron states. To better understand the relative difference between the two crystals, it is interesting to plot in the same figure the excitation spectra from the same input wavelength, as in Fig. 3.11.

Even in this case, we find a shift of 20 *nm* in the position of the maximum counting. In particular, the maximum of CsI(Tl) number 407 is placed at 575 *nm*, while the CsI(Tl) number S2-7 has the maximum emission corresponding to 555 *nm*. The wavelength reported normally for a standard crystal of CsI(Tl) (see Tab. 3.1) is 565 *nm*. Also in this case a difference is also seen in the shape of the two spectra, denoting the different sharing of the components.

The spectrometer used for the IBIL and fluorescence measurements (Fig. 3.12) can work also as a monochromator. In this way it was possible to consider in the photoluminescence measurements a particular wavelength of the emission spectrum and to study the intensity of the light produced at this fixed wavelength changing the excitation wavelength ([Qua05]).

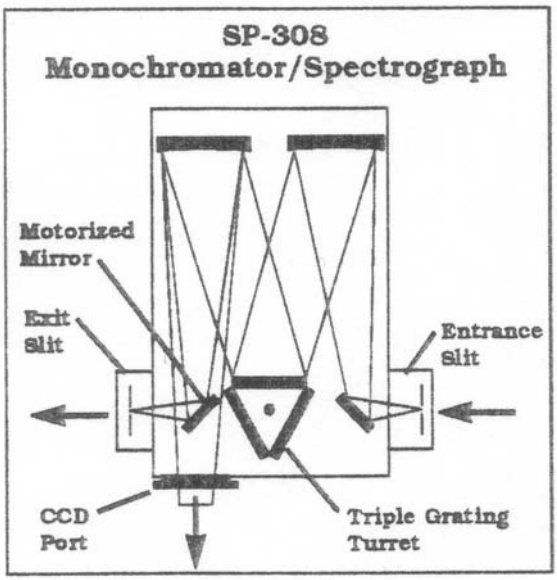

Fig. 3.12 : Scheme of the Monochromator/Spectrograph used for the IBIL and luminescence measurements.

In the Fig. 3.13, the emission spectra at 420 *nm* and 530 *nm* for the two crystals as a function of the incident wavelength are shown. In Fig. 3.14, a direct comparison between the two crystals selecting the emitted spectra at 530 *nm* in a normalized scale to better understand the relative difference can be seen. The difference in the position of the peak is corresponding to the maximum number of count is in this case around 10 *nm*. In particular for CsI(Tl) number 407 the maximum in the emission at 530 *nm* is in coincidence with an incident wavelength of 330 *nm*, while for the CsI(Tl)

number S7-2 the maximum in the emission at 530 *nm* is when the incident wavelength is around 320 *nm*.

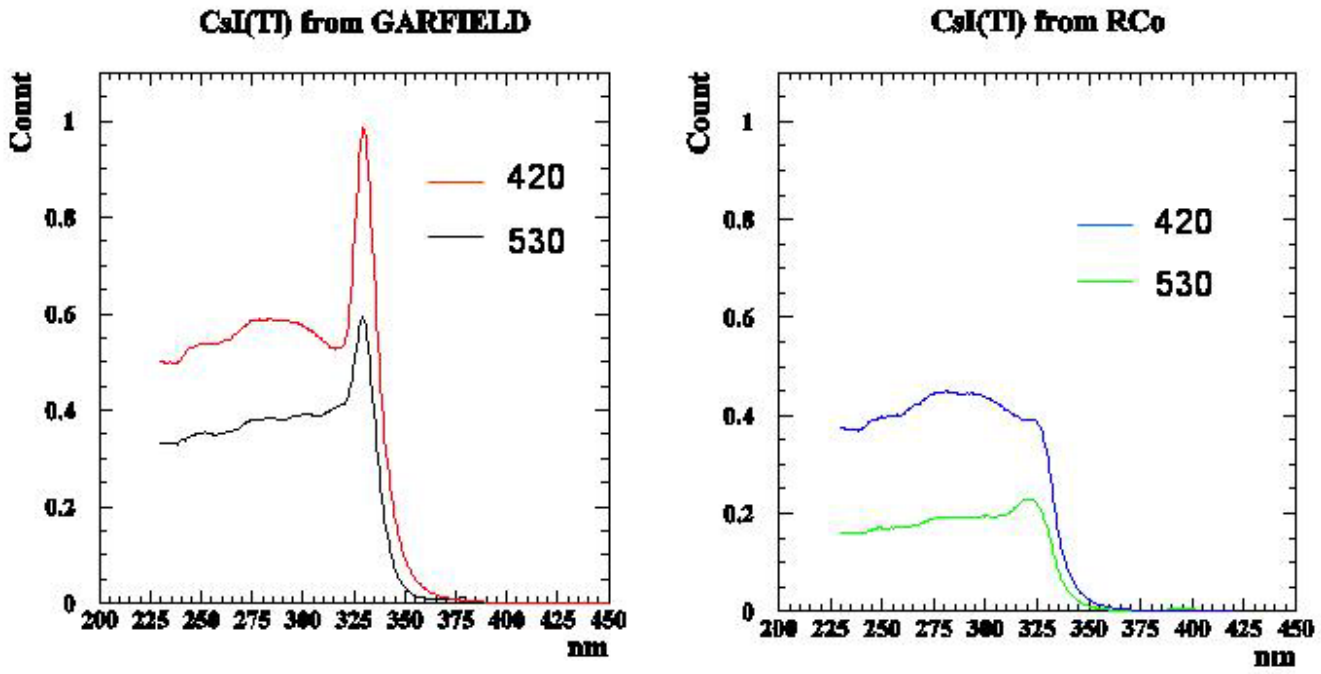

Fig. 3.13 : Excitation spectra of the two CsI(Tl) crystals from GARFIELD (left plot) and RCo (right plot) for two different selected emission wavelength.

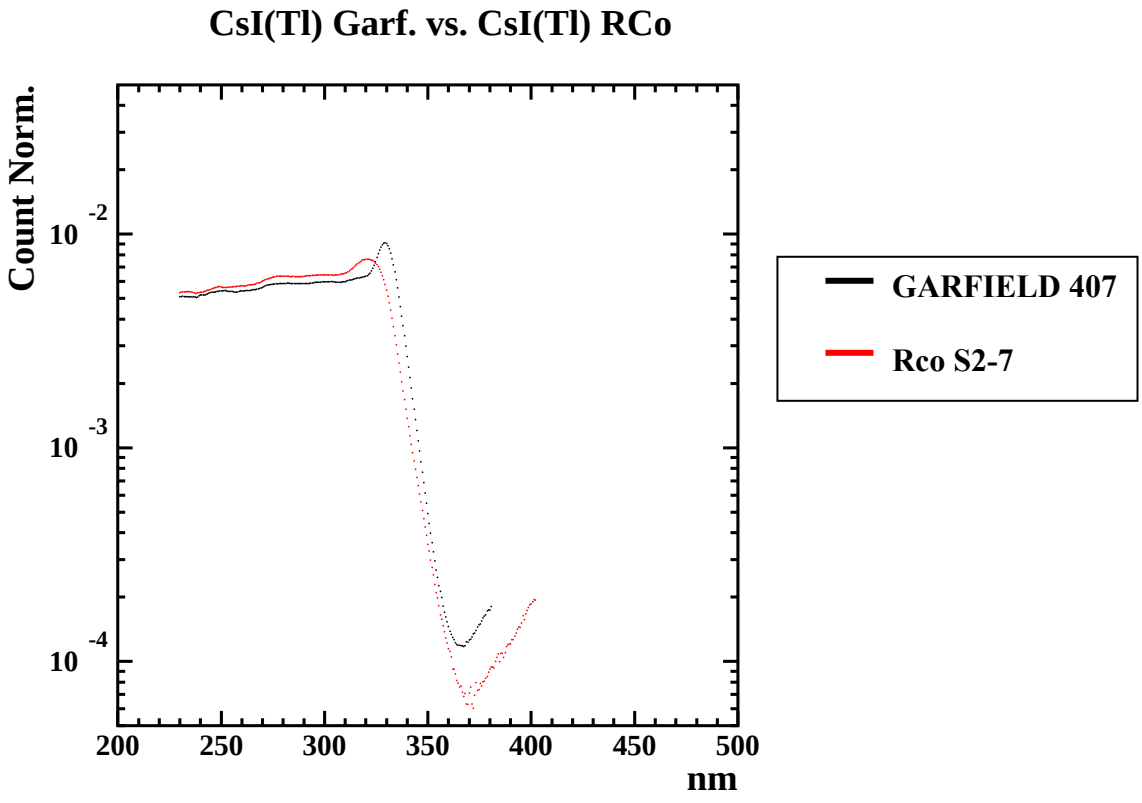

Fig. 3.14 : Comparison of the excitation spectra fixing the emission wavelength at 530 nm for the two CsI(Tl) crystals. The counts are normalized to the integral.

From all the different performed tests, it appear clearly a structural difference in the crystal of the two CsI(Tl) which can depend on the lattice structure and/or on the doping percentage, with relevant effects both in the resolution energy and in the resistance to radiation damage.

3.4 The BaF_2 crystal

BaF_2 scintillator detectors are commonly used for the measurement of γ-rays over a wide energy range because of the relatively high detection efficiency and the fast response which allows sub-nanosecond timing, important characteristics to discriminate neutrons from γ-rays using a Time of Flight technique ([Lav83]). They are generally used to form γ-rays multiplicity filters or arrays devoted to high energy γ-rays.

The photons can interact with the matter using 3 different mechanisms: the photoelectric effect, the Compton effect and the creation of an electron-positron pair. The photoelectric phenomenon can be described as the interaction of the photon with a bound atomic electron. The energy of the photon is completely transferred to the electron, which becomes free with a kinetic energy E_c, which can be written as

$$E_c = h\nu - B_e \qquad \textbf{(3.1)}$$

where v is the frequency of the incident photon and B_e is the binding energy of the hit electron. The photoelectron is most likely emerging from K shell. The typical binding energies vary from a few *KeV* for low-Z materials to tens of *KeV* for materials with higher atomic number. The vacancy created by the photoelectric emission is quickly filled by the electron rearrangement. In this process, the binding energy B_e is released either in the form of a characteristic X-ray or an Auger electron. The Auger electrons have a short range because of their low energy. On the contrary, the X-ray can travel a certain distance before being reabsorbed through a photoelectric interaction with less tightly bound electrons of the atom. Normally the escape of these X-rays is not relevant and so the detected spectra through the photoelectric effect will appear as a single peak in the position of the incident energy.

In the case of Compton effect, the interaction of the photon occurs with one of the most external electrons. In this case the electron can be considered as free. The energy of the photon will be then distributed between the scattered photon and the electron. The energy of the scattered γ-ray E_γ in terms of its scattering angle θ is given by

$$E_\gamma = h\nu' = \frac{h\nu}{1+\frac{h\nu}{m_o c^2}(1-\cos\vartheta)} \qquad \textbf{(3.2)}$$

where $m_o c^2$ is the rest mass energy of the electron (0.511 *MeV*).

Considering the angular dependence of the energy of the scattered γ-ray, two extreme cases can be identified:

- $\theta \cong 0$, for which Eq. 3.2 predicts $E \cong h\nu' \cong h\nu$, i.e. the scattered γ-ray has nearly the same energy as the incident γ-ray,
- $\theta \cong \pi$, a head-on collision in which the γ-ray is backscattered toward its direction of origin. In this case there is the maximum in the energy transferred to the electron and the initial energy of the incident photon is shared by the electron and the scattered γ as

$$E_\gamma = h\nu'\Big|_{\theta=\pi} = \frac{h\nu}{1+2\frac{h\nu}{m_o c^2}} \qquad \textbf{(3.3)}$$

$$E_e = h\nu - h\nu'\Big|_{\theta=\pi} = h\nu\frac{2h\nu/m_o c^2}{1+2h\nu/m_o c^2}$$

In normal circumstances, all scattering angle will be seen by the detector. Therefore, a continuum of energies can be transferred to the electron, ranging from zero up to the maximum predicted by Eq. 3.3.

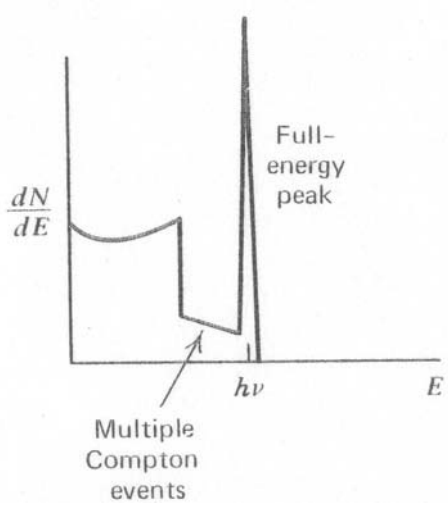

Fig. 3.15 : Schematic picture of the number of photons detected per unity of energy as a function of the incident energy after the Compton scattering [Kno79].

Therefore, what we should expect is a final distribution of the detected energy as shown in Fig. 3.15, where there is a peak corresponding to the full-energy detected and a continuous distribution

(*Compton continuum*) if only the part relative to the kinetic energy of the electron is detected. The events called "multiple Compton events" are intermediate and correspond to those events in which there is an escaping of one or more multiple scattered γ-ray.

A couples e^+/e^- can be created only if the energy of the incident photon is greater than two times the electron mass, that is 1.022 *MeV*. In this case the interaction is with the electric field created by the presence of atoms and the incident photon, which has an energy greater than the minimum quantity needed to create the couple e^+/e^-, is transformed in kinetic energy shared between them. Both electron and positron travel usually few millimeters before loosing all their kinetic energy. The positron will annihilate with an electron of the absorbing medium producing a couple of γ-rays of energy 0.511 *MeV* each, traveling back to back. If the detection of the kinetic energy of the produced couples e^+/e^- and of the annihilation γ-rays is complete, we can reconstruct completely the initial energy of the incident photon. If one or both of the annihilation γ escape from the detector, the net effect is the formation of a *single* or *double escape peak* in the distribution of the detected energy, at distance of 0.511 *MeV* or 1.022 *MeV* from the original incident energy.

Every one of the described interaction of γ-rays with matter is dominant in one particular range of energies. Photoelectric absorption is predominant for low-energy γ-rays (up to several hundreds of *KeV*), pair production is predominant for high-energy γ-rays (above 5-10 *MeV*) and Compton scattering is the most probable process between the two extremes. The cross sections for these processes are also connected to the charge Z of the absorber. In fact, the photoelectric cross section is proportional to $Z^{4,5}$, the Compton effect increases linearly with the Z and pair production is approximately proportional to the square of the atomic mass of the absorber.

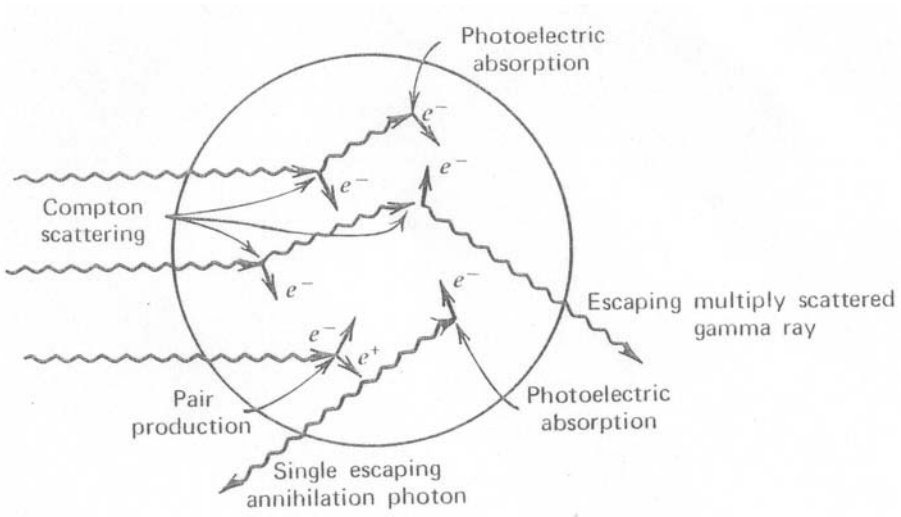

Fig. 3.16 : Picture of a typical interaction of a γ-ray with a detector [Kno79].

Considering a high energy photon, we can imagine a chain of interactions which starts with pair production and high energy Compton scattering down to photoelectric absorption with also the possibility to lose some of the secondary γ-rays produced, as shown in Fig. 3.16.

Every interaction process can be characterized by a fixed probability of occurrence per unit path length in the absorber. The sum of these probabilities is simply the probability per unit path length that the γ-ray is absorbed

$$\tau(photoeletric) + \sigma(Compton) + \kappa(pair) \qquad \textbf{(3.4)}$$

and it is called the linear attenuation coefficient. The probability of the photon to interact as a function of the distance *t* covered in the absorber material is described by $e^{-\mu t}$. Normally, in the comparison between the different materials, instead the mass attenuation coefficient μ/ρ is used, where ρ is the density of the absorber material. The most effective process to detect the whole γ-ray energy is the photoelectric effect. A scintillator material, like the BaF_2, with a high-Z has to be preferred to maximize this effect.

	Density (g/cm3)	**Emission spectra**		**Decay Time (ns)**	**Fast component light output relative to BaF_2**	
		Region (nm)	**Peak position (nm)**		**T=300 K**	**T=80 K**
CsF	4.11	220-500	265,300,310,335,385	2.9	10	10
CsCl	3.98	200-300 (300-500)	245,270 (390)	0.88 (>500)	50	50
CsBr	4.44	220-280 (300-500)	250 (390)	0.07 (>500)	1	100
CsI	4.51	250-350 (350-600)	305 (~500)	10 (1000-4000)		
RbF	3.55	200-450	235,380	1.3	10	10
BaF_2	4.88	180-290 (290-440)	220,195 (315)	0.8 630	100	100

Tab. 3.5: Table of general characteristics of some inorganic scintillator materials that can be used for γ-detection [Kub90].

In the Tab. 3.5 some general characteristics of the BaF_2 are compared to other scintillators [Kub90].

Using the same technique described in the case of CsI(Tl) crystals, we have performed on IBIL test using the 2 *MeV* of α-beam also on a small BaF_2 crystal. As one can see from Fig. 3.17, due to the lack of efficiency of the IBIL apparatus at wavelength smaller then 250 *nm*, only the second peak, relative to the slow emission, is visible. Fig. 3.18 shows the behavior of the BaF_2 bombarded by an

α-beam, for different integrated charges, in a similar way of the measurements previously described for CsI(Tl) crystals.

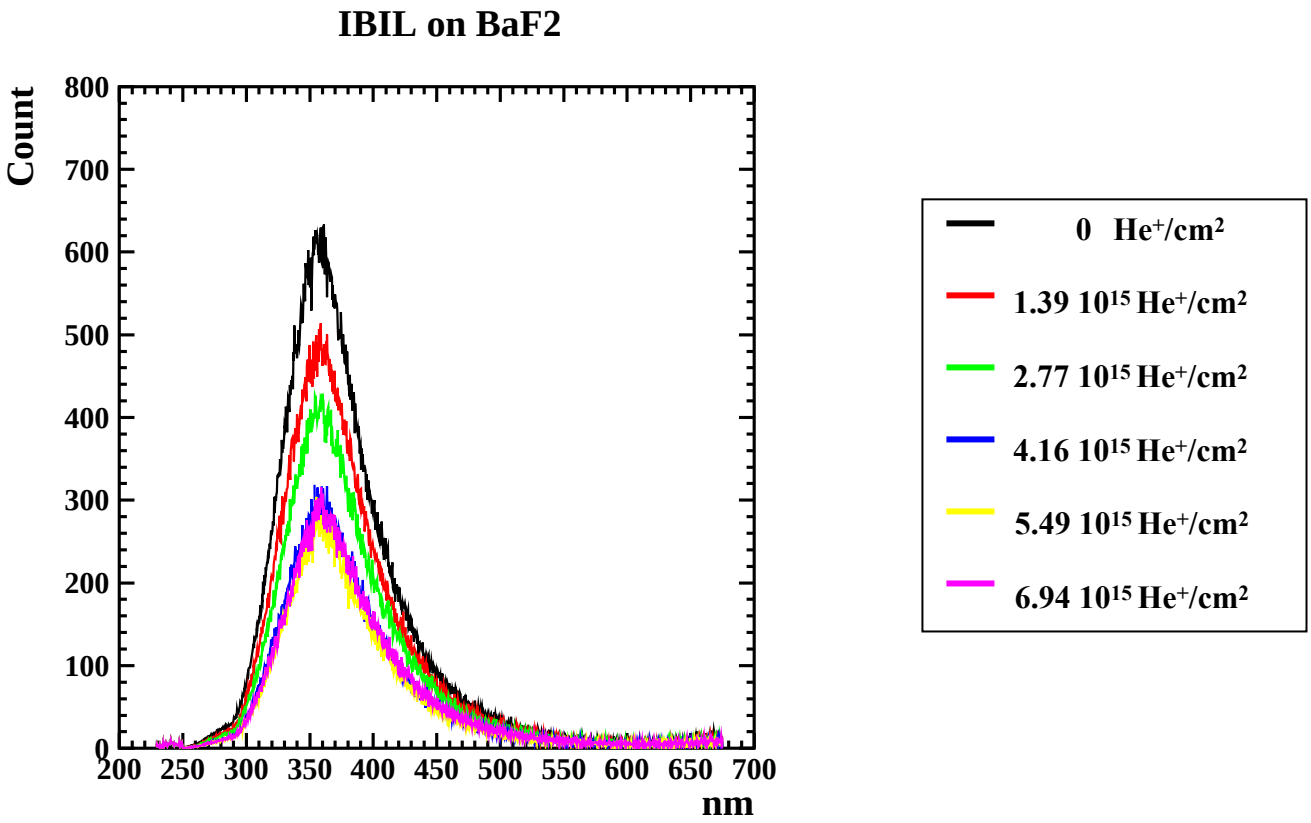

Fig. 3.17 : Emission spectra from a BaF_2 crystal. Different colors are linked to the different total charge absorbed.

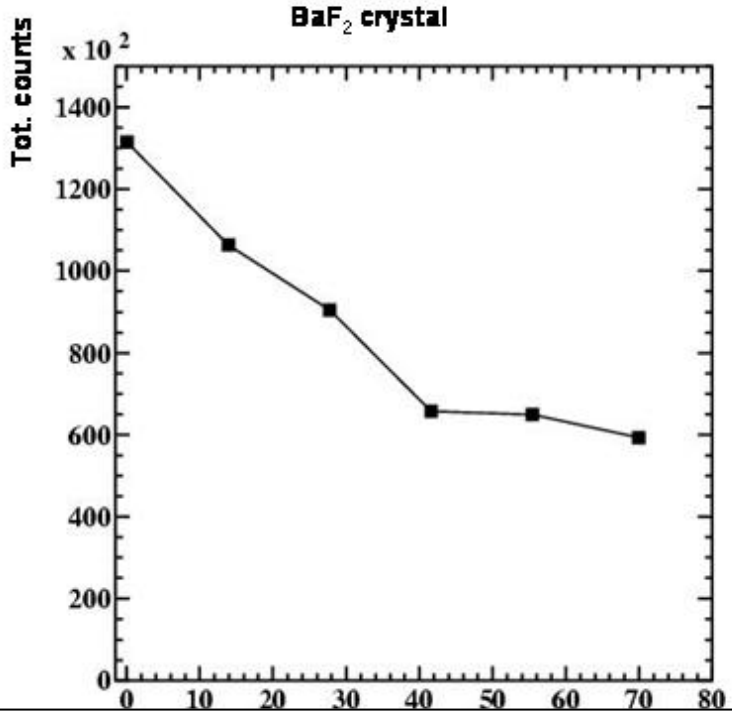

Fig. 3.18 : Integral of the emission spectra as a function of the ion fluence (He^+ at 2.2 MeV).

In this picture, one can recognize a decay of the luminescence efficiency due to the quenching phenomena which occurs for the radiation damage up to a fluence of 4.16×10^{15} He^{+}/cm^{2} (equal to 60 μC absorbed). After this measurement, the light output is practically the same, at least up to 6.94×10^{15} He^{+}/cm^{2} (100 μC). In other words there is an evident saturation of the quenching due to the radiation damage.

3.5 The LBO(Ce^{3+}) and LBO(Eu^{3+}) glass for neutrons detection

During the nuclear reaction, a lot of neutrons are normally produced and they can be detected only through the charged particle emitted in the nuclear reaction induced by them. All these processes contribute to the total cross section of neutrons on the matter, with a different weight depending from the energy of neutrons:

- elastic scattering (n, n);
- inelastic scattering (n, $n'\gamma$);
- nuclear reaction (n, p), (n, α), (n, Xn);
- radiation capture (n, γ);
- nuclear fission

In our case, we want to test some scintillating glasses made of Lithium and Boron which have high efficiency for the neutrons capture at low energy ($E_n \leq 1$ MeV). This material is amorphous and the luminescence process is improved by the presence of an activator element, Ce^{3+} in one case and Eu^{3+} in the other.

The interaction of the neutrons with the ^{10}B creates an alpha particle with the reaction

$$n + {}^{10}B \begin{cases} \longrightarrow {}^{7}Li + \alpha \quad E_\alpha = 1.78\ MeV \qquad \text{prob.} = 94\% \\ \longrightarrow {}^{7}Li^{*} + \alpha \quad E_\alpha = 1.47\ MeV \qquad \text{prob.} = 6\% \end{cases}$$

while in the case of ^{6}Li the reaction is

$$n + {}^{6}Li \longrightarrow {}^{3}H + \alpha \qquad E_\alpha = 2.05\ MeV$$

The relative isotopic abundances of ^{10}B and ^{6}Li in nature are 20% and ~ 7.4%, respectively. To improve the efficiency of n-capture enriched isotopic materials are needed. In Fig. 3.19, the behavior of the n-capture cross sections as a function of the neutron energy is shown for the two reactions. At lower incident energies a trend $\sigma \sim 1/v$ is followed, where v is the velocity of the entrance neutron, while at higher incident energies some resonances are more evident. It is clear that such types of detectors can not perform the spectroscopy of the neutrons because they are effective only in the region of thermal neutrons. Moreover, the α-particles produced by the induced nuclear reaction are monochromatic and without memory of the neutron energy.

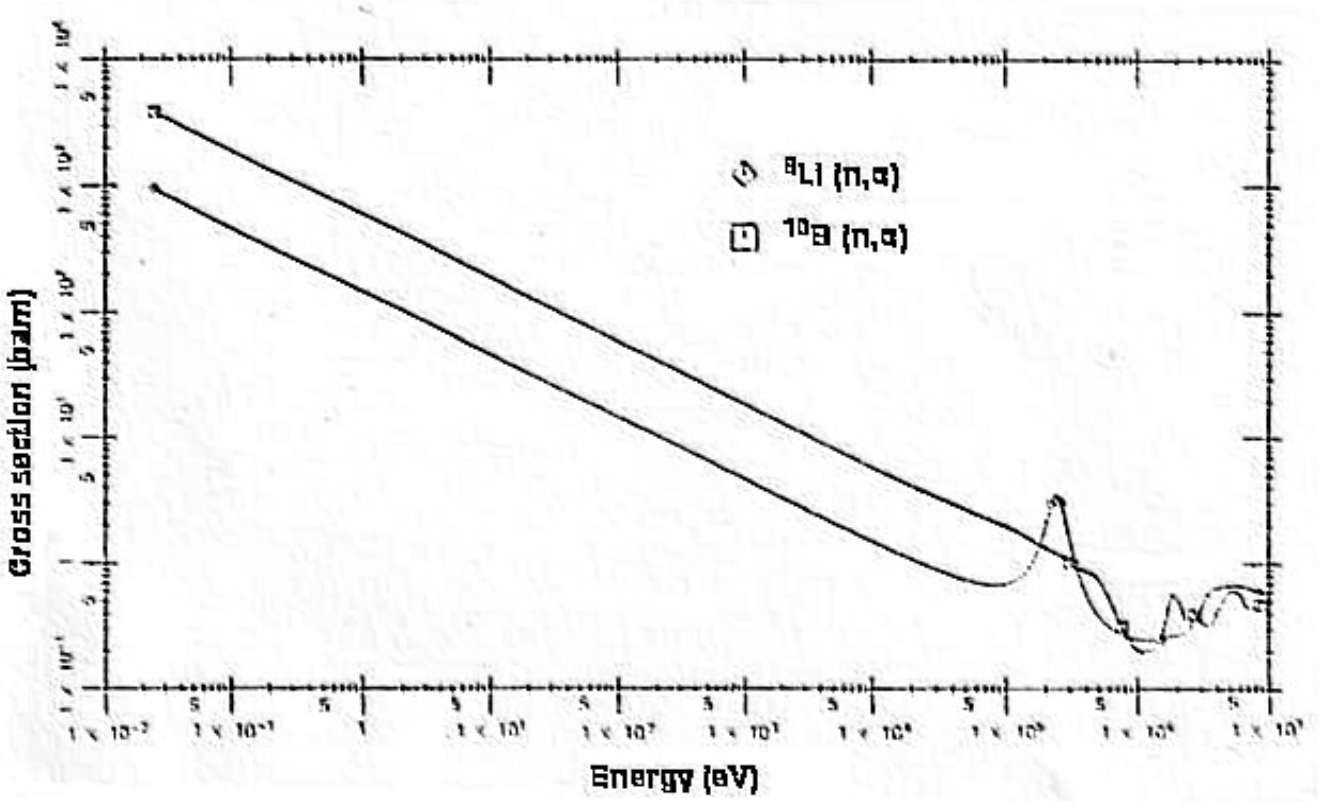

Fig. 3.19 : Cross section of the ^{6}Li (n, α) ^{3}H and ^{10}B(n, α) ^{7}Li as a function of the neutron energy.

Adding an opportune moderator, these materials can be used as neutron counters with high efficiency. In the Tab. 3.6, the general characteristics of the two scintillator glasses produced by the Russian company "ATOM-INTECH" Ltd are listed. The two samples used for these preliminary tests are relatively small, but the Russian company guarantees possible sizes up to 50 *cm* of length and 15 *cm* of diameter. The IBIL test under α-beam as previously described has been performed also for these two glasses.

The obtained results are shown in the Fig. 3.20 and 3.21.

"ATOM-INTECH" Ltd

PHYSICAL AND DETECTOR CHARACTERICTICS

Parameter	LBO:Ce^{3+}	LBO:Eu^{3+}
Softening temperature, °C	510-530	510-530
Density, g/cm^3	2.28	2.28
Effective atomic number	7.28	7.28
Hardness, Moos's scale	6	6
Hygroscopicity	feeble	feeble
Refractive index	1.54	1.54
Optical transparency region, nm	362-2760	304 – 2760
Luminescence maximum, nm	395	612
Decay time, ns	$\tau_1 = 5.4$ $\tau_2 = 43.0$	-
Size (mm)	∅20 x 20	∅20 x 20
Concentration of dopant-atoms, weight %	0,5	0,5

Tab. 3.6 : Table of the general characteristics of the two samples of the LBO glasses produced by the ATOM-INTECH Ltd.

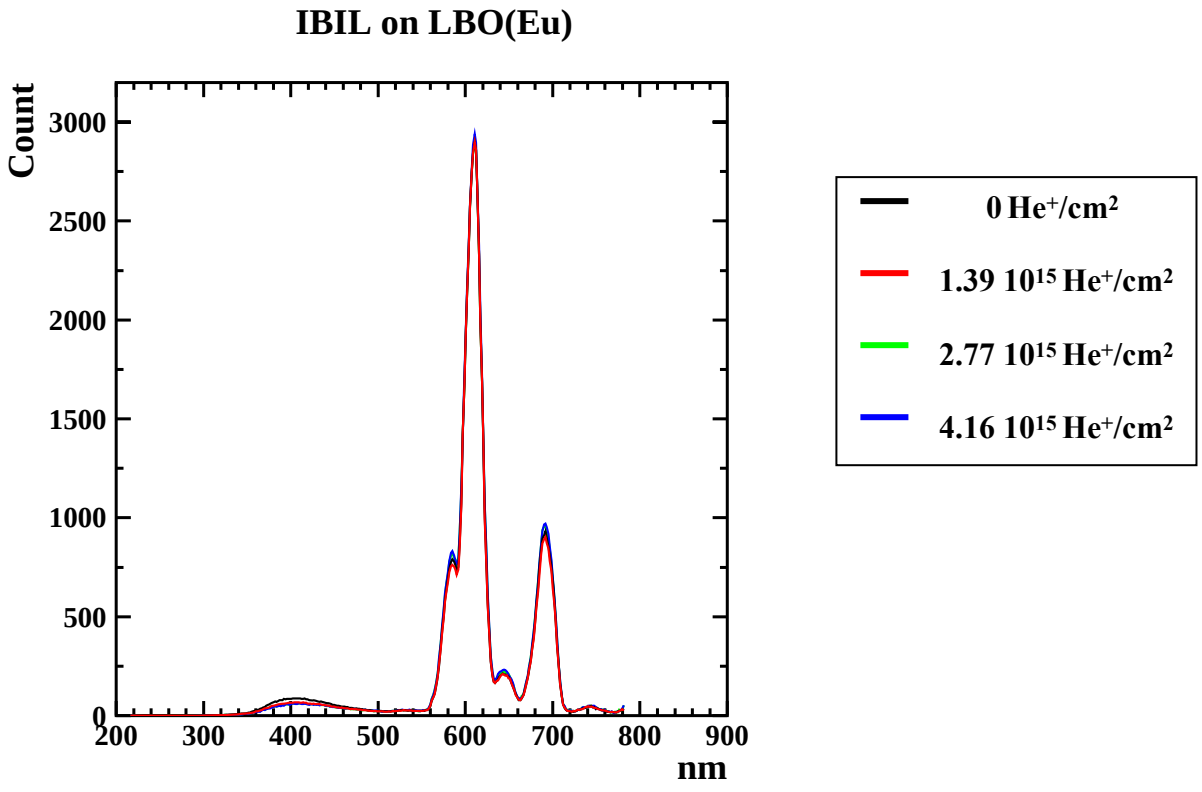

Fig. 3.20 : Emission spectra from the LBO(Eu^{3+}) glass for different total charge absorbed.

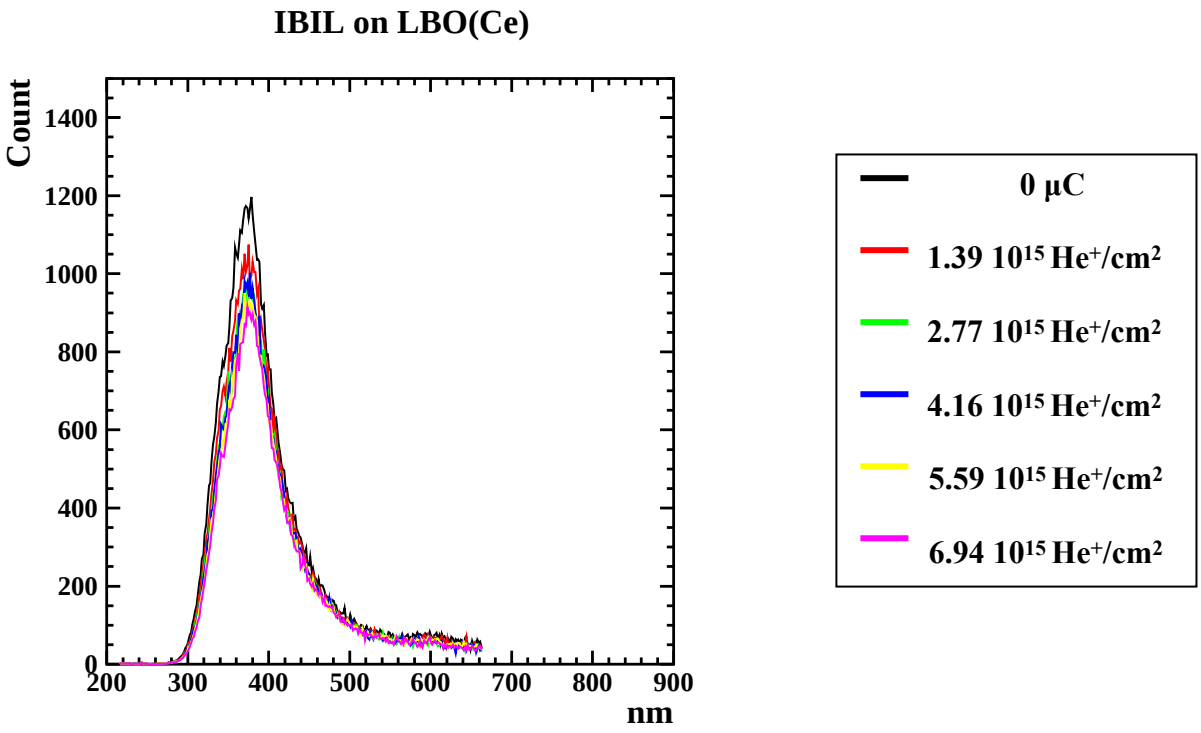

Fig. 3.21 : Emission spectra from the LBO(Ce^{3+}) glass for different total charge absorbed.

In this IBIL test the typical emission structure of the Eu^{3+} has shown up. This is starting at 600 *nm* and it is formed by 4 different peaks at 580 *nm*, 610 *nm*, 645 *nm* and 690 *nm,* respectively. Also a second emission from this crystal is present, peaked at 410 *nm* and is quite large. A third small peak can be recognized at wavelength around 750 *nm*. These emissions are not at all connected with the Eu^{3+}activator. In the case of glasses doped with Ce^{3+}, only a unique large peak is visible, with the maximum emission peaked at 374 *nm*.

Fig. 3.22 shows total number of counts of the two glasses as a function of the ion fluence (i.e. the total integrated charge). In the case of glass doped with Eu^{3+}, there is no significant decreasing of the luminescence efficiency. The possible explanation of this fact can be in the really small concentration of this doping element, so small that quenching effect due to the increasing of the quenching centers close to the activators atoms as a function of the integrated charge are not present because a sudden saturation of this is already reached at the beginning of the irradiation. The Ce^{3+} doped glass appears more sensible than the other to radiation damage.

Even in this case, photoluminescence test using a monochromator has been performed. The results are shown in Fig. 3.23. For the LBO(Eu^{3+}) glass, two different wavelengthes were used excite the glass scintillators. The blue line in the Fig. 3.23 relative to LBO(Eu^{3+}) glass was obtained exciting with a wavelength of 395 *nm*. It corresponds to the excitation of the Eu^{3+}.

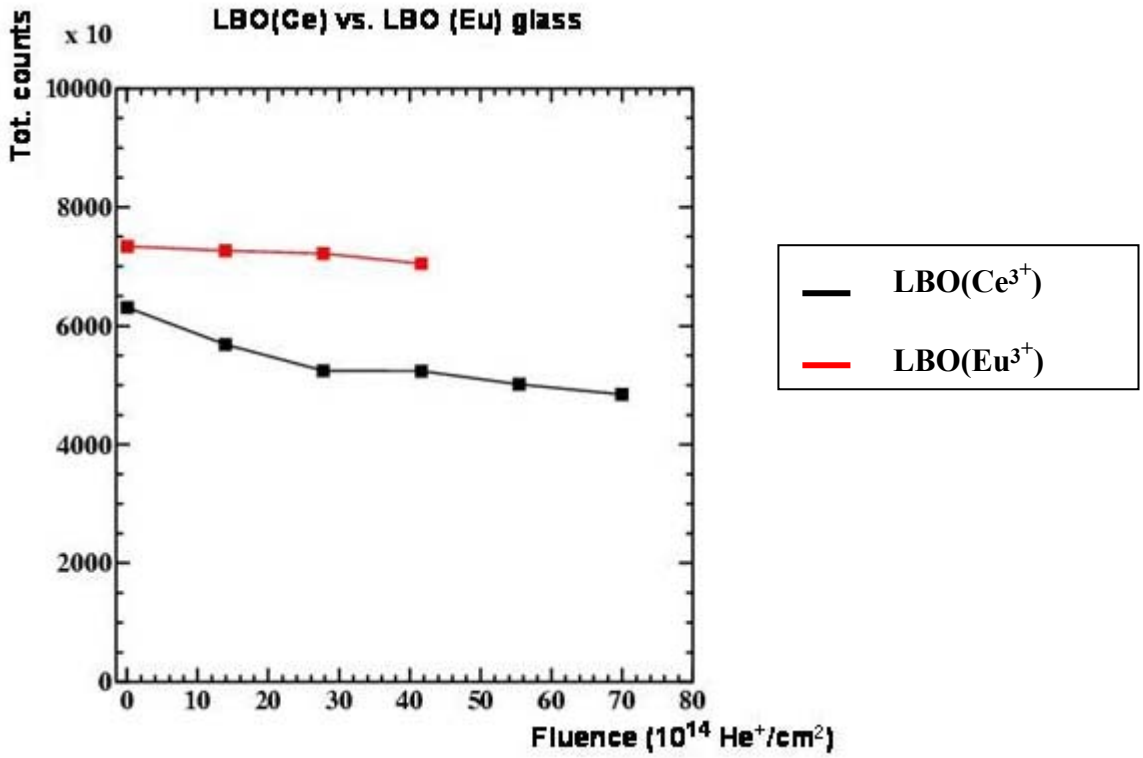

Fig. 3.22 : Integral of the emission spectra of the two different glasses as a function of the ion fluence (He^+ at 2.2 MeV).

.

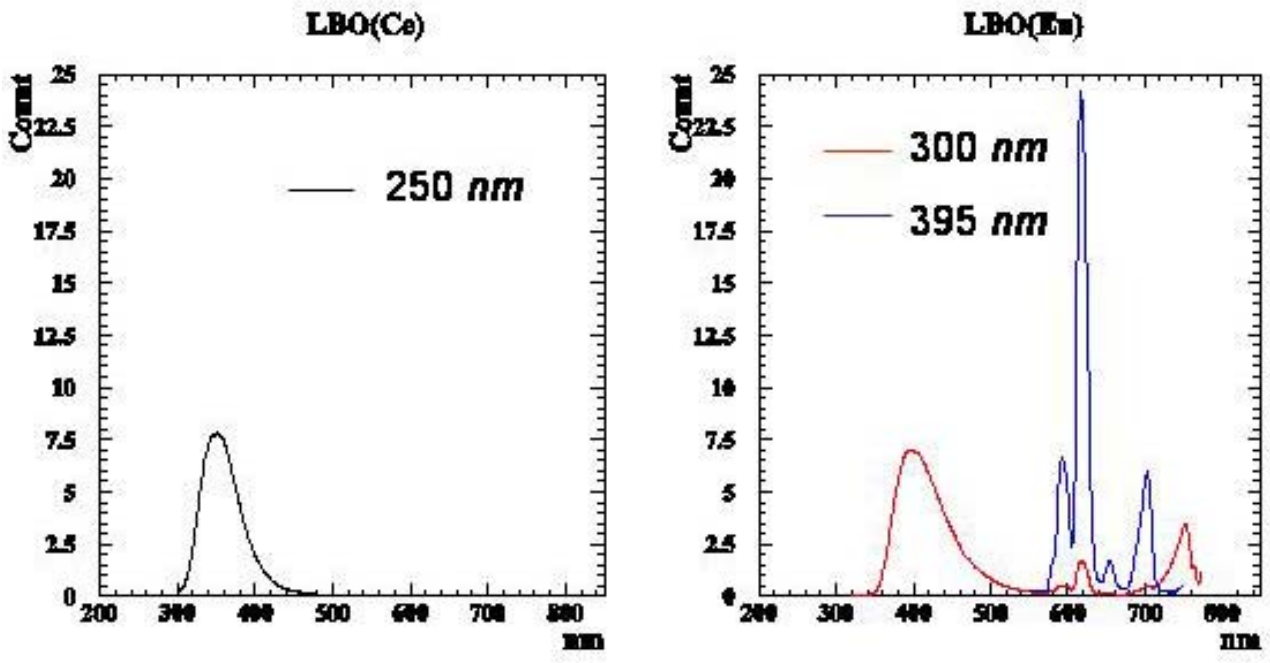

Fig. 3.23 : Emission spectra from the LBO(Ce^{3+}) (left plot) and LBO(Eu^{3+}) (right plot) glass scintillators for different input wavelengthes.

In fact, one can recognize a structure of peaks with maximums around 590 *nm*, 615 nm, 650 *nm* and 700 *nm*, values compatible with the previous values extrapolated from the IBIL test. The red line,

obtained with an incident wavelength of 300 *nm*, reflects the second emission outlined in the IBIL test and it can be due to the contamination of another doping element or can be also the glass which produces, with low efficiency, a luminescence emission in this region. Using this test it is possible to discriminate between the two hypothesis, because if the LBO glass is able to emit itself some luminescence light, this contribution must be present also in the LBO(Ce^{3+}) glass.

The emission for the Ce^{3+}, as it appears from the excitation through a 250 *nm* wavelength, is peaked at 350 *nm* (375 *nm* from the IBIL), while the emission from the contamination element of the LBO(Eu^{3+}) glass is peaked at 395 *nm* (410 *nm* from the IBIL measurement). The two peaks are very close. It is not possible, therefore, to distinguish between them, but it is possible to note that the second peak due to the contamination around 750 *nm* is not present in the case of LBO(Ce^{3+}) glass. This fact suggests the presence of other doping element in the LBO(Eu^{3+}) glass instead of an intrinsic luminescence from the LBO amorphous structure.

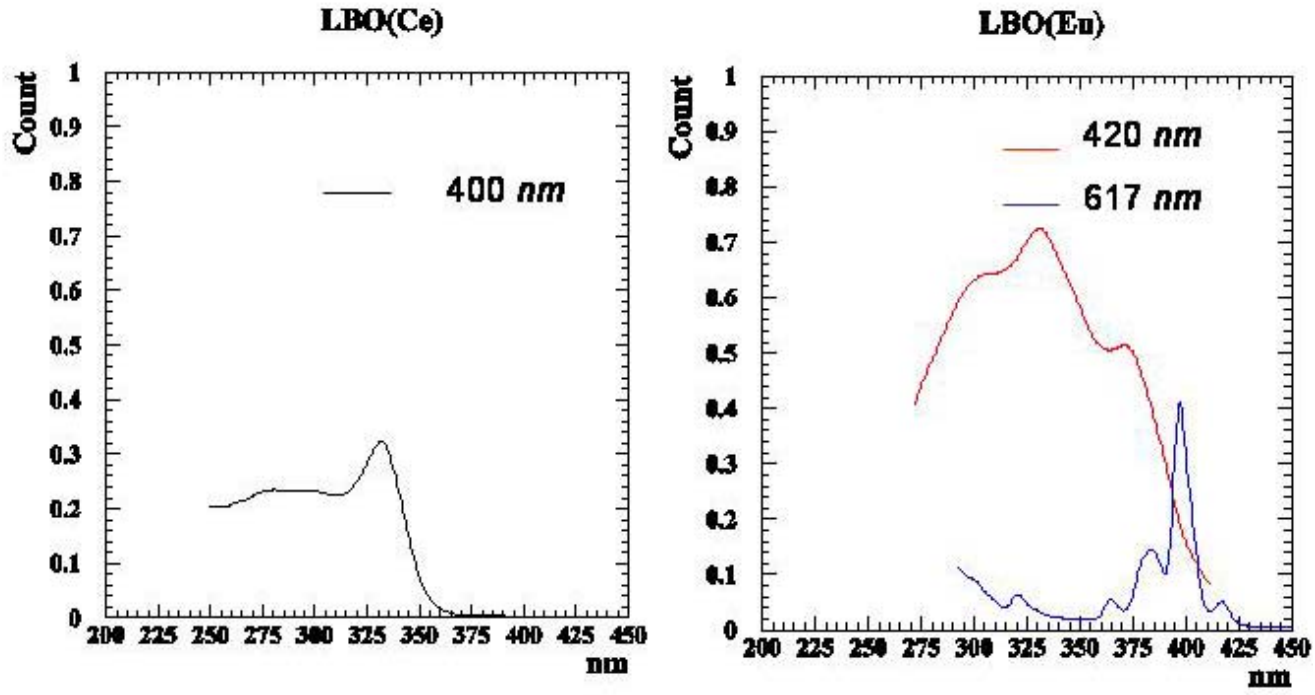

Fig. 3.24 : Intensity of the emitted spectra from the LBO(Ce^{3+}) (left plot) and LBO(Eu^{3+}) (right plot) scintillator glasses at different wavelengthes as a function of the incident radiation.

Using the same technique described before for the CsI(Tl) crystal, one can select a wavelength in the emission spectrum and study the intensity of the light as a function of the incident wavelength. The results obtained for the glass scintillators are shown in Fig. 3.24. For the LBO(Ce^{3+}) glass, the emission at 400 *nm* is greater with an incident wavelength of 330 *nm*. For the LBO(Eu^{3+}) glass, the

emission at 420 *nm* is connected to an absorption of incident wavelength flat in the region between 300 *nm* and 320 *nm* and peaked around 331 *nm*. The intensity of light emitted at 617 *nm* reproduced the peak structure of the Eu^{3+} with 4 peaks corresponding to excitation wavelength of 363 *nm*, 383 *nm*, 397 *nm* and 417 *nm*.

Other tests are needed to better understand the typology and the quantity of the contamination element in the LBO(Eu^{3+}) crystal and it will be also important to test the efficiency in the detection of neutrons from this glass using neutron source or neutron beam, opportunely thermalized.

Chapter 4

PRESENTATION OF EXPERIMENT

Introduction

The GDR experiment was performed at the National Laboratory of Legnaro (LNL) using a pulsed beam from the Tandem XTU and the LINAC ALPI accelerators. In particular, the experiment is proposed to study and compare the de-excitation modes via high energy γ-rays from the Giant Dipole Resonance and the light charged particles emitted by the nucleus ^{132}Ce formed through a symmetric and very asymmetric entrance mass channel at different excitation energies. In the tab. 4.1, the reactions and beam energies used are listed.

REACTION	ENERGY (MeV)	COMPOUND NUCLEUS	v_{cm} (cm/ns)	v_{beam} (cm/ns)
^{64}Ni + ^{68}Zn	500	^{132}Ce with E*= 203 MeV	1.88	3.89
^{64}Ni + ^{68}Zn	400	^{132}Ce with E*= 151 MeV	1.69	3.48
^{64}Ni + ^{68}Zn	300	^{132}Ce with E*= 100 MeV	1.46	3.01
^{16}O + ^{116}Sn	250	^{132}Ce with E*= 206 MeV	0.66	5.49
^{16}O + ^{116}Sn	130	^{132}Ce with E*= 100 MeV	0.48	3.96

Tab 4.1 : List of the reactions measured in the GDR experiment.

The campaign of measurements was performed in three different periods, and the analysis of all the experimental data is still in progress. In this work the results from the first two reactions induced by the Nickel beam will be compared to the reaction induced by the Oxygen beam at 250 *MeV*. Some of the results of this analysis are just published and presented at international conference ([Cam05], [Gra05], [Wie05], [Bar05]). The two couples of PSPPAC, used to detect the Evaporation Residues and described in the Chapter 2, are symmetric with respect to the beam and they cover the angular range $4° < \theta < 12°$. This position should be considered as a compromise between different

necessities, i.e. to stay as close as possible to the beam line to collect a higher number of Evaporation Residues and the problem due to the presence of the elastic beam which can completely blind the detectors due to the high counting rates and even deteriorate them. The selected position is the same for all the different studied reactions. Due to the different kinematics, the fraction of angular distribution of the ER that we can detect is different for the three reactions, especially if we compare the symmetric versus the asymmetric case, as one can see from Fig. 4.1. In chapter 5, we will point out again this difference between the selection of the ER of $^{64}Ni + ^{68}Zn$ at 500 *MeV* and $^{16}O + ^{116}Sn$ at 250 *MeV* reactions which can lead to some kinematical correlation seen as a different counting rate in the different sectors of GARFIELD.

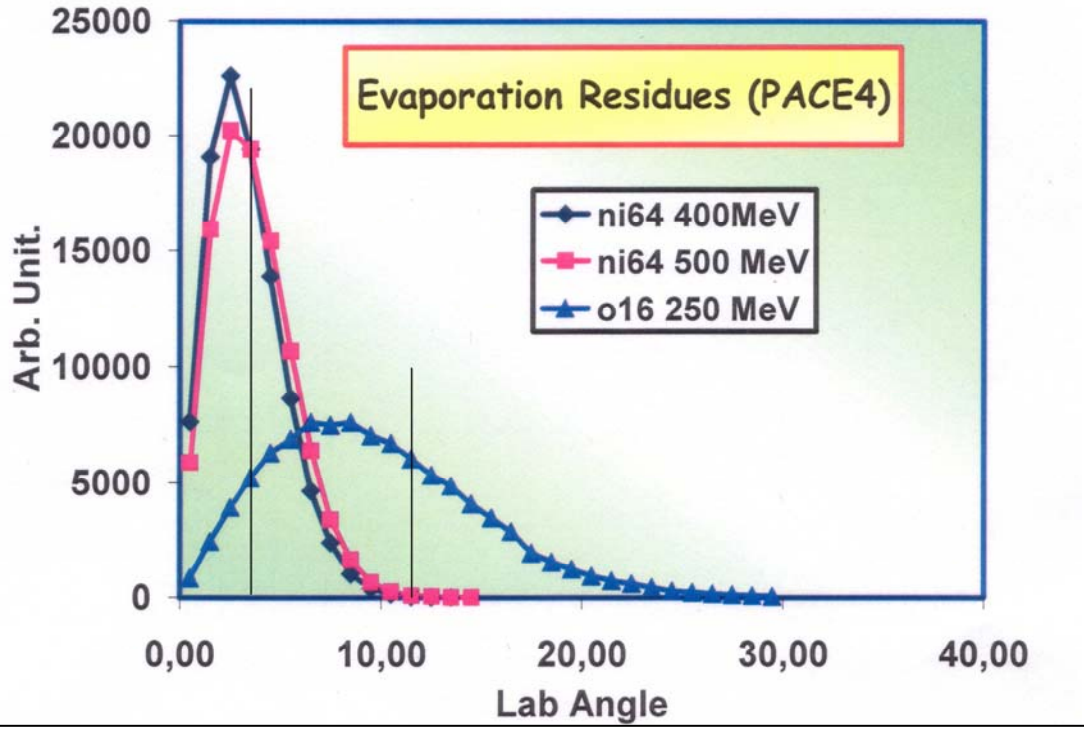

Fig 4.1 : Angular distribution of the Evaporation Residues for the 3 studied reactions calculated using PACE4 code. The two black lines show the angular range covered by the PSPPAC.

In this chapter, we will describe all the different aspects of the experimental measurement performed, with particular attention to the aim of the experiment, the choice of the trigger and the complicated setup needed for the processing of the signals coming from the apparatus. The chapter of trigger will be divided in two parts, one dedicated to describe the trigger scheme from an hardware point of view (Par. 4.2), the second will explain the possibility of an off-line selection of the trigger using some peculiarities of acquisition system of GARFIELD (Par. 4.4).

4.1 Aim of the experiment

A quite recent campaign of measurements has been performed at Berkeley, in the U.S.A, by Kelly et al. [Kel97], to underline the importance of considering and evaluating the contribution of pre-equilibrium emission in the determination of the excitation energy of the remaining equilibrated source. The experimental work was devoted to study the reaction $^{18}O + ^{100}Mo$ leading to the formation of a compound system in the Sn region.

Different and separated measurements were performed on the system, using the same asymmetric mass entrance channel:

1. measurement of Light Charged Particles through a detection system made by several CsI crystal disposed at different angles (20°, 30°, 40°, 50°, 90° and 140°), tagged by a gate on $E\gamma > 10$ *MeV* detected through a big NaI crystal at a bombarding energy of $E_{beam} = 200$ *MeV*;
2. measurement of inclusive γ-ray spectra at different bombarding energies (from 122 to 214 *MeV* corresponding to excitation energy for complete fusion from 108 to 186 *MeV*)
3. measurement of Evaporation Residue cross section at different angle using a monitor detector for the normalization to the elastic scattering at $E_{beam} = 200$ *MeV* .

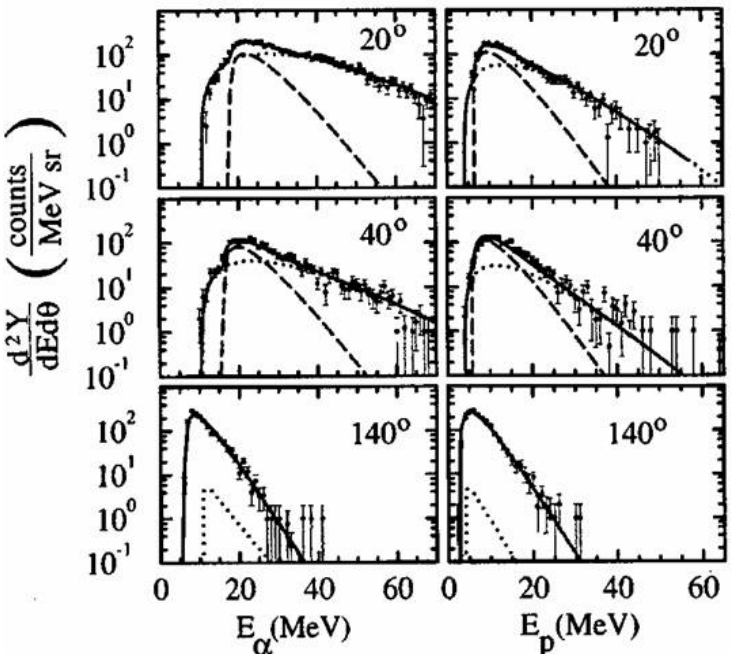

Fig 1.11 : α and proton energy spectra for different angles in the Laboratory system. The dashed line is the evaporative component of the fit, the dotted line represents the pre-equilibrium emission. The continuous line is the sum of the two components [Kel99].

The Light Charged Particle spectra (proton and α-particles) have been analyzed using a moving source fit analysis (Fig.1.11) [Kel99]. The data have been fit considering two maxwellian

distributions, one with the velocity of the CN and an other one, which simulates the emission from a pre-equilibrium source, with an intermediate velocity free to vary between the CN velocity and the beam velocity. From this fit, it is possible to obtain an average temperature for the equilibrated CN using the slope parameter of the first maxwellian and also to separate the contribution given by the evaporative emission from that one given by pre-equilibrium. A more detailed discussion of the technique, we will be described in the Chapter 5 in our analysis work.

In the Kelly experiment, combining the information of the moving source fit analysis with the estimation of cross section for α-particles and protons and the measurement of the fusion cross section, it was possible to obtain the average number of pre-equilibrium light particles emitted. From that, assuming the average energy of particles emitted, they estimated the average energy lost by the emitting system before equilibration. In their work, the neutrons were taken into account using theoretical simulation results. Finally, an estimation of 20% was obtained in this analysis for the energy lost through pre-equilibrium particle emission by the compound system before equilibrium in the reaction $^{18}O + ^{100}Mo$ with $E_{beam} = 200\ MeV$.

The importance of this result is particularly linked to a possible different explanation on the behavior of the GDR width as a function of the temperature: the conclusion claimed by the group of Kelly is, in fact, that a possible overestimation of the temperature of the CN was possible for the high energy measurements performed in the past. This is attributed to a missing correction for the energy lost in the early phases of the reaction due to pre-equilibrium particle emission. It is clear that to be justify such a conclusion many other experiments are needed. In fact, one should take into account that all the particle spectra analysis in Kelly work have been performed only at one bombarding energy and only in the case of an asymmetric mass entrance channel. Moreover, the measurement was not properly exclusive because the analyzed particles and the γ-spectra were not tagged with the Evaporation Residues and the analysis of the γ-spectra have been done in a different inclusive measurement.

Even though the information from the previous described experiment is not complete, the results obtained are undoubtedly important because, mixing up the information from light charged particles and γ-rays, they give a signal of alert in the definition of the characteristics of the equilibrated emitting source as far as excitation energy and/or size.

The measurements, on which this work of thesis is based, followed the idea of adding information on this delicate subject, using a more complete experimental apparatus and studying a variety of reactions. In particular, we studied central collisions in which the same compound system should be formed using both symmetric and asymmetric mass entrance channels.

4.2 The hardware trigger

The choice of the logic of the trigger is a crucial problem for every experiment because it is strictly connected to the selection of the reaction mechanism that you are going to study. Normally, more then one processes are of interest inside an experiment. Therefore, the main trigger is practically obtained by performing logical condition of chosen signals coming from the different detectors. This leads to a selection of events with a relevant meaning from the point of view of the physics. In the case of the GDR experiment, the main process to select was the Compound Nucleus formation, which is the fusion of the projectile with the target into an equilibrated hot and thermalized system. During the following decay of this CN, we have a production of light particle and γ-rays that we want to study. For this reason an important signal for our experiment was coming from the detection of Evaporation Residues, made through an opportune anticoincidence condition in the PSPPAC.

The main trigger is then obtained from the OR of different trigger signals of interest. In particular, we got the OR-GARFIELD (OR of all CsI(Tl)), which gives the "inclusive" trigger for light charged particles and fragments, the OR-BaF_2 which gives the "inclusive" trigger of γ-rays. These trigger signals were opportunely reduced to diminish the counting rates. The most important trigger for the experiment were coming from the coincidence between OR-GARFIELD with Evaporation Residues (PSPPAC) and OR-BaF_2 with Evaporation Residues.

To put all signals in coincidence, due to the very different response of the detectors plus different time of flight of the reaction products, faster signals ($BaF_2 < 1$ *ns*) have been opportunely delayed to enter the coincidence with the slower signals (PSPPAC from 30 *ns* to 300 *ns*, GARFIELD from 250 *ns* and 300 *ns*). In addition to these signals, we put in the main trigger also the AND logical condition between the left and right forward PSPPAC to study possible events coming from a fission process. In Fig 4.1, one can see a scheme of the main trigger.

The last two signals of the Fig. 4.1 inserted in the main trigger were used only for particular tasks and were not switched on during the real data taking. In particular, the pulser trigger is used to make routinely inside the experiment some control runs where the signals of electronics come from controlled and known pulser input signals.

The use of a standard input source, like a pulser, is crucial in this experiment because it makes possible to check the stability of the electronics during the measurement and especially to compare this experiment to a previous one, performed in February 2002, where many elastic reactions have been measured permitting the calibration of every single telescope in GARFIELD. In this way to

calibrate GARFIELD in GDR experiment, we can use the old calibration data reporting them with a pulser factor that takes into account all possible changing in the amplification used in the different measurements. We will discuss this procedure in detail in the Chapter 5.

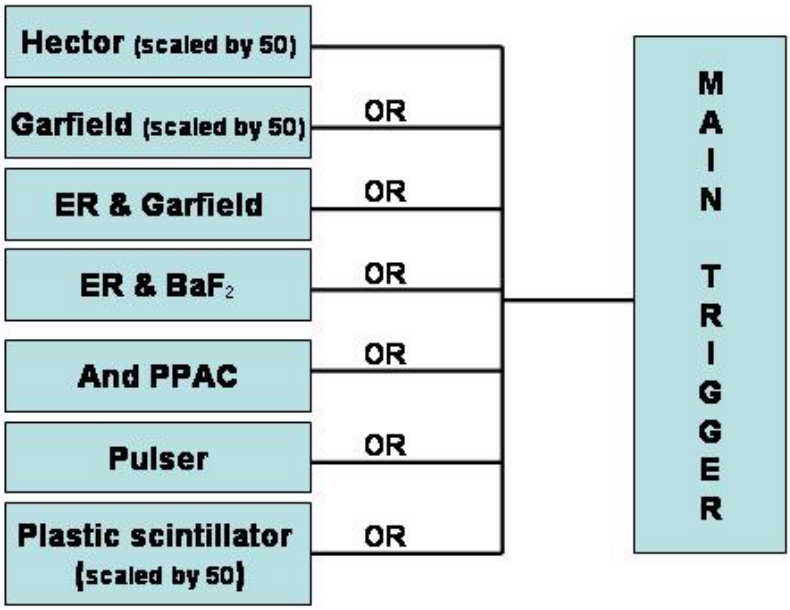

Fig 4.1 :Scheme of the main trigger of the GDR experiment

The last trigger is from 4 plastic scintillators that were positioned all around the beam line at small angles ($\theta < 2°$). In this way, they could collect the elastic scattering and produce a time spectra from which it was possible to determine and keep under control the time resolution of the beam. From time to time, a pure elastic scattering measurement (using a gold target) was performed to have a clear time of flight spectrum to control the beam time structure. A continuous monitoring was anyway performed during the whole measurement to take under control possible deterioration of the pulsed beam. This was necessary both for the BaF_2 and for the PSPPAC time reference. For the GDR experiment, in fact, we needed to discriminate neutron from γ-rays in the BaF_2 scintillators, with a time resolution around 1 *ns*. So the possibility to check the time resolution every time a new beam was delivered together with a check of stability during the data acquisition was very important. A relevant characteristic of the GaARFIELD apparatus is the fact that using a simple Labview interface, it is easy to modify the main trigger adding o removing every single signal. In this way, if needed, one can perform a pulser run or a test run to check the time resolution of the beam without changing the hardware connection and without entering in the experimental bunker.
This is possible because a CAMAC module was used for the logic of the trigger and an opportune graphical Labview based interface, based on GPIB-ENET connection, are used to set and control it.

In the Fig. 4.2, one can see a typical time spectra from one of these plastic scintillators obtained putting in the main trigger only the signal from the plastic scintillators and subtracting the Radiofrequency reference. The sigma parameter of the Gaussian fit is around 0.45 ns.

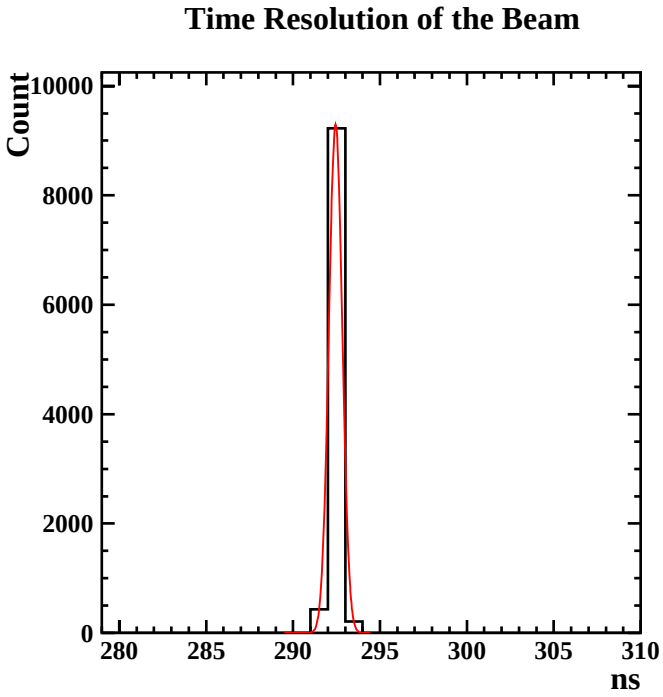

Fig 4.2 :Picture of the time resolution of the beam produced as difference between the auto-coincidence of one plastic scintillator subtracted of the Radiofrequency time.

4.3 The off-line analysis of the trigger from acquisition system

Due to the existence of the segment controller in the acquisition system of GARFIELD (see Ch. 2.5), it is possible during the off-line analysis to recognize event by event which of the signal put in the main trigger in OR logical condition was really the responsible of the trigger signal.

Every segment controller is formed by 6 bit, from which three are filled with some of the triggers that are in the main trigger, the first one is filled with the main trigger and the last two are not free and are fixed respectively to “1” logic state and “0” logic state. Considering that in GARFIELD’s acquisition we have 4 segment controllers, all the single triggers of the experiment could be considered. So segment by segment, taking into account the bit corresponding to a single trigger, it

will be in the logical condition “1” if the main trigger is in coincidence with that signal, in the logical condition “0” if not. Thus, for each segment controller, when the main trigger is due to a signal present only in another segment controller, the only bit in the logical condition “1” would be the first one, connected to main trigger. Event by event the acquisition system reads and stores the state of the bit of every segment controller, so, if needed, we can perform a complete off-line analysis. In tab. 3.2 one can see the complete scheme of the bit of segment controller of GDR experiment. The first column indicates the channel number in the spectrum of each trigger pattern of every segment controller. The second column indicates the combination of bits in logical condition “1”, while column 3, 4 and 5 indicate the name of the trigger and the possible coincidences between them.

CHANNEL SPECTRA	**BIT ON**	**SEGMENT 1**	**SEGMENT 2**	**SEGMENT 3**
17	2^4+2^0	Main Trigger	Main Trigger	Main Trigger
19	$2^4+2^1+2^0$	OR Garf.	Pulser	Pulser Hector
21	$2^4+2^2+2^0$	OR plastic scint.	AND PSPPAC	OR Baf_2
23	$2^4+2^2+2^1+2^0$	OR Garf in coincidence with OR plastic scint.	Pulser in coincidence with AND PSPPAC	OR BaF_2 – pulser Hector
25	$2^4+2^3+2^0$	ER & OR Garf	ER & BaF_2	BIT NOT USED
27	$2^4+2^3+2^1+2^0$	OR Garf in coincidence with (ER & OR Garf)	Pulser in coincidence with (ER &BaF_2)	OR BaF_2
29	$2^4+2^3+2^2+2^0$	OR plastic scint. in coincidence with (ER & OR Garf)	AND PSPPAC in coincidence with (ER & BaF_2)	Pulser Hector
31	$2^4+2^3+2^2+2^1+2^0$	All the trigger in coincidence	All the trigger in coincidence	All the trigger in coincidence

Tab 4.2 : Scheme of the meaning of the bits in the different segment controller.

Chapter 5

CALIBRATION AND EXPERIMENTAL RESULTS

Introduction

To extract the complete information from a complex measurement like this campaign, one needs to calibrate all the detectors used in the experiment, i.e. the GARFIELD apparatus, the PSPPAC detectors and the 8 BaF_2 crystals of the HECTOR apparatus. For every one of these a long and non trivial work is needed. Matching the competences in the analysis of the GARFIELD data from the Nuclex group with those regarding the analysis of the γ-spectra obtained by the BaF_2 scintillators from the HECTOR group, it has been possible to produce very interesting results like the proton and alpha spectra in coincidence with the Evaporation Residues or in triple coincidence with ER and γ-rays. It has been also possible to study the γ-emission and, as a first result, to isolate the GDR emission from a thermalized source for the symmetric mass entrance channel. In the case of the asymmetric mass entrance reaction channel, the analysis of the LCP will permit us to better characterize the emitting source that should be used for the characterization of the γ-emission, taking into account the energy and mass lost by the system due to pre-equilibrium emission. The quantitative part of the analysis for the γ emission is still in progress, while information about the light charged particle will be described in this thesis.

In this chapter, we will describe the calibration procedure used for every detector in the experiment, with particular attention to that one employed for the GARFIELD apparatus. Moreover, all the results regarding the symmetric mass entrance channel reactions will be described, together with the main results from the light particle analysis for asymmetric reaction.

5.1 The Garfield calibration.

As explained in chapter 2, the GARFIELD apparatus is a 4π detector formed by two separated chambers based on the identification of charged particles and fragments through the ΔE-E technique. This means a great number of signals that should be collected and calibrated. Even though in our experiment only one chamber was used, the calibration procedure was really long and difficult due to several cross checks needed. In fact, every microstrip, every CsI(Tl) crystal has characteristic slightly different one from the other, and also the amplification of the single electronic channel can be slightly different. So we need a particular calibration of every microstrip and CsI(Tl) crystal that are in the apparatus (94 ΔE signals and 94 residual energy signals in the present case). Besides that, every preamplifier was fed into two different amplification chains, in order to have a better collection of the low energy signals. Due to the known dependence of CsI(Tl) light output from the energy, mass and charge of the incident particle and the dependence on energy of the drift chamber, to perform a proper calibration some elastic reactions are needed, because only through the known properties of the scattered particles one can directly obtain the mass, charge and energy dependence of the detectors. This information gives the effective response of the single detector, and it makes then possible to calibrate each of them. Unfortunately, it is not always possible to perform several elastic measurements before each experiment, so it becomes important to have the possibility to export the calibration produced in a single campaign to all other possible measurements performed in similar conditions.

REACTION	ENERGY (AMeV)	GRAZING ANGLE
$^{12}C + ^{181}Ta$	8	50°
$^{12}C + ^{181}Ta$	6	85°
$^{12}C + ^{93}Nb$	6	40°
$^{16}O + ^{181}Ta$	8	49°
$^{16}O + ^{181}Ta$	6	83°
$^{12}C + ^{181}Ta$	10	36°

Tab. 5.1: List of the reactions used for the GARFIELD calibration.

Just before this GDR campaign of measurements, the GARFIELD apparatus was used to perform an experiment devoted to the measure of the cross section of Carbon and Oxygen induced reactions

on Carbon, Calcium, Niobium and other targets at different bombarding energies ([Gra02], [Gra04b]). In this case, it was quite easy using this light beams and a heavy target like Tantalum, to collect elastic scattering data. Due to the combination of target, projectile and energy, some of these reactions were characterized by a large grazing angle so that the elastically scattered carbon and oxygen particles could cover practically all the angular range of the forward drift chamber ($30° < \theta < 85°$). Using the reactions written in Tab 5.1, it was possible to calibrate all the detectors of GARFIELD for this experiment. Besides this, a standard procedure was created to compare the response of each detector in different pulser runs, in order to correct for possible changing in the amplification gains during the different measurements. In this way, with relatively small corrections, it was possible to use the calibration performed in the Carbon and Oxygen induced measurement in all the following experiments.

The calibration of the ΔE signal produced in the gas chamber of Garfield is more easy than the signal from the CsI(Tl) because the gas microstrip detectors are expected to produce a signal directly proportional to the energy lost by the ionizing particle. The trajectory of the elastic scattered particles can be simulated with an opportune energy loss calculation code which takes into account all the different layers of GARFIELD (the mylar entrance window, dead layer of gas CF_4, gas region corresponding to the microstrip down, dead layer, microstrip up, dead layer, exit window of the gas chamber and mylar on the crystal of CsI(Tl)). It is then possible to draw the linear correlation between the energy lost in the two different microstrip and the measured channel, as one can see in Fig 5.1.

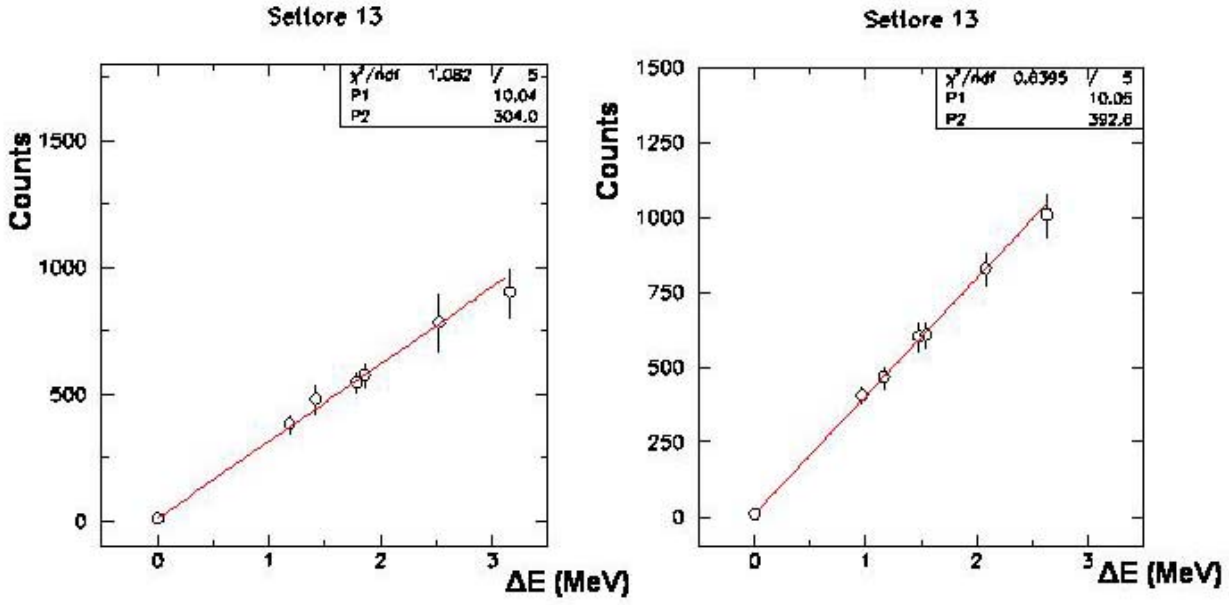

Fig 5.1 : The linear calibration of the microstrip down (left side) and up (right side) for the sector 13. Every point is a different reaction from Table 4.1 or a different θ angle of emission (and different CsI(Tl) hit) for the same reaction.

Considering different θ angles of emission for the particle, corresponding to different CsI(Tl) hit by the particle, the ΔE calculation gives a different result because the length of the track in every layer can change significantly. This gives us several calibration points for the microstrip detectors.

For the CsI(Tl) crystals, the procedure is more complicated because the response of these detectors is not linear and it is correlated to the charge (and in minor way to the mass) of the particle. A semi-empirical formula to give the Light Output of the crystal, in arbitrary units, as a function of the energy and the charge of the entrance particle has been obtained in the past and published in [Mas93]. It was derived using several measurements of the light output of the CsI(Tl) as a function of different impinging particles with different energies. The proposed formula, which is linked to the Birks formula ([Bir64]) of the light output is given by:

$$L = \gamma E + \beta\left(e^{-\alpha E} - 1\right) \qquad \textbf{(5.1)}$$

where α, β and γ are parameters which show a dependence on Z. An improved formula has been recently found which better describes the low energy region, while it will superimpose to the previous one for the high incident energies ([Cas04]).

Using the elastic run of the previous experiment, it was possible to obtain a linear relation between the Light Output channel used in the Carbon and Oxygen induced experiment and the Light Output channel used to create the theoretical formula, as one can see in Fig. 5.2. In this way, transforming the experimental data in the arbitrary Light Output channel was used to write the formula 5.1, it is possible to link the experimental L.O. to the residual energy lost in the CsI(Tl) crystal, just after the determination of the charge of the particle.

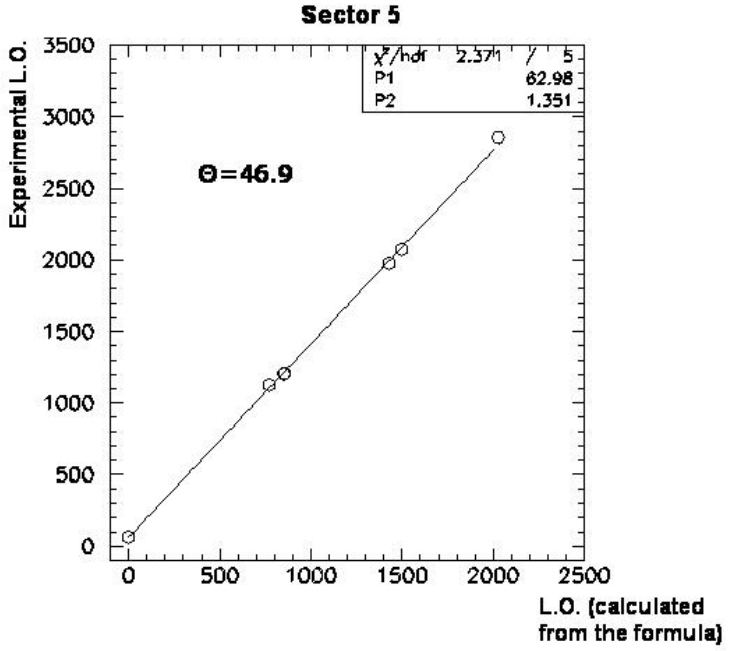

Fig 5.2: The calibration line of a CsI(Tl) of Garfield.

The procedure that, using the pulser spectra, permits us to follow the amplification changing of a single electronic channel on the different campaign of measurements and also inside the same experiments to keep under control the stability of the electronics was developed during my Master thesis work in Bologna ([Bar02]).

In the Fig 5.3 two typical pulser spectra are shown, one from a high gain channel and the other from a low gain channel. The pulser signal was produced through a time calibrator and it consists in a signal equal in amplitude but repeated at fixed intervals of time. In the case of the energy signals from GARFIELD, the pulser signal, opportunely formed through a Time Amplitude Converter (TAC), was sent into all the preamplifiers. In this way we got a set of signals with fixed increasing amplitude able, after the amplification through the high and low gain electronic chain, to cover the Analogical to Digital Converter range with a sequence of peaks with constant distance one from the other.

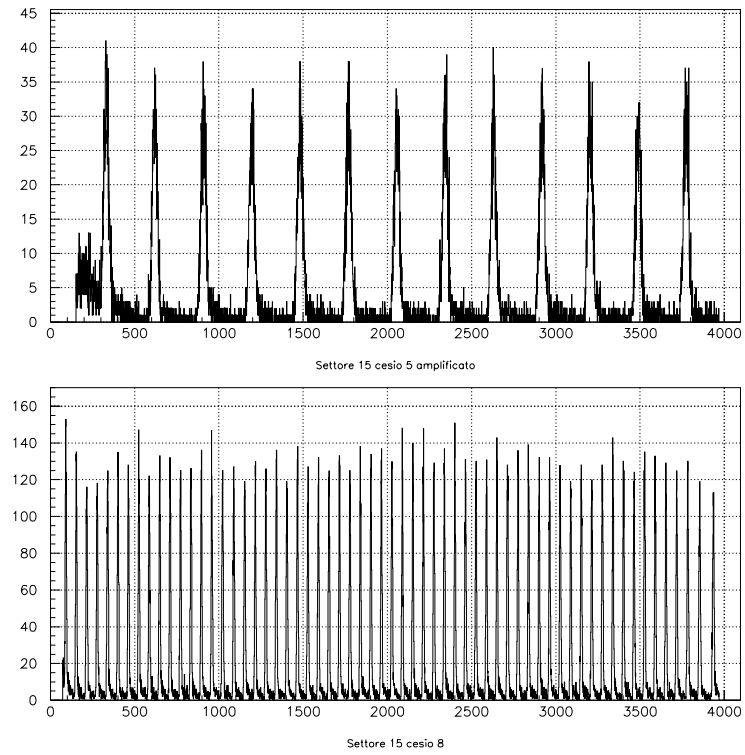

Fig 5.3: Two typical pulser spectra from Garfield. The top one is from the high gain amplification, the other from the low gain amplification.

It is clear that the relative distance between the two peaks becomes a sign of the amplification used for this detector during the experimental run. Thus, making with an opportune computer code the recognition of every peak, it is possible to have the average distance between two following peaks in every experiment performed with GARFIELD. In particular, we applied the comparison

procedure between the carbon induced experiment and the GDR experiment. This has permitted to normalize our GDR data on the data of the calibration experiment. Another application of this comparison procedure on different pulser spectra is to check the electronic stability during a long time experiment. In fact, if one did not change manually the amplification factor, the result of the matching of two following pulser runs in the experiment should show no variation. Using this method, one can see if there are some channels with problems and estimate the maximum variation in the electronic gain due, for example, to external and internal fluctuation of temperature.

The last thing to take into account is the normalization between the low and the high gain for every detector. This separation is important during the data acquisition moment because it doubles the number of signals for the Light Charged Particles detectors, but it permits a better identification of those products which lose the great part of the energy in the gas chamber and give only a small signal in the CsI(Tl) and the opposite type which leave a strong signal as residual energy but only a small signal as ΔE. In the analysis this double amplification has to be converted into a unique signal which will be linked to the energy information. Using the pulser, one can easily get the correct correlation between the high gain and the low gain factors. These values are normally dependent on the fixed internal factor of the amplifiers made by the producer. Before every new experiment a check is important to control that no anomalies are present.

Combining all these procedures, one can plot the ΔE-L.O. plot obtained with the ΔE signal from the microstrip calibrated in *MeV*, and the L.O. signal from the CsI(Tl) crystals transformed in the same channel used in the theoretical L.O. formula (Eq. 5.1). Normally, some small corrections are needed, like possible small changing of the pedestal that must be subtracted to the signal before calibrating. In Fig. 5.4 one can see a typical ΔE-L.O. scattered plot from GARFIELD calibrated in this way compared to energy loss calculations, corresponding to different Z of the detected particle. The residual energy in *MeV* of the calculation is obviously transformed in L.O. with the improved formula to perform a correct comparison.

For every particle, it is possible to have a correct Z-identification minimizing the distance to the different theoretical lines. Knowing the charge of incident particle, one can invert the LO formula to have the residual energy. Adding the energy lost in all the dead layers, then one can have for every particle of the event the complete set of information needed for a good identification: charge *Z*, total energy *E* and angles of emission θ and φ defined by the telescope hit in Garfield.

In the GDR experiment the complete event can contain also the coincidence with the products detected in the other detectors. In fact, one of the most important aspects of this experiment is that using the signals from the PSPPAC and the BaF_2 crystal, one can tag the particle which was emitted in coincidence with an ER or in coincidence with a γ-ray or with both of them.

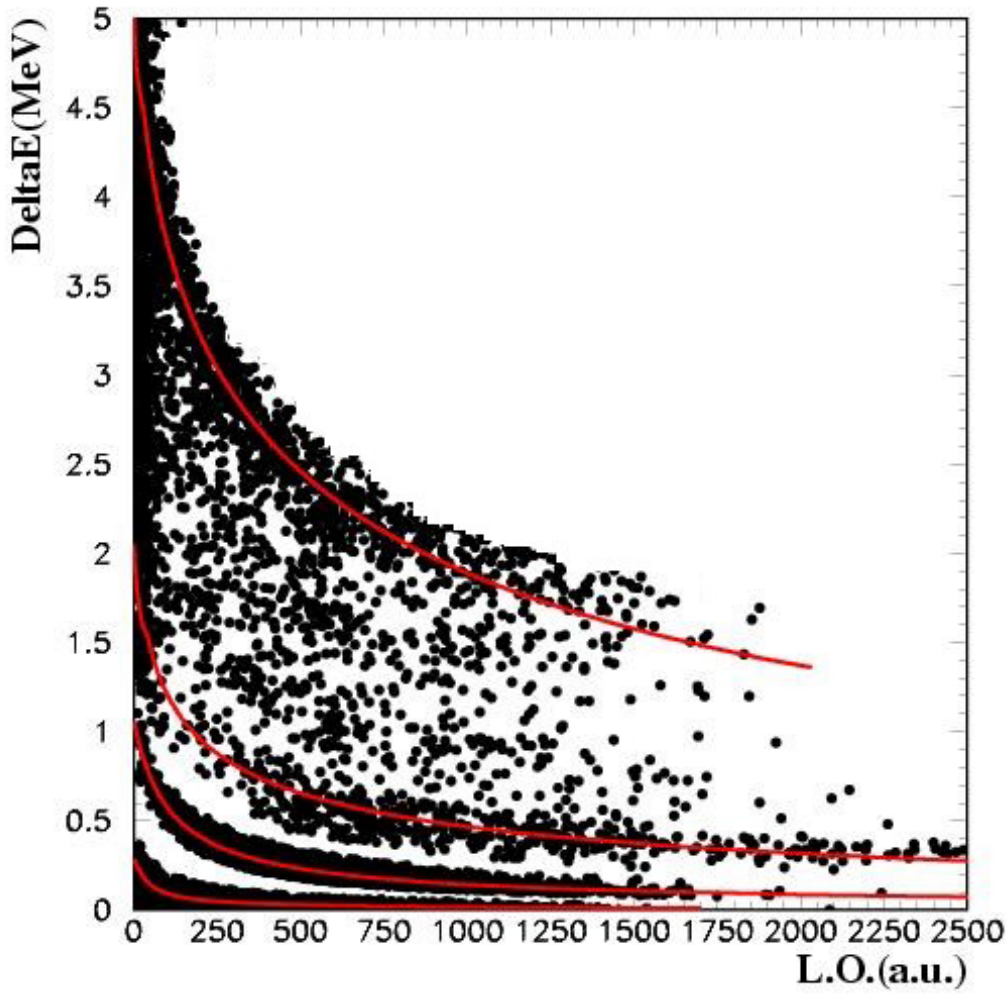

Fig 5.4 : A typical matrix ΔE-E where the ΔE signal coming from the gas chamber is calibrated in MeV and the residual energy signals from the CsI(Tl) crystals is in L.O. channels.

In the following part, we will describe the calibrating procedure of the two couples of PSPPAC and of the 8 BaF_2 crystals.

5.2 The PSPPAC calibration

The set-up used to detect the Evaporation Residues and to select them with respect to the elastic scattered beam and/or fast projectile-like fragments was formed by two couples of Position Sensitive Parallel Plate Avalanche Counter (PSPPAC) positioned symmetrically with respect to the beam. Every couple was made by two PSPPACs one in front of the other and in the middle between them a foil of 25 μm of Upilex was used as absorber for low velocity product, like ER. As already described in the Chapter 2, every PPAC produces 5 signals of time: 4 signals to identify the incident

position of the particle and one from the cathode used for the Time of Flight analysis. All these signals are produced as a difference between a START signal given by the main trigger and the STOP signal given by the detector.

In this case we need to calibrate the Time to Digital Converters (TDCs), by means of a calibrated signal formed by a time calibrator. The pulser signal fed into the Constant Fraction Discriminator which produce the STOP signal for every TDC, is seen as a repetitive structure of peaks equally spaced. The distance and the range are the settings of the time calibrator. In our experiment the Δt was fixed at 20 *ns* and the range to 2 μs. Using a routine similar to that one employed to follow the electronic amplification in the ADC, one can calibrate all the TDCs and control their stability during the experiment. In this way the correct calibration in nanoseconds is obtained.

To perform a good Time of Flight measurement, a precise benchmark to which refer is needed. The main trigger is not reliable because it is formed by different triggers with different reaction time which jitter a lot. A corrected reference point is, therefore, needed: the radiofrequency used to produce our pulsed beam is the opportune signal. So the real ToF spectra, on which one can make the selection of the events, is not simply the calibrated spectra produced by the cathode of the PPAC, but the event by event difference spectrum between the STOP cathode signal and the calibrated radiofrequency.

During the experiment, it is not certain that the relative distance between the incoming pulse beam and the radiofrequency will be always the same. Small changing, on the order of a few *ns*, are absolutely normal but in case of problem on the beam, like question of timing or problem with the transport of the beam, this relative distance can be changed completely. Considering this fact, it is clear that to sum the result from the different experimental runs, if one wants to keep constant the gate applied to recognize the ER, one must check run by run the position of the radiofrequency and correct for all the possible displacements.

The best way to identify in the ToF spectra the peak corresponding to the ER is to plot the spectra corresponding to the forward PSPPAC with that one from the backward PSPPAC. As one can see in Fig 5.5, the peak connected to the ER is strongly suppressed in the backward PSPPAC. Putting a gate on this region on the forward cathode together with the request that no signals are present in the second PSPPAC, one can conclude, event by event, if an ER was detected.

The position information was essentially used as a check of this result, and the same was for the information carrying from the Si-Li detectors. Due to the very low cross section for the GDR events, in fact, a total integration on all the different ER had to be performed. For this reason, all the PSPPAC events with at least one cathode signal from one of the two forward PSPPAC have been considered, in anticoincidence with their respective backward partners.

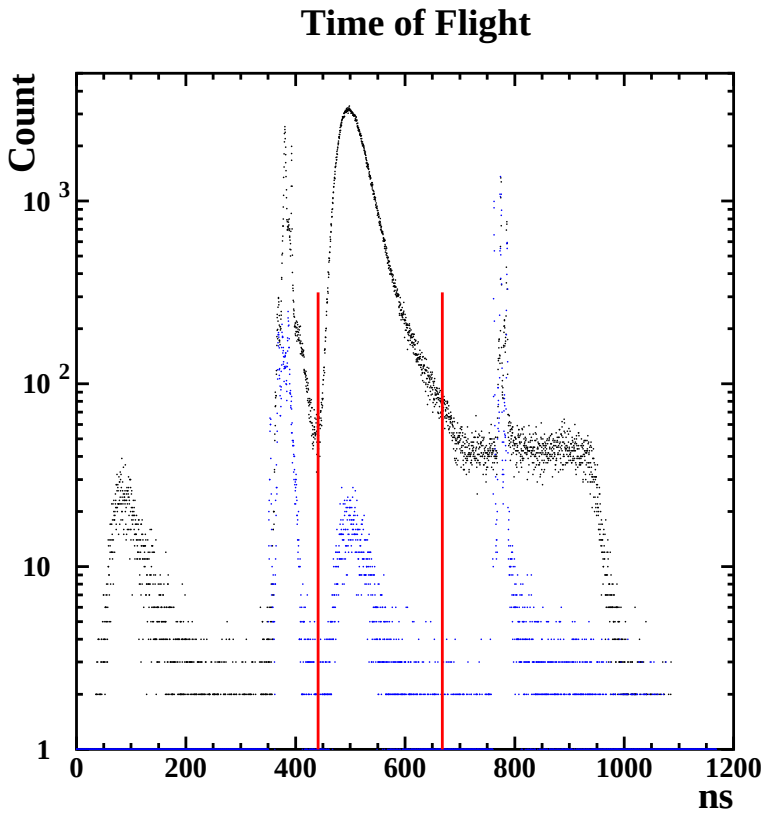

Fig 5.5 : The ToF spectra from a couple of PSPPAC. The black line corresponds to the forward PSPPAC, the blue line to the backward PSPPAC. The red lines show the gate considered.

The anti-coincidence signal of the two couple of PSPPAC was recorded only if in coincidence with GARFIELD or with the OR from the BaF_2 crystals: in this way only LPC-ER or γ-ER coincidences were collected during the whole experiment, together with inclusive from GARFIELD and BaF_2 opportunely reduced. On the contrary, only one run for reaction was performed with the ER trigger in single coincidence in order to have a normalization factor necessary to calculate the particle multiplicity, as shown in the following sections.

5.3 The BaF_2 calibration.

In the case of BaF_2, we have to calibrate a time signal used for a ToF analysis able to discriminate the γ-rays from the neutrons, and two energy signals, characterized by a "fast" and a "slow" integration, from which one can extract the energy of the γ emitted and the dependence on the shape of the signal of the detected particle (fast vs. slow signal).

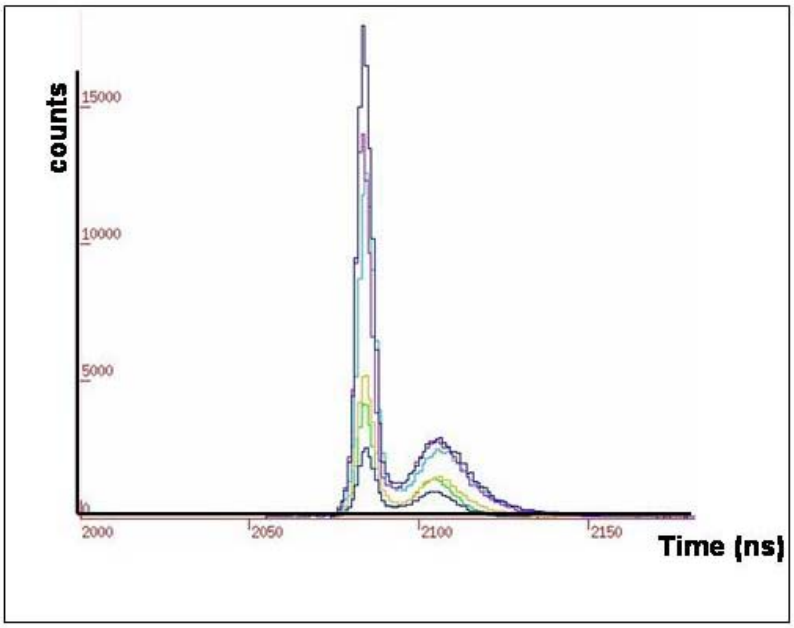

Fig. 5.6 : The ToF spectra from the different BaF2. Every crystal corresponds to a different color in the plot.

The calibration procedure of the time signal is similar to that one just seen for the PSPPAC. The time signal collected by the BaF_2 crystal is proportional to the time distance between the START signal given by the main trigger and the STOP signal given by the detectors. Also in this case the channel by channel calibration of the TDC and the subtraction to the radiofrequency signal are needed. The best way to discriminate the γ emission from the neutron emission is a two-dimensional cut in the ToF versus energy plot. In this case the difference between the γ-rays, which are without mass, and the neutrons is really easy to see, even in the case of fast neutrons. From the two dimensional plot one can check that the separation between neutrons and γ-rays is good for all energies. Considering this cut as reference, one can make directly on the ToF spectra a more simple one-dimensional cut, as one can see in Fig 5.6, which is very easy to implement in the analysis.

After this process, we can select the γ-rays, eliminating the neutrons. To characterize and calibrate the energy the situation is similar to that one studied for the GARFIELD apparatus: we need a γ-signal produced at well known energy. The answer of BaF_2 crystals is linear on the γ-energy, so in principle one calibration point is enough to calibrate the detectors. This point in our experiment was given by an opportune nuclear reaction included only for this purpose. In particular, we have collected the γ-emission produced by ^{12}C with excitation energy of 16.1 *MeV* produced with the reaction

$$^{11}B + {}^{2}D \rightarrow n + {}^{12}C^{*} \qquad E_{lab}\,(^{11}B) = 45\ MeV$$

and using also a gold layer of absorber on the target to moderate the Carbon recoil.

The Carbon nucleus can decay with the emission of one γ-ray of 15.1 *MeV* in the 90% of the cases or through the emission of two following γ-rays, one of 11.7 *MeV* and the other of 4.4 *MeV* (with probability of 2%). The high energy γ-emission of 15.1 *MeV*, energy which is comparable with the energy of the γ of GDR, is a correct point for the calibration. Some of the crystals have been calibrated using a second calibration point at low energy produced by a ^{60}Co radioactive source. The source was positioned close to one crystal, so for geometrical reasons it could not illuminate every crystal. The ^{60}Co nucleus emits two energetic lines, one at 1.173 *MeV* and the second at 1.333 *MeV*, which will be seen as a unique line due to the low resolution of the BaF_2 crystal. To complete the calibration, one should also take into account the Doppler effect, which is present during all the measurement. Every wave emitted by a moving source, like for example ^{12}C in this case or also the recoil nucleus, is affected by a shift in the wavelength due to the relativistic effects. This shift on wavelength is directly connected to a shift in the energy through the relation $E_\gamma = \hbar c/\lambda$.

The Doppler correction can be expressed as

$$E_{corrected} = E \frac{1 - \frac{v_s}{c}\cos\theta}{\sqrt{1 - \frac{v_s^2}{c^2}}} \qquad \textbf{(5.2)}$$

where v_s is the source velocity and c the light velocity. This correction is related to the angular position of the crystal. In our case the BaF_2 was arranged on 4 different angles, so we have 4 different correction factors. A simulation is also needed to take into account all the different interaction mechanisms that a γ-ray will undergo inside the crystal: a response function is then produced, which is dependent on the energy of the incident γ-ray and on the geometry of the detector itself.

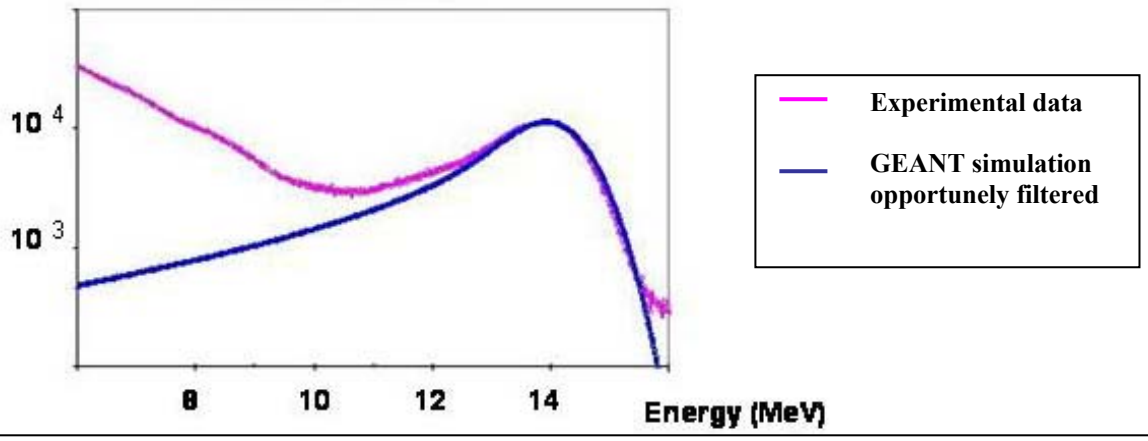

Fig. 5.7 : Matching between the GEANT simulation and the experimental spectra where the simulation is opportunely filtered to take into account the response function of the BaF_2 crystal.

Using the GEANT library, a complete filter of the HECTOR apparatus was made to correct all the simulations in order to be comparable to the experimental spectra, where a deformation is present due to different detection efficiency as a function of the energy of the incident γ-ray. After the comparison with the data obtained from the 15.1 *MeV* γ-rays from the calibration reaction, using the pedestal, i.e. the channel in the experimental spectra which corresponds to zero energy, and also the response to the ^{60}Co γ-rays where this is available, one can calibrate every single BaF_2 with a linear relation.

A final check is made by comparing all calibrated spectra of BaF2. The overall check is particularly necessary when some characteristics of GDR emission, like for example the a_2 coefficient, which is linked to the angular distribution, are needed. This comparison is also important when the integration of all the data is needed to collect more statistics for a more precise analysis, like in the present experiment.

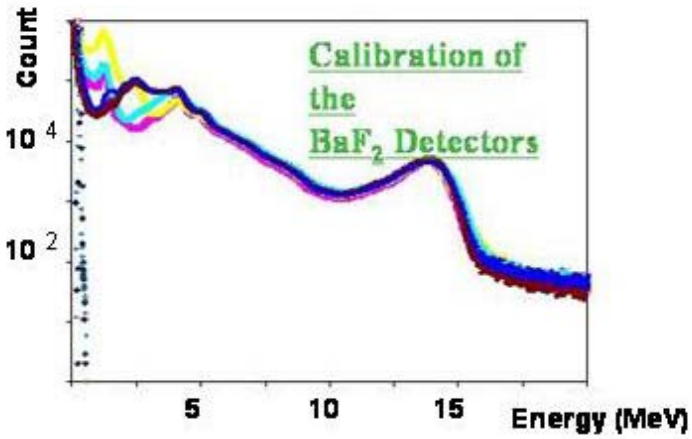

Fig. 5.8 : Overlapping of the calibration of the 8 BaF_2 crystals which form the Hector apparatus.

If the spectra coming from different angles (i.e. different crystals) are not internally compatible, it is clear that the obtained results can not be relevant. In the Fig 5.7, one can see the signal of a single BaF_2 crystal compared with the theoretical calculation opportunely filtered. In Fig 5.8, it is shown the perfect overlapping of the different BaF_2 crystal after the calibration.

5.4 The analysis.

From the raw data, opportunely organized according to the sequences of Segment Controllers, ADC and TDC, we arrive to some data files where all physical parameters are listed. In particular, for the

GARFIELD apparatus we can obtain information on charge (Z), energy (E), angular position θ and φ and drift time inside the gas chamber (t_{drift}) for each reaction product. From the BaF_2 crystal, we obtain the angular position θ and φ, the energy E and the time of flight t_{TOF_b}, while from the PSPPAC the information on the spatial position x and y and the time of flight t_{TOF_p}, which can be integrated by the residual energy E_{res} from the Si-Li detectors placed after the forward PSPPAC at angle $10° < \theta < 12°$ for one and $8° < \theta < 12°$ for the other.

Introducing the opportune calibration factor into the raw data, we can create a so called "partially calibrated" data files, where all the time information is just reported in *ns* and all the energy information in *MeV*. Setting opportunely the time gates on the BaF_2, we can select those events which are only due to γ-ray, disregarding the neutron information which is not useful in this form for the experiment. An opportune analysis of the PSPPAC signal permits to select those events regarding the Evaporation Residues, which are well separated from the faster particles. So a further selection, besides the anti-coincidence hardware trigger is also performed through time of flight recognition.

Setting all these constrains on the data to be processed we prepare different files of data devoted to study the charged particles or the γ-rays, in single, double or triple coincidences.

Starting from the "partially calibrated" files, the set of parameter selected and written for every detected particle in GARFIELD is the following: an increasing number of event, number of telescope of GARFIELD (which can be directly put in relation with the angle of emission of the particle), ΔE signal from the microstrip, residual energy from CsI(Tl) crystal (still expressed in normalized Light Output channels) and a code which identifies if the particles was emitted as single coincidence, double coincidence (it means together with a ER) or in triple coincidence (ER and γ-rays). In case of triple coincidence, it is also specified the BaF_2 crystal which emits the signal and the energy of the detected γ-ray.

The chain of programs written to process the partially calibrated data to arrive to a final calibrated file starts with the Z-identification, performed through a minimization process of the distance of the experimental data in the ΔE-L.O. plane with respect to the theoretical lines calculated for different charges. Knowing the charge of the detected particles, an opportune code can transform the residual energy from arbitrarial unit into *MeV*, inverting numerically Eq. 5.1. Correcting for the energy lost by the particle in the dead layer of GARFIELD and eventually adding the ΔE information from one of the two microstrip when missing, which are calculated through an energy loss code, it is possible to obtain as a final output the total energy of the particle. We have then the set of parameters chosen for GARFIELD to define a well calibrated event. The energy spectra for each kind of detected

particle can be obtained as a first analysis, summing over all available experimental runs the statistics for each individual telescope.

5.5 The definition of the used set of data.

Obviously, the first step of the work of analysis on the calibrated data is to classify the events according to specific criteria. It is obvious that every time we ask for a coincidence event, the collected statistics is diminished because of the composite detection efficiencies. The main problem is, therefore, to find out a good set of data able to highlight the physical aspect requested with the greater statistics possible.

For each reaction we can show, as an example, the spectra of α particles detected at $\theta = 34.7°$ for one sector of GARFIELD, showing the difference between single, double and triple coincidences (Fig. 5.9). The smaller difference between 400 *MeV* Nickel induced reaction and 250 *MeV* Oxygen reaction is due to the fact that in these cases the inclusive triggers were reduced with respect to the exclusive triggers, while this was not the case in the 500 *MeV* Nickel reaction.

The loss in the overall efficiency with the coincident events is in any case evident for the three measurements. Nevertheless, also the shape of the energy distribution is different, especially in the low energy region around the Coulomb barrier. There is no doubt that this is an indication that in the inclusive spectra a strong contribution from different mechanisms is present. On the contrary, the most important consideration is the fact that the shape of the distribution of the triple coincidences appears very similar to that one shown by the events in double coincidences.

This is evident in the examples of Fig. 5.9, for the three reactions. Taking in account this consideration, the choice of selecting the double coincidences as the set of data for the following analysis is safe enough. All results obtained for this kind of events are then checked on the triple coincidences spectra for confirmation.

5.5.1 The φ distribution in GARFIELD.

As already underlined, a characteristic of GARFIELD is that it is divided in 24 sectors for a full coverage of the φ angle. This permits to have nominally 24 sets of spectra, each of them complete

of the 4 θ angles corresponding to the 4 crystals of CsI(Tl), on which the moving source fit technique can be applied.

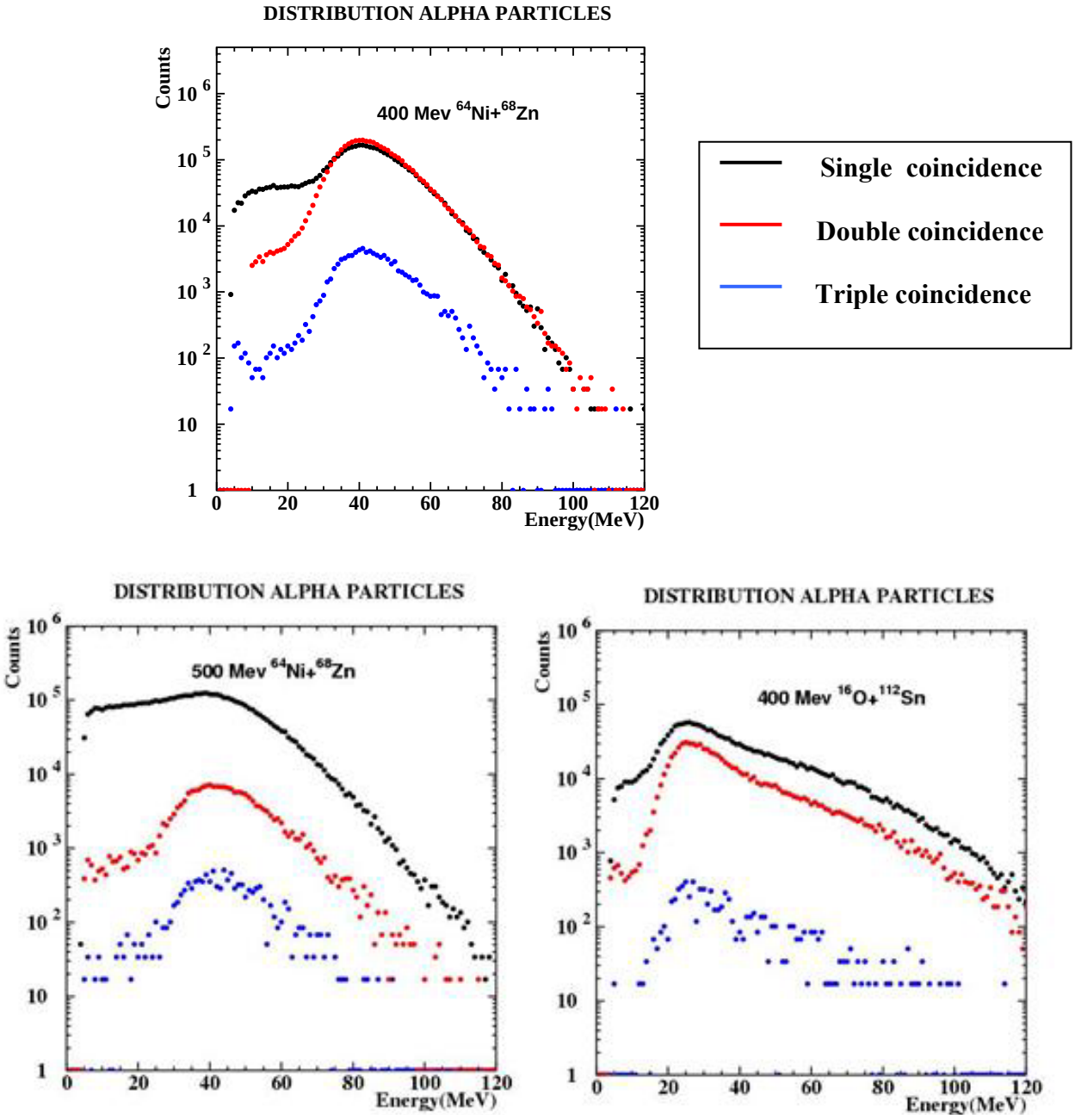

Fig. 5.9 : Energy spectra of α-particles detected at θ = 34.7° for one sector of GARFIELD for the 400 *MeV* and 500 *MeV* ^{68}Ni + ^{64}Zn and 250 *MeV* ^{16}O + ^{116}Sn. The black points represents single coincidences, red points double coincidences and blue points triple coincidences.

Actually even a finest granularity could be obtained (every sector could be divided in two parts and the θ angle could be reconstructed through the drift time), but this is not necessary for the present analysis. Making a complete analysis on the sectors, we have observed in the 500 *MeV* and 400 *MeV* ^{64}Ni + ^{68}Zn reactions a dependence on the φ angle of total number of particles detected. This

dependence is also reflected in the values of the fitting parameters of the moving fit analysis, which is explained in the following paragraph. This in-plane/out-of-plane effect is more evident for α-particles than for protons. In the 250 *MeV* $^{16}O + ^{116}Sn$ reaction the effect is almost zero. This trend is not present when the single spectra are represented, as it is clearly shown in Fig. 5.10.

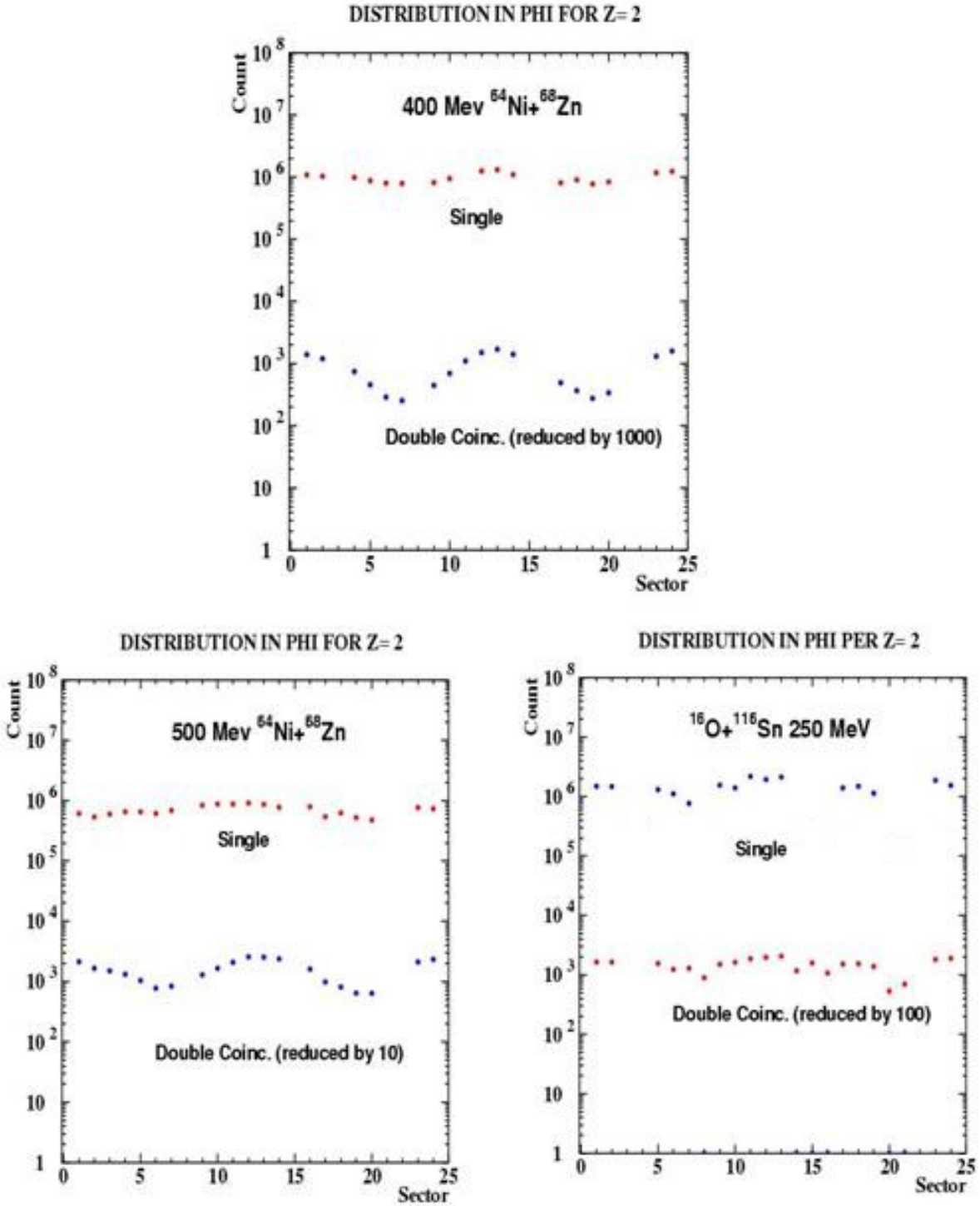

Fig. 5.10 : The total number of particles detected for the different sectors of Garfield in case of single and double coincidence for the reaction $^{64}Ni + ^{68}Zn$ at 500 *MeV* and 400 *MeV* of bombarding energy and $^{16}O + ^{112}Sn$ at 250 *MeV*. The in-plane sectors show a greater number of counts.

A possible explanation of this behaviour can be connected to the selection of the ER because while the Garfield apparatus is able to cover completely the φ angle, the PSPPAC cover only a limited part ($-4° < \varphi < 4°$). Thus, the in-plane selection of the ER can consequently favourite the collection of particles in the in-plane sector of Garfield (sectors with numbers 1, 2, 12, 13, 14, 15, 23 and 24) rather then in the out of plane sector (numbers 6, 7, 8, 18, 19 and 20). The phenomenon can be more evident for α-particles then for protons for the difference in angular momentum coupling. In the case of oxygen reaction, the plot of the total experimental number of protons and α-particles detected sector by sector does not show so clearly the same structure of that one from Nickel induced reaction. In this case the mass entrance channel is obviously completely different. Moreover, with the fixed selected position of the PSPPAC one is able to detect practically all the residues angular distribution for the asymmetric entrance mass channel while only the tail of the angular distribution of the ER is covered for the symmetric reaction, corresponding to the more angulated ER (see Fig. 4.1). This difference in the ER selection might explain the difference in the relation between the total number of counts as a function of the different GARFIELD sectors for the symmetric and asymmetric reaction. Certainly, to clarify this aspect other studies and comparison with filtered simulation codes are needed.

5.5.2 The moving source fit of the LCP data.

One of the most used analysis of the light charged particles data utilized when multiple sources of emission are supposed to be present is a so called “moving source” global fit ([Hil79]). It is based on the fact that the different sources which at relatively low energy can emit light charged particles can be supposed to emit these products following a Maxwellian shape where the maximum of the yield is linked to the velocity of the source and to the Coulomb energy (if the particles are charged products), while the inverse of the slopes is related to the temperature of the emitting source.
Generally moving source fits are used in fusion-fission measurements in order to disentangle between pre and post scission evaporative particles, where three sources are present (Fission Fragment, Fission Fragment and CN), or when, like in out case, a pre-equilibrium emission should be discriminated against the emission from a thermalized source. The important thing to be underlined is that the fit has to be performed over all the angular distribution of the experiment. In fact, in the different angular region the contribution of the emission sources is different, so only a global fit would be able to describe this variation.

In the present experiment the energetic distribution of LCP tagged in coincidence with an Evaporation Residues has to be fit with a superposition of two Maxwellian distributions which are characterized by two different assumed emitting sources: the first distribution is chosen to be linked to a fully thermalized source with a velocity which is the centre of mass velocity of the system, while the second is linked to a probable pre-equilibrium source which can be characterized by a velocity which can vary in between the velocity of the centre of mass and that one of the projectile.
With this approach, we can describe in the centre of mass reference system the number of particles emitted for unity of solid angle and energy from the fully thermalized source (called also evaporative source) with the formula

$$\frac{d^2N_1}{d\Omega dE} = \frac{N_1}{4\pi T_1^2}(E - V_c)e^{\frac{-(E-V_c)}{T_1}}(1 + \alpha_2 P_2(\cos\vartheta)) \qquad \textbf{(5.3)}$$

while the emission from the pre-equilibrium source becomes

$$\frac{d^2N_2}{d\Omega dE} = \frac{N_2}{2(\pi T_2)^{3/2}}\sqrt{(E - V_c)}e^{\frac{-(E-V_c')}{T_2}} \qquad \textbf{(5.4)}$$

where N_1 and N_2 are the total number of particles, respectively, emitted after and before the thermalization process of the compound system, T_1 and T_2 are the temperatures of the two sources, V_c and V'_c are the Coulomb barriers for the two processes, α_2 is an angular distribution parameter (equal to zero for protons), P_2 is the Legendre polynomial and θ is the emission angle in the centre of mass reference system. This expression for each source should be transformed to the laboratory reference system using the relation

$$\frac{d^2N_{lab}}{d\Omega dE_{lab}} = \left(\frac{E_{lab}}{E'}\right)^{\frac{1}{2}}\frac{d^2N'}{d\Omega' dE'} \qquad \textbf{(5.5)}$$

where E_{lab} is the energy in the laboratory frame and E' is the correspondent energy in the centre of mass system of the emitting source and can be expressed as a function of the emitting angle with

$$E' = E_{lab} + \frac{1}{2}mv_s^2 - 2\cos\vartheta\sqrt{\frac{1}{2}mv_s^2 E_{lab}} \qquad \textbf{(5.6)}$$

on which m is the mass of the particle and v_s is the velocity of the source with respect to the lab (i.e. the velocity of the Compound Nucleus in the case of evaporation).
From the Eq. 5.3 and 5.4, one assumes that in the centre of mass system the pre-equilibrium source is simulated by an isotropic emission, while the evaporative source is almost isotropic (there is a small anisotropic contribution from the α_2 parameter for the α-particles and IMF for the coupling of

the angular momentum). Considering the following transformation described by Eq. 5.5 and 5.6, in the laboratory system the evaporative source will be connected by the momentum given by the velocity of the CN, but the pre-equilibrium emission will be much more peaked towards the forward angles due to the much higher velocity of the source. In our analysis, the values of the parameters N, T, V_c and α_2 are derived from the global fit of the experimental data on the different detection angles θ = 74.6°, 60.05°, 46.9° and 34.7°, a range large enough to have relevant results.

In the following Fig. 5.11, Fig. 5.12, Fig. 5.13, Fig. 5.14 and Fig. 5.15 the energy spectra of protons and α-particles are shown, respectively, for the reactions ^{64}Ni + ^{68}Zn at 400 *MeV,* ^{64}Ni + ^{68}Zn at 500 *MeV* and ^{16}O + ^{112}Sn at 250 *MeV* and compared to moving source fit distributions. Tab. 5.1, 5.2 and 5.3 report the parameter values obtained from the fitting procedure for all the available sectors of GARFIELD.

In the case of the symmetric mass entrance reaction channel (Fig. 5.11, Fig. 5.12 and Fig 5.13), the red line, which represents the result of the fit and reproduces quite properly the data, is formed only by the evaporative source. On the contrary, for the reaction ^{16}O + ^{116}Mo at 250 *MeV* (Fig. 5.14 and Fig. 5.15), one can see the contribution of the two components of the fit. In fact, the yellow line is linked to the evaporative source and the black line to the pre-equilibrium source.

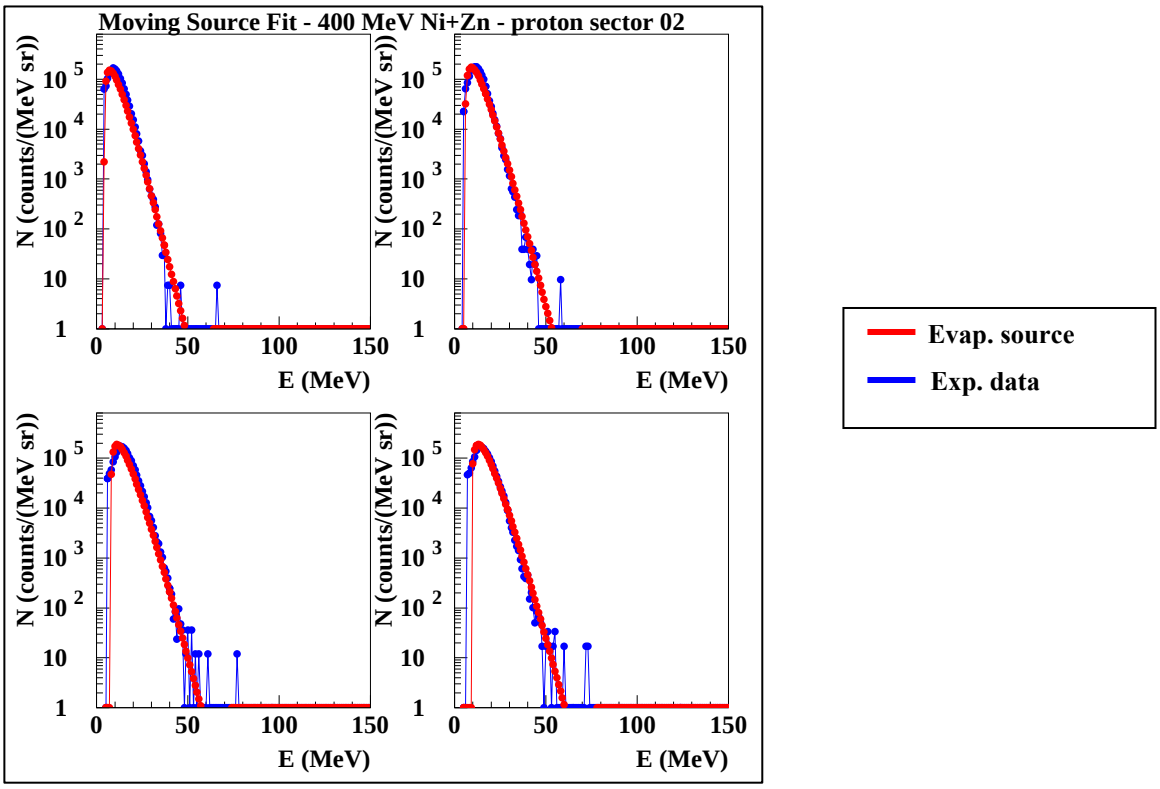

Fig. 5.11: Comparison between the protons spectra for the reaction ^{64}Ni + ^{68}Zn at 400 MeV and the moving source fit (evaporative part).

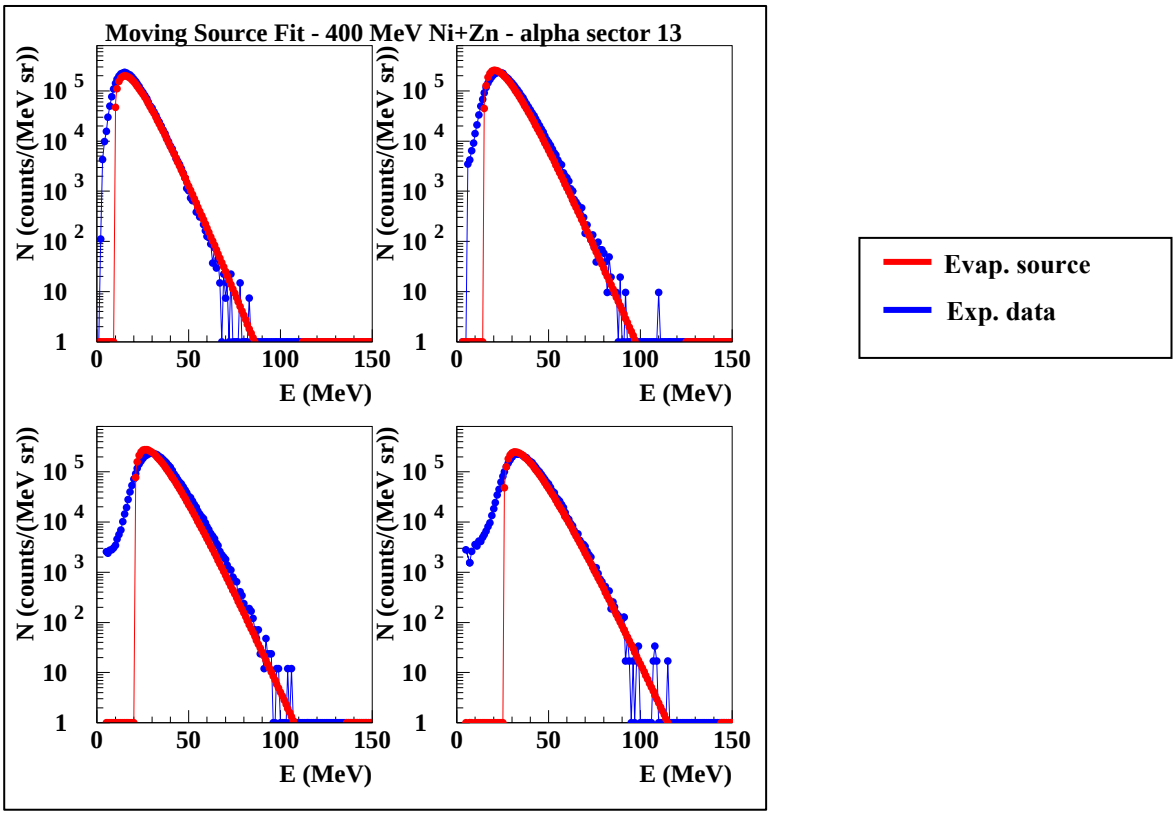

Fig. 5.12: α-energy spectra for the ^{64}Ni + ^{68}Zn at 400 MeV reaction compared with the moving source fit (evaporative part).

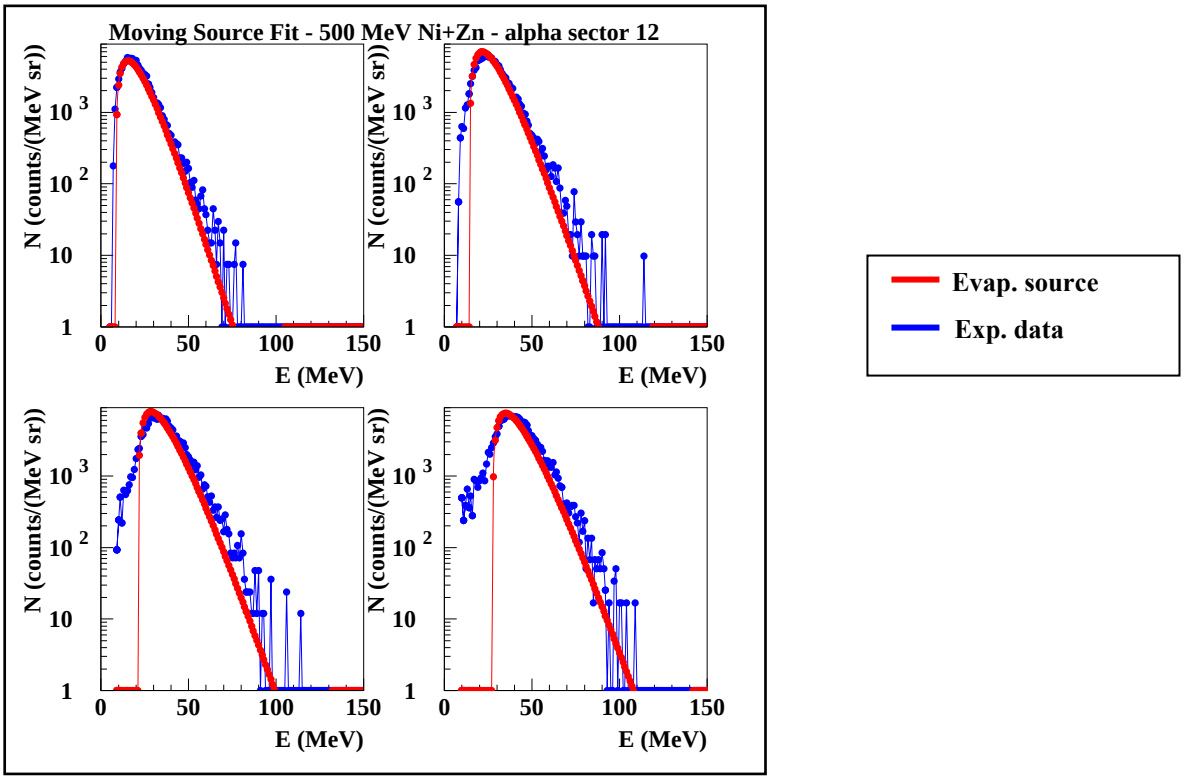

Fig. 5.13: α-particles spectra for ^{64}Ni + ^{68}Zn at 500 MeV reaction compared with the moving source fit (evaporative part).

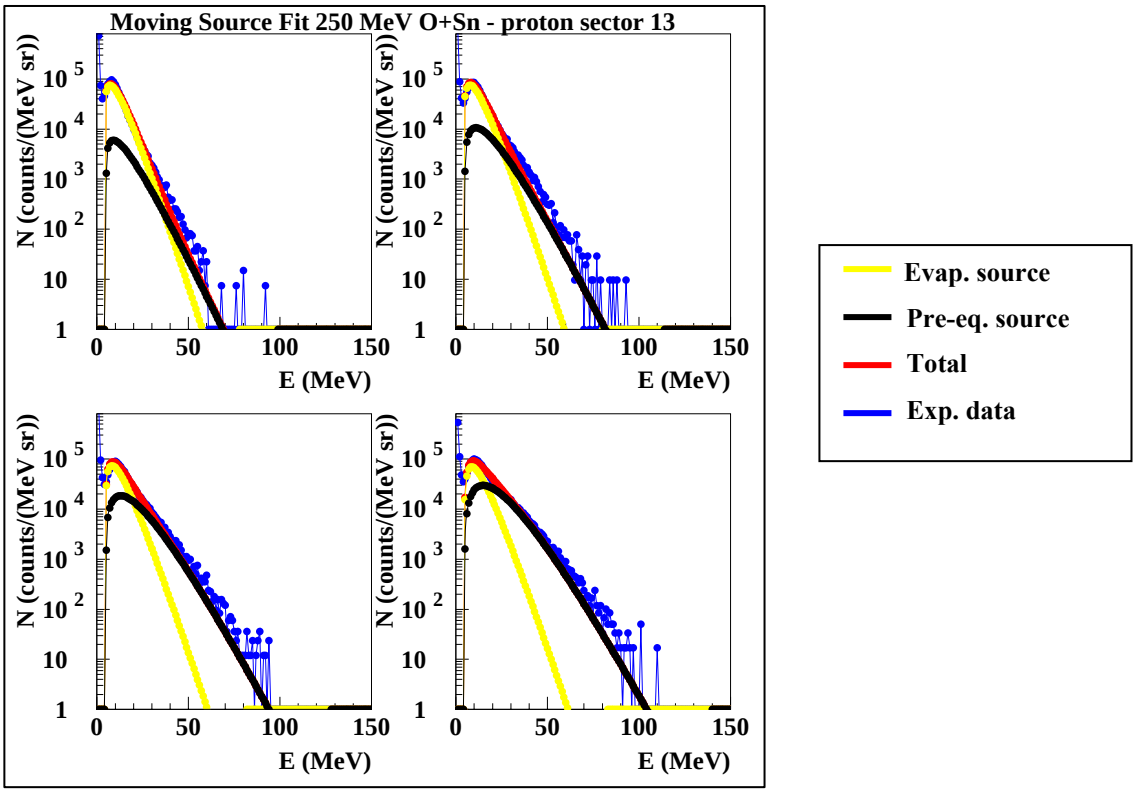

Fig. 5.14: Protons spectra for ^{16}O + ^{116}Mo at 250 MeV reaction compared with the moving source fit (evaporative + pre-equilibrium components).

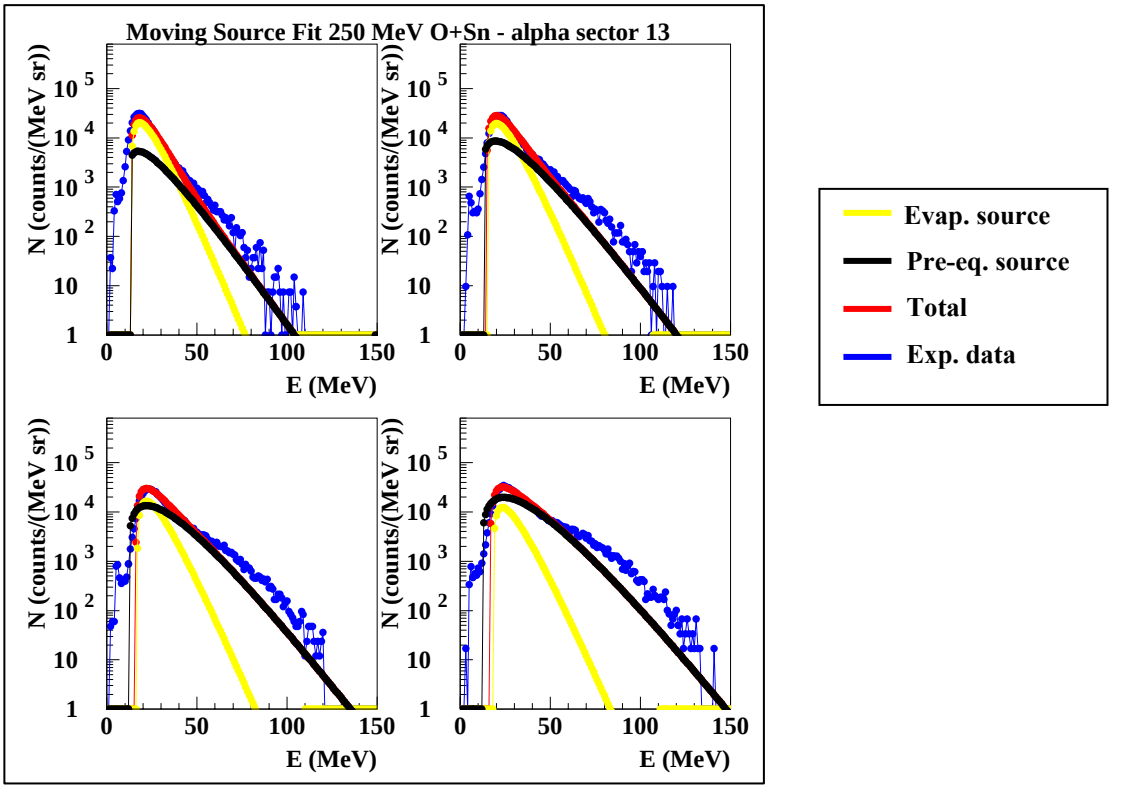

Fig. 5.15: α-particles spectra for ^{16}O + ^{116}Mo at 250 MeV reaction compared with the moving source fit (evaporative + pre-equilibrium components).

^{64}Ni + ^{68}Zn at 400 MeV

PROTONS

Sector	N_1	α2	V_{c1} (MeV)	T_1 (MeV)
1	14034000	0	4.68	2.76
2	12805000	0	5.69	2.58
3	26489000	0	5.67	3.52
4	13659000	0	5.41	2.44
5	10495000	0	5.39	2.25
6	10136000	0	5.40	2.23
7	9437400	0	5.95	2.15
9	13742000	0	5.40	2.87
10	14056000	0	3.59	2.90
12	17620000	0	3.63	3.12
13	16238000	0	3.53	3.05
14	16269000	0	3.09	2.95
15	18897000	0	3.35	3.60
16	5367800	0	3.56	3.01
19	8807900	0	3.25	2.48
20	5697700	0	3.52	2.16
23	15410000	0	3.23	2.82
24	16021000	0	3.54	2.85

ALPHA PARTICLES

Sector	N_1	α2	V_{c1} (MeV)	T_1 (MeV)
1	21634400	-0.39	11.57	4.20
2	19245000	-0.31	11.52	4.14
3	8763400	-0.03	13.68	4.29
4	12237000	-0.17	12.11	3.98
5	8066700	0.18	12.10	3.50
6	5350100	0.42	12.24	3.21
7	5063800	0.70	12.91	3.62
9	7187100	0.07	12.89	3.68
10	9464500	-0.72	12.26	3.74
12	22492000	-0.58	12.30	4.39
13	24703000	-0.62	12.22	4.22
14	23430000	0.06	11.57	4.14
15	11618000	0.03	12.19	4.32
16	6552100	-0.10	12.32	4.15
19	4615400	0.26	12.32	3.31
20	6664000	0.42	12.90	3.36
23	20830000	-0.35	11.60	4.16
24	22850000	-0.63	11.58	4.33

$v_s = v_{cm} = 1.69$ *cm/ns*

Tab. 5.1 : Parameters of the moving source fit analysis for the proton and α-spectra in the reaction ^{64}Ni + ^{68}Zn at 400 MeV.

^{64}Ni + ^{68}Zn at 500 MeV

ALPHA PARTICLES

Sector	N1	α2	Vc1 (MeV)	T1 (MeV)
1	599570	-0.72	12.03	4.74
2	413080	-0.80	12.18	4.17
3	464360	-0.04	12.23	4.11
4	383250	-0.23	12.32	4.11
5	329340	0.26	12.24	3.60
7	284940	0.42	12.42	3.85
9	357000	-0.42	12.17	3.80
10	457480	-0.56	12.09	3.88
12	731000	-0.80	11.51	4.81
13	858690	-0.25	12.13	4.76
14	709780	-0.62	12.03	4.59
15	286640	-0.46	12.28	3.93
16	272910	0.08	12.38	4.31
23	729430	0.02	12.12	4.40
24	690380	-0.46	12.13	4.54

$v_s = v_{cm} = 1.88$ *cm/ns*

Tab. 5.2 : Parameters of the moving source fit analysis for the alpha spectra in the reaction ^{64}Ni + ^{68}Zn at 500 MeV.

$^{16}O + ^{116}Sn$ at 250 MeV

PROTONS

Evaporative fit	Pre-equilibrium fit

Sector	N_1	α2	V_{c1} (MeV)	T_1 (MeV)
1	7839900	0	2.89	4.03
2	7147000	0	2.90	3.64
5	4921900	0	3.42	3.10
6	4645000	0	3.77	3.22
9	7382000	0	3.06	3.81
10	7354100	0	2.95	3.73
11	8831100	0	3.16	3.71
12	8569100	0	3.02	3.99
13	7960100	0	3.16	3.54
17	6102600	0	3.31	3.15
18	6780800	0	3.27	3.09
23	8202900	0	3.10	3.69
24	7318400	0	3.03	3.44

Sector	N_2	V_{c2} (MeV)	T_2 (MeV)	v_s (cm/ns)
1	1564500	4.99	4.89	4.53
2	1850300	4.98	5.07	3.77
5	2499200	3.59	4.22	3.12
6	3140800	1.92	4.76	3.29
9	2310600	4.84	5.00	3.23
10	2491500	4.87	5.17	2.92
11	2205000	4.98	5.00	4.43
12	2143700	4.96	5.27	3.82
13	2279900	4.89	5.00	3.97
17	1579900	4.83	3.79	2.80
18	2172500	4.95	3.60	3.79
23	1878700	3.71	4.19	4.72
24	2306600	4.81	4.93	3.40

v_{cm}= 0.66 *cm/ns*

Tab. 5.3 : Parameters of the moving source fit for the proton and α-spectra in the reaction $^{16}O + ^{116}Sn$ at 250 MeV.

$^{16}O + ^{116}Sn$ at 250 MeV

ALPHA PARTICLES

Evaporative fit	Pre-equilibrium fit

Sector	N_1	α2	V_{c1} (MeV)	T_1 (MeV)
1	1485800	-0.8	12.30	4.42
2	1475200	-0.8	12.30	3.93
5	1304100	-0.8	12.30	4.16
6	1110000	-0.8	12.40	4.5
7	766660	-0.8	14.00	3.50
9	1552000	-0.8	12.30	4.5
10	1392500	-0.8	12.31	4.5
11	2172000	-0.8	12.30	4.5
12	1941300	-0.8	12.30	4.5
13	2138900	-0.8	12.30	4.5
17	1392900	-0.8	12.40	4.5
18	1488000	-0.8	12.30	4.30
19	1136200	-0.8	12.30	4.5
23	1865200	-0.8	12.30	4.5
24	1539300	-0.8	12.30	4.07

Sector	N_2	V_{c2} (MeV)	T_2 (MeV)	v_s (cm/ns)
1	1862000	12.06	7.74	1.70
2	1892800	11.41	7.65	1.83
5	1879200	12.73	6.70	1.70
6	1753900	11.01	6.74	1.93
7	1931600	12.66	6.50	2.40
9	1612600	12.71	6.84	1.98
10	2026500	11.88	6.94	1.73
11	1828400	12.34	6.93	2.39
12	2121500	12.69	7.68	1.95
13	2195200	11.63	7.49	2.10
17	1640100	12.81	6.95	1.70
18	1807200	11.47	6.56	2.24
19	1685900	12.63	6.66	1.73
23	1965200	10.84	7.15	2.03
24	2279700	12.42	7.63	1.63

v_{cm}= 0.66 *cm/ns*

Tab. 5.4 : Parameter of the moving source fit analysis for the α-particles in the reaction $^{16}O + ^{116}Sn$ at 250 MeV.

From the spectra shown in Fig. 5.11 and 5.12, it is evident that the lower bombarding energy is completely described by the emission from a thermalized source. The same is evident for the 500 MeV α-particles spectra, even if in this case a very small deviation can be seen on the tail of the distribution and will be discussed more in detail in the following section.

For this reaction, due to some cuts in the protons spectra, the resulted values of temperature are too low. This can be due to an artificial problem linked to un-homogeneous experimental cuts in the high energy tail of the proton distributions. We decide not to consider for the moment these values, which are not determining in the analysis, as explained in the following. Further cross checks are still in progress. In the case of 250 *MeV* $^{16}O + ^{116}Sn$ reaction there is an extra bump at high energy (60-70 *MeV*) in the α-particles spectra which is not well described by the pre-equilibrium source assumed. This can be clearly seen in Fig. 5.15. The possible origin of this bump will also be discussed in the following section.

The obtained results for the fit parameters from the moving source fit technique are to be considered within the right framework. About the meaning of temperature when dealing with a nucleus and the different procedure to extract it, a detailed discussion was reported in Chapter 1.2. As was told previously, the inverse of the slope of the energy distribution is linked to an "average" temperature parameter. In fact, an experimental spectrum is the ensemble of particles emitted during a large cascade and, therefore, the final results will describe an average behaviour and not an absolute value. From the previous tables, it seems to be present a φ angle dependence of the evaporative temperature of the source in the symmetric mass entrance channel. This behaviour is similar to that one just observed in Paragraph 5.5.2 for the total number of particles detected as a function of the GARFIELD sectors. More accurate studies are needed to discriminate if this evaporative source temperature dependence on the φ angle, reflected by the moving source fit in slightly different values of the temperature parameters for different sectors of GARFIELD, is artificially introduced by the geometric selection of the Evaporation Residues performed by the PSPPAC (see Paragraph 5.5.2) or if it has a deeper physical meaning. Certainly, even the fit can introduce some small fluctuations in the parameter values, but the variation observed seems to be out of the expected fluctuations.

All these aspects should be taken into account in the evaluation of the reliability of the values of the parameters. The average of the values of the parameters for the in-plane sectors of GARFIELD (sector numbers 1, 2, 12, 13, 14, 23 and 25) are listed in Tab. 5.5 for the Nickel induced reactions. In the case of Oxygen induced reaction, there is not a clear signature of a φ dependence of the fitting parameters. Thus, in the Tab. 5.6 the values of the fitting parameters are averaged on all the available sectors. The errors considered are always the maximum dispersion on the average value.

This is a large estimation of the error which gives us a quite good confidential range in the more important physical variables, as the temperature and the Coulomb barrier, while becomes a no-sense estimation in the case of the α_2 parameter for the ^{64}Ni + ^{68}Zn at 400 *MeV* and 500 *MeV*.

^{64}Ni + ^{68}Zn at 400 MeV and 500 MeV

	PROTON				ALPHA			
	N_1	α_2	V_{c_1}(MeV)	T_1(MeV)	N_1	α_2	V_{c_1}	T_1
Ni 400 *MeV*	**(15±3)x10^6**	**0**	**3.97±1.3**	**2.91±0.58**	**(22±3)x10^6**	**-0.40±0.39**	**11.77±0.39**	**4.23±0.13**
NI 500 *MeV*	**nd**	**nd**	**nd**	**nd**	**(72±13)x10^4**	**-0.47±0.41**	**11.89±0.31**	**4.64±0.2**

Tab. 5.5 : Averaged values over the in-plane sectors (numbers 1, 2, 12, 13, 14, 23 and 24) of the fitted parameters from the moving source fit in the reaction ^{64}Ni + ^{68}Zn at 400 *MeV* and 500 *MeV*.

^{16}O + ^{116}Sn at 250 MeV

	Evaporative source				Pre-eq. source			
	N_1	α_2	V_{c_1}	T_1	N_2	V_{c_2}	T_2	v_s
Proton	**(7±2)x10^6**	**-0.20±0.01**	**3.16±0.44**	**3.55±0.47**	**(22±7)x10^5**	**4.49±0.7**	**4.68±0.84**	**3.68±0.87**
Alpha	**(15±5)x10^5**	**-0.80±0.01**	**12.43±0.85**	**4.33±0.5**	**(19±3)x10^5**	**12.09±0.99**	**7.08±0.62**	**1.94±0.39**

Tab. 5.6 : Averaged values over all available sectors of the parameters of the moving source fit in the reaction ^{16}O + ^{116}Sn at 250 *MeV*.

The most easy parameter to be controlled is the source velocity. The evaporative source velocity is fixed at centre of mass velocity of the CN, while the pre-equilibrium source velocity is usually around the middle of the distance between the centre of mass and the projectile velocity. If the CN and beam velocities are too much close, it can happen that the moving fit technique is not able to disentangle the two maxwellian distributions. In our case, in the asymmetric mass entrance channel the velocities are respectively 0.66 *cm/ns* and 5.49 *cm/ns* for the centre of mass and beam velocity for the ^{16}O + ^{112}Sn at 250 *MeV* reaction, 1.88 *cm/ns* and 3.89 *cm/ns* for the ^{64}Ni + ^{68}Zn at 500 *MeV* and 1.69 *cm/ns* and 3.48 *cm/ns* for the ^{64}Ni + ^{68}Zn at 400 *MeV* reaction. No problems, therefore, exist in our case.

Nevertheless, the main goal of the moving source fit technique is the separation of pre-equilibrium emission from the full thermalized emission that we will discuss in the following paragraph.

5.5.3 Consideration on evaporation multiplicities and pre-equilibrium emission.

The moving source fit technique can provide us information useful for a proper calculation of the multiplicity of emitted particles. In fact, the values of the parameters N_1 and N_2 are the total number of particles obtained by the integration of the angular and energies distributions, for the evaporative and the pre-equilibrium source respectively. Normalizing this numbers on the total number of Evaporation Residues, one can obtain the multiplicity values.

The total number of ER is the sum of the number of ER which has emitted at least one particle in the GARFIELD apparatus or at least one γ-ray in the HECTOR apparatus plus all the ER single events. Generally we do not have really single ER events, but events in which the coincident emitted product has not been detected by the experimental apparatus. In our case these products are neutrons and all charged particles or γ-rays emitted in angular regions not covered by our set-up or in the dead zones of the detectors themselves. The first types of ER are recorded in the experimental data and so they can be easily counted, while the second type, i.e. the single trigger from the PSPPAC, was registered one time for each reaction in order to have a normalization factor between the double coincidence PSPPAC-GARFIELD and single PSPPAC.

The number of N_1 and N_2 can be considered the correct integration over the angular distribution because they are derived from a fit to the experimental data, based on assumed distributions. Therefore the result for multiplicities are shown in Tab. 5.7, using N_1 and N_2 from the moving fit analysis normalized to the total number of ER. Obviously, the values provided for the symmetric entrance mass channels are evaporative multiplicities while in the Oxygen induced reaction we can distinguish between evaporative and pre-equilibrium multiplicities. These lat are needed to estimate the energy lost by the system before the complete thermalization.

	Ni 400 MeV	**Ni 500 MeV**	**O 250 MeV**		
			M_{tot}	**$M_{ev.}$**	**$M_{pre\text{-}eq.}$**
Proton	0.54 ± 0.02	Not available	1.08 ± 0.02	0.83 ± 0.01	0.25 ± 0.01
Alpha	0.78 ± 0.03	0.60 ± 0.03	0.39 ± 0.02	0.17 ± 0.01	0.22 ± 0.01
	E/A= 6.25 MeV/u	**E/A = 7.81 MeV/u**	**E/A = 15.63 MeV/u**		

Tab. 5.7 : Evaporative multiplicities for the 400 MeV and 500 MeV ^{64}Ni + ^{68}Zn reactions and evaporative plus pre-equilibrium multiplicities for ^{16}O + ^{116}Sn at 250 MeV.

From the results obtained in the asymmetric reaction and from the comparison to the results of several measurements performed and collected in the work of [Cab03], we can conclude that the amount of pre-equilibrium emission in our system is compatible with the literature and smaller then the Kelly result as far as we consider the multiplicities of charged particles. This is well shown by Fig. 5.16.

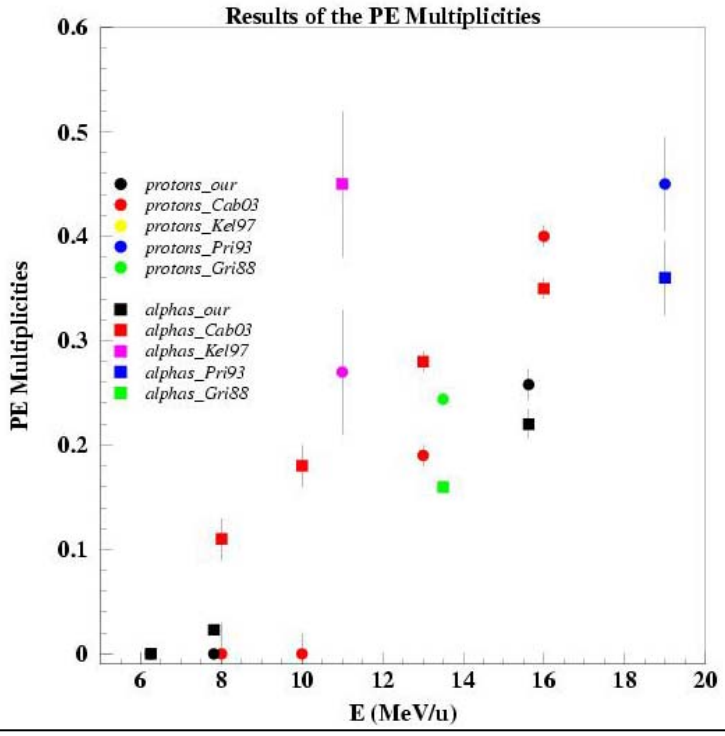

Fig. 5.16: Pre-equilibrium multiplicity for different reaction from [Cab03] together with the results of this work (in black).

The missing information for the multiplicity of neutrons emitted before the complete thermalization of the CN can be estimated using the comparison with the available experimental data found in literature (Tab.5.8).

E/A (MeV/u)	$Mp_{pre\text{-}eq.}$	$M\alpha_{pre\text{-}eq.}$	$Mn_{pre\text{-}eq.}$
8	0	0.11 ± 0.02	0.23 ± 0.15
10	0	0.18 ± 0.02	0.32 ± 0.19
13	0.19 ± 0.03	0.28 ± 0.01	0.58 ± 0.23
16	0.40 ± 0.03	0.35 ± 0.01	0.98 ± 0.25

REFERENCE:
[Hol83]
[Hin92]
[Lee92]
[Awe81]
[Pri93]

Tab. 5.8 : Multiplicity values of the pre-equilibrium emission as a function of the bombarding energy collected by [Cab03] from the available literature.

Starting from these values, we can estimate the energy lost from pre-equilibrium emission multiplying the average pre-equilibrium multiplicity for protons, alpha particles and neutrons for the average energy taken away from the each particle, which can be expressed as a sum of the

binding energy of the particle and the average kinetic energy. The first approximation of the energy lost due to pre-equilibrium in the $^{16}O + ^{112}Sn$ at 250 *MeV* reaction is shown in Tab. 5.9.

$^{16}O + ^{116}Sn$ at 250 MeV

	Average kinetic energy (MeV)	Binding energy (MeV)	Pre-eq. Multiplicity	Energy lost (MeV)
α	30.0 ± 3.7	-0.5	0.22 ± 0.02	6.5 ± 1.0
p	18.2 ± 3.3	6.0	0.25 ± 0.02	6.0 ± 0.9
n	10.5 ± 1.5	10.8	0.95 ± 0.25	20.2 ± 6.1
				TOT. (32.7 ± 6.2) MeV

Tab. 5.9 : Estimation of the energy lost by pre-equilibrium emission in the $^{16}O + ^{112}Sn$ at 250 *MeV* reaction.

If we go back now to the consideration of the α-spectra shown in Fig. 5.15 for the Oxygen induced reaction, we must underline the small contribution of an extra-yield at relatively high energy (around 60 *MeV* - 70 *MeV*) which is not reproduced by the pre-equilibrium source. A reasonable explanation of this "bump" is the break-up of the Oxygen projectile into a Carbon and α-particle, with the α-particle detected by GARFIELD and the Carbon which fuses with the target to create a CN. The break-up of the projectile occurs when the relative kinetic energy and the relative distance between the two splitting component of the projectile (P_1 and P_2) exceed, respectively, their potential barrier height and barrier radius. In our case, the favourite channel of break-up from the energetic point of view is the separation of the projectile into alpha particle and carbon, as one can see from Tab. 5.10 where the binding energies for different break-up reactions are listed.

		Binding energy (MeV)
^{16}O	$d + ^{14}N$	20.7
	$^{3}He + ^{12}C$	22.8
	$\alpha + ^{12}C$	7.2
	$^{6}Li + ^{10}B$	30.8

Tab. 5.10 : Binding energies for the different break-up reaction starting from the ^{16}O

Some recent publication shows the relevance of the reaction of break-up of the projectile when very asymmetric mass entrance channels are used. In fact, considering the reactions ^{6}Li, $^{7}Li + ^{209}Bi$ at different energies ([Das02], [Gom04]), the complete-fusion cross section was found to be lower

than that one predicted by fusion models by 35% and 25% for ^{6}Li and ^{7}Li respectively. To estimate an upper limit of the contribution of this phenomenon in our experiment, one can try to reproduce the experimental data relative to α-particles assuming a third emission source. We take for simplicity still a maxwellian shape as a first approximation, characterized by values of velocity, Coulomb barrier and Temperature the closest possible to a simulated break-up mechanism. The Fig. 5.17 represents a first attempt in this direction. We fixed the parameters of the third simulated source, linked to the break-up of the Oxygen, in order to have values not to far from a physical meaning: the velocity of the source is fixed at 5.49 *cm/ns*, i.e. the velocity of the beam, the temperature is fixed at T = 8.0 *MeV,* which is a little higher than the temperature associated to the used pre-equilibrium source, and the potential barrier is calculated as the Coulomb interaction between an α particle touching a Carbon fragment. This value for the barrier can be improved considering also the nuclear potential interacting between α, C and the ^{112}Sn target, but these more refined calculations to estimate also this contribution are still in progress.

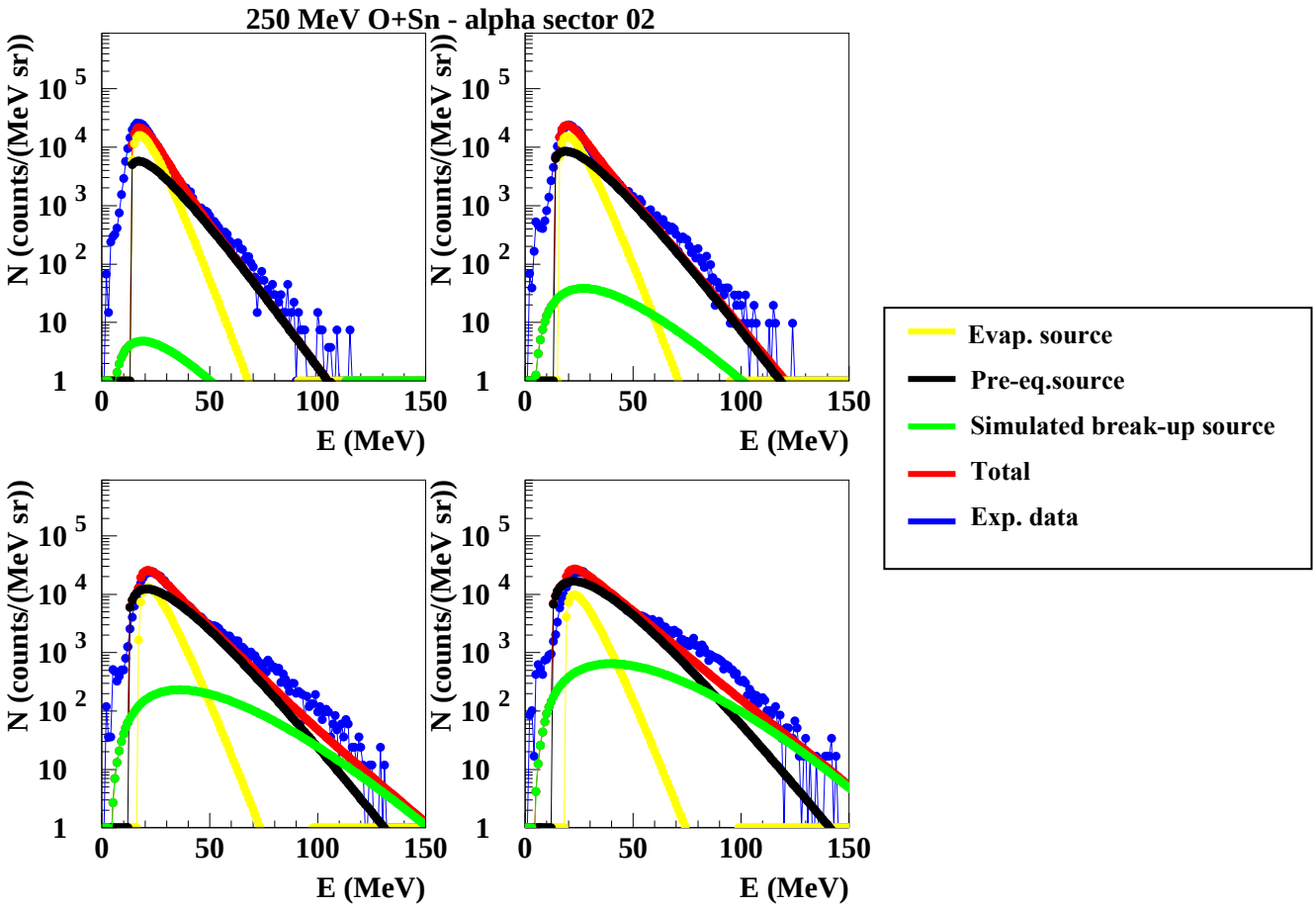

Fig. 5.17: Moving source fit analysis using the evaporative and pre-equilibrium components on alpha spectra from ^{16}O + ^{116}Mo at 250 MeV plus the simulated break-up source.

The yield used is $N = 0.1\ (N_1 + N_2)$, i.e. a 10% of the total counts. Considering a binding energy of 7.2 *MeV* from Tab. 5.9, an average kinetic energy of 45.7 *MeV* coming from the simulated spectrum, the contribution of this third simulated source is only 2.1 *MeV*. In this first attempt the emission of particle from the break-up source is considered isotropic in the centre of mass system of the source. The really high velocity (5.49 *cm/ns*) compared to the centre of mass velocity of the CN (0.66 *cm/ns*) peaks the emission in the laboratory system. A proper description of possible angular dependence of the break-up emission is still in progress even if we think that the final number of percentage of this break-up mechanism followed by incomplete fusion will not change dramatically. A second consideration was left in our previous discussion with respect to the α-spectra from 500 *MeV* ^{64}Ni + ^{68}Zn reaction. If one compares the spectrum for the lower incident energy (Fig. 5.12) where all the cross section is easily reproduced by the evaporative fit, it can be seen that in Fig. 5.13 a very small contribution of the α-yield is not completely described by the evaporative fit.

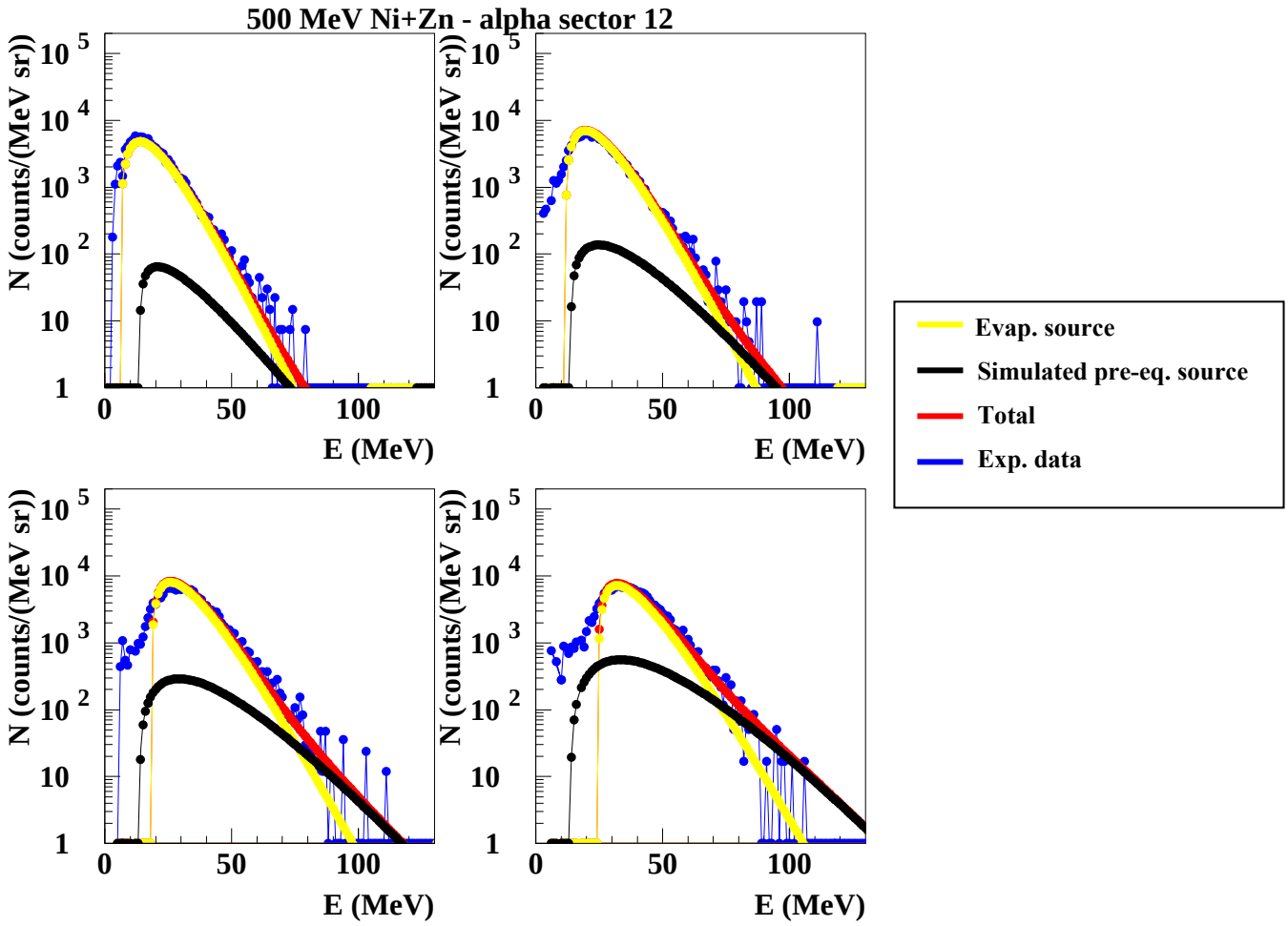

Fig. 5.18: Alpha particles spectra of ^{64}Ni + ^{68}Sn at 500 *MeV* using the evaporative source from the moving fit analysis (yellow line) adding a simulated pre-equilibrium source (black line).

The contribution of the yield not well fitted is so small that the moving source fit procedure did not manage to recognize a second emission source. Nevertheless, we can simulate a pre-equilibrium source also in the ^{64}Ni + ^{68}Zn at 500 *MeV* calculating a maxwellian function where reasonable values are inserted as input parameters with a small interval of variation and leaving the parameter N_2 free to vary to better describe the extra yield.

The Fig. 5.18 shows the result of our simulation using as input parameter for the pre-equilibrium maxwellian source a velocity of 3.0 *cm/ns* (approximately half between v_{cm}= 1.88 *cs/ns* and v_{beam}= 3.89 *cm/ns*), a temperature of 7.68 *MeV* similar to that one produced by the moving source fit in the Oxygen case. The resulting ratio of the yields is $N_{pre\text{-}eq.}/N_{evap.}$ = 0.1 (10%). This can be considered the higher limit of possible pre-equilibrium contribution for α-particles. From the systematic measurement collected by [Cab03] reported in Tab. 5.8, we can evaluate the pre-equilibrium multiplicity for neutrons (0.23 ± 0.15 appears to be reasonable) and have again the confirmation that the proton contribution to the pre-equilibrium at this bombarding energy is negligible.

^{64}Ni + ^{68}Zn at 500 MeV

	Average kinetic energy (MeV)	**Binding energy (MeV)**	**Pre-eq. Multiplicity**	**Energy lost (MeV)**
α	38.6 ± 3.0	-0.5	0.038 ± 0.002	1.40 ± 0.10
n	10.5 ± 1.5	10.8	0.23 ± 0.15	4.90 ± 3.20
				TOT. 6.3 ± 3.2

Tab. 5.11 : Calculated energy lost from pre-equilibrium α-particles multiplicity in the reaction ^{64}Ni + ^{68}Zn at 500 MeV. Neutrons multiplicity is derived from the systematic of [Cab03].

As one can see from Tab. 5.11, the upper limit for the energy lost by pre-equilibrium emission in the ^{64}Ni + ^{68}Zn at 500 *MeV* reaction is (6.3 ± 3.2) *MeV*, a percentage of (3.1 ± 1.6)% with respect to the total excitation energy of 203 *MeV*.

As a final conclusion, from the moving fit source technique, supported also by the comparison with other experimental data, we can conclude that the pre-equilibrium contribution in the ^{64}Ni + ^{68}Zn at 400 *MeV* reaction is zero, in the ^{64}Ni + ^{68}Zn at 500 *MeV* reaction is minor or equal to (6.3 ± 3.2) *MeV* , a so small contribution that can be considered negligible, and equal to (34.8 ± 6.2) for the ^{16}O + ^{116}Sn at 250 *MeV* reaction obtained summing up the 32.7 *MeV* due to pre-equilibrium with the 2.1 *MeV* from the break-up mechanism. The comparison with the other experimental data is satisfactory, as one can see from Tab. 5.12.

Bombarding energy (MeV)	E*	Energy loss due to PE (%)	Ref.
6.25	**151**	**0**	**Our**
7.81	**203**	**≤ 3.1**	**Our**
11.1	174	21.4	[Kel97]
13.0	197	12.7	[Cab03]
13.0	201	13.9	[Cab03]
15.6	**206**	**16.9 ±3.0**	**Our**
16.0	251	15.9	[Cab03]
16.0	201	18.5	[Cab03]

Tab. 5.12 : Comparison of the percentage of E* lost due to pre-equilibrium emission between our studied reactions and other different measurements.

5.5.4 Preliminary comparison with statistical models.

The energy distribution of LCP can also be compared with the results of statistical models, like PACE4 or CACARIZO, where a thermalized source is supposed to decay and all the cascade has been taken into account. It is, however, important to underline that at high excitation energies the emission yields of different particles are not well reproduced by existing models, because they are not complete in the description of all open channels. Different yields mean different emission probability along the cascade and this is reflected on the emission temperatures which are derived.

The calculation for the light charged particles spectra shown in the following picture were performed with the Monte-Carlo code PACE4 (Projection Angular-momentum Coupled Evaporation), a modified version of JULIAN Monte-Carlo code coupling angular momentum, which was developed by M. Hillman, Y. Eyal (code JULIAN), A. Gavron (code PACE) and O. Tarasov (transfer of PACE code to MS Windows). In Tab. 5.13 the most important input parameter used to perform the simulation are listed.

In these simulation codes, the excitation energy of the emitting source can be approximately considered directly proportional to the T^2 through the level density parameter a, defined as $a=A/K$ where A is the mass of the emitting source and K is a parameter which is normally equal to 8 at low energy. The K value has a dependence with the temperature and can reach even high values up to 14 in certain cases [Gon90].

THE MAIN INPUTS OF THE PACE4 CODE	
NCASC = 100000	Number of events considered in the simulation
INPUT = 1	Mass of the projectile and target given as input
BARFAC = 0	A. J. Sierk modified rotating liquid drop barrier
FACLA	Level density parameter varied to get the best fit with each different reaction
IDIST = 1	In the output, the detailed angular and energy distribution of ER and LCP was obtained
MDIR = 0	CN is initially at M=0 states and the z-axes is the recoil axes
NOSHL = 1	Updated Audi and Wapstra mass table was used. Classical transmission probability was used for a one-dimensional barrier.
L = 2 ħ	Diffuseness value (default). The fusion cross section was taken from Bass model.

Tab. 5.13 : List of the selected values for the main input of the PACE4 simulations used for the comparison with the experimental data.

Fig. 5.19 shows the alpha particles spectra from the four detection angles of GARFIELD in the centre of mass system confronted with a PACE4 simulation for three studied reaction. The three simulation are calculated with K=14.6 for the ^{64}Ni + ^{68}Zn at 500 *MeV* and ^{16}O + ^{116}Sn at 250 *MeV* and with K=13 for ^{64}Ni + ^{68}Zn at 400 *MeV*, and the standard input parameters for the code reported in Tab. 5.13. Fig. 5.20 show the protons spectra for the ^{64}Ni + ^{68}Zn at 400 *MeV* and ^{16}O + ^{116}Sn at 250 *MeV* reaction fitted with a value of the density of level parameter K equal to 11 for the symmetric mass entrance channel and to 12 for the asymmetric one.

Considering a complete fusion between the projectile and the target and subtracting the rotational energy of the CN that is not available to heat the nucleus, one can easily obtain a kinetic temperature (see Chapter 1.2.2) for every selected value of the parameter K. It is clear that the present comparison is not complete. A full study of the statistical code parameters is still in progress. The results shown are used simply as a first comparison with the moving source fit analysis. The first results show a good agreement between the information coming from the moving source fit analysis and from the statistical simulation code in the centre of mass system. In fact, it is completely confirmed the evaporative nature of the emission from the symmetric mass entrance reaction channel ^{64}Ni + ^{68}Zn at 500 *MeV* and 400 *MeV*, while for the asymmetric entrance channel it is obviously confirmed the relevant extra-yield due to pre-equilibrium emission. Moreover, also the temperatures extracted from these two approaches are compatible, as reported for the moving source fit analysis in Tab. 5.5 and Tab.5.6 and for the statistical code in Tab. 5.14.

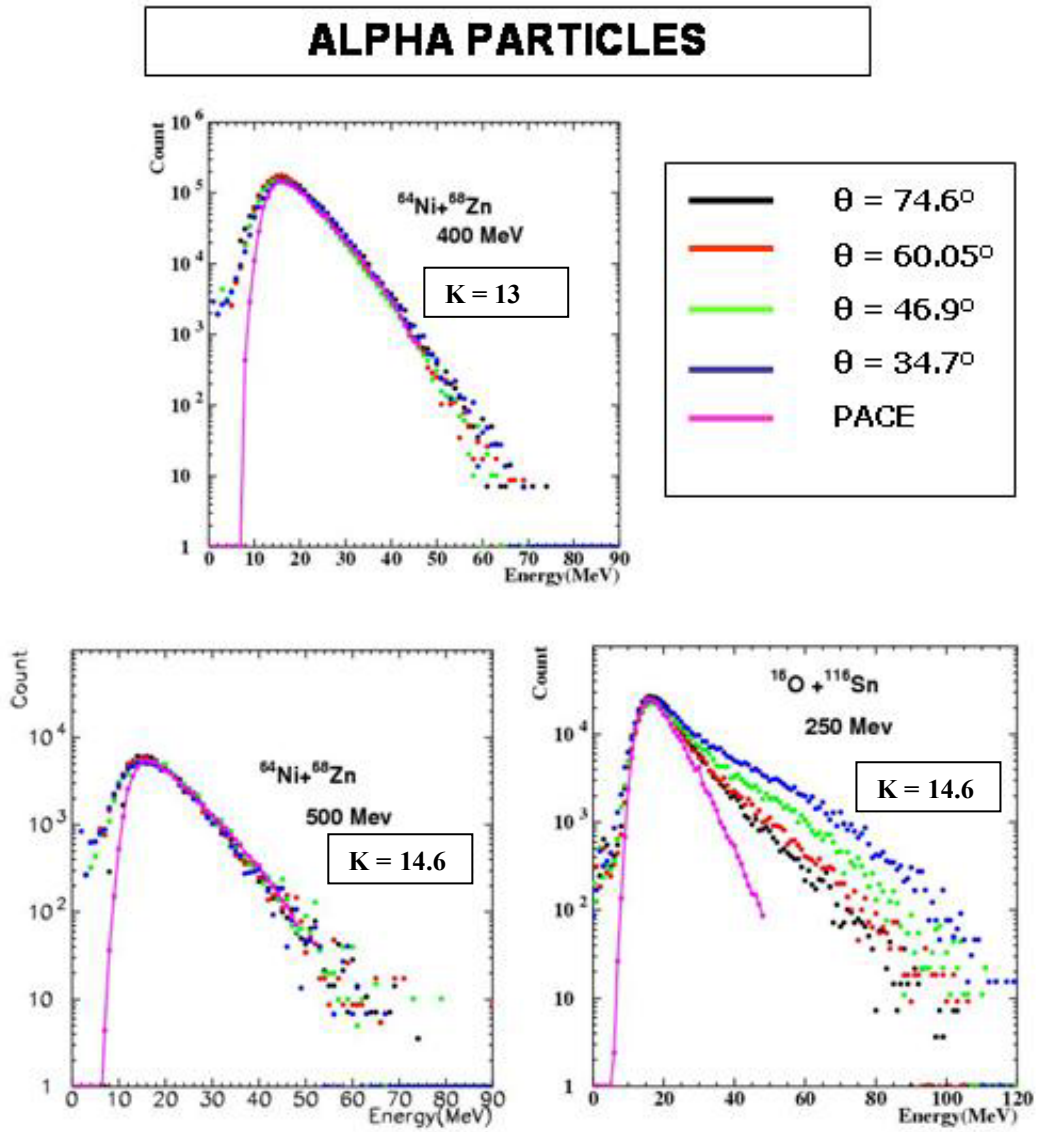

Fig. 5.19: Comparison of the alpha spectra of the three studied reaction in the centre of mass system with the calculation from a statistical code PACE4.

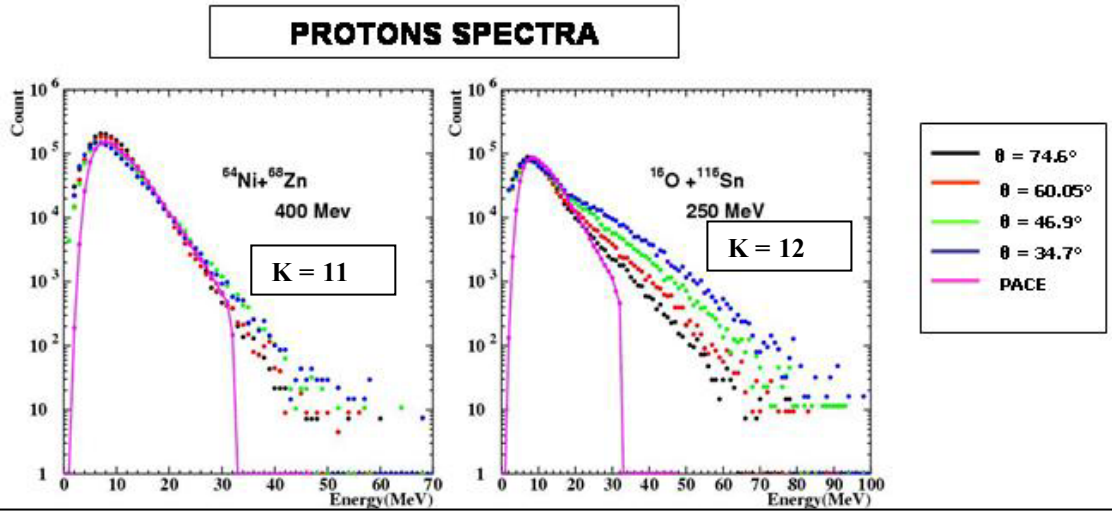

Fig. 5.20: Comparison of the alpha spectra of the three studied reaction in the centre of mass system with the calculation from a statistical code PACE4.

	$^{64}Ni+^{68}Zn$ 400 MeV	$^{64}Ni+^{68}Zn$ 500 MeV	$^{16}O+^{112}Mo$ 250 MeV
Alpha	**K= 13 T=3.67**	**K=14.6 T=4.56**	**K=14.6 T=4.56**
Proton	**K=11 T=3.37**	**Not available**	**K=12 T=4.1**

Tab. 5.14: Table of the temperatures extracted from the simulation calculated using PACE4 code able to fit the spectra in the centre of mass system.

5.5.5 The γ-rays experimental results.

From the point of view of the γ-ray analysis, all the information coming out from the particle spectra analysis can be condensed in these two crucial pieces of information:

- with the symmetric mass entrance channel $^{64}Ni + ^{68}Zn$ at 500 *MeV* and 400 *MeV*, it is possible to create a completely thermalized compound system. For this reason, the mass, the charge and the excitation energy of the emitting γ-source can be calculated starting from the complete merging of projectile and target nucleus using the Eq. 1, corrected for a small amount deriving essentially from the energy lost in the target thickness.
- In the asymmetric mass entrance channel, the pre-equilibrium emission plays really an important role. For this reason, a correct analysis of the γ-rays spectra can not be performed before estimating the quantity of A, Z, E^* lost by the compound system before being thermalized.

The standard technique employed to recognize the GDR emission in a γ-rays spectrum is to compare the experimental data with a computer simulation performed with the statistical code, like CASCADE. The γ-spectra detected by HECTOR are produced by the de-excitation of CN formed by the nuclear fusion reaction, but also from the daughter nuclei emission created in the decay cascade. To correctly reproduce the experimental spectrum, it is needed to take into account the γ-ray production along the whole cascade steps involved and sum all the contributions opportunely weighted with the probability of the selected decay channel. Moreover, the CN and its daughter nuclei are formed with a spin distribution which should be simulated by the calculation. Changing the spin distribution of the emitting source, the shape of the γ-ray spectrum is modified because the relative ratio between the different typologies of γ-ray emission (GDR, emission from rotational

band called type E_2 [see Chp. 1 for more detail] and statistical γ-ray emission from the yrast line) is different.

Fig. 5.21 shows the best fit obtained setting all the parameter in the proper way to minimize the chi-square with respect the experimental data for the two reactions ^{64}Ni + ^{68}Zn at 500 *MeV* and 400 *MeV*. In the small windows inside these pictures, a zoom of the spectra on the GDR emission region is presented. They are obtained removing from the experimental data and from the simulation the contribution of a "pure" statistical γ-emission, which ignores the GDR emission. This is an other version of the CASCADE program where the GDR probability emission is switched off. In this way, one can emphasize the contribution of the GDR emission which is important when E_γ is greater then 10 *MeV* and the statistics drops down, making possible to recognize the typical resonance Laurentian shape described in Chp.1 are then recognizable.

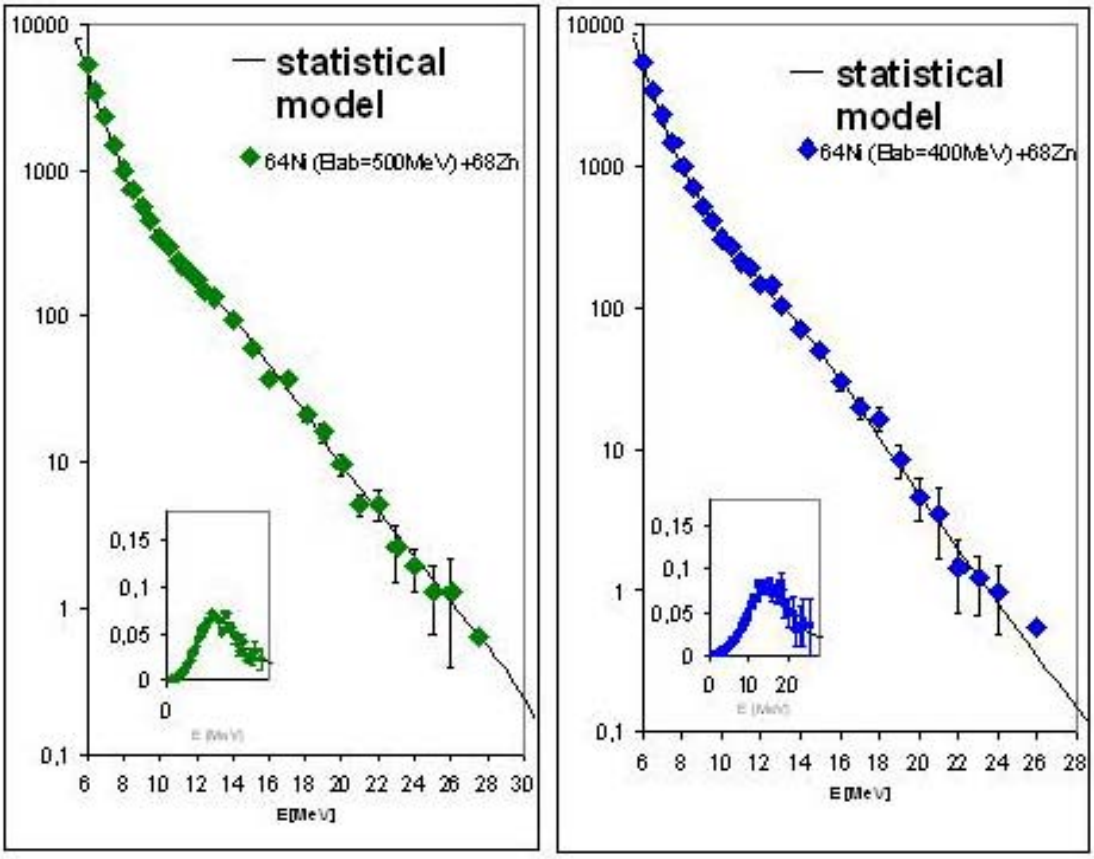

Fig. 5.21 : Analysis of the γ-ray spectra for the reactions ^{64}Ni + ^{68}Zn at 500 MeV and 400 MeV. In the small windows, the difference between the data and the statistical code is showed to emphasize the GDR emission.

The lower bombarding energy for the symmetric entrance reaction channel, i.e. bombarding energy of 300 *MeV*, have also been studied for the γ-rays part. Basing the confirmation that a complete fused system was formed at the higher bombarding energy (500 *MeV*), the analysis of the ^{64}Ni + ^{68}Zn at 300 *MeV* data could be performed assuming a complete fusion of the target and projectile nucleus independently on the light charged particles data.

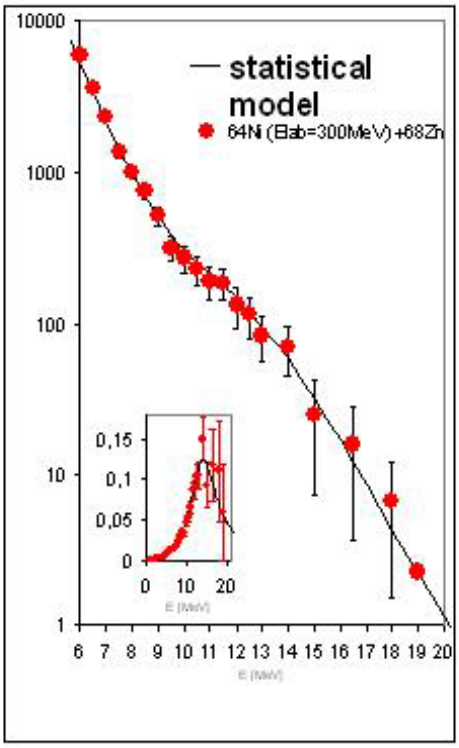

Fig. 5.22 : Analysis of the γ-rays spectra for the reactions ^{64}Ni + ^{68}Zn at 300 MeV. In the small window, the difference between the data and the statistical code is showed to emphasize the GDR emission.

The Fig. 5.22 shows the results of the γ analysis in this reaction ^{64}Ni + ^{68}Zn at 300 *MeV*.

As final result, in Tab. 5.14 the complete characterization of the GDR emission in the studied reaction ^{64}Ni + ^{68}Zn at 500 *MeV*, 400 *MeV* and 300 *MeV* is reported [Wie06].

E_{beam} (MeV)	E* (MeV)	GDR pos (MeV)	GDR width (MeV)
500	200	13.6	14.1
400	150	14.0	12.4
300	100	14.0	7.9

Tab. 5.14 : Characterization of the GDR emission from the reaction at ^{64}Ni + ^{68}Zn at 500 *MeV*, 400 *MeV* and 300 *MeV*.

Analysis is still in progress for the Oxygen induced reaction where a possible pre-equilibrium emission even from the part of the high energy γ-rays could be present, confirming some results which have been recently found. In this case, the pre-equilibrium γ-ray emission is produced at the beginning of the fusion process before the equilibration of the compound nucleus [Bru04].

CONCLUSION

In this work, a study of the characteristics of the emission from the Compound Nucleus formed using the reactions ^{64}Ni + ^{68}Zn at 400 *MeV*, ^{64}Ni + ^{68}Zn at 500 *MeV* and ^{16}O + ^{116}Sn at 250 *MeV* especially from the point of view of the light charged particles emitted and from the point of view of high energy γ-ray emission is described. To perform these measurements the GARFIELD apparatus was used to detect the light charged particles and fragments, the HECTOR apparatus for the γ-rays and some PSPPACs have been employed to detect the Evaporation Residues, to have a tagging of the studied events. Particularly important in this campaign of measurements is the comparison between the ^{64}Ni + ^{68}Zn at 500 *MeV* and ^{16}O + ^{116}Sn at 250 *MeV* reactions because they are supposed to create nominally the same CN (^{132}Ce with excitation energy of ~200 *MeV*), while our analysis underlines a large difference between them. In fact, a strong contribution of the emission before the complete thermalization of the system is evident in the most asymmetric case, which probably depends both on the different bombarding energy and on the entrance channel mass asymmetry.

The LCP spectra are analyzed using the moving source fit technique which simulates the emission from the thermalized system and from a fast source created in the early stage of the nuclear reaction: two maxwellian sources are applied, with velocities which are, respectively, equal to the centre of mass velocity and intermediate between the centre of mass and the projectile velocity. The moving source fit has to be applied simultaneously at all experimental data detected at different angles. This gives the possibility to disentangle the contributions of the evaporative source with respect to the pre-equilibrium source, using the different relative weight of the two contributions as a function of the θ angle in the laboratory system (the pre-equilibrium source shows a more peaked distribution toward the forward angles because of the greater velocity of the source).

Using the information which can be obtained from the moving source fit analysis, it was possible to estimate a temperature of the emitting sources. This is the compound nucleus temperature for the symmetric entrance channel reaction, while the situation was more complex for the Oxygen case. An estimation of the strong pre-equilibrium component was possible for this last reaction, together with some information on the percentage of break-up of the projectile. This last reaction channel is linked to the possible break-up of the ^{16}O projectile which goes in an α-particle plus a Carbon fragment which continues its road towards the incomplete fusion with the target.

The energy lost for the pre-equilibrium emission is (32.7 ± 6.3) *MeV*, while the break-up contribution is about 2.1 *MeV*, from a first simplified estimation.

In the symmetric entrance channel at 400 *MeV* only pure evaporation from a thermalized source has been observed. At higher bombarding energy a very small contribution which appears in the tail of the α-spectra could be attributed to fast emission. An evaluation of this contribution, which takes care also for the part deriving from the neutrons emission, brings to an upper limit of (6.3 ± 3.2) *MeV*. Confirmations of the results of our investigation come from the comparison to a systematics made on the bases of collected experimental results, as one can see from Tab. C.1.

Bombarding energy (MeV)	**E***	**Energy loss due to PE (%)**	**Ref.**
6.25	**151**	**0**	**Our**
7.81	**203**	**≤ 3.1**	**Our**
11.1	174	21.4	[Kel97]
13.0	197	12.7	[Cab03]
13.0	201	13.9	[Cab03]
15.6	**206**	**16.9 ±3.0**	**Our**
16.0	251	15.9	[Cab03]
16.0	201	18.5	[Cab03]

Tab. C.1 : Comparison of the percentage of E* lost due to pre-equilibrium emission between our studied reactions and other different experimental measurements.

From these considerations, in the γ-ray analysis of the symmetric mass entrance channel we can consider the mass, the charge and the excitation energy of the emitting γ-source as calculated starting from an almost and practically complete merging and thermalisation of projectile and target nucleus, correcting for a very small (negligible, in the case of the analysis for the gamma ray spectra) amount deriving essentially from the energy loss of the projectile in the targets.

E_{beam} (MeV)	E* (MeV)	GDR pos (MeV)	GDR width (MeV)	T (MeV)
500	200	13.6	14.1	3.69±0.15
400	150	14.0	12.4	2.79±0.10
300	100	14.0	7.9	1.83±0.05

Tab. C.2 : Characterization of the GDR emission from the reaction at ^{64}Ni + ^{68}Zn at 500 MeV, 400 MeV and 300 MeV.

The results obtained from the analysis of the Giant Dipole Resonance emission for the three reactions ^{64}Ni + ^{68}Zn at 500 *MeV,* 400 *MeV* and 300 *MeV* are listed in Tab. C.2.

Particularly important is the result obtained at highest excitation energy, where according to the paper of Kelly et al. [Kel97] a strong evidence of pre-equilibrium should be present. Our experiment has clarified the crucial role of the bombarding energy of the projectile and of the symmetry of the mass entrance channel. We have shown that it is possible to form a practically fully thermalized system also at high temperature (around 4 *MeV*) using a symmetric reaction (the upper limit for pre-equilibrium emission for the ^{64}Ni + ^{68}Zn at 500 *MeV* reaction is (3.1 ± 1.6) % of the total excitation energy).

The effect of this result on the data relative to the behaviour of the width of GDR as a function of the nuclear temperature is quite strong. In the paper of Kelly et al., an energy loss around 20 % was estimated for the pre-equilibrium emission. This loss was attributed to all the measurements performed at high excitation energy without taking into account the difference between the entrance channels of the reactions, neither from the beam energy or the mass asymmetry point of view. Our results on the asymmetric case underline furthermore that the estimation of the percentage of energy lost by pre-equilibrium emission seem to be overestimated in the Kelly experiment (considering also the systematics reported in Tab. C.1).

Nevertheless, even our experiment can not be considered completely conclusive. Other experiments are, in fact, needed to clarify the role of the mass asymmetry in the entrance channel when the energy involved is in the region where the pre-equilibrium emission is predicted to start. It could be, for example, interesting to study the ^{64}Ni + ^{68}Zn reaction at the same bombarding energy of the oxygen case (15.8 *MeV/u*).

In Fig C.1 the behaviour of the width of GDR as a function of the nuclear temperature is reported. In this plot data from [Gar83] and [Voi89] are included together with the experimental data coming from our measurements ^{64}Ni + ^{68}Zn at 300 *MeV,* 400 *MeV* and 500 *MeV*. Two theoretical calculations are compared to the experimental data: the fist (thin line) performed using only the thermal fluctuation model ([Orm97a], [Orm97b]), the second considering a further contribution to the width due to the uncertainty of the decay time of the Compound Nucleus (width induced by particle evaporation [Kus03]). Moreover, the average deformation $<\beta>$ calculated by the Thermal fluctuation model (scale on the right axis) is plotted with the dashed line.

In the plot, it is shown that the inclusion of the evaporation width (continuous thick line) is necessary to interpret the higher temperature results, where an increase of the experimental values of the width is present and well reproduced by the calculation. Considering that our data correspond to the same average spin, this width increase in the region T > 2 *MeV* is only due to the increasing

of temperature. The plot shows also that the behavior of the average deformation is substantially similar to that one of the GDR width calculated without the contribution of the evaporation compound width, pointing that the GDR width increase reflects an increase of the deformation of the compound nucleus. At temperature close 2 *MeV*, the timescale connected to the deformation of the nucleus and the timescale of the particle emission become similar and, therefore, the inclusion of the evaporation width becomes necessary. These results are in agreement with a picture of the damping mechanism which was obtained from the lower temperature showing that the GDR width increase is due to deformation and thermal averaging effects and not to an increase of the intrinsic width Γ_o [Bra95]. In other words, the increase of the width is due to the splitting of the three components of the GDR (one for each axis) for thermal and structure fluctuations. If the single components split, the final spectrum, which is the coinvolution of the three, will appear with a larger width. It is also clear that in the case of the ^{132}Ce*, the GDR quenching will appear for temperature greater than 4 *MeV*, which can be measured in a future experiment.

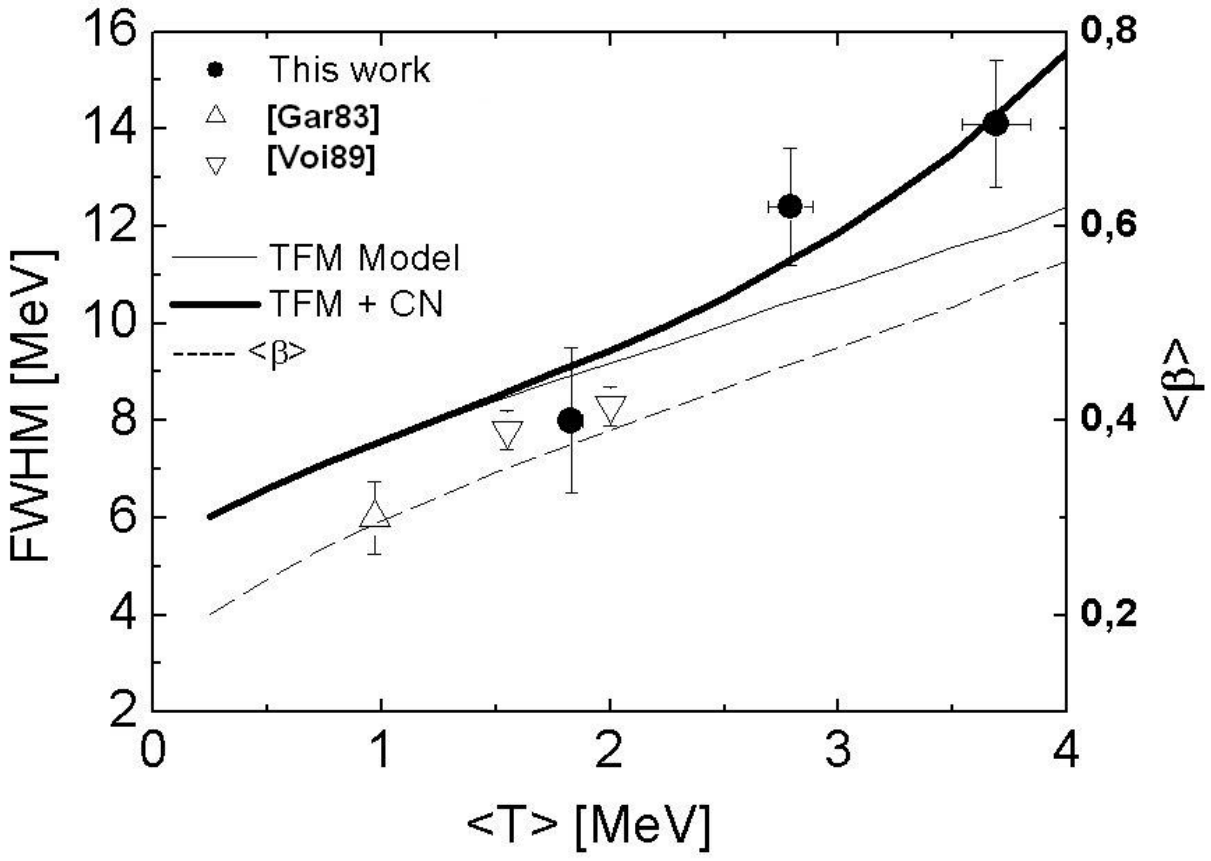

Fig. C.1: Width of the GDR as a function of the nuclear temperature. The thick continuous line shows the calculations where the compound lifetime is included while the thin continuous line indicates the results where such effect is not included. With the dashed line it is shown the average deformation calculated within the Thermal fluctuation model (scale on the right axis).

The analysis of the γ-rays spectrum of the asymmetric mass entrance channel is still in progress, as the study of the intermediate fragments emission ($Z > 2$). The comparison with models is under study, both using standard low energy statistical models like CACARIZO and PACE4, and more complete models like GEMINI, which can predict also IMF sequential emission. Some calculations with dynamical models to study the dynamics of entrance channel effect are also in progress.

APPENDIX

To perform all the calibration and analysis showed in the previous chapters several programs were studies and realized by the candidate. In this appendix, we report, as example, two programs used on the calibrated data to realize some of the results of the analysis. The first one was used to compare single, double and triple coincidences with the statistical code, while the second one is the fortran program used to perform the moving source fit analysis.

A. COMPARISON WITH STATISTICAL CODE

```
macro centro
ve/del *
igset mtype 20
set csiz 0.3
set pmci 1
*set mtype 7
opt logy
opt ndate

*************************************************************************
****CHECK Z AND THE REACTION BEFORE TO RUN (1=NI500, 2=NI400, 3=O250)***********
*************************************************************************
z=2
reaz=1
ve/cr zeta(1) r [z]
ve/cr reazio(1) r [reaz]
message ***************** STARTING OF PROGRAM ***********************************
message analysing Z =
ve/write zeta
message analysing reaction number →
ve/write reazio

message insert number of sector (1-24)
read set
message for plot in center of massa digit 1
read plot
message insert the density of level (8,9,9.5,10,11,12,13,14.6)
read kdens

if ([plot].eq.1) then
if ([z].eq.2) then
null 0 90 0 100000
else
null 0 80 0 1000000
endif
else
if ([z].eq.2) then
null 0 120 0 1000000
```

```
else
null 0 70 0 1000000
endif
endif

tele=[set]*100
set *fon 20
set *wid 15
set *size 0.8
set xval 0.7
set xlab 1.7
set xmgl 2.5
if [z].eq.1 then
title 'DISTRIBUTION PROTONS PARTICLES'
else
title 'DISTRIBUTION ALFA PARTICLES'
endif
set *wid 6
set *size 0.5
atitle 'Energy(MeV)' 'Counts'

igset txfp -60
igset chhe 0.6
if [z].eq.1 then
itx 40 10000 '500 Mev ^64!Ni+^68!Zn '
else
*itx 45 10000 '500 Mev ^64!Ni+^68!Zn '
endif

do cs=5,8



ve/del *
ve/cr norm(4) r 0.1342 0.1027 0.0838 0.0592
ve/cr E33(250) r
ve/cr count33(250) r
ve/cr E2(250)
ve/cr count2(250)
ve/cr E3(250)
ve/cr count3(250)
ve/cr E4(250)
ve/cr count4(250)
ve/cr E5(250)
ve/cr count5(250)
ve/cr E6(250)
ve/cr count6(250)


ve/cr n_count33(250) r
ve/cr n_count2(250) r
ve/cr n_count3(250) r
ve/cr n_count4(250) r
ve/cr n_count5(250) r
ve/cr n_count6(250) r

ve/cr cm_count33(250) r
ve/cr cm_count2(250) r
ve/cr cm_count3(250) r
ve/cr cm_count4(250) r
ve/cr cm_count5(250) r
ve/cr cm_count6(250) r
```

```
*****************************************************************************
************************   READING OF INPUT FILE   ***************************
*****************************************************************************

******* SINGLE COINCIDENCE ***************************
tele=[set]*100+[cs]*10+3
i=int([tele]/100)
if ([i].le.9) then
ve/read E2,count2 trisni500_0[tele]_zeta[z]code100.faby2
else
ve/read E2,count2 trisni500_[tele]_zeta[z]code100.faby2
endif

******** TRIPLE COINCIDENCE ***************************
tele=[set]*100+[cs]*10+3
i=int([tele]/100)
if ([i].le.9) then
ve/read E33,count33 trisni500_0[tele]_zeta[z]code111.faby
else
ve/read E33,count33 trisni500_[tele]_zeta[z]code111.faby
endif

******** DOUBLE COINCIDENCE ***************************
tele=[set]*100+[cs]*10+3
i=int([tele]/100)
if ([i].le.9) then
ve/read E6,count6 trisni500_0[tele]_zeta[z]code110.faby2
else
ve/read E6,count6 trisni500_[tele]_zeta[z]code110.faby2
endif




*****************************************************************************
***************** NORMALIZATION ON THE SOLID ANGLE  *************************
*****************************************************************************
dd=[cs]-4
fatt=norm([dd])
do i=1,250
dum2=count2([i])/[fatt]
dum33=count33([i])/[fatt]
dum6=count6([i])/[fatt]
ve/input n_count2([i]) [dum2]
ve/input n_count33([i]) [dum33]
ve/input n_count6([i]) [dum6]
enddo

*****************************************************************************
********* TRANSFORMATION OF THE ENERGY IN THE CENTRE OF MASS SYSTEM **********
*****************************************************************************

ve/cr vcm(3) r 1.884 1.685 0.66
ve/cr massa(6) r 1. 4. 7. 9. 11. 12.
ve/cr theta(4) r 74.6 60.05 46.9 34.7
ve/cr theta2(4) r
ve/cr Ecm(250) r
ve/cr r_Ecm(250) r

c=29.98
sigma theta2=theta*(3.141592654/180)
m=massa([z])*938.27
dd=[cs]-4
```

```
th=theta2([dd])
v=vcm([reaz])
ve/cr rad(1) r
ve/cr sqr(1) r
ve/cr coseno(1) r
m2=[m]/([c]*[c])

do i=1,250

Elab=E6([i])
radice=0.5*[m2]*[v]*[v]*[Elab]
ve/input rad(1)  [radice]
sigma sqr=rad**0.5
sigma coseno=cos([th])
ciccio=sqr(1)
ciccia=coseno(1)
EEcm=[Elab]-2*sqr(1)*coseno(1)+0.5*[m2]*[v]*[v]
ve/input cazzo(7) [EEcm]
ve/input r_Ecm([i]) [EEcm]
EEEcm=int([EEcm]+0.5)
ve/input Ecm([i]) [EEEcm]
enddo


*******************************************************************************
********** TRASFORMATION OF COUNTS IN THE CENTRE OF MASS SYSTEM *************
*******************************************************************************

ve/cr fat(1)
ve/cr pepe(1)
ve/cr popo(1)
do i=1,250
dum=r_Ecm([i])
ve/input pepe(1) [dum]
ve/input popo(1) [i]
sigma fat=(pepe/popo)**0.5
fatt=fat(1)
dum2=n_count2([i])*[fatt]
dum33=n_count33([i])*[fatt]
dum6=n_count6([i])*[fatt]
ve/input cm_count2([i]) [dum2]
ve/input cm_count33([i]) [dum33]
ve/input cm_count6([i]) [dum6]
enddo

ve/cr cm_count6b(250) r
ve/cr cm_count2b(250) r
ve/cr cm_count33b(250) r

do kk=1,250
dum6=cm_count6([kk])
dum2=cm_count2([kk])
dum33=cm_count33([kk])
ve/input cm_count6b([kk]) [dum6]
ve/input cm_count2b([kk]) [dum2]
ve/input cm_count33b([kk]) [dum33]
enddo

do kk=1,250
do jj=[kk]+1,250
pippo=Ecm([kk])
pippa=Ecm([jj])
if ([pippo].eq.[pippa]) then
```

```
dum2=cm_count6b([kk])
dummy2=cm_count6b([jj])
dum3=cm_count2b([kk])
dummy3=cm_count2b([jj])
dum33=cm_count33b([kk])
dummy33=cm_count33b([jj])
conti=([dum2]+[dummy2])/2
conti2=([dum3]+[dummy3])/2
conti33=([dum33]+[dummy33])/2
ve/input cm_count6b([kk]) [conti]
ve/input cm_count2b([kk]) [conti2]
ve/input cm_count33b([kk]) [conti33]
endif
enddo
enddo


do kk=1,250
do jj=[kk],250
dum=Ecm([kk])
dummy=Ecm([jj])
if ([dum].eq.[dummy]) then
dum2=cm_count6b([kk])
dum3=cm_count2b([kk])
dum33=cm_count33b([kk])
ve/input cm_count6b([jj]) [dum2]
ve/input cm_count2b([jj]) [dum3]
ve/input cm_count33b([jj]) [dum33]
endif
enddo
enddo


*****************************************************************************
******************************** PLOTTING ***********************************
*****************************************************************************
fine=150

if ([plot].eq.1) then
********** single coincidence in centre of mass ************************
set pmci [cs]-4
ve/plo cm_count2b(1:[fine])%Ecm(1:[fine]) -s
********** double coincidence in centre of mass ************************
set pmci [cs]-4
ve/plo cm_count33(1:[fine])%Ecm(1:[fine]) -s
********** triple coincidence in centre of mass ************************
set pmci [cs]-4
ve/plo cm_count6b(1:[fine])%Ecm(1:[fine]) -s
endif


if ([plot].ne.1) then
****** single coincidence in laboratory system ************************
set pmci [cs]-3
ve/plo n_count2(1:[fine])%E2(1:[fine]) -s
****** double coincidence in laboratory system ************************
set pmci [cs]-3
ve/plo n_count33(1:[fine])%E33(1:[fine]) -s
****** triple coincidence in laboratory system ************************
set pmci [cs]-3
ve/plo n_count6(1:[fine])%E6(1:[fine]) -s
endif
```

```
ve/cr ciccio(1) r
ve/input ciccio(1) [tele]


sompi=0
do kk=1,10
pippo=cm_count6b([kk])
sompi=[sompi]+[pippo]
enddo
ve/cr int(1) r [sompi]
message total number of experimental count
ve/write int
enddo


*******************************************************************************
************************   WRITING OF THEORETICAL FILES ************************
*******************************************************************************
ve/cr E_t(49) r
ve/cr E_t2(49) r
ve/cr neutro_t(49) r
ve/cr proto_t(49) r
ve/cr alfa_t(49) r
ve/cr proto_t2(49) r
ve/cr alfa_t2(49) r

if [kdens].eq.8 then
***** normalization factors
fat_tp=4.5
fat_ta=4.28

ve/read E_t,neutro_t,proto_t,alfa_t pace_500_8.tab
endif

if [kdens].eq.9 then
***** normalization factor
fat_tp=5.87
fat_ta=5.12

ve/read E_t,neutro_t,proto_t,alfa_t ni500-9.txt
endif

if [kdens].eq.9.5 then
***** normalization factors
fat_tp=8.21
fat_ta=5.12

ve/read E_t,neutro_t,proto_t,alfa_t ni500-9.5.txt
endif


if [kdens].eq.10 then
***** normalization factors
fat_tp=5.20
fat_ta=5.12

ve/read E_t,neutro_t,proto_t,alfa_t ni500-10.txt
endif

if [kdens].eq.11 then
***** normalization factor
fat_tp=7.72
```

```
fat_ta=5.12

ve/read E_t,neutro_t,proto_t,alfa_t ni500-11.txt
endif

ve/cr E_tc(64) r
ve/cr neutro_tc(64) r
ve/cr proto_tc(64) r
ve/cr alfa_tc(64) r
fat_tpc=55
fat_tac=2
ve/read E_tc,neutro_tc,proto_tc,alfa_tc cac_ni500.dat



if [kdens].eq.12 then
***** normalization factors
fat_tp=7.15
fat_ta=5.31

ve/read E_t,neutro_t,proto_t,alfa_t ni500-12.txt
endif

if [kdens].eq.13 then
***** normalization factors
fat_tp=6.80
fat_ta=3

ve/read E_t,neutro_t,proto_t,alfa_t pace_500_13.tab
endif

if [kdens].eq.14.6 then
***** normalization factors
fat_tp=6.37
fat_ta=3.268

ve/read E_t,neutro_t,proto_t,alfa_t  pace_500_best.tab
endif



do kk=1,49
pippo=E_t([kk])
pluto=proto_t([kk])/[fat_tp]
pluta=alfa_t([kk])/[fat_ta]
ve/input E_t2([kk]) [pippo]
ve/input proto_t2([kk]) [pluto]
ve/input alfa_t2([kk]) [pluta]
enddo


ve/cr proto_t2c(64) r
ve/cr alfa_t2c(64) r
ve/cr E_t2c(64) r
do kk=1,64
pippo=E_tc([kk])
pluto=proto_tc([kk])/[fat_tpc]
pluta=alfa_tc([kk])/[fat_tac]
ve/input E_t2c([kk]) [pippo]
ve/input proto_t2c([kk]) [pluto]
ve/input alfa_t2c([kk]) [pluta]
enddo
```

```
if ([plot].eq.1) then
set plci 6
set pmci 6
set lwid 7

if [z].eq.1 then
graph 49 E_t2 proto_t2 pl
set plci 5
set pmci 5
set lwid 7
*graph 64 E_t2c proto_t2c pl
endif

if [z].eq.2 then
set plci 6
set pmci 6
set lwid 7
graph 49 E_t2 alfa_t2 pl
set plci 5
set pmci 5
set lwid 7
*graph 64 E_t2c alfa_t2c pl
endif

endif

sompit=0
do kk=10,48
if [z].eq.2 then
pippot=alfa_t([kk])
endif
if [z].eq.1 then
pippot=proto_t([kk])
endif
sompit=[sompit]+[pippot]
enddo
ve/cr intt(1) r [sompit]
message total number of counts of the theoretical data
ve/write intt


return
```

B. MOVING SOURCE FIT PROGRAM

```
      program moving_source
      call minnew
      stop
      end
c--------------------------------------------------------------------------
c   *********   evaporative fit only   *****************
c--------------------------------------------------------------------------
      subroutine fcn(npar,g,chi,d,iflag)
      implicit double precision (a-h,o-z)
      integer*4 ierr,kdat
      PARAMETER (n=4000)
      PARAMETER (pluto=50)
      dimension D(18),fth(n,pluto),cp(n,pluto),re(n,pluto),err(n,pluto),
     * pippo(n,pluto)
      dimension rpippo(n,pluto),p2(n,pluto),recm(n,pluto),vlab(n,pluto)
      dimension vrapp(n,pluto),thecmr(n,pluto),pezzo(n,pluto)
      dimension renne(n,pluto),ajacob(n,pluto),respo(n,pluto)
      dimension rompi(n,pluto),nrighe(pluto)
      real zeta,vcm,massa,PI,enrecm,c,massa1,massa2
      dimension theta(pluto),thetar(pluto),omega(pluto),cotanthe(pluto)
      dimension ndat(pluto),costhcm(n,pluto),costhe(pluto),sinthe(pluto)
      save

      GO TO (10,20,20,20,20,20),iflag
 10   continue
          PI=3.141592
      open(unit=14,file='moving_fit_ni12e.dat',status='old',iostat=ierr)
c
c      esempio .dat
c      3 4 2 0.4    ! numero file da leggere, massa,zeta,vcm(v/c)
c      30 60.  ! theta,omega(msr)
c      1 2     ! e(i) pippo(i)
c      2 4
c      3 9
c      ......
c      20 9
c      ...........

      if(ierr .ne. 0)then
        write(*,'(a)')'This file does not exist'
        stop
      endif
       read (14,*,err=22,end=22)numfile,massa,zeta,vcm
         kdat=0
        do k=1,numfile
         ndat(k)=0
        end do

          do i=1,4000
        do j=1,50
        rpippo(i,j)=0.0
        end do
        end do

       do k=1,numfile
       read(14,*,err=22,end=22)theta(k),omega(k),nrighe(k)
```

```
       do I=1,nrighe(k)

         read(14,*,err=22,end=22)re(i,k),pippo(i,k)
         rpippo(i,k)=pippo(i,k)/omega(k)
         err(i,k)=sqrt(pippo(i,k))/omega(k)
                ndat(k)=ndat(k)+1
         if (err(i,k).eq.0) then
         err(i,k)=0.5
         end if
c        write (*,*) re(i,k),pippo(i,k),rpippo(i,k),err(i,k)
c               kdat=kdat+ndat(k)
c       write (*,*) 'kdat=',kdat
         enddo
         kdat=kdat+ndat(k)
         enddo
 22   continue
       close(14)
       open(unit=6,file='fit_movingsource_1.out')
        open(unit=20,file='fit_check.out')
 20     CHI=0.
        do k=1,numfile


           do i=1,ndat(k)

          p2(i,k)=0.0
          vlab(i,k)=0.0
          vrapp(i,k)=0.0
          thecmr(i,k)=0.0
          costhcm(i,k)=0.0
          rompi(i,k)=0.0
          recm(i,k)=0.0
          renne(i,k)=0.0
          respo(i,k)=0.0
          pezzo(i,k)=0.0
          fth(i,k)=0.0
          ajacob(i,k)=0.0
          cp(i,k)=0.0

         end do
        end do

        do k=1,numfile
c        calcolo l'angolo nel cm in radianti
         thetar(k)=theta(k)*PI/180.
         cotanthe(k)=1/tan(thetar(k))
         costhe(k)=cos(thetar(k))
         sinthe(k)=sin(thetar(k))

         do i=1,ndat(k)
c         calcolo la velocita' nel laboratorio
          massa1=massa*938.27
          c=29.98
          vlab(i,k)=c*((2*re(i,k)/massa1)**0.5)
c         write(20,*) 'vlab', vlab(i,k)
c         calcolo il rapporto vlab/vcm
c          vrapp(i,k)=sin(thetar(k))*(vlab(i,k)/vcm)
c         calcolo il rapporto vlab/vsource
           vrapp(i,k)=sin(thetar(k))*(vlab(i,k)/d(5))
c          thecmr(i,k)=1/tan(cotanthe(k)-1/vrapp(i,k))
           thecmr(i,k)=atan((vlab(i,k)*sinthe(k))/(vlab(i,k)*costhe(k)-d(5)))
           costhcm(i,k)=cos(thecmr(i,k))
```

```
c         calcolo l'energia nel cm della particella
c             enrecm=0.5*massa*(vcm**2)
                  massa2=massa1/c**2
               enrecm=0.5*massa2*(d(5)**2)
c                enrecm=0.5*massa2*(vcm**2)
             rompi(i,k)=(enrecm*re(i,k))**0.5
          recm(i,k)=re(i,k)+enrecm-(2*rompi(i,k)*costhe(k))
c             write (20,*) 'recm',recm(i,k),'costhcm',costhcm(i,k)
              ajacob(i,k)=(re(i,k)/recm(i,k))**0.5
           end do
          end do

          do k=1,numfile
           do i=1,ndat(k)
          p2(i,k)=0.0
            end do
          end do
          do k=1,numfile
           do i=1,ndat(k)

c           input fit parameters
c           note that vsource2 should be close to vcm
c           evap d(1)=N2 d(2)=a2 d(3)=T2 d(4)=Ec2 d(5)=vsource2

            p2(i,k)=1.5*(costhcm(i,k)**2)-0.5
            renne(i,k)=d(1)*(1+d(2)*p2(i,k))


c            write(20,*) 'jacob  ','   p2  ','enne  '
c           write(20,103) ajacob(i,k),p2(i,k),renne(i,k)
 103         format(2x,(3(2x,f12.3)))
             respo(i,k)=exp((d(4)-recm(i,k))/d(3))
             pezzo(i,k)=(recm(i,k)-d(4))*ajacob(i,k)*respo(i,k)

            fth(i,k)=(pezzo(i,k)*(renne(i,k))/((4*PI)*(d(3)**2)))

             if (fth(i,k).le.0) then
                 fth(i,k)=0.0
             endif


            cp(i,k)=((fth(i,k)-rpippo(i,k))**2)/(err(i,k)**2)

           chi=cp(i,k)+chi
c          write(20,*) 'espo  ','   pezzo  ','fth  '
c           write(20,103) respo(i,k),pezzo(i,k),fth(i,k)

         end do
          end do
        if(iflag.ne.3)return
        write(6,*)' chinorm/(np-npar)=', chi/(kdat-npar-1)
        write(6,*)' kdat',kdat
       write(6,*)'      energia      yield th    yield spe       cp
     *  nfile'

c     fit data
      open(unit=21,file='fit_vect_1.out')
c     experimental data
      open(unit=31,file='fit_vect_1a.out')
c
        open(unit=41,file='cs5exp.dat')
        open(unit=42,file='cs6exp.dat')
        open(unit=43,file='cs7exp.dat')
```

```
        open(unit=44,file='cs8exp.dat')
        open(unit=45,file='cs5fit.dat')
        open(unit=46,file='cs6fit.dat')
        open(unit=47,file='cs7fit.dat')
        open(unit=48,file='cs8fit.dat')
c
          do k=1,numfile
           do i=1,ndat(k)
         write(6,111) re(i,k),fth(i,k),rpippo(i,k),cp(i,k),k
         write(21,114) fth(i,k)
          write(31,114) rpippo(i,k)
         end do
        end do
c
          do numfile=1,1
          do i=1,ndat(numfile)
           write(41,114) rpippo(i,numfile)
           write(45,114) fth(i,numfile)
           end do
           end do
c
          do numfile=2,2
          do i=1,ndat(numfile)
            write(42,114) rpippo(i,numfile)
            write(46,114) fth(i,numfile)
          end do
          end do
c
          do numfile=3,3
          do i=1,ndat(numfile)
            write(43,114) rpippo(i,numfile)
            write(47,114) fth(i,numfile)
          end do
          end do
c
          do numfile=4,4
          do i=1,ndat(numfile)
            write(44,114) rpippo(i,numfile)
            write(48,114) fth(i,numfile)
          end do
          end do
c
111      format(1x,4(1x,f12.2),3x,i2)
114       format(1x,f12.2)
        close(20)
        close(6)
        close(21)
        return
         end
```

```
        program moving_source2
      call minnew
      stop
      end
c-------------------------------------------------------------------------
c   *********   evaporative + preequilibrium fit  *****************
c-------------------------------------------------------------------------
      subroutine fcn(npar,g,chi,d,iflag)
      implicit double precision (a-h,o-z)
       integer*4 ierr,kdat
       PARAMETER (n=4000)
```

```
       PARAMETER (pluto=50)
       dimension d(20),fth(n,pluto),r(10)
       dimension vlady1(n,pluto),vlady2(n,pluto)
      dimension cp(n,pluto),re(n,pluto),err(n,pluto)
      dimension pippo(n,pluto),nrighe(pluto),vlab(n,pluto)
      dimension rpippo(n,pluto),p2(n,pluto),recm(n,pluto)
      dimension renne(n,pluto),ajacob(n,pluto),respo(n,pluto)
      dimension recm2(n,pluto),ajacob2(n,pluto),respo2(n,pluto)
      dimension vrapp(n,pluto),thecmr(n,pluto),pezzo(n,pluto)
      dimension vrapp2(n,pluto),thecmr2(n,pluto),pezzo2(n,pluto)
      dimension rompi(n,pluto),rompi2(n,pluto),costhe(pluto)
      dimension sinthe(pluto)
      dimension theta(pluto),thetar(pluto),omega(pluto),cotanthe(pluto)
      dimension ndat(pluto),costhcm(n,pluto),costhcm2(n,pluto)
      real zeta,vcm,massa,PI,c,massa1,enrecm,enrecm2,massa2
      save


        GO TO (10,20,20,20,20,20),iflag
 10   continue
         PI=3.141592
      open(unit=14,file='moving_fit_o02a.dat',status='old',iostat=ierr)

c      example .dat
c      3 4 2 0.4    ! numero file da leggere, massa,zeta,vcm(v/c)
c      30 60 50  ! theta,omega(msr),nrighe
c      1 2     ! e(i) pippo(i)
c      2 4
c      3 9
c      ......
c      20 9
c      ...........

       if(ierr .ne. 0)then
          write(*,'(a)')'This file does not exist'
          stop
       endif
      read (14,*,err=22,end=22)numfile,massa,zeta,vcm
         kdat=0
        do i=1,4000
         do j=1,50
         rpippo(i,j)=0.0
         end do
        end do

         do k=1,numfile
          ndat(k)=0
         end do
        do k=1,numfile

        read(14,*,err=22,end=22)theta(k),omega(k),nrighe(k)

      do I=1,nrighe(k)

          read(14,*,err=22,end=22)re(i,k),pippo(i,k)
          rpippo(i,k)=pippo(i,k)/omega(k)
          err(i,k)=sqrt(pippo(i,k))/omega(k)
                 ndat(k)=ndat(k)+1
         if (err(i,k).eq.0) then
         err(i,k)=0.5
         end if
c        write (*,*) re(i,k),pippo(i,k),rpippo(i,k),err(i,k)
c               kdat=kdat+ndat(k)
```

```
c       write (*,*) 'kdat=',kdat
         enddo
         kdat=kdat+ndat(k)
         enddo
 22    continue
       close(14)
       open(unit=6,file='fit_movingsource_preeq_3.out')
        open(unit=20,file='fit_check_preeq_3.out')
 20     CHI=0.


          do k=1,numfile
           do i=1,ndat(k)
          p2(i,k)=0.0
          vlab(i,k)=0.0
          vrapp(i,k)=0.0
          vrapp2(i,k)=0.0
          thecmr(i,k)=0.0
          thecmr2(i,k)=0.0
          costhcm(i,k)=0.0
          costhcm2(i,k)=0.0
          rompi(i,k)=0.0
          rompi2(i,k)=0.0
          recm(i,k)=0.0
          recm2(i,k)=0.0
          ajacob(i,k)=0.0
          ajacob2(i,k)=0.0
          renne(i,k)=0.0
          respo(i,k)=0.0
          respo2(i,k)=0.0
          pezzo(i,k)=0.0
          pezzo2(i,k)=0.0
          fth(i,k)=0.0
          cp(i,k)=0.0
            end do
         end do

c            Here is a possibility to fix the fitting parameters
c            The same could be done by putting error=0.0 in the shell
c            O 250 parameters
c           d(5)=3200000.
c           d(6)=0.11777
c           d(7)=4.5
c           d(8)=12.645
c           d(9)=0.69792

        do k=1,numfile
c        calcolo l'angolo nel cm in radianti
         thetar(k)=theta(k)*PI/180.
         cotanthe(k)=1/tan(thetar(k))
         costhe(k)=cos(thetar(k))
         sinthe(k)=sin(thetar(k))

         do i=1,ndat(k)
c         calcolo la velocita' nel laboratorio
          massa1=massa*938.27
          c=29.98
          vlab(i,k)=c*((2*re(i,k)/massa1)**0.5)
c         write(20,*) 'vlab', vlab(i,k)
c         calcolo il rapporto vlab/vcm
c          vrapp(i,k)=sin(thetar(k))*(vlab(i,k)/vcm)
c         calcolo il rapporto vlab/vsource
           vrapp(i,k)=sin(thetar(k))*(vlab(i,k)/d(9))
```

```
            vrapp2(i,k)=sin(thetar(k))*(vlab(i,k)/d(4))
c           thecmr(i,k)=1/atan(cotanthe(k)-1/vrapp(i,k))
c           thecmr2(i,k)=1/atan(cotanthe(k)-1/vrapp2(i,k))
            thecmr(i,k)=atan((vlab(i,k)*sinthe(k))/(vlab(i,k)*costhe(k)-d(9)))
             thecmr2(i,k)=atan((vlab(i,k)*sinthe(k))/
     +      (vlab(i,k)*costhe(k)-d(4)))
            costhcm(i,k)=cos(thecmr(i,k))
            costhcm2(i,k)=cos(thecmr2(i,k))

c          calcolo l'energia nel cm della particella
c              enrecm=0.5*massa2*(vcm**2)
                 massa2=massa1/c**2
                enrecm=0.5*massa2*(d(9)**2)
                if (enercm.le.0.) then
                enercm=0.
                end if
               enrecm2=0.5*massa2*(d(4)**2)
                 if (enercm2.le.0.) then
                enercm2=0.
                end if
              rompi(i,k)=(enrecm*re(i,k))**0.5
              rompi2(i,k)=(enrecm2*(re(i,k)-d(3)))**0.5
             recm(i,k)=re(i,k)+enrecm-(2*rompi(i,k)*costhe(k))
            recm2(i,k)=re(i,k)-d(3)+enrecm2-(2*rompi2(i,k)*costhe(k))
            if (recm(i,k).le.0.) then
            recm(i,k)=0.001
            end if
            if (recm2(i,k).le.0.) then
            recm2(i,k)=0.001
            end if
c            write (20,*) 'recm2',recm2(i,k),'costhcm2',costhcm2(i,k)
               ajacob(i,k)=(re(i,k)/recm(i,k))**0.5
                ajacob2(i,k)=((re(i,k)-d(3))/recm2(i,k))**0.5
          end do
         end do

          do k=1,numfile
           do i=1,ndat(k)

c            input fit parameters
c           note that vsource2 should be close vcm
c            evap d(5)=N2 d(6)=a2 d(7)=T2 d(8)=Ec2 d(9)=vsource2
c            preeq d(1)=N1 d(2)=T1 d(3)=Ec1 d(4)=vsource1

            p2(i,k)=1.5*(costhcm(i,k)**2)-0.5
c            renne(i,k)=d(1)*(1+d(2)*p2(i,k))

            renne(i,k)=d(5)*(1+d(6)*p2(i,k))

c           write(20,*) 'jacob3  ','   p2  ','enne  '
c           write(20,103) ajacob2(i,k),p2(i,k),renne(i,k)
 103         format(2x,(3(2x,f12.3)))
              respo(i,k)=ajacob(i,k)*(exp((d(8)-recm(i,k))/d(7)))
              respo2(i,k)=ajacob2(i,k)*(exp(-1*recm2(i,k)/d(2)))
         pezzo(i,k)=renne(i,k)*((recm(i,k)-d(8))*respo(i,k))
         pezzo2(i,k)=d(1)*(((recm2(i,k))**0.5)*respo2(i,k))
        vlady1(i,k)=4*PI*(d(7)**2)
        vlady2(i,k)=2*((PI*d(2))**1.5)

         fth(i,k)=(pezzo(i,k)/vlady1(i,k))+(pezzo2(i,k)/vlady2(i,k))

          if (pezzo(i,k).le.0) then
             pezzo(i,k)=0.0
```

```
           endif

           if (pezzo2(i,k).le.0) then
              pezzo2(i,k)=0.0
           endif

           if (fth(i,k).le.0) then
               fth(i,k)=0.0
           endif


c       (pezzo(i,k)/vlady1(i,k))
c       (pezzo2(i,k)/vlady2(i,k))

                cp(i,k)=((fth(i,k)-rpippo(i,k))**2)/(err(i,k)**2)

                  chi=cp(i,k)+chi
c              write(20,*) 'vlady1th', vlady1th(i,k),'vlady2th', vlady2th(i,k),
c            write(20,*) 'espo2  ','   pezzo2  ','fth  '
c             write(20,103) respo2(i,k),pezzo2(i,k),fth(i,k)
c
           end do
            end do
          if(iflag.ne.3)return
          write(6,*)' chinorm/(np-npar)=', chi/(kdat-npar-1)
          write(6,*)' kdat',kdat
         write(6,*)'      energia      yield th    yield spe       cp
        *  nfile'

c        summed fit data
         open(unit=21,file='fit_vect_doppio2.out',status='old')
c        experimental data
         open(unit=31,file='fit_vect_doppio3.out',status='old')
c        evaporative part fit
         open(unit=41,file='fit_vect_doppio4.out',status='old')
c        preequilibrium part fit
         open(unit=51,file='fit_vect_doppio5.out',status='old')
c
           open(unit=61,file='cs5fit.dat')
           open(unit=62,file='cs6fit.dat')
           open(unit=63,file='cs7fit.dat')
           open(unit=64,file='cs8fit.dat')
           open(unit=65,file='cs5exp.dat')
           open(unit=66,file='cs6exp.dat')
           open(unit=67,file='cs7exp.dat')
           open(unit=68,file='cs8exp.dat')
           open(unit=71,file='cs5evap.dat')
           open(unit=72,file='cs6evap.dat')
           open(unit=73,file='cs7evap.dat')
           open(unit=74,file='cs8evap.dat')
           open(unit=75,file='cs5preeq.dat')
           open(unit=76,file='cs6preeq.dat')
           open(unit=77,file='cs7preeq.dat')
           open(unit=78,file='cs8preeq.dat')
c
            do k=1,numfile
             do i=1,ndat(k)
           write(6,111) re(i,k),fth(i,k),rpippo(i,k),cp(i,k),k
           write(21,114) fth(i,k)
           write(31,114) rpippo(i,k)
           write(41,114) pezzo(i,k)/vlady1(i,k)
           write(51,114) pezzo2(i,k)/vlady2(i,k)
            end do
```

```
        end do
c
           do numfile=1,1
           do i=1,ndat(numfile)
            write(61,114) fth(i,numfile)
            write(65,114) rpippo(i,numfile)
            write(71,114) pezzo(i,numfile)/vlady1(i,numfile)
            write(75,114) pezzo2(i,numfile)/vlady2(i,numfile)
            end do
            end do
c
           do numfile=2,2
           do i=1,ndat(numfile)
            write(62,114) fth(i,numfile)
            write(66,114) rpippo(i,numfile)
            write(72,114) pezzo(i,numfile)/vlady1(i,numfile)
            write(76,114) pezzo2(i,numfile)/vlady2(i,numfile)
            end do
            end do
c
           do numfile=3,3
           do i=1,ndat(numfile)
            write(63,114) fth(i,numfile)
            write(67,114) rpippo(i,numfile)
            write(73,114) pezzo(i,numfile)/vlady1(i,numfile)
            write(77,114) pezzo2(i,numfile)/vlady2(i,numfile)
            end do
            end do
c
           do numfile=4,4
           do i=1,ndat(numfile)
            write(64,114) fth(i,numfile)
            write(68,114) rpippo(i,numfile)
            write(74,114) pezzo(i,numfile)/vlady1(i,numfile)
            write(78,114) pezzo2(i,numfile)/vlady2(i,numfile)
            end do
            end do
c
111      format(1x,4(1x,f12.2),3x,i2)
114       format(1x,f12.2)
        close(20)
        close(6)
        close(21)
        close(31)
        close(41)
        close(51)
        return
         end
```

BIBLIOGRAPHY

[Alb85] *S. Albergo et al.* NUOVO CIMENTO A89 1 (1985)

[Awe81] *T.C.Awes, G. Poggi, C.K. Gelbke, B.B.Back, B.G. Glagola, H. Brener, and V.E. Viola Jr.*, Phys. Rev. C24, 89 (1981)

[Bar02] *S. Barlini*, **"Multiframmentazione in reazioni fra ioni pesanti con l'apparato GARFIELD. Calibrazioni e risultati preliminari.",** Graduation Thesis, University of Bologna July 2002

[Bar05] *S. Barlini, V.L. Kravchuk, O. Wieland, F. Camera, F. Gramegna, A. Maj, G. Benzoni, N. Blasi, S. Brambilla, M. Brekiesz, M. Bruno, G. Casini, M. Chiari, E. Geraci, A. Giussani, M. Kmiecik, S. Leoni, A. Lanchaisj, P.F. Mastinu, B. Millon, A. Moroni, A. Nannini, A. Ordine, G. Vannini, L. Vannucci* , **"Studio delle emissioni di particella carica e di γ di GDR nel nucleo di Ce formato a diverse energie di eccitazione attraverso le reazioni ^{64}Ni + ^{68}Zn e ^{16}O + ^{116}Sn",** XCI Congresso Nazionale Società Italiana di Fisica, Catania 2005

[BBB98] *P.F. Bortignon, A. Bracco and R.A. Broglia*, "**Giant Resonance Nuclear Structure at Finite Temperature",** Contemporary Concepts in Physics Volume 10, Harwood academic publishers

[Ber75] *B. L. Berman, S.C. Fultz*, Rev. Med. Phys. 47:713 (1975)

[Bet37] *H. A. Bethe*, Rev. Med. Phys. 9 69-244 (1937)

[Bir64] *J.B. Birks*, **"The theory and Practice of Scintillation Counting"**, Pergammon Press, Oxford 1964

[Boa84] *D.H. Boal*, Phys. Rev. C30: 749-751 (1984)

[Boi] *Ciro Boiano*, Private communications

[Boh75] *A. Bohr and B. R. Mottelson,* Nuclear Structure Vol 2 New York (1975)

[Bor91] *P.F. Bortignon et al*., Phys. Rev. Lett. 67, 3360 (1991)

[Bra89] *A. Bracco, J.J. Gaardhøje, A.M. Bruce, J.D. Garret, B. Herskind, M. Pignarelli, B. Barneoud, H. Nifinedier, J.A. Pinston, C. Ristori, F. Shlusser, J. Bacelar and H. Hofmann*, Phys. Rev. Lett. 62, 2080 (1989)

[Bra95] *A. Bracco et al.*, Phys. Rev. Lett. 74(1995) 3748

[Bru04] *B. Martin et al.,* **"Evolution of the prompt dipole γ-ray emission with incident energy in fusion heavy-ion reactions"**, presented at 5th Italy-Japan symposium, Nov. 2004 Naples, available on internet

[Cab03] *J. Cabrera, Th. Keutgen, Y. El Masri, Ch. Dufauquez, V. Roberfroid, I. Tilquin, J. Van Mol, R. Règimbart, R.J. Charity, J.B. Natowitz, K. Hagel, R. Wada, D.J. Hinde*, Phys. Rev. C68 (2003)

[Cam92] *F. Camera*, **"Le Fluttuazioni di forma e di orientamento in nuclei caldi e la distribuzione angolare dei γ della Risonanza gigante di Dipolo",** Ph. D. Thesis, University of Milan

[Cam05] *F. Camera, M. Kmiecik, O. Wieland, G. Benzoni, A. Bracco, S. Brambilla, F. Crespi, P. Mason, A. Moroni, B. Millon, S. Leoni, A. Maj, J. Styczen, M. Brekiesz, W. Meczynski, M. Zieblinski, F. Gramegna, S. Barlini, V.L. Kravchuk, A. Lanchais, P.F. Mastinu, M. Bruno, M. D'Agostino, E. Geraci, A. Ordine, G. Casini and M. Chiari* ,**"GDR in hot nuclei: new measuremets",** ACTA PHYSICA POLONICA B36(4) 1145-1153 APR 2005

[Car71] *P. Carlos et al.*, Nucl. Phys. A172, 437 (1971)

[Car05] *S. Carturan, A. Quaranta, A. Vomiero, M. Bonafini, G. Maggioni and G. Della Mea*, **"Polyimide-Based scintillators studied by Ion Beam Induced Luminescence"**, IEEE Transaction on Nuclear Science Vol.52 NO.3, June 2005

[Cas99] *G. Casini*, "**Calibration of PPAC of the GARFIELD array"**, LNL-PAC proposal 99/52

[Cas04] *G. Casini, M. Chiari, A. Nannini, S. Barlini, R. Cavaletti, G. Giordano, F. Gramegna, B. Guiot, V.L. Kravchuk, A. Lanchais, A. Moroni, a. Ordine, M. Ottanelli, L. Vannucci for the NUCLE-EX collaboration,* **"Refining energy calibration of the Nucle-ex CsI(Tl) scintillators",** Annual report L.N.L. (2004)

[Chi02] *M. Chiari, A. Lanchais, F. Tonetto, L. Travaglini*, Nucl. Instr. and Meth. A484: 111-117 (2002)

[Dan58] *M. Danos*, Nucl. Phys. 5,23 (1958)

[Dio01] *I. Dioszegy et al.,* Phys. Rev. C63, 47601 (2001)

[DST01a] *D. Durant, E. Surant, B. Tamain*, "**Nuclear Dynamics in the nucleons regime"**, IOP, 2001 Chapter 5

[DST01b] *D. Durant, E. Surant, B. Tamain*, "**Nuclear Dynamics in the nucleons regime"**, IOP, 2001 Chapter 2

[Gaa85] *J.J. Gaardhøje*, "**Frontiers in nuclear dynamics",** Vol. 25 Plenum Press (1985)

[Gaa92] J.J. *Gaardhøje,* Ann. Rev. Nucl. Part. SCI 42: 483 (1992)

[Gaa92b] J.J. *Gaardhøje, A. Maj, T. Tveter, Z. Zelazny, F. Camera, A. Bracco, B. Millon, M. Pignarelli,* XXVII Zakopane school of Physics 1992

[Gaa92c] J.J. *Gaardhøje, A. Atac, A. Maj, A. Bracco, F. Camera, B. Millon, M. Pignarelli, E. Rebesco,* Nucl. Phys. A538 (1992) 573c-584c

[Gar83] *E.F. Garman et al.*, Phys. Rev. C28, 2554 (1983)

[Gel93] *N. Gelli*, "**Studio di sistemi nucleari prodotti con reazioni tra ioni pesanti tramite la Risonanza Gigante di Dipolo"**, Ph. D. Thesis, University of Florence (1993)

[Gia05a] *M.Giacchini, P.F. Mastinu, F. Gramegna, A.R. Gadea,* "**VPS- Versatile Power Supply Control System",** 14 th IEEE-NPS Real Time Conference 2005, June 4-10, 2005 Stockolm

[Gia05b] *M.Giacchini, G.Bassato, F. Gramegna, R. Lange,* "**A tiny EPICS IOC based on PC104",** 10 th ICALEPCS 2005 International Conference on Accelerator and Large Experimental Physics Control System, October 10-14, Geneva

[Gil65] *A. Gilbert and A.G.W. Cameron*, Can. J. Phys. 43: 1446-1496 (1965)

[Gon90] *M. Gonin et al.*, **"Dynamical effects on the de-excitation of hot nuclei with A ~ 160"**, Phys. Rev. C42: 2125-2142 (1990)

[Gra] *The Garfield proposal*, F. Gramegna, not published

[Gra94] *F. Gramegna*, "**Procedings of the international workshop on Microstrip Gas Chambers"**, Legnaro 1994, editors G. Della Mea, F. Sauli

[Gra97] *F. Gramegna et al*., Nucl. Instr. And Meth. A389: 474-478 (1997)

[Gra02] F. *Gramegna, P.F. Mastinu, A. Lanchais, S. Barlini*, *A. Moroni, A. Giussani E. Galbusera, E. Gadioli, A. Ottolenghi, F. Albertini, G. Casini, M. Chiari, A. Nannini, P.M. Milazzo, A. Ordine,* "**Misure di sezione d'urto di interesse per la radioterapia ed i rischi da radiazione per astronauti: reazioni indotte da fasci di carbonio."**, Bollettino S.I.F. (2002) pag.85 LXXXVIII Congresso Nazionale S.I.F.

[Gra03a] *F. Gramegna, P.F. Mastinu, L. Vannucci, E. Boscolo Marchi,R. Cherubini, A. Moroni, A. Bracco, F. Camera, B. Millon, O. Wieland, G. Benzoni, S. Leoni, A. Airoldi, R. Sacchi, E. Galbusera, A. Giussani, A. Ottolenghi, E. Gadioli, F. Ballarin, A. Maj, M. Brekiesz, M. kmiecik, S. Barlini et al.*,**"New perspectives for studies of reaction Mechanism at low-medium energies",** ACTA PHYSICA POLONICA B34(4) 2253-2363 APR 2003

[Gra03b] F. *Gramegna, S. Barlini et al*., "**Heavy Ion Reaction Mechanism Studies at Low-Medium energies with the GARFIELD apparatus"**, XLI Winter Meeting on Nuclear physics, Bormio (Italy) 2003

[Gra04a] *F. Gramegna, A. Moroni, G. Casini, M. Bruno, U. Abbondanno, R. Bassini, S. Barlini, et al.* **"GARFIELD: a General Array for Fragment Identification and for Emitted Light particles in Dissipative collisions",** 2004 IEEE Rome

[Gra04b] *F. Gramegna, S. Barlini, V.L. Kravcouk, A. Lanchais, E. Boscolo Marchi, P.F. Mastinu, L. Vannucci, F. Cerutti, E. Gadioli, A. Moroni, M. Murano, M. Cavinato, E. Fabrici, E. Gadioli-Erba, a. Giussani, M. Bruno, M. D'Agostino, E. Geraci, G. Casini, A. Nannini, M. Chiari, P. Del Carmine, F. Ballarini, A. Ottolenghi,* **"Large angle α-particle emission in $^{12}C + ^{12}C$ interaction up to 20 MeV",** Annual report L.N.L. (2003)- Rep. INFN XXX/2004

[Gra05] *F. Gramegna, S. Barlini, V.L. Kravchuk, A. Lanchais, O. Wieland, A. Bracco, A. Moroni, G. Casini, G. Benzoni, N. Blasi, S. Brambilla, M. Brekiesz, M. Bruno, F. Camera, M. Chiari, F. Crespi, E. Geraci, B. Guiot, M. Kmiecik, S. Leoni, A. Maj, P.F. Mastinu, P. Mason, B. Millon, A. Nannini, A. Ordine, and G.Vannini* ,**"Light Charged Particle emission and the Giant Dipole Resonance in Ce nucleus",** ACTA PHYSICA POLONICA B36(4) 1155-1160 APR 2005

[Gri88] *K.A. Griffoen et al*., Phys. Rev. C37, 2502 (1988)

[Hah87] *D. Hahn and H. Stöcker*, Phys. Rev. C35: 1311-1315 (1987)

[Hah88] *D. Hahn and H. Stöcker*, Nucl. Phys. A476: 718-772 (1988)

[Hil79] *D. Hilscher et al*., Phys. Rev. C20 (1979) 576

[Hin92] *D.J. Hinde, D. Hilscher, H. Rossner, B. Gebauer, M. Lehmann and M. Wilpert,* Phys. Rev. C45, 1229 (1992)

[Hol83] *E. Holub, D. Hilscher, G. Ingold, V. Jahnka, H. Orf and H. Rossner,* Phys. Rev. C28, 252 (1983)

[Hui72] *J.R. Huizenga and L.G. Moretto*, Kun. Rev. Nucl. Sci. 22: 427-464 (1972)

[Kel97] *M.P. Kelly, J.F. Liang, A.A. Sonzogni, K.A. Snover, J.P.S. van Schagen and J.P. Lestone*, Phys. Rev. C56: 3201-3209 (December 1997)

[Kel99] *M.P. Kelly, K.A. Snover and J.P.S. van Schagen*, Phys. Rev. Lett. Vol.82 NUM.17: 3404-3407 (April 1997)

[Kno79] *G.F. Knoll,* "**Radiation Detection and Measurement**", Printed in the U.S.A.

[Kub90] *S. Kubuta, J. Ruan(Gen), M. Itoh, S. Hashimoto and S. Sakuragi,* **"A new type of luminescence mechanism in large band-gap insulators: proposal for fast scintillation materials.",** N.I.M. A289 (1990) 253-260

[Kus03] *D. Kusnezov and W. E. Ormand*, Phys. Rev. Lett. 90 (2003) 042501-1 and reference therein

[Lan01] *A. Lanchais*, "**GARFIELD: un apparato per misure di reazioni tra ioni pesanti ad energie imtermedie"**, Graduation Thesis, university of Bologna

[Lav83] *M. Laval, M. Moszynski, R. Allemand, E. Cormoreche, P. Guinet and R. Odrn*, **"Barium Fluoride- Inorganic scintillator for subnanosecond timing"**, N.I.M. 206 (1983) 169-176

[Lee92] *H.K.W. Leegte, A.L. Boonstra, J.D. Hinnefeld, E.E. Koldenhof, R.H. Siemssen, K. Siwek-Wilczynska, Z. Sosin, J. Wilczynski and H.W. Wilschut,* Phys. Rev. C46, 991 (1992)

[Lej86] *A. Lejeune, P. Grange, M. Martzolff, and J. Cugnon*, Nucl. Phys. A453, 189 (1986)

[Ma97] *Y.G Ma et al.*, Phys. Lett. B390: 41 (1997)

[Maj94] *A. Maj et al*., Nucl. Phys. A571, 1 (1994)

[Majk96] *Z. Majka et al.*, preprint TAM 96-03 (1996)

[Mas93] P.*F. Mastinu, P.M. Milazzo, M. Bruno, M. D'Agostino and L. Manduci*, Nucl. Instr. and Meth. A338 (1994) e A343 (1993) 663

[Mor85] *D.J. Morrissey, W. Benenson, E. Kashy, C. Bloch, M. Lowe, R.A. Blue, R.M. Ronningon B. Sherrill, H. Utsunomiya, I. Kelson*, Phys. Rev. C32: 877-886 (1985)

[Mor94] *D. Morrissey, W. Benenson and W.A. Friedman,* **"Measurement of temperature in nuclear reaction**", MSUCL-922 Feb. 1994

[Mor05] *A. Moroni, M. Bruno, L. Bardelli, S. Barlini, S. Brambilla, G. Casini, R. Cavaletti, M. Chiari, A. Cortesi, M.D'Agostino, J. De Sanctis, E. Geraci, G. Giordani, A. Giussani, F. Gramegna, B. Guiot, V. Kravchuk, A. Lanchais, G.V. Margagliotti, A. Nannini, A. Ordine, S.*

Piantelli, G. Vannini, L. Vannucci, **"The Ring Counter (Rco): a high resolution IC-Si-CsI(Tl) device for heavy ion reaction studies at 10-30 AmeV",** accepted by N.I.M

[New81] *J.O. Newton, B. Herskind, R.M. Diamond, J.E. Dines, J.E. Draper, K.H. Lindenberger, C. Schuck, S. Shih and F. Stephens*, Phys. Rev. Lett. 46:1383 (1981)

[Ord95] *A. Ordine, A. Boiano and E. Vardaci*, "**FAIR: a new fast read out bus system for large detector array"**, Fifth Annual Le Croy Conference on electronics For Particle Physics, May 1995, Le Croy Corporation, Chestnut Ridge, New York, USA, G.J. Blanar and R.L. Summer Eds, 1851-1858

[Ord98] *A. Ordine et al*., IEE Transaction on Nuclear Science, Vol. 45, N°3 June 1998

[Orm97a] *W. E. Ormand et al.*, Nucl. Phys. A617(1997) 20

[Orm97b] *W. E. Ormand et al.*, Nucl. Phys. A614(1997) 217

[Poc95] *J. Pochodzalla et al.*, Phys. Rev. Lett. 75: 1040 (1995)

[Pri93] *D. Prindle, R. Vandenbosch, S. Kailas, A. Charlop, and C. Hyde-Wright*, Phys. Rev. C48, 291 (1993)

[Qua02] *A. Quaranta, A. Vomiero, S. Carturan, G. Maggioni and G. Della Mea*, **"Polymer film degradation under ion irradiation studied by Ion Beam Induced Luminescence (IBIL) and optical analysis"**, N.I.M. B 191(2002) 680-684

[Qua05] *A. Quaranta*, **"Recent developments of Ion Beam Induced Luminescence: radiation hardness study of thin film plastic scintilators"**, N.I.M. B 240(2005) 117-123

[Sno86] *K.A. Snover*, Ann. Rev. Nucl. Part. Sci. 36,545 (1986)

[Sur89] *E. Surand, Ch. Grègoire and B. Tamain*, Prog. Part. and Nucl. Phys. 23, 357-467 (1989)

[Tam91] *B. Tamain*, Proc. Intl. Sch. Of Phys. CXII, Varenna (North Holland, 1991) 1-36

[Ton99] *F. Tonetto et al.*, Nucl. Instr. and Meth. A420, 181 (1999)

[Tsa96] *B. Tsang et al.*, Phys. Rev. C53: R1057 (1996)

[Voi89] *R.K. Voijtech et al.*, Phys. Rev. C40, 2441 (1989)

[Yos90] K. *Yoshida et al*., Phys. Lett. B245, 7 (1990)

[Wad89] *R. Wada et al.*, Phys. Rev. C39, 497 (1989)

[Wei37] *U. F. Weisskopf*, Phys. Rev. 52, 295-303 (1937)

[Wie05] *O. Wieland, S. Barlini, V.L. Kravchuk, A. Bracco, F. Camera, F. Gramegna, A. Maj, G. Benzoni, N. Blasi, S. Brambilla, M. Brekiesz, M. Bruno, G. Casini, M. Chiari, E. Geraci, A. Giussani, M. Kmiecik, S. Leoni, A. Lanchais, P.F. Mastinu, B. Millon, A. Moroni, A. Nannini, A. Ordine, G.Vannini, L. Vannucci*, Journal of Physics G31(2005)S1973

[Wie06] *O. Wieland, A. Bracco, F. Camera, G. Benzoni, N. Blasi, S. Brambilla, F. Crespi, A. Giussani, S. Leoni, B. Millon, S. Barlini, V.L. Kravchuk, F. Gramegna, A. Lanchais, P.F. Mastinu, A. Maj, M. Brekiesz, M. Kmiecik, M. Bruno, M.D'Agostino, E. Geraci, G. Vannini, G. Casini, M. Chiari, A. Nannini, A. Ordine, E.Ormand,* **"GDR in the hot and thermalized 132Ce nuclei: damping of collective modes at finite temperature",** to be published

RINGRAZIAMENTI

Considerando che i ringraziamenti li sto scrivendo nella notte del 1 gennaio, il termine ultimo imposto dalla Faby è già scaduto per cui anche tu Vlady dovrai cominciare a parlare e leggere l'italiano e quindi puoi cominciare ad allenarti usando i miei ringraziamenti.....

Prima di tutto devo ringraziare il mio relatore, il Prof. Paolo Mazzoldi per la sua gentilezza e disponibilità e la Dott. Fabiana Gramegna per l'attenzione con cui mi ha seguito e guidato lungo tutti questi 3 lunghi anni di dottorato, francamente senza di lei dubito che avrei intrapreso questa strada.... Devo poi citare Vladimir Kravchuk ed Oliver Wieland per l'affetto e l'aiuto fondamentale che mi hanno dato nell'analisi dei dati GDR, insieme abbiamo discusso, lavorato e dibattutto ed è stato per me un piacere lavorare con persone così simpatiche ed intelligenti.

Come non citare poi la mia mitica vespa che, risorta dalle sue ceneri dopo il disgraziato grippaggio durante la tesi di laurea, mi ha scarrozzato qui a Padova durante questi anni di dottorato, nella buona e nella cattiva sorte, con la pioggia e con il sole, con la neve e con il ghiaccio, più fedele e meno costosa di una moglie? Un saluto anche ai ragazzi del Noviziato Kairos ai quali faccio servizio come educatore scout durante i week-end, una sorta di doppio lavoro che però mi rende pieno di gioia e felicità.

Un ringraziamento anche alla mia famiglia, che anche se mi vede sempre meno sballottato come sono tra Padova e gli scout ed i mille pensieri che ho sempre per la mente, sò che è sempre presente e che posso sempre contare su di loro.

Non mi resta che concludere usando una frase che il capitano dell'Enterprise James T. Kirk usa in uno dei suoi mille film di cui sono appasionato:

"Tutto quello di cui ho bisogno è di un buon equipaggio, una buona nave ed una stella verso la quale andare..... "